**PhD Dissertation**

---

**International Doctorate School in Information and Communication Technologies**

DISI - University of Trento

# Novel Design Solutions for High Reliability RF MEMS Switches

Francesco Solazzi

Advisor:

Dr. Benno Margesin

Head of MEMS Group - FBK

Co-Advisor:

Dr. Alessandro Faes

---

April 2010

# Abstract

*This doctorate thesis focuses on the analysis, design and characterization of Radio-Frequency (RF) Micro-Electro-Mechanical System (MEMS) switches for space applications. The work was inspired and supported by the European Space Agency (ESA) Contract No. ITT AO/1-5288/06/NL/GLC High Reliability Redundancy Switch. The main purpose of the project is the design and realization of high-reliability RF MEMS switches for satellite payload redundancy networks. Up to now, the common satellite architecture implements redundancy networks by means of bulky devices. RF MEMS switches allow for extremely miniaturized networks along with outstanding performances in terms of losses, power consumption and linearity, not really achievable with solid state devices. As requirements for such an application, RF MEMS switches have to survive under extremely harsh environmental and operating conditions. In particular the device should handle continuous bias voltage (at least for 10 years), 5 W of RF input power and around 1000 actuation cycles without meaningful electrical and mechanical failure. The thesis proposes novel mechanical solutions to accomplish this task, exploiting active restoring mechanisms able to restore the previous status of switch in case of reversible failure. This work also provides a deep insight on the main reliability aspects of a RF MEMS device such as dielectric charging, contact degradation and power handling.*

**Keywords**

[RF MEMS Switches, Redundancy Networks, Active restoring mechanisms, Reliability]

# List of publications

## Conference Papers

- P. Farinelli, **F. Solazzi**; C. Calaza, B. Margesin, R. Sorrentino, "A Wide Tuning Range MEMS Varactor Based on a Toggle Push-Pull Mechanism", *Proceedings on 38th European Microwave Conference (EuMC), 2008*, pp. 474-477, Amsterdam, 27-28 Oct. 2008.

- **F. Solazzi**, P. Farinelli, B. Margesin, R. Sorrentino, "35 GHz Analog Phase shifter based on push-pull Toggle MEMS Varactor", *Proceedings on 9th International Symposium on RF MEMS and RF Microsystems*, Heraklion, 2008.

- **F. Solazzi**, A. Repchankova, P. Farinelli, J. Iannacci, A. Faes, B. Margesin, "Contact Modeling of RF MEMS Switches based on FEM Simulations", *Proceedings on 10th International Symposium on RF MEMS and RF Microsystems*, Trento, 2009.

- A. Tazzoli, E. Autizi, M. Barbato, **F. Solazzi**, J. Iannacci, P. Farinelli, F. Giacomozzi, B. Margesin, R. Sorrentino, G. Meneghesso, "Impact of Continuous Actuation on the Reliability of Dielectric-less Ohmic RF MEMS Switches, *Proceedings on 10th International Symposium on RF MEMS and RF Microsystems*, Trento, 2009.

- A. Tazzoli, E. Autizi, M. Barbato, G. Meneghesso, **F. Solazzi**, P. Farinelli, F. Giacomozzi; J. Iannacci, B. Margesin, R. Sorrentino, "Evolution of electrical parameters of dielectric-less ohmic RF-MEMS switches during continuous actuation stress", *Proceedings of the European Solid State Device Research Conference, (ESSDERC) 2009*, pp. 343-346, 14-18 Sept. 2009.

- J. Iannacci, D. Macii, B. Margesin, A. Repchankova, **F. Solazzi**, "Una procedura per la stima degli effetti dell'incertezza di processo sulle prestazioni di dispositivi RF-MEMS", *Atti del XXVI Congresso Nazionale del Gruppo Misure Elettriche ed Elettroniche*, pp. 121-122, Salerno,16-19 Sept. 2009.
- C. Palego, **F. Solazzi**, S. Halder, J.C.M. Hwang, P. Farinelli, R. Sorrentino, A. Faes, V. Mulloni, B. Margesin, "Analysis of Power Capacity of RF MEMS Capacitive Shunt Switches Fabricated on Silicon or Quartz Substrates", *Proceedings on 11th International Symposium on RF MEMS and RF Microsystems*, Otranto, 2010.
- **F. Solazzi**, C. Palego, S. Halder, J.C.M. Hwang, A. Faes, V. Mulloni, B. Margesin, P. Farinelli, R. Sorrentino, "Electro-thermal analysis of RF MEM capacitive switches for high-power applications," *Proceedings of the European Solid-State Device Research Conference (ESSDERC), 2010*, pp. 468-471, 14-16 Sept. 2010.
- C. Palego, **F. Solazzi**, S. Halder, J.C.M. Hwang, P. Farinelli, R. Sorrentino, A. Faes, V. Mulloni, B. Margesin, "Effect of substrate on temperature range and power capacity of RF MEMS capacitive switches,"*Proceedings on European Microwave Conference (EuMC), 2010*, pp. 505-508, 28-30 Sept. 2010.
- **F. Solazzi**, A. Tazzoli, P. Farinelli, A. Faes, V. Mulloni, G. Meneghesso, B. Margesin, "Active recovering mechanism for high performance RF MEMS redundancy switches,"*Proceedings on European Microwave Conference (EuMC), 2010*, pp.93-96, 28-30 Sept. 2010.

- **F. Solazzi**, J. Iannacci, A. Faes, F. Giacomozzi, B. Margesin, A. Tazzoli, G. Meneghesso, "Modeling and characterization of a circular-shaped energy scavenger in MEMS surface micromachining technology," *Proceedings on SPIE Microtechnology 2011*, Prague, April 2011.
- **F. Solazzi**, G. Resta, V. Mulloni, B. Margesin, P. Farinelli, "Influence of beam geometry on the dielectric charging of RF MEMS switches," *Accepted at European Microwave Conference (EuMC), 2011*, pp.93-96, 28-30 Oct. 2011.

## Journal Papers

- **F. Solazzi**, C. Palego, S. Halder, J.C.M. Hwang, A. Faes, V. Mulloni, B. Margesin, P. Farinelli, R. Sorrentino, "Effect of the Substrate on RF Power-Handling Capability of Micro-Electromechanical Capacitive Switches", Accepted for publication on *Solid State Electronics Journal - Special Issue from ESSDERC/ESSCIRC Conference 2010*, Elsevier.
- **F. Solazzi**, A. Tazzoli, P. Farinelli, A. Faes, V, Mulloni, G. Meneghesso, B. Margesin, "Design and characterization of an active recovering mechanism for high performance RF MEMS redundancy switches", Accepted for publication on *International Journal on Microwave and Wireless Technologies - Special issue on RF MEMS*, Cambirdge University Press.

# Acknowledgments

During my Ph.D activity I met an amazing number of people who really gave a fundamental contribution to my personal and professional growth. I do not know if I will be able to really thank all of them.

First of all, a special and deep acknowledgment is for my advisor Benno Margesin. He was really a mentor in the world of Research. His guidance and his constant encouragement were always precious, and his extensive scientific knowledge of almost *everything* never stops surprising me.

I do not know how I have to do to pay back my colleague and co-advisor Alessandro Faes for the constance and patience he showed me in reviewing this thesis and almost all the papers I published.

Then I absolutely have to thank all the MEMS group. First, Jacopo Iannacci, whose professional guidance and also friendship helped me a lot in overcoming some critical moments. A special thank goes to Flavio Giacomozzi, who welcomed me for first in FBK when I was just a master student. His valued suggestions and huge experience are still fundamental to make all my designs work.

I am deeply in debt with my colleagues Viviana Mulloni and Sabrina Colpo. I was often stressful towards them, but both have always been helpful and I always received a positive answer for anything I asked. I am in debt too with Giuseppe Resta, whose contribution in the measurement setups was fundamental for my recent scientific works.

I want also to thank my past colleagues, Carlos Cabana (who introduced me in the finite element method world for first), Parisa Savadkoohi and Alena Repchankova (who are now pursuing their carriers outside the MEMS World), and my most recent officemates, Dan Vasilache, Claudia

Giordano, and Abdul Qureshi.

I am grateful to Prof. Roberto Sorrentino from University of Perugia for his support and the opportunity he gave me when he proposed me to pursue a Ph.D in Trento, and especially when he provided me the connection for my US experience. A big thank goes to Paola Farinelli from RF Microtech, who introduced me in the MEMS World for first. She was the first person who found a researcher in me. Her constant support during all my activity and her expertise helped me really a lot in acquiring a wide and complete vision of all my research field. I reserve a special thanks to Augusto Tazzoli from University of Padova, who really supported me with suggestions and hard work at any hours of the day in most of my published papers.

I would like also to thank all the people I met during my precious experience in United States. I am grateful to Prof. James Hwang who accepted me as a member of his research group, making me feel like part of it from the very beginning. I want to express all my deep acknowledgment to Cristiano Palego, David Molinero Giles and Bora Baloglu, who behaved with me like a family during my stay in Bethlehem. I will never forget their outstanding contribution to my professional growth. A big thanks also to the other members of the CSTL group at Lehigh University, Steven Peng, Weike Wang, Guanghai Ding, Xi Luo, Subrata Halder, Cheng Chen and Renfeng Jin.

I want also to acknowledge all the people from DISI department who contributed to my professional grow. In particular, a special thanks is for Prof. Gianfranco Dalla Betta, Prof. Dario Petri and Dr. David Macii.

A final thank goes to all the people from MTLab and FBK and to all the people that supported me during these years.

*To my Parents*
*To Simeone and Milena*

***Neo***: *"What are you trying to tell me,*
*that I can dodge bullets?"*
***Morpheus***: *"No Neo. I'm trying to tell you*
*that when you're ready, you won't have to."*

(*The Matrix*, 1999)

# Contents

# List of Tables

# List of Figures

# Chapter 1

# Introduction

In the last decade *Micro-Electro-Mechanical System* (MEMS) devices have experienced a tremendous development in various fields of the Information and Communication Technologies (ICT). Especially the recent trends towards the interaction between integrated circuits (IC) components and external environment pushed for the design of innovative devices and technologies able to couple electrical properties with several different physical domains. In particular MEMS devices exploit a miniaturized movable structure whose movement or position can interact with electrostatic, thermal, magnetic, fluidics, electromagnetic signals. Reliability, compactness and high integration were some of the key factors for the achievement of successful market products, such as ST Microelectronics accelerometers for car airbag and Nintendo Wii controller, Apple I-Phone gyroscopes, ink-jet units, Texas Instruments digital micro-mirror devices (DMD) for projectors.

One of the most promising application field of MEMS technology is related to microwave and radio-frequency (RF) communication circuits and devices. When MEMS technology is applied to the microwave world, one usually refers to that as RF MEMS.

## 1.1 Radio Frequency MEMS

In recent years, the spreading of novel wireless communications standards has introduced new challenges in the design of the transceiver hardware. At the device level, low power consumption, high linearity and large bandwitdh are among the most important requirements that every component has to fulfill in order to achieve high performance wireless systems. At the system level, highly-reconfigurable circuits allow the modern wireless systems to be multi-platform, that is, to integrate all the most-diffused communication standards (such as UMTS, GSM, WiFI, Bluetooth, WiMax) without loosing compactness and quality. RF MEMS technology allows for the creation of devices and circuits that may respond to the requirements and capabilities mentioned above.

The idea behind RF MEMS is to use miniaturized movable structures to implement high performance resonators, varactors, inductors, and switches. The application fields embrace mobile phone terminals, base stations, phased array antennas, multi-purpose radars, high quality test instruments and satellite payloads. Recently, most of the attention has been turned to *electrostatic* RF MEMS switches.

RF MEMS switches exhibit superior performance in terms of losses, linearity, power consumption and cut-off frequency with respect to commercial solid-state devices, such as PIN diodes or FET (Field-Effect Transistor) switches. A MEMS switch is essentially a passive device, so it may be employed to build low-power and low-loss re-configurable filters and attenuators, impedance matching networks, digital phase shifters, and switching networks. Still, it can be easily integrated in microstrip, slotline and coplanar waveguides by means of the surface micro-machining fabrication process.

An interesting application for RF MEMS switches is the switching matrix for satellite payload applications. Satellite systems usually consist of several redundant payloads, which aim at improving the lifetime of the whole system itself. For this purpose redundancy devices are implemented into the system to commute among different payloads. Nowadays, satellite systems employ bulky mechanical switches built in coaxial and waveguide technology to implement the commutation circuits. Solid state switches may be considered as a valid substitution of mechanical switches, but they usually exhibit high loss, high power consumption and poor linearity. On the other hand, RF MEMS switches may effectively replace such a technology offering comparable RF performances in terms of loss and linearity, allowing also for a drastic reduction of the size.

The design and the development of high-reliability redundancy RF MEMS switches in Ka-band for satellite payload applications is the main objective of an European project inspired and funded by the European Space Agency (ESA) (Contract No. ITT AO/1-5288/06/NL/GLC High Reliability Redundancy Switch). This thesis focuses on the deep study and comprehension of the reliability aspects and failure mechanisms involving the electrostatic RF MEMS switch functionalities.

## 1.2 Reliability of RF MEMS

The main concern about the usage of redundancy switches in RF MEMS technology is their *reliability*. RF MEMS reliability may refer to their capacity to survive to either a very large number of actuations (*cycling stress*) or a long-time actuation (*long-term stress*) without any significant degradation of electrical and mechanical performances. In addition, further sources of stress like high power signal, temperature variation, shock and vibration contribute to the reliability assessment of RF MEMS switches, and often most of these physical and environmental phenomena are closely related among each other.

In particular, RF MEMS switches for satellite redundancy networks have to accomplish to very strict requirements in terms of long term stress, space radiation and high temperature variation. The main goal of a redundancy switch is to keep the same state (ON or OFF) for very long time. Then it is supposed to switch status in less than one second when required. The worst case is when the switch is continuously biased and the membrane is kept in the down position for 10-15 years. When the suspended membrane is not able to self-recover after the removal of the bias voltage, a *stiction* failure occurs.

There are two physical phenomena which may considerably impact on the long term reliability and eventually cause stiction:

- *Dielectric charging*: a dielectric layer is usually put on the top of the actuation pad to separate actuation pads and membrane after the actuation. When a bias voltage is applied, charges are injected into the oxide by strong the electric field. This may induce a shift in the actuation voltage, and after a period of time the membrane may not self-release and remain stuck to the actuation pad. In this case the stiction is temporary since the dielectric tends to discharge, but the prediction of the recovering is not straightforward.

- *Contact degradation*: RF currents can be concentrated on the small-size contact spots, generating high density currents which locally produces a large amount of heat. At very high local temperature, microwelding can occur, and in some cases such a stiction is not reversible, causing a permanent failure of the switch.

In addition, the following operating conditions highly influence the phenomena described above:

- *Temperature variation*: A temperature stress can contribute to the relaxation or to the increase of the residual stress, which is always present in suspended thin metal layers after the manufacturing process. Moreover, at higher temperature values the dielectric charging and discharging mechanisms can be accelerated.

- *Medium and high RF Power*: RF power may induce thermal, electric and electro-mechanical stress on the switch, causing a variation of the actuation voltage or in some cases a permanent degradation of the material. In case of capacitive switches, high power levels can cause the snap-down or the latching of the membrane, and induce charge injection into the dielectric realizing the capacitance. In case of ohmic switches, the power-dependent current densities can seriously and permanently affect the metal-to-metal contact as described previously.

## 1.3 Analysis and solutions

The long term reliability aspects of RF MEMS switches involve complex physical mechanisms, and most of them are not completely understood. The successful design of a reliable switch cannot be achieved regardless a deep analysis and comprehension of these mechanisms.

In this thesis, some advances in the analysis of the stiction phenomena and power handling capabilities are reported for the first time. These analyses allow not only for a better insight into the reliability assessment, but also for innovative design methodologies aiming at minimizing such problems. As a proof of concept, different geometries and configurations concerning the suspended membrane and the actuation pads are also investigated to minimize the charge injection and improve the power handling.

Furthermore, this thesis proposes the usage of an active push/pull mechanism to recover the RF MEMS switch from stiction. The *up* and *down* positions of the membrane are actively driven by a couple of electrically-separated actuation pads. By biasing the *pull-in* pads, the membrane switches to its down position. By applying a voltage to the *pull-out* pads, the membrane is moved far from the RF line, assuming its up position. The latter can be also used to effectively restore the *up* position when the membrane remains stuck to the down position, and vice-versa. The same concept is also exploited to realize a bi-stable switch, where the membrane no longer needs a continuous bias voltage to keep its status. In this case, the long-term dielectric charging problem is completely avoided.

All the proposed designs are manufactured by the in-house foundry of Fondazione Bruno Kessler (FBK), and tested in the specialized laboratories of University of Padova, University of Perugia and Lehigh University.

## 1.4 Structure of the Thesis

This thesis is organized as follows. **Chapter 2** reports a deep analysis on the state-of-the-art of redundancy RF MEMS switches, focusing on the failure models, process, and design solutions proposed so far. In **Chapter 3**, a brief overview on the mechanical and electromagnetic models of RF MEMS switches is presented. **Chapter 4** explains in details the failure mechanisms involved in the stiction of the RF MEMS under continuous stress, offering some important results concerning RF MEMS switches manufactured in FBK. **Chapter 5** offers a deep analysis on the power handling capacity of RF MEMS switches, and presents for the first time a compact multiphysics model useful both for design purposes and prediction of failure. Novel design concepts for long-term reliability improvement are reported in **Chapter 6**, along with analytical model, finite element analysis, and experimental characterization. Finally, **Chapter 7** will conclude and summarize this work.

# Chapter 2

# State of the art

## 2.1 Introduction

Radio-frequency (RF) redundancy switches are extensively used to build switching networks for satellite payloads applications. These switches need to accomplish very strict requirements for their utilization in space environment [1], such as low loss, low power consumption, high linearity, low sensitivity to temperature variation, robustness to space radiation, mechanical shock and vibrations.

Nowadays redundancy switch units are realized in coaxial and waveguide technologies. These units are essentially based on *electro-mechanical* devices. The space reliability of mechanical switches has been widely demonstrated and high RF performances can be achieved in K/Ka band [2]. However, they are extremely bulky, and this implies an additive cost in both the satellite system implementation and the launch process. Therefore recent research activities focused on the development of miniaturized switches with comparable or superior performances with respect to mechanical switches.

In this chapter, a brief overview of the RF switches designed and manufactured in MEMS (*Micro-Electro-Mechanical Systems*) technology is presented, with a particular focus on their usage as redundancy switches for satellite communications. A critical comparison between RF MEMS and solid state switches is also reported. In addition, the main failure mechanisms affecting the full functionality of RF MEMS switches are briefly introduced.

## 2.2 RF MEMS switches

### 2.2.1 Basics of RF MEMS

RF MEMS refer to a large variety of miniaturized devices manufactured by using a combination of CMOS (*Complementary-Metal-Oxide-Semiconductor*) process, and surface and/or bulk micro-machining process [3], which allows for the realization of physically movable parts.

RF MEMS components [4] have been extensively studied in the last 15 years. Although the idea behind MEMS technology is quite old, and the first MEMS sensors and actuators were developed at the beginning of Nineties, preliminary works about such a technology applied to RF and microwave circuits started to appear at the end of the same decade [5].

In general it is important to distinguish between MEMS devices and *micro-machining* devices for RF applications. The latter exploit surface and bulk micro-machining technology to develop miniaturized antennas and filters. On the other hand, although they can be realized with similar techniques, devices can be considered as MEMS if they employ a *movable part* for their full operability [6].

In a RF MEMS device, the position of the movable part can be adjusted by providing an external control. According to the physics which describes the relationship of such a control with the mechanical displacement, RF MEMS are classified in *electrostatic*, *magneto-static*, *electro-thermal*, or *piezoelectric*.

The *electrostatic* control is usually considered the best solution to employ in complex wireless systems. In this case a difference of potential is applied between a membrane, which acts as the movable electrode of a capacitor, and a *bias pad*, which acts as the fixed electrode. The bias pad can be a part of the transmission line or separated from the transmission line. The bias pad is usually covered by a *dielectric layer*, in order to avoid the direct metal-to-metal contact between the electrodes.

Also the preferential movement direction (*lateral* or *vertical*) provides a sort of classification, which basically depends on the adopted fabrication technology.

The most common RF components that have been designed and manufactured so far by means of MEMS technology are:

- *RF Switches*: A switch can assume two functional states, *ON* and *OFF*. Conventionally the switch state is ON when a voltage higher than a threshold voltage $V_{ON}$ is provided from the switch bias network. RF switches can be monolithically integrated in microstrip, slotline and coplanar transmission line, and, according to their topology, they can be *series* or *shunt*.

- *Switched capacitors*: in this case, one or more RF switches are used with or without metal-insulator-metal (MIM) capacitors in order to realize a high-Q tunable capacitance integrated in microwave circuits.

- *Varactors*: A varactor is a variable capacitance where the position of the moveable membrane can be slightly tuned by means of an analog control. Varactors are usually implemented in circuits where an analog control is needed in place of a digital control.

RF MEMS switches and switched capacitors represent one of the dominant application fields of MEMS technology for RF. A switch can be seen as a *two-ports network*. As shown in Fig. 2.1, a *shunt* switch is *OFF* when

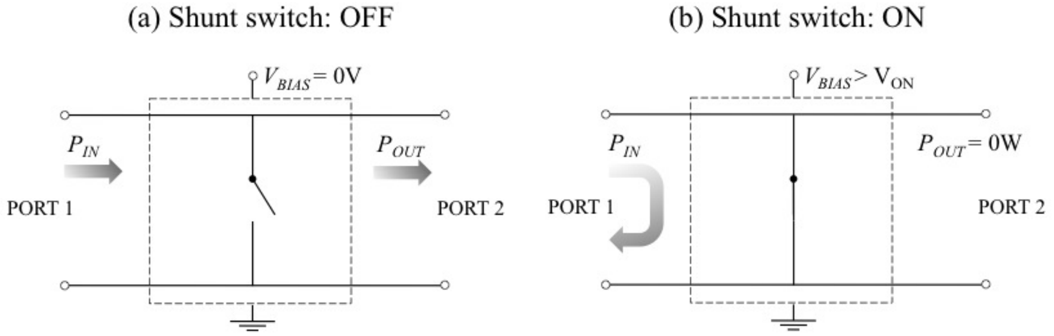

Figure 2.1: RF switches in *shunt* configuration: a) OFF state and b) ON state.

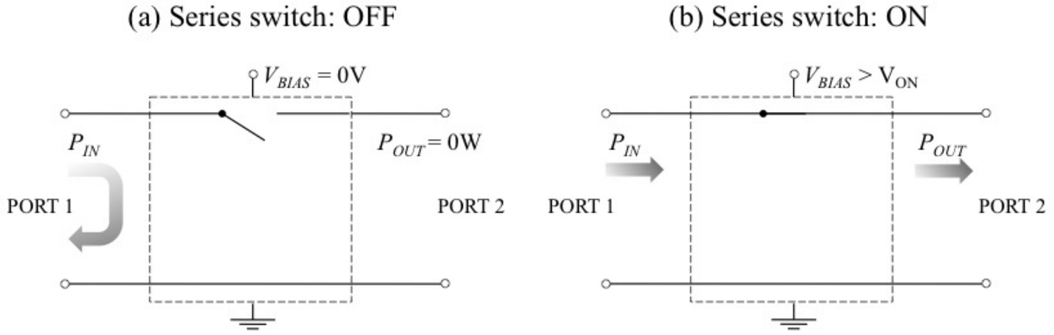

Figure 2.2: RF switches in *series* configuration: a) OFF state and b) ON state.

ideally all the delivered RF signal power can travel through it. From a RF point of view, this means ideally *no signal reflections* (*return loss* [7] equal to zero). The shunt switch is *ON* when it realizes a *short* to the ground, which is achieved when a voltage $V_{BIAS} > V_{ON}$ is provided.

On the other hand, when a *series* switch is *OFF*, no signal can go through the device, and input and output are ideally *isolated* (Fig. 2.2). When the switch is *ON*, all the RF power flows from input to output.

The above classification is general and can be applied to any kind of solid-state or mechanical switch.

RF MEMS switches can be also distinguished in *capacitive* and *ohmic* according to the nature of the movable membrane - RF line contact.

In a *capacitive* switch, the status ON or OFF is given by the value of the capacitance realized between the moveable membrane and the transmission line. Therefore a figure of merit of capacitive switches is the ratio between ON and OFF capacitance, that is, the *capacitance ratio*. Because of their characteristics, capacitive switches provide *narrowband* isolation.

In *ohmic* switches, the contact is between two *metal* surfaces. Typical figures of merit are the values of the contact resistance $R_{ON}$ and the OFF state capacitance $C_{OFF}$. Very low values of $R_{ON}$ correspond to an excellent insertion loss, whereas a low value for $C_{OFF}$ means very high isolation for a wide frequency band.

Since RF switches are usually adopted even in the realization of switched capacitors, one usually considers them as the same family. A capacitive switch usually shows a very high capacitance ratio, of the order of 100-150:1. A switched capacitor may have a capacitance ratio of 4:1, which is enough, for example, for high-Q filters [8]. A varactor can be realized by using a capacitive switch as well, but it requires a fine control of the capacitance value and a wide tuning range. Moreover, a drastic variation of the capacitance, such as in capacitive switches, has to be avoided, so varactors usually require more complex geometries.

From now on only *vertically-movable electrostatic* RF MEMS *switches* will be considered.

### 2.2.2 Advantages of RF MEMS

RF MEMS switches promise to replace solid-state switches such as PIN diode or FET (*Field Effect Transistor*) on GaAs (*Gallium-Arsenide*) substrates. The advantages with respect to these devices are numerous.

PIN diodes are largely utilized for re-configurable networks. They show high cut-off frequency (around 3-4 THz), but power consumption can be up to 100 mW. GaAs FETs have low power consumption, but they suffer from intrinsic non-linearity. For both PIN diode and FET devices, microwave losses are significantly high above 10 GHz [4].

On the other hand, typical performances for a RF MEMS switch are [8]:

- *Extremely low loss*: insertion loss better than 1 dB and return loss better than 20 dB have been demonstrated from 0.1 to 40 GHz.
- *Power consumption*: almost zero power ($\approx$ pW) is needed for static and dynamic operations.
- *High linearity*: IIP3 is usually much higher than 60 dBm, which corresponds to 20-40 dBm more than what it is for switches on GaAs technology for same input power.
- *High Q factor*: since the suspended membrane electrical resistance is usually low ($<$ 0.2-0.4 $\Omega$), quality factor is greater than 400 from 1 to 100 GHz.
- *Power handling*: some MEMS capacitive switch have been demonstrated to handle up to 5 W without any performance degradation.
- *Operating voltage*: it is usually high (5-60 V, depending on the design).

In addition, since MEMS devices involve a mechanical movement rather than a carrier transport mechanism, they are intrinsically slower than solid-state devices. The switching time is in the order of few $\mu$s, whereas FET devices are much faster (around tens of ns). Recent works [9] presented innovative MEMS switches showing a faster switching time (some hundreds of ns). This property is accomplished by reducing membrane dimensions and gap. However, for typical RF MEMS applications, the switching time is not a relevant issue.

High operating voltage is still considered one of the factor that slowed down the diffusion of RF MEMS in mobile handsets, which usually work by means of a 3.3-5 V battery. However, recent development of dedicated

DC-DC converters (such as charge pumping circuits) provided a successful solution to this issue [10].

The main focus that needs to be put on MEMS switches concerns their *reliability*. The difficulty in this task is that all the failure mechanisms are often strictly related among each other, and they involve a wide set of physical domains (mechanical, electrical, thermal, electro-thermal, electromagnetic, etc.). Innovative process techniques, design and packaging solutions were proposed in order to improve RF switch lifetime and performances. The demonstration of the MEMS reliability is the key factor for a successful spreading of RF MEMS components in the commercial market.

### 2.2.3 RF MEMS today in research and market

RF MEMS switch performances and reliability have been largely improving during the last years. Many examples of successful concepts for RF switches can be found in academia and companies. Table 2.1 reports a summary of state-of-the-art MEMS switches. Some of them are also depicted in Fig. 2.3. Among all the listed devices, there are few switches products which are up to be pushed into the market. WiSpry is now selling different circuits and components based on tunable MEMS digital capacitors [22]. Most of the WiSpry products, like impedance matching networks, tunable antennas, and filters, are designed to be easily integrated in mobile handsets [23]. One of the greatest advantages supplied by these components is to prevent the frequent call drops that affect, for example [24].

Radant demonstrated the reliability of a metal-contact switch able to handle 10 W up to 200 billion of cycles [11]. Omron [15] company utilizes a silicon movable membrane instead of a metal membrane. Such a solution allows the switch to handle high power, at the expense of a decreased quality factor.

Companies as WiSpry, Radant, MEMtronics [16] are *fabless*, so they are

Table 2.1: List of state-of-the-art RF MEMS switches from [8]

| **Company** | **Contact** | **Actuator** | **Material** | **Substrate** | **Pull-in (V)** | **Package** | **Reliability** | $R_{ON}$ ($\Omega$) | **Cap. Ratio** |
|---|---|---|---|---|---|---|---|---|---|
| Radant [11] | ohmic | Cantilever | Au | Silicon | 90 | Hermetic wafer cap | >200 Bilions | 4 | - |
| Raytheon [12] | capacitive | Air Bridge | Al | Silicon | 30-40 | Hermetic wafer cap | >200 Bilions | - | 50:1 |
| RFMD [13] | ohmic | Cantilever | Au | SOI | 90 | Hermetic dielectric cap | 1 Bilion | 1-2 | - |
| MIT-LL [14] | ohmic | Cantilever | Al | Silicon | 55-65 | Hermetic wafer cap | >600 B | - | 150:1 |
| Omron [15] | ohmic | Air bridge | Silicon | Silicon | 10-20 | Wafer package | 10 Milion | 0.5 | - |
| XCOM [8] | ohmic | Cantilever | Au | Silicon | 90 | Ceramic hermetic cap | 100 Milion | 1-2 | - |
| MEMtronics [16] | capacitive | Air bridge | Al | Glass | 25-40 | Wafer Level Liquid | >100 Bilion | - | 20:1 |
| WiSpry [8] | capacitive | Cantilever | Au | Silicon | 35 | Thin film cap | N/A | - | 20:1 |
| UCSD [17] | capacitive | Cantilever | Au | Fused Silica | 30-40 | Unpackaged | 100 Bilion | - | 7:1 |
| UCSD [18] | capacitive | Air bridge | Au | Fused Silica | 30-40 | Unpackaged | >20 Bilion | - | 5:1 |
| Limoges [19] | capacitive | Cantilever | Au | Fused Silica | 60 | Unpackaged | >1 Bilion | - | 9:1 |
| NXP [20] | capacitive | Air bridge | Al-Cu | Silicon | 20 | Hermetic wafer cap | N/A | - | 50:1 |
| RF$\mu$Tech [21] | ohmic | Cantilever | Au | Silicon | 55 | N/A | > 1 milion | 4 | - |

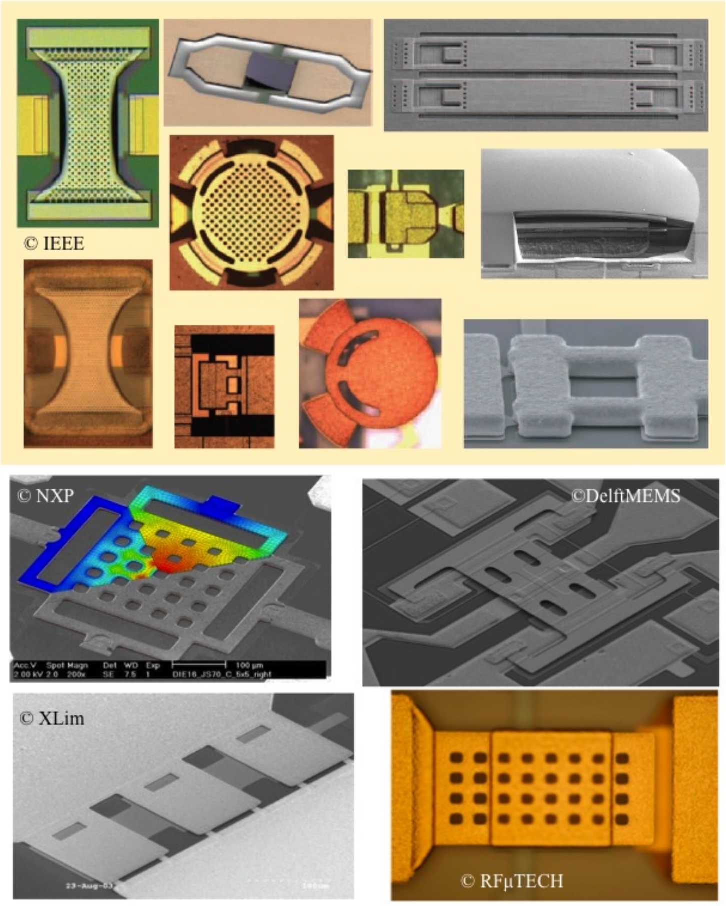

Figure 2.3: Pictures of state-of-the-art RF MEMS devices [8].

supported by external foundries (such as IBM, IMT, and others), which in most of the cases are developing a MEMS process integrated with standard CMOS process or GaAs process. Instead Peregrine [25] is developing and stabilizing a promising fabrication process on *silicon on sapphire* (SOS). Such a technology allows for the realization of low loss and highly-linear FET devices, showing also high integration capabilities with MEMS switches [26].

Despite the good promises for the near future, a mass production and a demonstration of the RF MEMS process yield for large volume of devices is what has been missing so far.

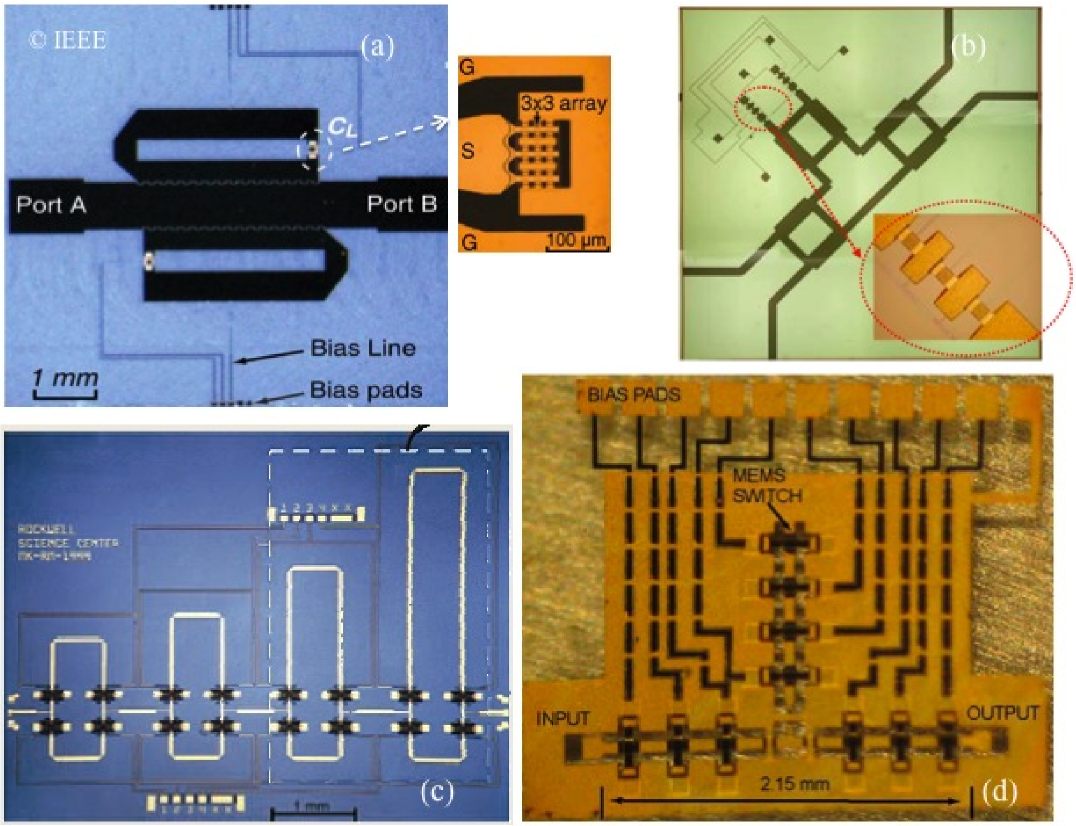

Figure 2.4: Pictures of state-of-the-art RF MEMS circuits: a) tunable filter [27], b) power divider [28], c) phase shifter [29], d) impedance matching network [30]

### 2.2.4 RF MEMS applications

RF MEMS switches and switched capacitors are the fundamental blocks for a large amount of circuits and components for the next generation of wireless systems (Fig. 2.4). Due to their outstanding performances, RF MEMS are still the preferential solution for the following microwave component areas.

- *Tunable filters and re-configurable networks*: Nowadays RF front-end transceivers require several components such as filters, diplexers and impedance matching networks in order to support the modern communication standard technologies. For this purpose the employment of *tunable* filters [23] can easily guarantee complexity reduction and compactness. The high Q-factor of MEMS capacitive switches and switched capacitors allows for the design and realization of very low-loss tunable filters, with also an extremely fine tunable capability [27]. An example of MEMS tunable filter is shown in Fig. 2.5. In addition RF MEMS switches may be successfully used in *re-configurable* impedance matching networks [30] and attenuator [31]. MEMS technology can be also used for multi-frequency antennas, where the physical dimensions of the antenna is changed by controlling a bank of MEMS switches [32].

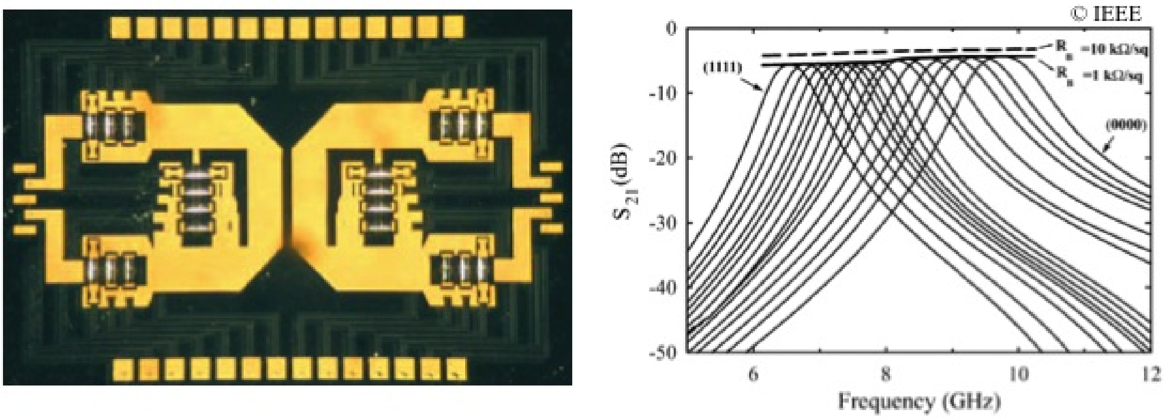

Figure 2.5: Tunable 4-bit filter based on RF MEMS switched capacitors [33].

- *Phase shifters*: MEMS switches are extremely suitable to be employed in re-configurable reflect-type, distributed-loaded transmission lines [34], true time delay phase shifters [29]. However, recent works on phase shifters based on CMOS and SiGe technology up to 100 GHz [35] slowed down the development of MEMS technology for this application. In spite of that, the low-loss, high-isolation, and linearity make RF MEMS still the best choice for wide-band true-time delay networks for phased-arrays [36] [8].

- *Single pole - N Throw (SPnT) and switching matrices*: RF MEMS

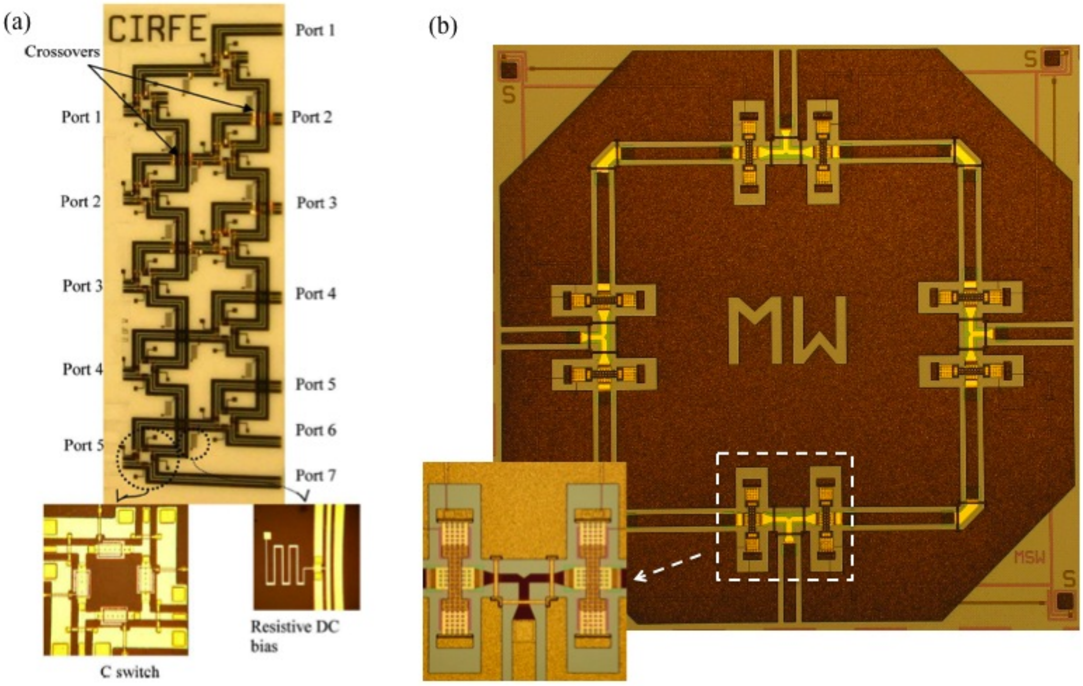

Figure 2.6: Examples of RF MEMS matrices from [37] (a) and [38] (b).

promise to replace solid-state or coaxial switches in order to have high-linearity low-loss components in switching networks. This would especially be an outstanding breakthrough for satellite applications, where MEMS switches may replace bulky coaxial switches, and keep similar performances. Example of manufactured RF MEMS matrices are shown in Fig. 2.6. This kind of application will be discussed in details in the next paragraph.

## 2.3 Redundancy networks for space applications

Satellite systems usually employ several payloads in order to avoid that the breaking of one of them compromises the full functionality of the whole system. Therefore switching networks are utilized to change the signal paths between the different payloads. The switching mechanism is implemented by means of high-performance RF switches named *redundancy*

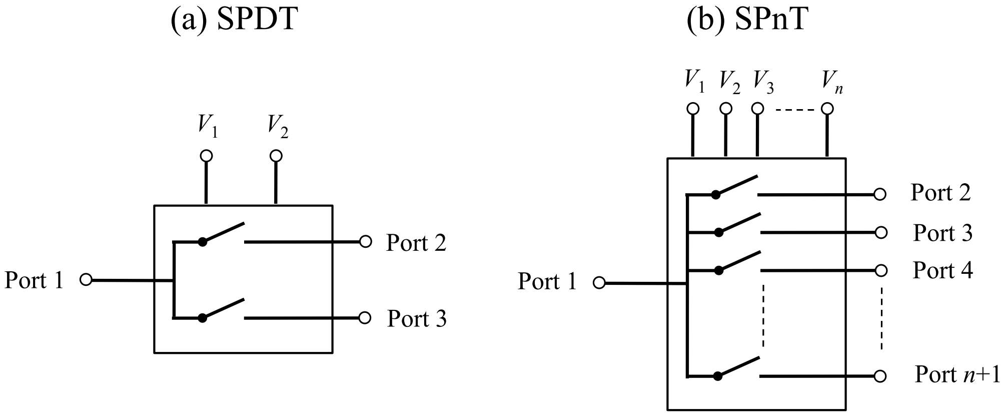

Figure 2.7: (a) Single Pole Double Throw(SPDT), and (b) Single Pole $n$ Throw switch unit schemes.

*switches.* In general, a *switch unit* (not necessarily designed for redundancy systems) can consist of one or more switches according to the number of inputs and outputs. Switch units with one input and one output are called *Single Pole Single Throw* (SPST) switches. For example, a RF MEMS switch or also a PIN diode are the simplest case of SPST.

The most common switch unit is the *Single Pole Double Throw* (SPDT) switch, which consists of one input and two outputs. When the number of outputs is greater than 3, the switch unit is referred as SP$n$T, where $n$ is the number of outputs (Fig. 2.7). These kind of circuits are extensively used in communication systems, where transmitter and receivers usually share the same antenna.

A set of switch units can be combined together to achieve a more complex switching network with several inputs and outputs. Such a configuration is also called *switching matrix.*

For satellite communications, the operational and robustness requirements that a switch unit has to accomplish are extremely challenging. Nowadays, satellite systems employ coaxial and electro-mechanical switches as the ones shown in Fig. 2.8-a. This is a very well-established technology that assures high RF performances and proved reliability [39]. A switch

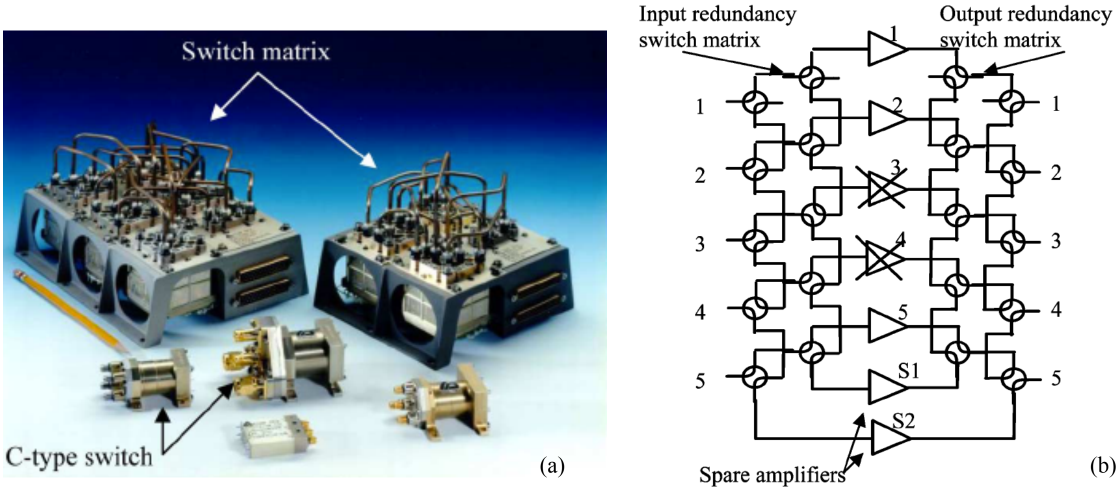

Figure 2.8: (a) Typical coaxial redundancy switch matrix and switch basic building blocks currently used in satellite systems, and (b) their application in a redundancy system [37].

unit will be an important part of a redundancy system inside the satellite, similar to the one depicted in Fig. 2.8-b.

The main disadvantage of mechanical switches is that they are extremely bulky, and replacing such switches with miniaturized devices will save space and reduce the overall cost of the system. RF MEMS switches are a good candidates to do this since they have comparable RF performances (*insertion loss* better than 1 dB and *isolation* better than 50 dB). As stated before, RF MEMS devices show also lower power consumption and higher linearity with respect to solid state devices. Up to now several works on RF MEMS SPDT switches have been reported. They have been applied, for example, as redundancy switches [37], and in switched line phase shifters [29][40]. An example of RF MEMS SPDT based on a T-junction [38] is shown in Fig. 2.9. In this case, a set of two RF MEMS switches per path is used. When a RF signal goes from Port 1 to Port 2, an ohmic series switch along the Port 2 path is ON, providing the contact between the two branches of signal line, and the capacitive switch next to it is OFF. Along the path to port 3, the ohmic switch is OFF, and the capacitive switch is ON, so that the isolation at higher frequencies is drastically improved

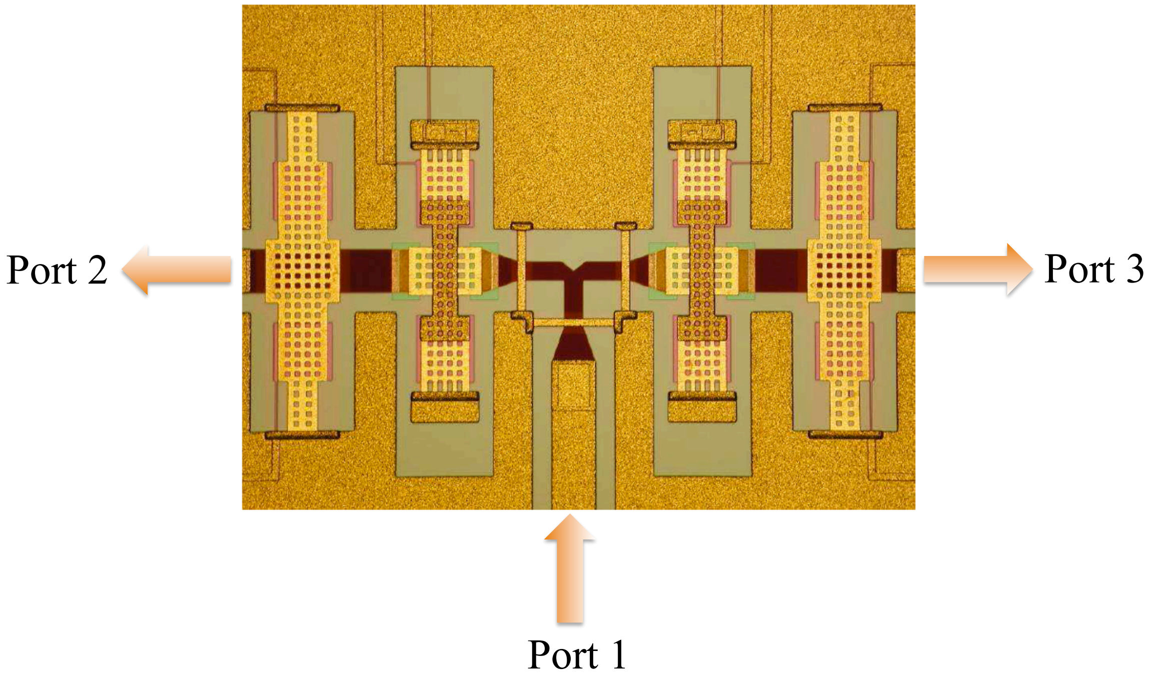

Figure 2.9: Single Pole Double Throw(SPDT) switch manufactured at FBK [38].

(better than 40 dB up to 30 GHz).

Although the high performances in terms of loss and isolation of RF MEMS switch units have been widely demonstrated, the reliability of such devices is still an open issue. This is especially true for redundancy switches, whose reliability assessment needs to accomplish rigorous requirements [41].

## 2.4 Reliability of RF MEMS

### 2.4.1 Definition

As mentioned previously, many aspects concerning the reliability of RF MEMS have not been solved yet [42], and this has really limited the real spreading of such a technology into commercial market. In micro-electronic industry, the term *reliability* usually refers to a statistical description concerning the mass production of the devices, aiming at predicting, for example, the *mean time to failure* (MTTF) [43]. In RF MEMS field, the term *reliability* pertains to a set of complex physical phenomena which may lead to a degradation of RF performances or also to the temporary o permanent failure of the device.

There is not a defined standard for the evaluation of the reliability of RF MEMS switches. However, it is extensively recognized that the goodness of a MEMS device can be determined on a set of *figures of merit* such as:

- *Life-cycle*: number of ON-OFF fast repetitive commutations that the device can handle without any sort of degradation or failure.
- *Temperature range*: Range of temperatures in which the switch can be considered still working.
- *Long-stress life-time*: period of time in which the switch can continuously keep the ON state and still commute to the OFF state when required.

The above figures are usually provided at a certain RF input power, and RF performances (isolation, insertion loss, linearity, operating frequency) or electric properties ($V_{ON}$) variations are monitored according to this figures. Shared criteria by which the variation of these parameters can be considered acceptable are still not well-defined, although a 5-10 % of variation from the expected values is utilized in most of the cases.

Especially for satellite redundancy switches, the requirements in terms of reliability are very stringent. In order to be suitable for space applications, an electronic device should be able to survive first to the satellite launch stage, and then to an extremely harsh environment, in according to the MIL-883E standard [1].

The long-stress lifetime is maybe the most important and difficult requirement to accomplish in space communications. A switch unit should remain in the same state until a fault occurs inside the subsystems. This means that, in case of a fault of an amplifier, a redundancy switch biased for a long time (i.e. ten years) must change its state in a time that should be as short as possible once the applied bias voltage is removed.

The phenomena affecting the lifetime of a RF MEMS switch embrace more physical domains, and they are often closely correlated among each other. Thus it is not easy to deal separately with a single failure mode without facing the effect of another one. Nevertheless, the main failure modes can be distinguished according to their origin.

### 2.4.2 Electrical-induced failures

Electrical-induced failure modes are related both to the propagation of the RF signal through the MEMS switch and the use of localized high electric fields in case of electrostatic control. The most important electrical-related physical phenomena which may cause a switch failure or degradation are:

- *Dielectric charging*

  The dielectric layer covering the bias pad can undergo high-intensity electric fields. When the suspended membrane touches the dielectric, charges can be injected inside the dielectric itself, exploiting the existence of defects in the dielectric material. Depending on the electrodes materials and dielectric material adopted for the switch, charges can be injected from the membrane (when in contact with the dielectric) or also from the bias electrode [44]. Mechanisms of slow dipole polarization may also be important for long stress even if the contact between membrane and dielectric does not occur [45]. The quality of the dielectric [46] [47], the operating temperature [48], and the substrate [49] impact on the charging process significantly. The main effect of this phenomenon is the creation of a built-in voltage that shifts the $V_{ON}$ value of the switch. For a *positive* shift, the switching operation no longer occurs if $V_{ON}$ becomes higher than $V_{BIAS}$. For *negative* shift, the switch could not turn back to the OFF state even if $V_{BIAS}$ is put equal to zero. In this case, since the membrane is *stuck* to the dielectric layer, such a phenomenon is conventionally called *stiction*. For very high electric fields, even a not-reversible localized *breakdown* of the dielectric can occur [50].

- *Contact Microwelding*:

  Ohmic switches operate by means of a metal-to-metal contact, which involves a very complex physics dependent on the temperature, the impact and the movement between the metals interfaces. The RF current density, which is related to the *power* of the propagating RF signal, has a strong impact on the metal-to-metal contact conditions. When the current increases, very high current densities are concentrated in contact micro-spots [51]. As a consequence, a very high temperature rise may occur, leading to a not-reversible degradation of the material, and also to localized *micro-weldings*. Even in absence of RF currents or with very low currents, welding phenomena can occur because of surface adhesion forces [52]. Other phenomenon related to the physics of the contact such as *wear*, *pitting* and *hardening* (which result from the impact and/or the sliding between two surfaces during the switching operations) may degrade the metal contact surface even though no micro-welding actually occurs. This in turns affects the equivalent *contact resistance*, leading to a deterioration of the overall insertion loss of the RF switch [53].

- *Electro-migration*:

  Electro-migration refers to the removal and drift of the atoms of a conductive material under high current densities. This phenomenon is especially evident at the metal-contact interface of ohmic switch. However, high RF power inducing high currents on the conductors may also cause electro-migration and material transfer in any points of the conductor material where the current density is particularly high. For example, some works [4] report that gold material can handle a current density up to 4 MA/cm$^2$.

Dielectric charging and contact micro-weldings give an upper limit to the long-stress lifetime of RF MEMS switches, which is fundamental in redundancy systems. Both the phenomena may lead to *stiction*, that is, the switch OFF-state is no longer achievable from an ON-state biased switch. In general stiction may be *reversible*, but the switch could take a very long and unpredictable time to fully recover.

### 2.4.3 Operational-induced failures

Some failures are related to the switch operations, and they are usually referred to as:

- *Power handling*:

  This is the amount of RF power that a switch can handle without failure or evident performance degradation. RF power may have several implications on the functionality of the switch, since it involves a lot of complex physical mechanisms. The root mean square (RMS) voltage of the RF signal power acts on the membrane as a bias voltage causing in some cases unwanted switch status commutations or also *latching* [54]. This phenomenon is referred to as *self-biasing.* The high power dissipated on the membrane produces a high temperature rise, which in turns affects the stress status of the membrane (*self-heating*). Moreover, the high density currents may seriously affect the metal properties, and produce electromigration phenomena, plastic deformation and material melting. Recently, some MEMS designs demonstrate to handle up to 10 W [55]. This topic will be treated in more detail in Chapter 5.

- *Electrostatic discharge*:

  An electrostatic discharge (ESD) is an instantaneous high current flowing through a dielectric because of a sudden electric potential difference between two points. This usually leads to an irreversible *breakdown* of the dielectric layer, which starts behaving like a conductor. ESD is a common problems in all the electronic circuits and it is prevented by the use of an appropriate protective circuitry. In MEMS devices a similar mechanism is difficult to integrate [56].

### 2.4.4 Mechanical failure modes

Since MEMS involve fast and repetitive mechanical movements, including large displacements (that is, the displacement of a movable structure is comparable with one of the dimension of the structure itself), also mechanical-induced failure modes affect the full functionality of the MEMS switch. The most important mechanical degradation mechanisms having a significant impact on the switch performances and lifetime are:

- *Fatigue*

  Fatigue consists in the progressive damage of a material subject to a cycling stress load. For high aspect-ratio structures like RF MEMS membranes, during the switching operations high concentrations of stress are present on the hinges or on the membrane corners. The effect of the cyclic loading is particularly important on these points. Where the stress is very high, cycling load can lead to the formation of surface *micro-cracks* that cause the slow weakening of the material over time and create localized plastic deformations and also *brittle fractures* [57]. The damage or crack of the material is detected by a degradation of electrical and electromagnetic parameters, since the switch stops working as expected [11].

- *Creep*

  Creep is the tendency of a material to move or deform permanently if subject to a long stress. Unlike fracture, which happens suddenly, creep is the result of a slow accumulation of strain in a long period of time. Then creep is a time-dependent and also a temperature-dependent phenomenon [58]. For redundancy RF MEMS switch requirements, it is then even more important than fatigue.

- *Vibration and shock*

  External vibrations can have a disastrous impact on MEMS devices. Vibrations contribute to accelerate the fatigue of the material, also inducing localized *fractures* that can compromise the functioning of the switch [59]. While a vibration is considered a set of random and repetitive loads, a *shock* refers to a single short mechanical impact that can lead to a significant break of the device. Basically it is a sudden transfer of mechanical energy all along the device. Vibrations and shocks are common events during the launch stage of a satellite system to the space [41].

### 2.4.5 Environmental failure modes

Finally, the failure of a MEMS device may happen even because of a change in the surrounding environmental conditions. The following aspects give the major contribution to any environmental variations:

- *Temperature*:

  A temperature variation has a direct effect on the mechanics of the MEMS switch. In fact, the residual stress of the deposited thin films may significantly change due to temperature variations. This happens because of the difference between the thermal expansion coefficients of the layers forming the suspended membrane, and the substrate, working as a support for the switch [60]. Also the intrinsic stress of the deposited materials due to molecular interaction or interfaces crystalline mismatch responds to a temperature variation. For very high temperature variation, also plastic deformation and material melting can be induced. Moreover the *buckling* of suspended structures may occur if critical values of stress are reached. It is clear that the primary effect of a stress variation is on the electro-mechanical parameters such as the $V_{ON}$. Different materials [61] and different switch designs [62] have been extensively studied to make the devices less sensitive to temperature variations.

- *Humidity*:

  Humidity has an important effect on increasing the adhesion forces between two contacting surfaces. Therefore, if the switch operates in a not-controlled environment, humidity affects its functionality, and it can also cause stiction in case of both metal-to-metal and metal-to-dielectric type of contact. Humidity also plays an important role in the dielectric charging [63].

- *Radiation*:

  High energy radiations are important especially in space environments. In electronic devices [1] radiations can cause bulk lattice damage and make materials more susceptible to fracture. Radiations can also induce space charges in dielectric layers, and then create a permanent electric field compromising the correct functioning of the device. In devices with mechanical-movable structures, like MEMS switches, some radiations can affect the Young modulus of the movable materials, causing a variation in the electro-mechanical properties [64].

### 2.4.6 RF MEMS Packaging

Another important reliability aspect of RF MEMS switches relies on the *package* implementation. A reliable package is fundamental for RF components high-volume production. For RF MEMS switches, a package has to work first as a *mechanical support* for the device, and also provide a *protection* from external humidity and any kind of contaminants. For this reason the package should be preferably *hermetic*. A vacuum package is largely used for MEMS resonators and sensors, but for RF MEMS switches the utilization of inert gases such as nitrogen is preferred in order to dump any sort of unnecessary mechanical oscillation [4].

In addition the evaluation of the reliability of a MEMS device in terms of lifetime and robustness may drastically change once the device is packaged. The design and the fabrication of an effective package for RF MEMS are not easy tasks. The package should not significantly affect the electromagnetic properties of a RF switch. Moreover, the realization process of a package should minimize the mechanical stresses on the switch die, to prevent any implications in the correct mechanical functionalities of the MEMS device [65].

Different packaging and chip assembly techniques have been developed so far. For example, *flip-chip assembly*, *ball-grid array*, *wafer level package* techniques can be found in literature [4]. Among these, an effective way to package a RF MEMS switch is a 0-level package or *wafer level package* (WLP) [66]. The package is implemented at the wafer level, allowing for an immediate protection of the device. This approach can help minimizing the parasitics with respect to a 1-level package, and it can also facilitate the subsequent device handling. However, many MEMS foundries are still investigating an effective and reliable process for the wafer-level MEMS packaging.

## 2.5 Review of the main anti-stiction mechanisms

Since the stiction is still the main concern related to the RF MEMS reliability, a lot of work has been done to reduce or completely avoid such a problem. The use of different metal alloys for a more robust ohmic contact [11], or different dielectric layers [47] have been the main strategies pursued so far.

The removal of the dielectric layer from the bias electrode, and, consequently, the adoption of stoppers has demonstrated to drastically improve the lifetime [19]. However, charging inside the substrate and/or dielectric underneath the electrodes still occurs. In some cases ON-state stiction can be reduced by improving the mechanical design in order to achieve a high self-restoring force of the MEMS membrane [67]. However, this cannot be enough to guarantee the switch functionality especially in case of very long bias time.

An effective strategy against stiction is the design of an *active* mechanism to restore the OFF state of the switch when stiction occurs. This approach promises to be an excellent solution especially for redundancy RF MEMS switch units, where the prediction of the contact and dielectric status in 10-15 years is not straightforward.

The idea of a third electrode, alternatively called *pull-out* or *OFF* electrode, to actively control the position of the suspended membrane is proposed in [68]. The pull-out electrode is added on top of the air-bridge by us-

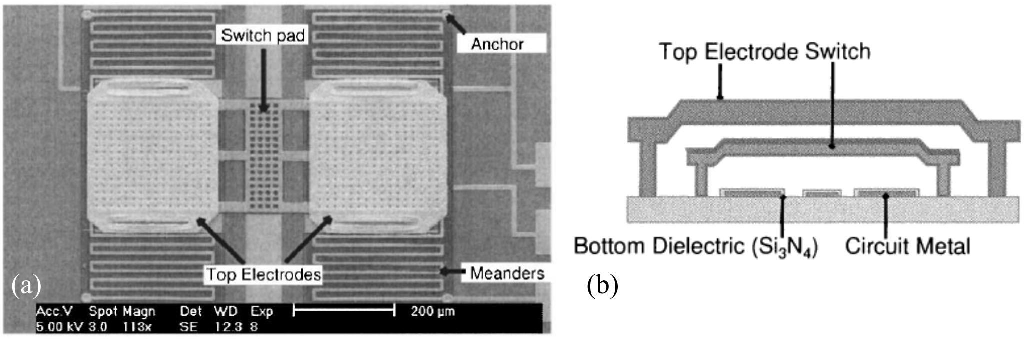

Figure 2.10: SEM photograph and schematic cross-sectional view of the switch fabricated with top electrode [68].

ing a two-stages sacrificial layer deposition. A SEM image and a schematic cross-sectional view of the resulting structure is shown in Fig. 2.10. Such a mechanism may be very effective in case of membrane stiction or latching. However, this device implies a more complex fabrication process and further electromagnetic parasitic effects to be considered.

The switch reported in [69] employs a thermal mechanism to actively restore the switch after the stiction. Buried high-resistivity polysilicon serpentines are implemented under the anchor points of a simple clamped-clamped structure. In case of stiction, a current flowing through the serpentines heats up the overall structure. The deformation induced by the temperature rise acts on the stiction area by means of a combination of vertical and shear forces, which contribute in releasing the stuck membrane.

The OFF electrode is placed at the same level of the ON electrode in [70], where the suspended membrane is anchor-less, and simply-supported by two pillars (Fig. 2.11). Moreover each extremity of the membrane works as a top electrode. The actuation electrodes are localized on both sides of each pillar, realizing a two-states device. Such a mechanism provides high flexibility and active control of the switch status. The concept has been validated also for an ohmic switch. However, no reliability tests have been available yet demonstrating the reliability of such a device for long term

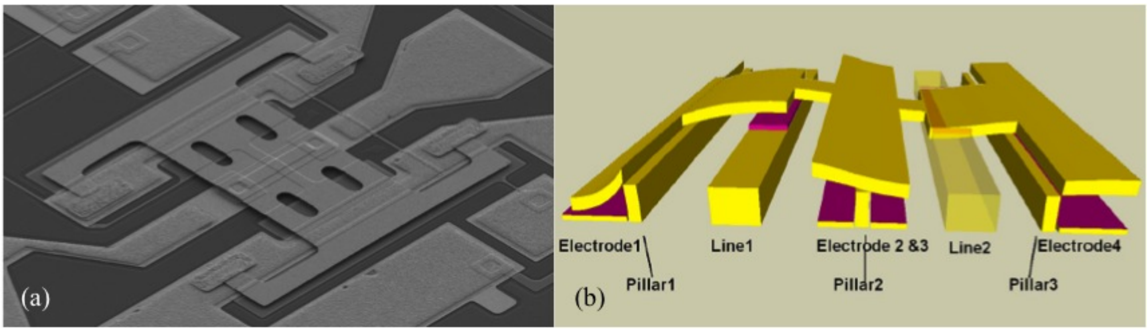

Figure 2.11: SEM photograph and schematic of the actively-controlled MEMS switch by DelftMEMS [70].

actuation.

A *toggle* or *push-pull* mechanism has been implemented in [71] by anchoring a cantilever by means of torsion springs. However high control of the stress gradient is required in this kind of structures in order to preserve their electro-mechanical performance.

Instead of using a cantilever, a *symmetric* toggle switch combining the advantages of the designs presented in [71] and [70] has been reported in [72]. The four torsion anchor springs allow for the implementation of the toggle mechanism, providing a (theoretical) effective restoring force in case of stiction over the ON-electrodes. This concept will be further analyzed in Chapter 6.

Alternatively a bi-stable mechanism can be implemented in the switch. The difference with the active control concepts described above is that the switch may maintain both the ON and OFF status without the need of any bias control. The bias voltage is provided only to switch from ON to OFF and vice versa, thus the dielectric charging problem due to long voltage stress could be completely avoided. Again, the bi-stable mechanism could also be effective in case of stiction due microwelding.

There are many example of bi-stable MEMS structures where the bistability is controlled thermally or electromagnetically. In [73] a thermally-

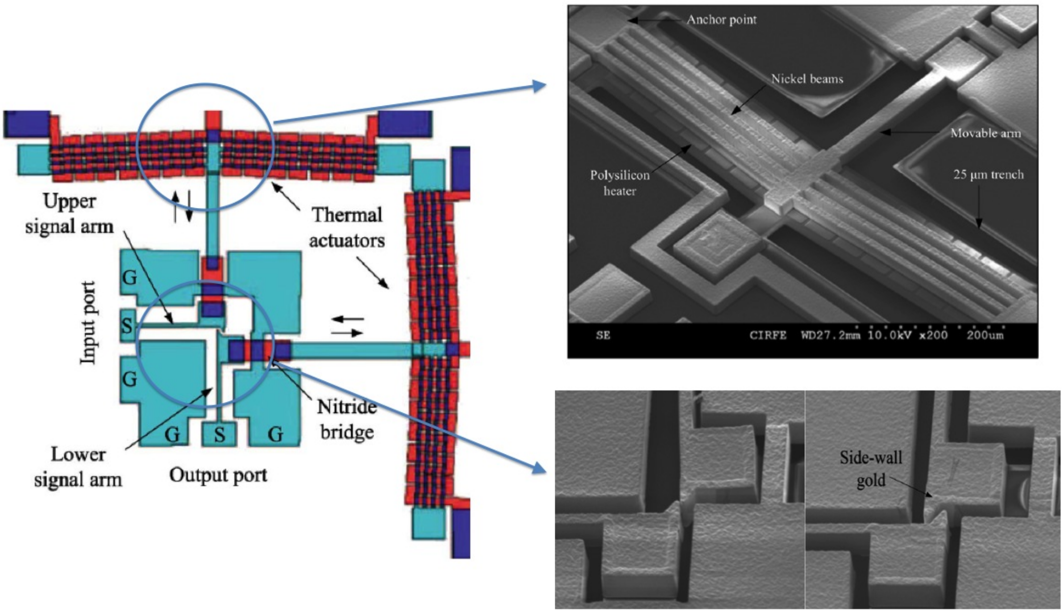

Figure 2.12: Layout and SEM images of the latching RF MEMS switch [73].

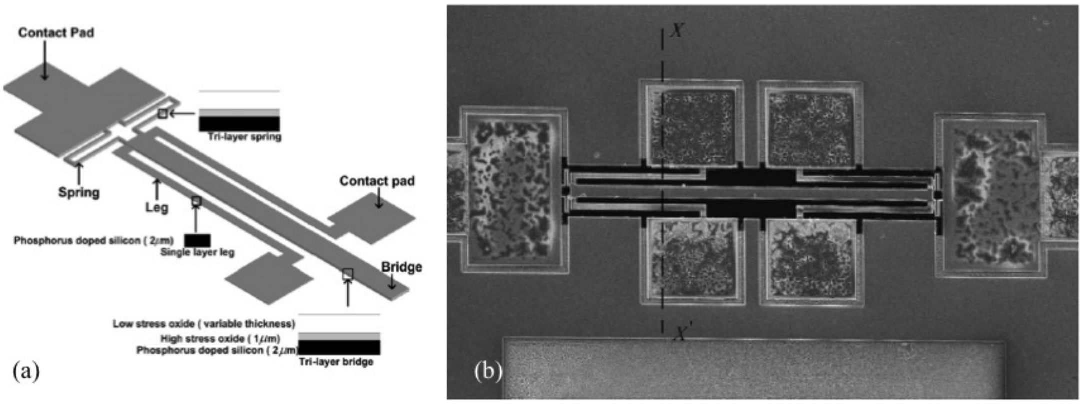

Figure 2.13: Out-of-plane bi-stable RF MEMS switch with thermal actuation [74].

controlled MEMS switch is reported. The switch employs two thermal actuators connected to two thin suspended arms which work as the signal line of a coplanar waveguide (Fig. 2.12). The switch is latched or un-latched when the actuators are sequentially activated, establishing the contacts between the two signal lines.

Another example of thermally-activated bi-stable MEMS is reported in [74]. In this case the membrane movement is *out-of-plane*. A schematic

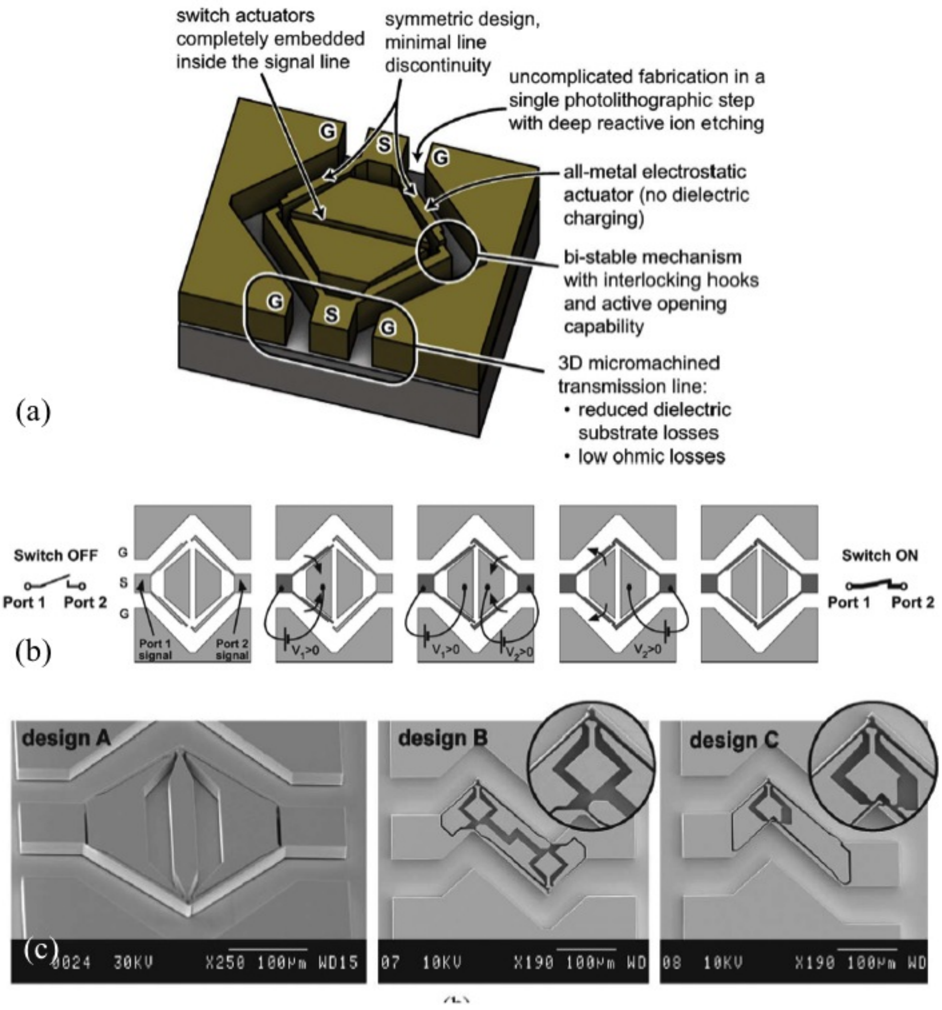

Figure 2.14: Bi-stable metal-contact RF MEMS switch integrated in a 3-D micromachined coplanar waveguide [75].

and a SEM image of the structure are reported in Fig. 2.13. Such a device is not presented as a RF MEMS and its integration capability on a microwave transmission line has still to be demonstrated.

An electromagnetic control is implemented in [76]. Two permanent magnets are used to keep alternatively the two stable positions of a cantilever beam. The power consumption is then extremely low even during the switching operation with respect to the thermally-activated device described previously. However, the presence of magnets makes difficult to integrate such a device in a CMOS-compatible process.

In [75] an electrostatic bistable contact switch exploiting an active opening mechanism is presented. Even in this case the horizontal movement of the suspended beams is exploited, and the switch is part of the signal line of a coplanar waveguide, as shown in Fig. 2.14. When a voltage is sequentially applied to a couple of 30-$\mu$m thick clamped-free beams, these lock together with the corresponding couple of beams, closing the signal line contacts. This concept is effectively implemented in a SPDT, showing good performances from 0 to 25 GHz (insertion loss better than 2 dB and return loss better than 15 dB). A detailed reliability study concerning the lifetime of such a device is still missing.

Bi-stable designs have not been successful so far because of their mechanical design and fabrication process complexity. The bi-stability based on an electrostatic control looks more difficult to implement with respect to a thermal control. To the author's knowledge, full-effective bi-stable RF MEMS switches and switch capacitors compatible with an electrostatic bias control and based on out-of-plane displacement are currently not available in literature.

## 2.6 Advances in FBK manufacturing process

The fabrication of RF MEMS devices is usually based on the standard manufacturing techniques used for integrated circuits [77]. All the devices that are described and analyzed in this thesis have been manufactured using a combination of CMOS-compatible process and *surface micro-machining* techniques. A surface micro-machining process [3] allows for the creation of movable or fixed metallic suspended structures, such as *cantilever beams* and *air bridges* by means of a supporting *sacrificial layer*.

The in-house clean room facilities available at Fondazione Bruno Kessler

(FBK) provide an advanced eight-mask process platform for RF MEMS switches, sensors, and actuators. A simplified sketch of the FBK process mask layers is depicted in Fig. 2.15. The main process steps are described as follows:

1. First, an appropriate substrate is chosen according to the target application of the RF MEMS switches that are going to be fabricated. For microwave applications, p-type high-resistivity silicon (HRSi) substrate provides the best cost-performances compromise. Substrate resistivity is in the order of 5000 Ω·cm, against ~10 Ω·cm of the standard silicon used for transistors. A 525-$\mu$m thick substrate is used for switches integrated in *coplanar* transmission line, while 200-$\mu$m thick silicon substrates are preferred for switches on *microstrip*. A 1-$\mu$m-thick thermal field oxide is grown on the silicon surface as insulating layer. In order to reduce the fixed oxide charge, the oxide is also annealed at 975°C in nitrogen. Also low-losses substrates such as quartz or sapphire can be used in place of silicon for better RF performances.

2. Then the switch electrodes and the bias network connections are defined. The material used is polysilicon. After growing 630-nm of un-doped polysilicon layer by LPCVD (*Low Pressure Chemical Vapor Deposition*), its conductivity properties are determined by the doping dose of the subsequent boron ion implantation. A 1500 Ω/□ polysilicon layer results in 20-40 kΩ bias resistors, which have also a meaningless impact on the switch loss if properly designed.

3. The electrical isolation between the switch bias electrodes and the metallic beam structure is provided by a layer of 300-nm thick oxide deposited by pyrolytic oxidation of tetraethylorthosilane (TEOS) using LPCVD at 718°C. LPCVD silicon nitride can be used as an alternative of the oxide layer. The dielectric layer is then removed by

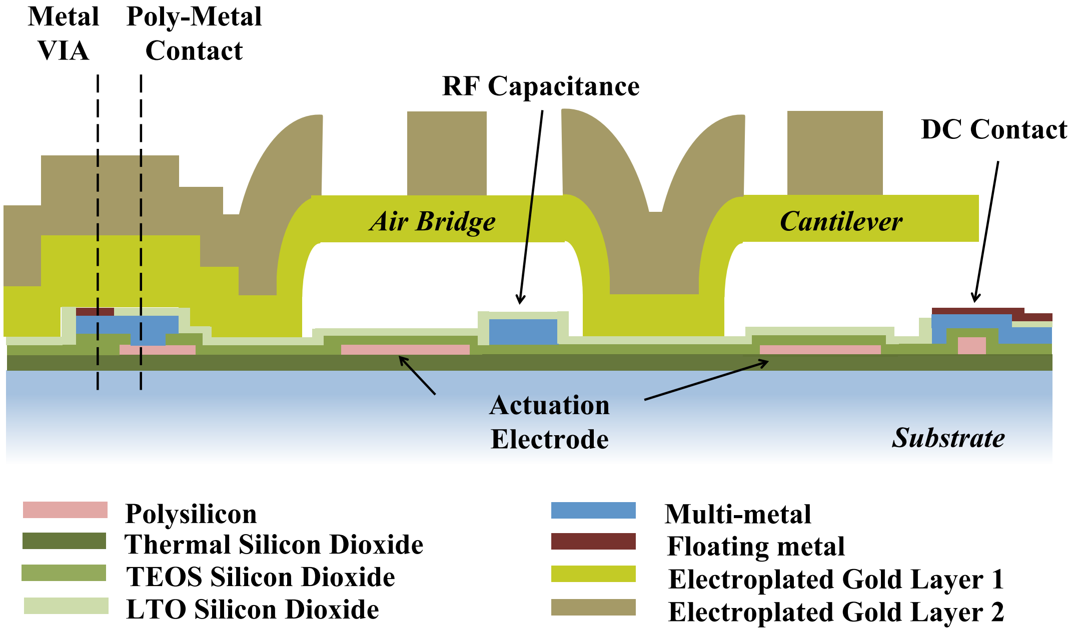

Figure 2.15: Side-view diagram of the 8-mask FBK base-line process. The thickness dimensions are exaggerated to better highlight the mask layers.

plasma etching where a contact-hole between polysilicon electrodes and the above metallic layer is needed.

4. The next step is the sputtering deposition of a Ti/TiN/Al/Ti/TiN multilayer *underpass* which joins the two portions of the central conductor or signal line under the suspended membrane. First 30-nm thick Ti layer and 50-nm thick TiN layer are deposited at 400°C, then a 410-nm thick Al−1%Si alloy and a 60-nm thick Ti layer are deposited at room temperature. Finally a 80-nm thick capping layer of TiN is deposited at 300°C in order to have a diffusion barrier between metal and gold. The total thickness of the multilayer was calculated in order to have the same height of the polysilicon bias electrodes. The multilayer underpass is also referred to as *metal* in the process definition.

5. The multilayer is covered with low temperature oxide (LTO). This

dielectric layer defines the ON-state capacitance in RF MEMS capacitive switches. The oxide is etched away where the contact (which in this case is called *via*) between the underpass and the above gold layer is needed.

6. A 150-nm of gold is then evaporated. A 5-nm chromium layer is deposited just before the gold and serves as an adhesive layer between the gold and the bottom layers. This gold layer is named *floating metal* since it can be used in capacitive switches to improve the capacitance ratio [78]. However, its main purpose is to cover with a noble metal the exposed electrical contacts of the ohmic switches in order to provide a better metal-to-metal contacts.
7. A 3-$\mu$m thick sacrificial layer is deposited where a suspended structure, clamped-clamped or free-clamped membrane, is needed.
8. A 150/2-nm thick gold/platinum-alloy layer is evaporated over the sacrificial layer in correspondence of electric contacts in ohmic switches. This solution aims at improving the hardness of the ohmic contact and then their lifetime under repetitive stresses.
9. A first 2-$\mu$m thick gold layer is electroplated by means of a commercial gold-cyanide bath on the top of a 2.5/25-nm thick chromium-gold seed layer.
10. The second gold mask is defined, and then a 3.5-$\mu$m thick gold layer is electroplated. This further gold layer can reinforce the suspended structures to guarantee membrane flatness.
11. Finally the air-bridges are released with a modified plasma ashing process (30 minutes at 200°C). An experimental low-temperature release has been recently introduced [79] in order to minimize the beam stress gradient (see Chapter 3).

A photo of the final result of the FBK RF MEMS switches fabrication process is also shown in Fig. 2.16. The manufacturing process is still under continuous development in order to improve the control of the process uniformity.

## 2.7 Conclusion

This Chapter reported a brief overview of the state-of-the-art of RF MEMS switches, presenting the main advantages with respect to solid state switches and the best-case performances. The main applications of RF MEMS switches were also described, with a particular focus on the their employment as redundancy switches for satellite communications. The most important failure modes affecting the MEMS reliability for short and long term operating conditions, such as dielectric charging, contact microweldings, and power handling, were also briefly described. The Chapter also provided a critical assessment of some anti-stiction mechanisms proposed in literature (such as the use of a third electrode, or the implementation of a bi-stable membrane), which can be used to improve the switch lifetime in case of long-term stress. Finally the Chapter reported some advances in the manufacturing process of RF MEMS based on the technology facilities available at FBK. Such a technology will be employed in the fabrication of all the original devices presented in the next Chapters.

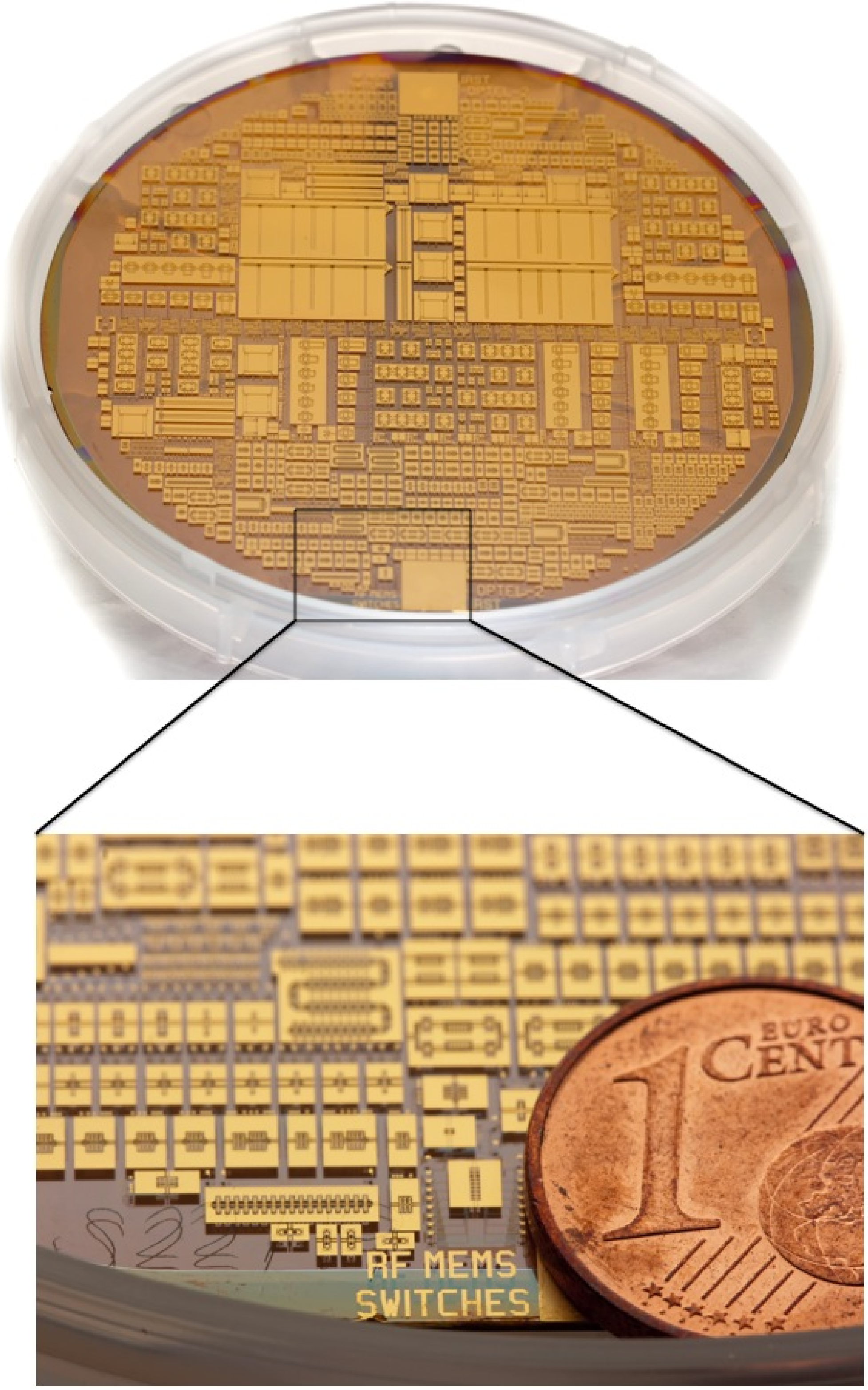

Figure 2.16: RF MEMS 4-inches FBK wafer on quartz substrate.

# Chapter 3

# Modeling of RF MEMS switches

## 3.1 Introduction

This chapter introduces the electro-mechanical and electro-magnetic models of an electrostatic RF MEMS switch, with a particular focus on the usage of numerical tools for the analysis of different typologies of MEMS switches. Simple 1-D models for pull-in and pull-out voltages are presented, along with the 2-port equivalent circuit network representation used for series and shunt switches. In addition, the main numerical tools for analysis and simulation of RF switches are briefly described. Finally some case studies are reported, focusing on the approach and methodology to be followed for the *multiphysics* and *full-wave* simulations.

## 3.2 Mechanical model

### 3.2.1 Linear stiffness

A MEMS switch is made of a suspended *conductive* membrane constrained to a fixed support (*substrate*). The membrane can be a *fixed-fixed beam* or a *cantilever beam* according to the type and the number of anchor points. A fixed-fixed beam or *air bridge* is usually anchored to the substrate by means of at least two anchor points or *anchor springs*. A cantilever beam or *free-clamped* beam is anchored at one or more points at the same side.

In electrostatic MEMS switches, the suspended membrane is flexible enough to be considered *elastically movable*. The movement is driven by an *electrostatic force* provided by applying a difference of potential between the membrane and a fixed electrode. The *reaction force* depends on the mechanical behavior of the membrane, which in most of the cases can be easily modeled by a *linear spring constant*.

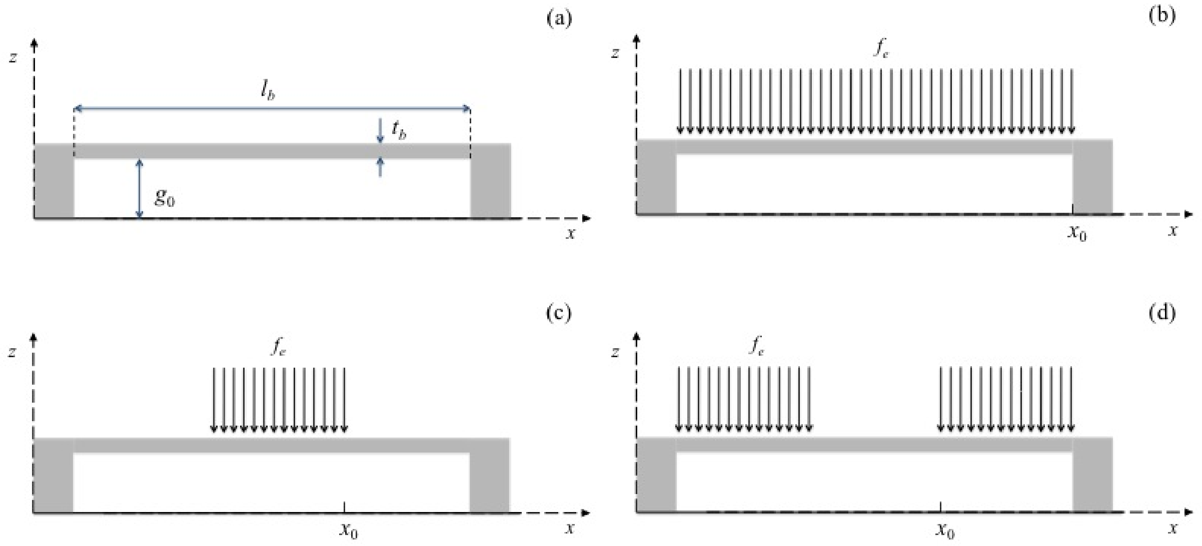

Figure 3.1: Sketch of fixed-fixed membrane used as *shunt* switch: (a) dimensions and reference system identification, (b) uniform distributed load, (c) center-distributed load, and (d) lateral-distributed load examples.

Fig. 3.1-a depicts the 2-D model of a clamped-clamped beam, and its related reference system. The beam is supposed to be rectangular-shaped, with length $l_b$, width $w_b$ ($y$-dimension, not shown in the Figure), and thickness $t_b$. The equivalent spring constant of such a structure is determined as the ratio between the applied force or *load* $F$ (N) and the maximum

displacement $\Delta z$ (m) along $z$-direction:

$$k = \frac{F}{\Delta z}. \tag{3.1}$$

In the real case the force is not concentrated to one point but *distributed* along a fraction of the length of the membrane, so the force per unit length $f$ must be considered. The value of $k$ usually depends on the beam dimensions and on the elastic characteristics of the material determined by the *Young Modulus* $E$ (Pa). In case of width comparable to length, the structure is modeled as a *plate*, and also the bi-axial elastic properties need to be accounted by considering the material *Poisson's ratio* $\nu$. The beam dimensions and shape determine the moment of inertia $I_b$. In addition it is possible to distinguish three common situations according to the position of the applied load [4]:

- *Uniform load*: If the load is uniformly distributed all along the membrane length, as depicted in Fig. 3.1-b, the spring constant is:

  $$k_u^{'} = 32Ew_b\left(\frac{t_b}{l_b}\right)^3. \tag{3.2}$$

- *Central load*: If the load is distributed over the central part of the membrane for a length defined with $x_0$ according to Fig. 3.1-c, the spring constant becomes:

  $$k_c^{'} = 32Ew_b\left(\frac{t_b}{l_b}\right)^3 \frac{1}{8(x_0/l_b)^3 - 20(x_0/l_b)^2 + 14(x_0/l_b) - 1}. \tag{3.3}$$

  This situation occurs when the fixed electrode is a part of the RF line, and the control voltage is provided together with the RF signal by means of an appropriate de-coupling circuitry.

- *Lateral load*: In case of lateral distributed load, as depicted in Fig. 3.1-

d, the spring constant is:

$$k_e^{'} = 32Ew_b\left(\frac{t_b}{l_b}\right)^3\frac{1}{(x_0/l_b)(1-x_0/l_b)}. \tag{3.4}$$

This case is applied when electrodes are placed beside the RF line, and they are also electrically isolated from it. This is also the solution adopted for the bias network of FBK switches.

The stiffness of a cantilever beam is derived in the same way. For uniform load applied over the entire beam, the spring constant is

$$k_a = \frac{2}{3}Ew_b\left(\frac{t_b}{l_b}\right)^3 \tag{3.5}$$

This case is illustrated in Fig. 3.2-a. For a load distributed over the tip of the cantilever (Fig. 3.2-b), one has:

$$k_t = 2Ew_b\left(\frac{t_b}{l_b}\right)^3\frac{1-(x_0/l_b)}{3-4(x_0/l_b)^3+(x_0/l_b)^4} \tag{3.6}$$

where in this case $l_b$ is still the beam length, and $x_0$ is the distance from the anchoring point, so the load is spatially applied from $x_0$ up to $l_b$. As a good approximation, the model described by Eq. (3.5) is usually employed for the most of the cantilever switches, even if the bias electrode length is a little bit shorter than the beam length.

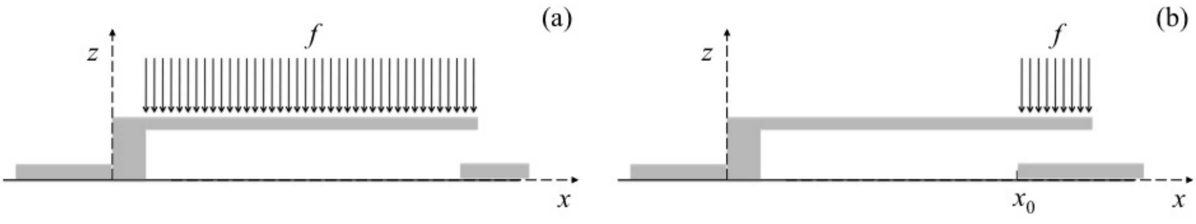

Figure 3.2: Sketch of a cantilever beam used as *series* switch: (a) uniform-distributed load, and (b) tip-distributed load.

### 3.2.2 Effect of residual stress

Since the clamped-clamped structures considered above are thin-film membranes, the dominant component of stiffness is actually due to the residual bi-axial stress. The residual stress $\sigma_0$ in thin film material depends on a combination of factors. First, changes in the thin-film materials mainly due to some manufacturing process steps generate localized strain and stress. In addition, some defects, such as vacancies and dislocations, in the material crystalline structure may already exist. This kind of stress is generally named as *intrinsic* stress. Moreover, the mismatch between the thermal expansion coefficient of the thin material and the one of the supporting substrate significantly contributes to the whole material stress. Such a condition is referred to as *thermal stress.*

The residual stress induced by the thermal expansion mismatch between a thin film layer, with expansion coefficient $\alpha_f$ and Young modulus $E_f$, and a thick bulk material (such as a substrate), with expansion coefficient $\alpha_b$, is:

$$\sigma_{th} = E_f(\alpha_f - \alpha_b)(T_1 - T_0) \tag{3.7}$$

where $T_0$ is the room temperature and $T_1$ is the temperature employed for the removal of the sacrificial layer during the release of the suspended structures (see Section 2.6). A negative stress ($\sigma_0 < 0$) is considered a *compressive* stress, and for critical values of such a component the *buckling* of the suspended beam can occur. A positive stress ($\sigma_0 > 0$) is *tensile*, which means that the clamped-clamped beam is *stretched.* The latter significantly contributes to the stiffness of the beam. Then the part of the spring constant due to residual stress is determined by modeling the clamped-clamped suspended membrane as a stretched wire [4]. Under this assumption, the spring constant is found to be:

$$k_u^{''} = 8\sigma_0(1-\nu)w_b\left(\frac{t_b}{l_b}\right), \tag{3.8}$$

$$k_c^{''} = 8\sigma_0(1-\nu)w_b\left(\frac{t_b}{l_b}\right)\frac{1}{(3-2x_0/l_b)}, \tag{3.9}$$

$$k_e^{''} = 4\sigma_0(1-\nu)w_b\left(\frac{t_b}{l_b}\right)\frac{1}{(1-x_0/l_b)}, \tag{3.10}$$

for uniform, central and lateral distributed load, respectively. As mentioned previously, these formulas can be applied only in the case of *tensile* residual stress.

The complete analytical expression for the spring constant is then:

$$k_{u,c,e} = k_{u,c,e}^{'} + k_{u,c,e}^{''}. \tag{3.11}$$

In case of cantilever beams, one side of the beam is clamped, while the other side is free to expand or contract. The residual stress is then released after the removal of the sacrificial layer, so it has no effect on the stiffness of the beam. However, manufacturing process of MEMS often requires the utilization of multi-layer structures. For example, this is necessary for those materials, like gold and copper, which require an *adhesion layer* such as chromium, titanium, or nickel, in order to adhere completely to the supporting substrate. Therefore different materials and different deposition conditions are the responsible of a *stress gradient* along the thickness direction of the suspended structure [79]. Such a stress gradient induces a *bending* moment $M_b$ on the cantilever, which in turn is responsible of the tip deflection $u_{max}$. This effect is clearly illustrated in the 3-D optical profile reported in Fig. 3.3.

The variation of the bi-axial stress along the deflection direction, which

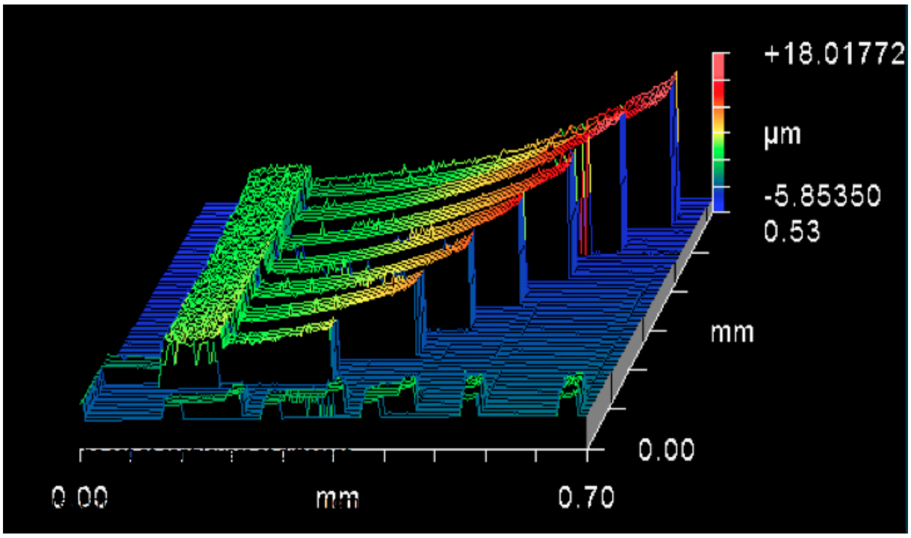

Figure 3.3: Optical profiler measurement of an array of cantilever beams used as test structures for the monitoring of stress gradient.

is supposed to be the $z$-axis of the beam reference system, is given by:

$$\sigma_0(z) = \Gamma_s z \tag{3.12}$$

where $\Gamma_s$ is the stress gradient, usually expressed in MPa/$\mu$m. In general the stress gradient is evaluated by measuring the tip displacement $u_{max}$ of a cantilever beam of length $l_b$, Young Modulus $E$ and uniform cross-section identified by a moment of inertia $I_b$:

$$\Gamma_s = \frac{M_b}{I_b} = 2\frac{E}{l_b^2}u_{max}. \tag{3.13}$$

Stress gradient is usually not significant in clamped-clamped structures, even though it is still present and may lead to some unwanted deformations if reenforcing membrane frames are used. However, it becomes important in cantilever beams, where the curvature produced by the release of stress gradient may change significantly the gap between the top and bottom electrodes. This may also affect the ON state contact area in series switches.

### 3.2.3 Electrostatic model

The movable part of an electrostatic RF MEMS switch, for both the cases of a clamped-clamped bridge or a cantilever beam, can be described in a compact form by using a 2-D model of the traditional parallel plates capacitor, as depicted in Fig. 3.4. In this case, the anchors of the membrane are modeled by a linear spring $k$, attached to the top electrode of the capacitor, which is free to move along the z-direction. A thin dielectric layer of thickness $t_d$ and dielectric constant $\varepsilon_r$ lays over the bottom electrode, which is fixed to the substrate, whereas the rest of the capacitor is filled with air. Note that such a capacitor works as the series of two capacitance, one filled only with air and one filled with the dielectric layer. When $V_{bias} = 0$ V, the air gap is much larger than the dielectric thickness, then the overall value of capacitance is:

$$C_0 = \varepsilon_0 \frac{A}{g} \tag{3.14}$$

where $A$ is the effective area of the parallel plates, $g$ is the distance between the electrodes, which is equal to $g_0$ in the beginning, and $\epsilon_0$ is the *vacuum permittivity* ($8.854 \times 10^{-12}$ F/m).

When the bias voltage is applied, a potential difference is established between the parallel plates, generating an electrostatic force $F_e$ acting on the top electrode:

$$F_e = -\frac{1}{2}\varepsilon_0 \frac{A}{g} V_{bias}^2 \tag{3.15}$$

The reaction force provided by anchor springs is:

$$F_m = k\Delta z. \tag{3.16}$$

where $\Delta z$ is the top electrode displacement due to the action of the electrostatic force.

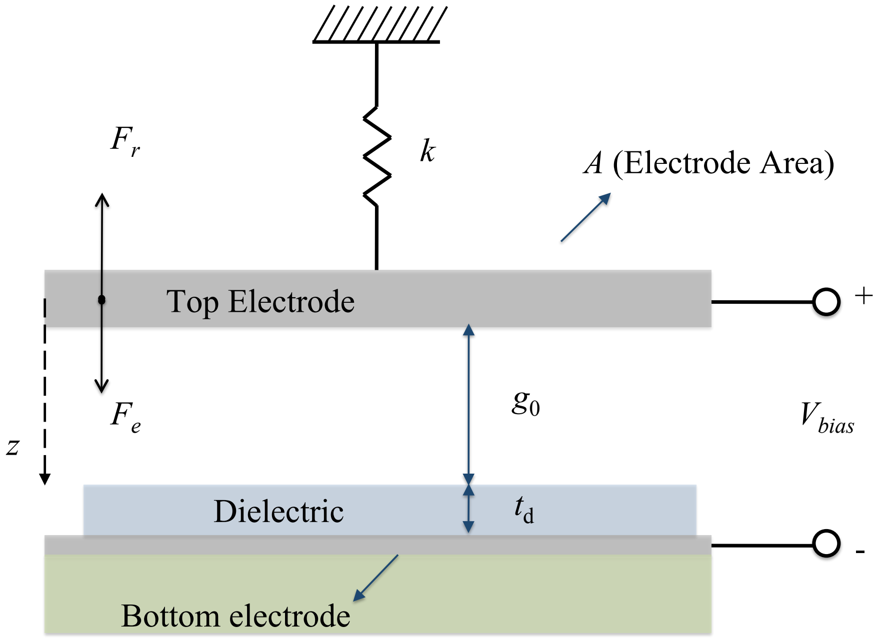

Figure 3.4: Spring-capacitance system modeling the electro-mechanical coupling in a MEMS switch.

As long as $F_e = F_m$ for increasing values of $g$, the applied force and the reaction force are in equilibrium. This means also that the bridge is kept in a stable position ($g = g_0 - \Delta z$). The increase of $\Delta z$ causes an increase of $F_e$, which is then subject to a *positive* feedback. Therefore for a certain value of $\Delta z$ the membrane reaches an *unstable* condition, after which it *snaps down* to the bottom electrode. By differentiating $F_e = F_m$ with respect to $g$ and calculating the zeros of the resulting Equation, it can be demonstrated that the bridge collapse occurs when $\Delta z = (1/3)g_0$. The value of $V_{bias}$ resulting in the membrane snap down is found by equating Eq. 3.15 and Eq. 3.16 and substituting $\Delta z$ with $(1/3)g_0$:

$$V_{PI} = V_{bias}(g_0/3) = \sqrt{\frac{8k}{27\varepsilon_0 A}g_0^3}. \tag{3.17}$$

The voltage at which the instability occurs is also called *actuation voltage* or *pull-in voltage*. For both series and shunt switches, $V_{ON} \geq V_{PI}$.

The limitations of Eq. 3.17 concern the definition of $k$, and $g_0$. The spring constant $k$ may have a complex analytical expression if the cross section of the beam is not uniform [80]. The definition of $k$ also depends on the deflection point used as a reference to evaluate the term $\Delta z$ in Eq. 3.1. Moreover, the membrane profile is not completely flat once the bias voltage is applied (and neither before for some geometries if residual stress or stress gradient are present). All these aspects make the pull-in voltage difficult to be estimated *a priori*. However, Eq. 3.17 still provides a good method for a rough evaluation of the electro-mechanical properties of a given membrane geometry.

After the actuation, the electro-static force acting on membrane accounts for the effect of the thin dielectric layer covering the bottom electrode. This layer usually provides the DC isolation between the electrodes. Then the capacitance after the actuation or *down-state* capacitance is:

$$C_{down} = \varepsilon_0 \epsilon_r \frac{A}{t_d}. \tag{3.18}$$

The switch remains actuated until the electrostatic force is higher than the restoring force (Fig. 3.4). The *hold-down* or *pull-out* voltage is defined as:

$$V_{PO} = \sqrt{\frac{2k_n}{\varepsilon_0 \varepsilon_r A} g_0 \left(\frac{t_d}{\epsilon_r}\right)^2}. \tag{3.19}$$

The spring constant $k_n$ is usually different from the one used in Eq. 3.17. In fact the pull-in can be seen as a large displacement with respect to the small thickness involved, so the linear mechanical model is no longer valid. Then a stretched component of the stiffness must also be considered. Moreover the top electrode contact surface may also change after the bias voltage approaches the pull-out value.

According to the above considerations, the displacement characteristic

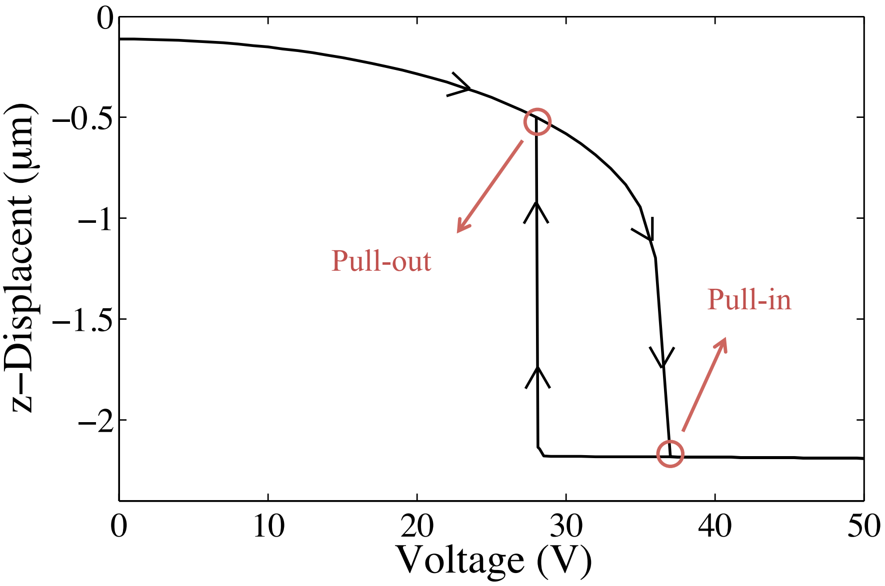

Figure 3.5: Displacement along $z$-axis of a clamped-clamped bridge as a function of bias voltage. Note the hysteresis loop that characterizes any kind of RF MEMS switch.

of the top electrode describes a *hysteresis* as a function of bias voltage, as illustrated in Fig. 3.5. The pull-out voltage is always smaller than the pull-in, since the electrostatic force, acting after the actuation and then depending on the down-state capacitance, is higher then the one acting before the snap-down. This situation is shown in Fig. 3.6 in more details by means of a spring-capacitance 2-D model. After the actuation occurs for $V_{bias} > V_{PI}$, the switch remains in its ON state for a bias voltage included between $V_{PO}$ and $V_{PI}$, with $V_{PO} < V_{PI}$. When the bias voltage is lowered so that $V_{bias} < V_{PO}$, the switch de-actuates, returning in its OFF state.

## 3.3 Electromagnetic model

As described in Section 2.2, a RF switch can assume a *series* or *shunt* configuration, according to its position with respect to the microwave transmission line (*t-line*). Generally a switch is considered ON if the actuation of the membrane occurs.

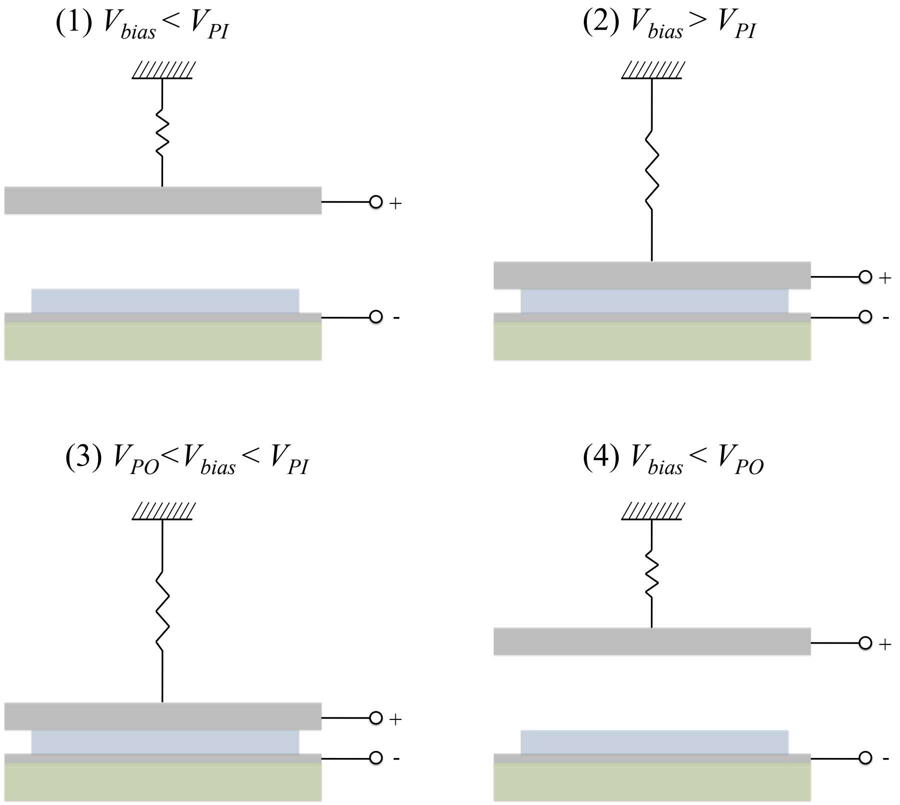

Figure 3.6: Spring-capacitance system configurations as a function of bias voltage: (a) bridge before the actuation, (b) bridge after the actuation, (c) bridge before the pull-out, and (d) bridge after the pull-out.

From an electromagnetic point of view, a MEMS switch is essentially a *passive linear two-ports network*. Its electromagnetic properties can be fully described by the scattering parameters (or S-parameters) of a two-ports network. Then the main figures of merit characterizing the switch performances at high frequencies are defined by means of S-parameters:

- Return Loss: provides the amount of power reflected back at the input port:

$$RL = -20\log_{10}|S_{11}| \tag{3.20}$$

  Ideally it should be *infinite* (in dB) when the shunt switch is OFF and the series switch is ON, which means that all the power is delivered to the output. It should be ideally equal to 0 dB (1 in linear scale) when the shunt switch is closed and the series switch is open.

- Insertion Loss: provides the amount of power delivered from port 1 to port 2 when the shunt switch is OFF or the series switch is ON:

  $$IL = -20 \log_{10} |S_{21}| \tag{3.21}$$

  Ideally it should be equal to 0 dB, that is, all the power can go through the network and delivered to the output port.

- Isolation: it is defined when the signal is supposed to be not transmitted through the network, and it provides the amount of power delivered from port 1 to port 2 when the shunt switch is ON or the series switch is OFF:

  $$IS = -20 \log_{10} |S_{21}| \tag{3.22}$$

  Ideally it should be *infinite*, that is, no signal is allowed to go through the network.

In the real case, a certain amount of power is reflected back even if the switch is in the transmission mode, and at the same way it is delivered to the output port when the switch is supposed to isolate the two ports. Fig. 3.7 and 3.8 show the ideal networks for shunt and series switches respectively, and the corresponding real networks, where the switch is modeled as a *complex impedance*.

Since the suspended membrane is usually very small if compared to the wavelength of the traveling wave, the complex impedance is represented with a set of *lumped elements*. In case of shunt configuration, the suspended membrane is usually anchored to the grounds of the transmission line, realizing a capacitance with the signal line. Therefore the MEMS switch is modeled as a *variable capacitance* $C_S$, in series with an *inductance* $L_S$

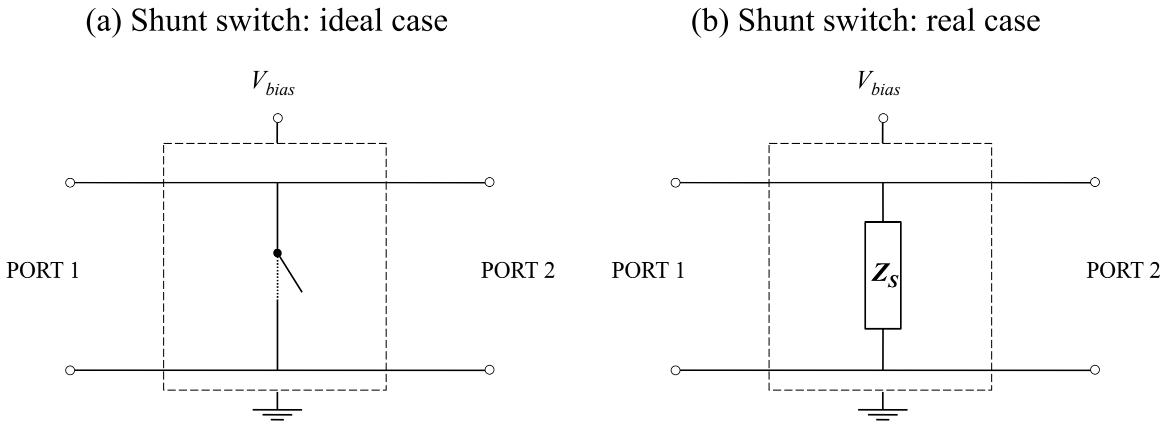
(a) Shunt switch: ideal case

(b) Shunt switch: real case

Figure 3.7: RF switches in *shunt* configuration: a) ideal network and b) real network where the switch is modeled as a complex impedance.

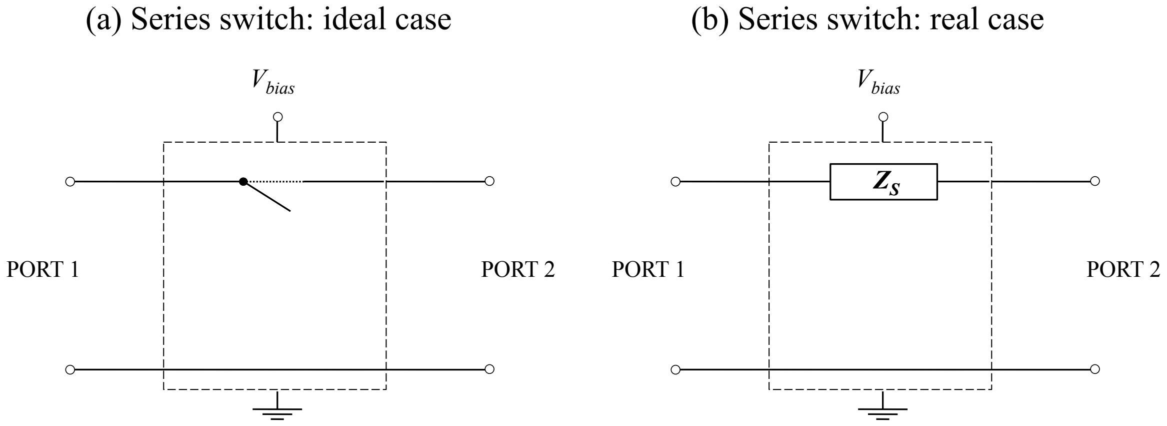
(a) Series switch: ideal case

(b) Series switch: real case

Figure 3.8: RF switches in *series* configuration: a) ideal network and b) real network where the switch is modeled as a complex impedance.

and a *resistance* $R_S$ (Fig. 3.9). The latter models the loss introduced by the membrane. When the switch is OFF, the capacitance assumes its lowest value or *up state* value $C_S = C_{OFF}$ (or $C_{up}$). The value of $C_{OFF}$ is calculated by using Eq. (3.14) with a slight modification, as follows:

$$C_{OFF} = \varepsilon_0 \frac{A}{g_0} + C_f \tag{3.23}$$

where $C_f$ accounts for the *fringing field* at the borders of the parallel plates of the capacitor, and it is usually considered equal to the 30 % of the total

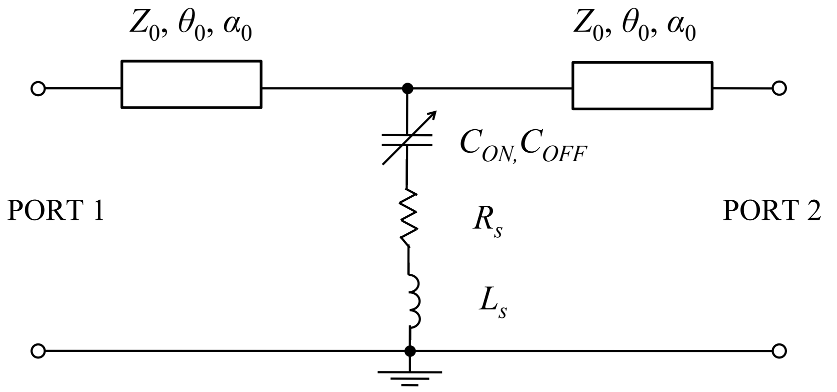

Figure 3.9: Equivalent circuit of a MEMS switch in *shunt* configuration.

OFF state capacitance value.

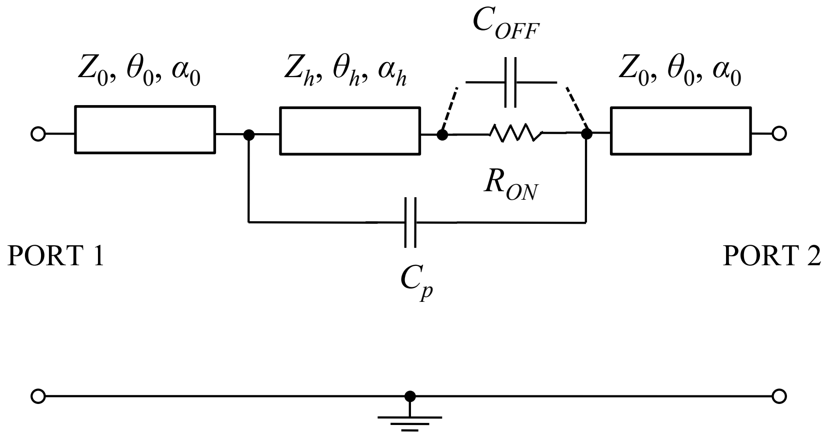

Figure 3.10: Equivalent circuit of a MEMS switch in *series* configuration.

When the switch is ON, the membrane snaps down to the stationary electrode, then $C_S = C_{ON}$ (or $C_{down}$):

$$C_{ON} = \varepsilon_0 \varepsilon_r \frac{A}{t_d} \tag{3.24}$$

where, as seen for Eq. (3.18), $t_d$ and $\varepsilon_r$ are the thickness and the permittivity of the dielectric layer. In general, the *capacitance ratio* $C_{ON}/C_{OFF}$ is considered an important figure of merit of capacitive switches. The higher the better the performance in terms of return loss and isolation.

Another figure of merit is the electromagnetic resonant frequency $\omega_0 = 1/\sqrt{L_S C_{ON}}$, and the corresponding *quality factor*, which particularly depends on the membrane resistance $R_S$. In accordance to the electromagnetic model described above, capacitive switches exhibit an intrinsic *narrowband* behavior, so that the maximum peak of isolation occurs at $\omega_0$.

In general the real value of $C_{ON}$ is significantly far from the geometrical value, since a thin air gap between electric and top electrode still remains because of the roughness of the dielectric. If $C_{ON}$ is designed to be around 7-8 pF, the real capacitance is typically around 0.8 - 1 pF. This value can be improved if the bias pad is in common with the RF line of the transmission waveguide, so the movable top electrode is forced to have a better contact with the dielectric surface, reducing the residual air-gap.

Another way to increase the ON state capacitance is to deposit a *floating metal* over the dielectric layer, so the residual air gap is completely avoided [78]. However, an ohmic contact between the floating metal and the top metal occurs, introducing all the issues concerning a metal-to-metal contact. Such a contact also affects the value of the equivalent membrane resistance, which in turn influences the Q-factor of the switch.

In case of series configuration, the switch is usually *ohmic*, that is, the membrane realizes a DC contact with the signal line. So the switch is modeled as a *resistance* $R_{ON}$ when the membrane is actuated, and as a capacitance $C_{OFF}$ when the membrane is in its up-state (Fig. 3.10). The pair of values $C_{OFF}$-$R_{ON}$ is the main figure of merit characterizing ohmic switches. These parameters are rather sensitive to process issues such as stress gradient. The higher the stress gradient, the higher the beam tip displacement, and then the lower the $C_{OFF}$ value.

An ohmic switch is intrinsically *wideband*, since it should be able to assure high isolation in up-state and high transmission capabilities in down state from DC to the cut-off frequency (defined as $f_T = 1/(2\pi R_{ON} C_{OFF})$).

In general, $C_{OFF}$ may be easily determined for both ohmic and capacitive switches from S-parameters measurements performed when the membrane is in the up-state. Conversely, $C_{ON}$, $R_S$, $L_S$ (capacitive switches), and $R_{ON}$ (ohmic switches) are extracted from S-parameters measurements at the membrane down-state. The membrane resistance in up-state is difficult to determine, and it is usually slightly different from $R_S$, since the density current distribution inducing losses by means of Joule effects changes between the two cases.

## 3.4 Simulation tools

### 3.4.1 Circuit simulators

The first tool easily applicable for the analysis of RF MEMS switches is a circuit simulator. As explained in Section 3.3, a MEMS switch can be represented by utilizing lumped elements for the modeling of the membrane and transmission line sections for the modeling of the surrounding circuit environment. Advanced Design System (ADS) from Agilent [81] offers a rich library of circuit elements and analysis tools such as S-parameters, AC, DC and harmonic balance analysis. Complex models for lumped elements or any circuit components can be defined, accounting also for critical design parameters. A typical use of this tool consists of the definition of a MEMS equivalent circuit, as those depicted in Fig 3.9 and 3.10. Indeed, once the S-parameters of a MEMS device have been measured and the resulting data file is loaded in the simulator environment, it is possible to fit the circuit model with the real data to extract the equivalent values of capacitance, inductance and resistance. The main advantage of a switch or circuit design approach based on circuit simulator is that it allows for fast design and optimization of the devices

### 3.4.2 Finite element method

Compact analytical models are extremely useful for a preliminary evaluation of RF MEMS switches at the design stage. However, the complexity of the physics involved in the functioning of RF MEMS switches requires the utilization of *numerical tools* for a more accurate and confident prediction of the switch behavior. This concept is valid especially for electro-mechanical and electro-magnetic physical domains. The *finite element method* or FEM [82] is a numerical method that discretizes a complex physical problem by means of several sub-domains, named as *elements*. The definition of such a discretization is the *mesh* of the model. The elements are connected among each other by means of *nodes*, and are modeled by a set of mathematical functions (low and high-order polynomials) describing the physics of the problem. Such functions are used along with the applied boundary conditions, in the definition of a set of linear equations, which is solved according to the available *degrees of freedom* of the problem.

A commonly used FEM software is ANSYS$^{\mathrm{TM}}$Multiphysics [83]. ANSYS provides a large element library for the modeling of very complex physics problems (structural, thermal, electric, fluidics), and it can also perform *static* or *dynamic* analyses. In Fig. 3.11 the descriptive scheme of a high-order structural 3D element (one of the most utilized elements for the simulations presented in this thesis) is depicted.

Among ANSYS capabilities, it is possible to couple different physical domains during the analysis, or to use special coupled-elements which provide a set of degrees of freedom related to more than one physics. This makes such a tool extremely suitable for the simulation of MEMS structures, which intrinsically require a multi-physics approach.

The most common and simple utilization of ANSYS for electrostatic

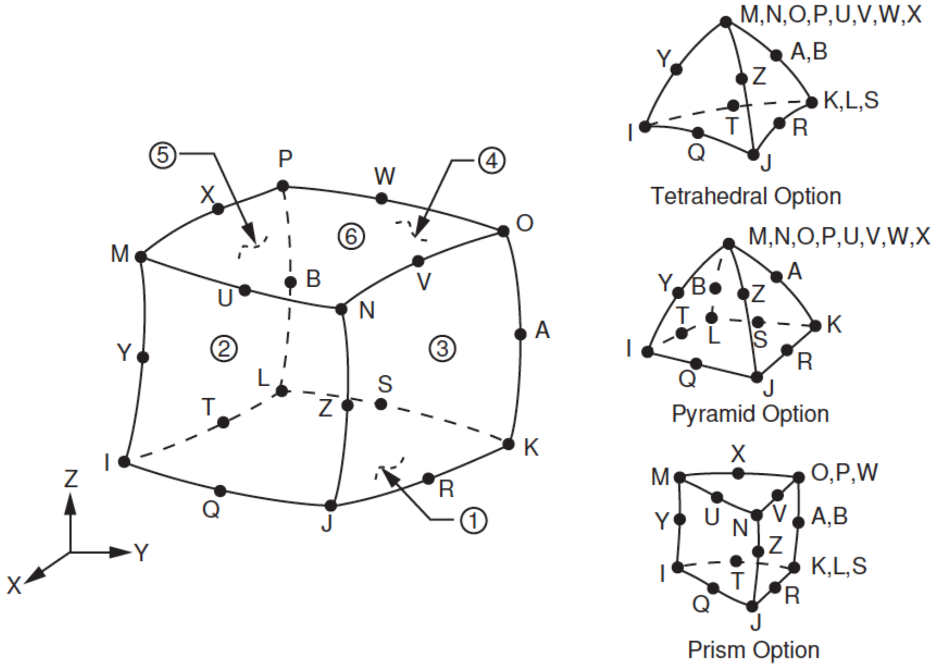

Figure 3.11: Structural 20-nodes SOLID186 element definition from ANSYS Help [83].

RF MEMS switches involves a special set of elements able to couple *electrical* and *mechanical* domains. As an example, the TRANS126 elements, sketched in Fig. 3.12, realize a direct electro-mechanical coupling between an elastic structure and an applied voltage load. Such an element is extensively used for the simulation of the pull-in and pull-out of RF MEMS switches.

Finite elements methods are also implemented for the modeling of electromagnetic problems [84]. Ansoft HFSS$^{\text{TM}}$ [83] is a *full-wave* tool for the simulation of the field propagation in structures and antennas in the *frequency domain*. One-order, second-order and mixed-order tetrahedra elements are available, allowing for the easy modeling of not-regular 3D structures, such as a planar MEMS circuit may be. It also provides complete information about the S-parameters, electromagnetic field and RF current density distribution. As it will be shown in Chapter 5, the solution values concerning the power loss due to RF currents can be easily imported

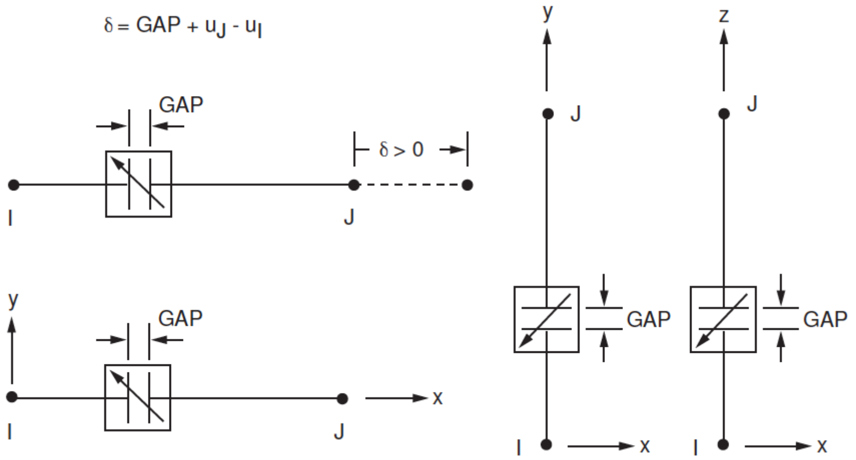

Figure 3.12: Coupled electro-mechanical TRANS126 element definition from ANSYS Help [83].

in ANSYS as a further load for a structural-thermal simulation.

### 3.4.3 Method of Moments

The *method of moments* (MoM) is a numerical method based on the discretization of the physical domain as well. It was developed as an efficient way to solve the Maxwell equations in planar structures [86] in *frequency* domain. It is an *integral method* as FEM, but it is computationally less expensive. A commercial software based on MoM is ADS Momentum [81], which is meant to analyze complex planar structures embedded in a multilayered dielectric substrate. The definition of *via* layers allows for the connection of conductors layers realizing the planar transmission line. A typical discretization of a conductor layer performed by Momentum is depicted in Fig. 3.13. Based on such a definition, the models built with this approach are usually considered 2.5 D. Such a method may be very fast and efficient for the simulation of high aspect ratio structures, like MEMS switches. Its integration capability with the circuit simulator implemented in ADS allows for quick design and optimization of any kind of circuit.

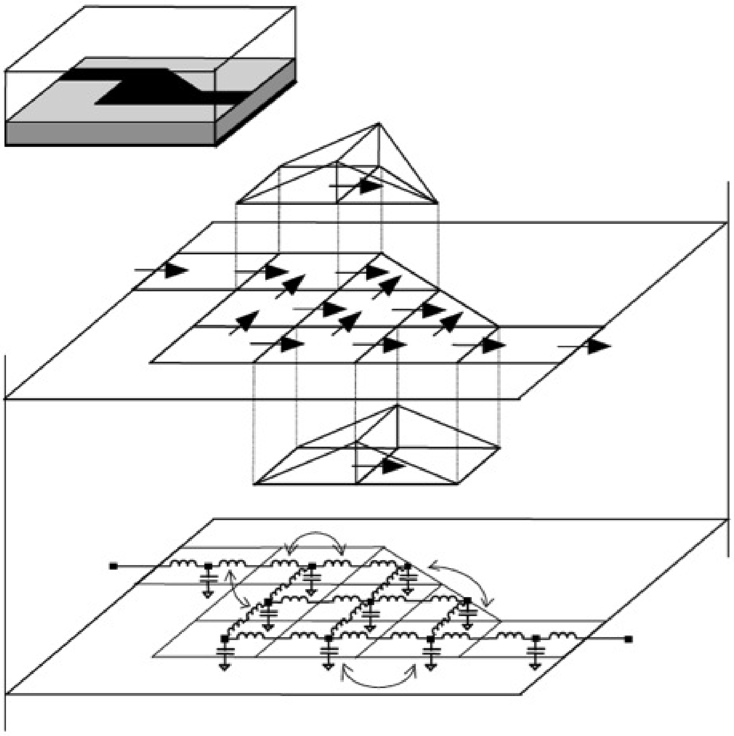

Figure 3.13: Equivalent network representation of the discretized MoM problem [85].

## 3.5 Case studies

### 3.5.1 Benchmark devices

In the following Section some examples of electromechanical and electromagnetic analysis of MEMS switches are reported. Electro-mechanical analysis were performed in FBK, whereas electro-magnetic analysis were performed by exploiting the software capabilities of University of Perugia and Lehigh University. The modeling examples were performed on devices manufactured at FBK according to the fabrication process described in Section 2.6. Both the devices are integrated in a coplanar transmission waveguide. One device is a fixed-fixed capacitive shunt switch, the other one is a cantilever series switch. The first switch comprises a rectangle-shaped movable membrane that is anchored on both ends to the ground conductors of a coplanar transmission line, but suspended over the center conductor of the transmission line and two actuation pads beside the center conductor. A picture of the capacitive switch is shown in Fig. 3.14-a. The second device is a free-clamped in-line series switch with the signal conductor of the coplanar transmission waveguide. A set of five contact bumps is placed under the tip of the cantilever, realizing the ohmic contact with the suspended beam after the actuation. The picture of the ohmic switch is reported in Fig. 3.14-b.

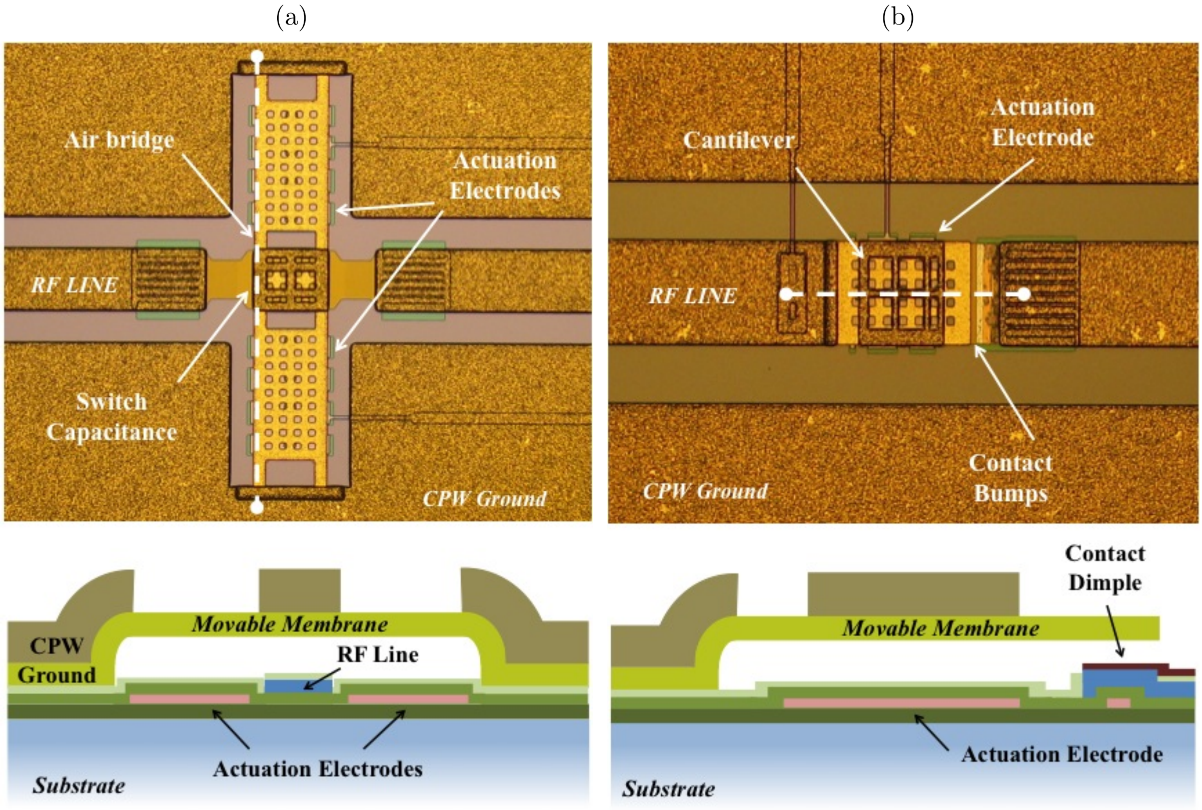

Figure 3.14: Photo of MEMS devices used as benchmark: (a) shunt capacitive switch (”D” type), and (b) series ohmic switch (”C” type) and the corresponding cross-section sketches. The colors of the layers are the same used for the process description reported in Fig. 2.15

### 3.5.2 Electromechanical model of a capacitive switch

ANSYS$^{TM}$Multiphysics software was utilized for the electro-mechanical finite-element model of such a device. A quarter of the switch geometry was built by placing the membrane thickness along the $z$-axis and the membrane longest dimension along the $y$-axis. Then the $yz$ and $zx$ symmetries were set to save computational time. After choosing SOLID186 as structural elements, a set of coupled electro-mechanical elements TRANS126 was generated from the bottom side of the membrane in correspondence of the actuation pads of the real structure. Each of these elements involves a couple of nodes, one (I) attached to a structural node, and the other one (J) mapped at a distance $g_0$ along the negative $z$-direction, emulating the gap distance between bottom and top electrode. Table 3.1 describes the element technology and material properties used for the simulation. The list of elements and the employed approach is not specific of the reported device and it may be applied to any kind of electrostatic MEMS structure.

Table 3.1: Finite element properties used in ANSYS simulations.

| **Parameter** | **Value** |
|---|---|
| Structural element type | SOLID186 |
| Coupling element type | TRANS126 |
| Mesh type | brick mapped mesh |
| Mesh size | 3-5 $\mu$m |
| Residual stress | 50 MPa |
| Gold Young modulus | 75 GPa |
| Gold Poisson's ratio | 0.42 |
| Act. pads gap | 2.7 $\mu$m |
| RF line gap | 2.4 $\mu$m |

In the static analysis for the calculation of pull-in and pull-out voltages the large-displacement option, considering a non-linear relationship between force and displacement, was activated, and a relaxed convergence criteria regarding the displacement degree of freedom was also chosen. Fig. 3.15 shows the resulting nodal $z$-displacement solution when $V_{bias} = 0$

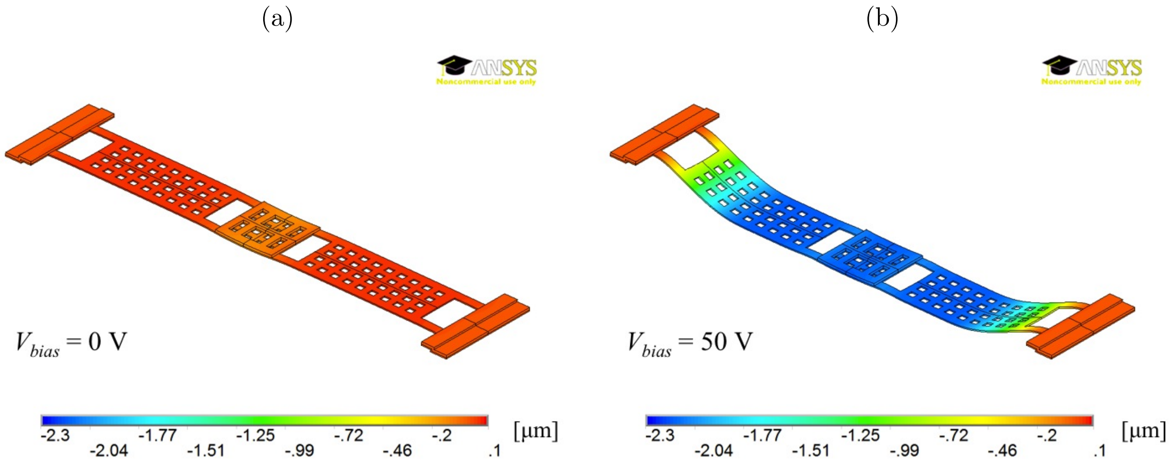
(a) (b)

Figure 3.15: Displacement solution along the $z$-axis of the capacitive switch shown in Fig. 3.14-a at $V_{bias}$ = 0 V and 50 V.

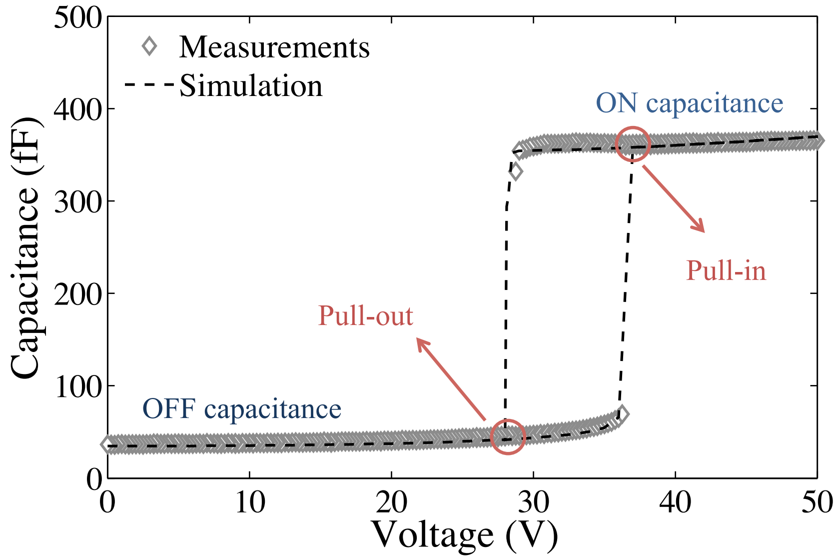

Figure 3.16: Capacitance versus bias voltage characteristic: comparison between measurements (symbols) and simulation (dashed line) of the capacitive switch of Fig. 3.14-a.

and $V_{bias}$ = 50 V are applied. In Fig. 3.16, simulation results are also compared with capacitance-voltage (CV) measurements. Good agreement is achieved with measured pull-in voltage (38 V) and pull-out voltage (29 V). Note that in order to achieve this matching an initial residual stress of 50 MPa (which is reasonable for the employed fabrication process) needs to be applied to the bridge material, producing also an initial membrane deformation (see next Section).

### 3.5.3 Residual stress modeling

As observed before, the residual stress in thin films arises from several factors, such as intrinsic material stress and thermal expansion mismatch between two contacting layers. The modeling of the initial stress conditions in the electro-mechanical simulation of MEMS switches is fundamental for the correct evaluation of the pull-in voltage. This task can be accomplished in ANSYS by exploiting the INISTATE command, which allows for the definition of an initial stress in all the directions of the selected material and/or element. In particular, if $z$ is the direction defining the thickness of all the layers, the stress components to set up are along $x$ and $y$ directions, so a realistic *bi-axial* stress of the thin film is reproduced. Another way to apply a residual stress to a structure is by utilizing an initial *thermal* load. However, although both the methods provide similar results, the INISTATE command produces a structure stiffness status closer to the reality, since it allows for considering the effect of the material intrinsic stress. Fig. 3.17 shows how the pull-in and pull-out voltage of the capacitive switch depicted in Fig. 3.14-a changes by varying the residual stress.

In case of cantilever beams, the attention turns to the modeling of the *stress gradient* by exploiting INISTATE command in the same way. The *bending* of a free-clamped beam of thickness $t_s$ is easily simulated by dividing the beam in two *layers* of the same thickness $t_1 = t_2 = t_s/2$. Then two values of residual stress are applied, $\sigma_1$ to the bottom layer and $\sigma_2$ to the top layer. For a given stress gradient $\Gamma_s$, the difference between the equivalent stress values $\sigma_2$ and $\sigma_1$ can be computed by balancing the bending moments induced to the two layers. Thus it results:

$$\Delta\sigma = \sigma_2 - \sigma_1 = \pm\Gamma_s \frac{t_s}{3}. \tag{3.25}$$

The cantilever tip bends *upward* for $\sigma_2 - \sigma_1 > 0$, whereas it bends *downward* if $\sigma_2 - \sigma_1 < 0$.

MEMS structures manufactured by surface micro-machining are usually very thin, and a very fine mesh is usually required to avoid high-aspect ratio elements (i.e. length or width much higher than thickness), which may compromise the correctness of the solution. Moreover, the mesh usually consists of only one or two elements along the MEMS thickness, so high order elements should be used [87]. In order to save computational time when a layer subdivision is needed to model the stress gradient, a good approach is to use *layered* brick elements (SOLID186 elements with layer option activated) or also *shells* (SHELL181 elements). In this case a multi-layered cross-section with different materials can be separately defined, making easier to set up the initial conditions of the real beam.

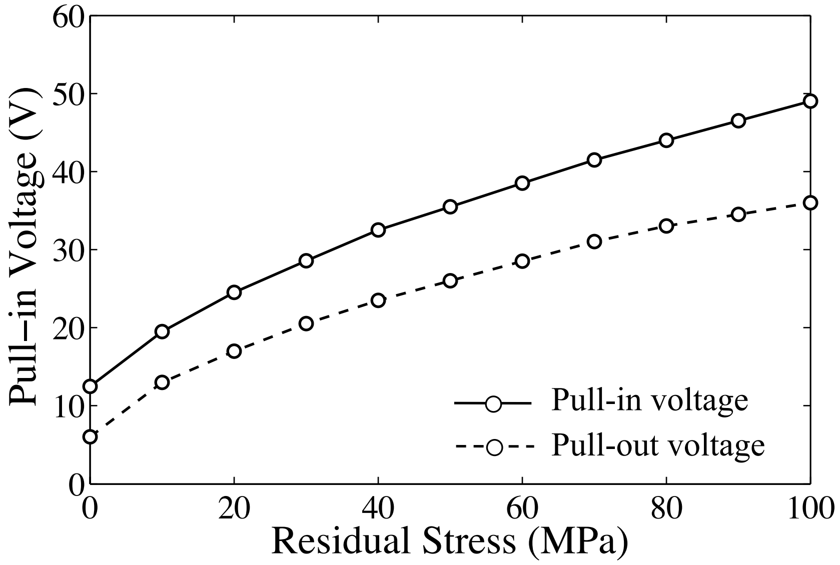

Figure 3.17: Simulated pull-in (continuous line) and pull-out (dashed line) voltage variation with residual bi-axial stress of the capacitive switch from Fig. 3.14-a.

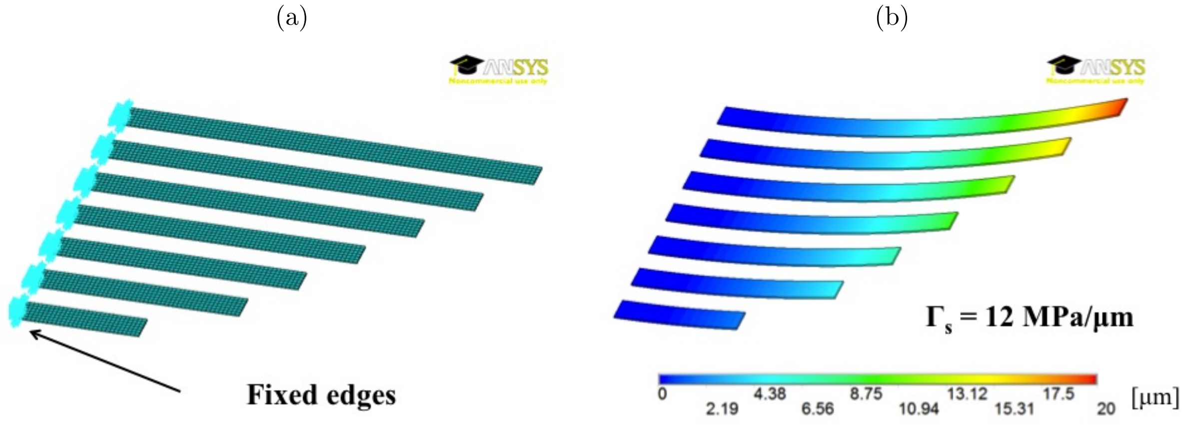

Figure 3.18: Test structure cantilever beams array: (a) finite element model based on layered brick elements, and (b) displacement nodal solution.

Fig. 3.18-a shows the finite element model of the array of cantilevers whose optical profiler image was previously reported in Fig. 3.3. A stress gradient was applied in order to reproduce as the same tip displacement as the one measured on test structures by optical profiler. A maximum tip-deflection of around 20 $\mu$m is achieved on the longest beam if the stress gradient $\Gamma_s$ is chosen equal to 12 MPa/$\mu$m, as reported in Fig. 3.18-b. Parameters and settings used for this simulation are listed in Table 3.2.

Table 3.2: ANSYS finite element properties used to simulate stress and stress gradient in the cantilever beams manufactured in FBK.

| **Parameter** | **Value** |
|---|---|
| Structural element type | SOLID186/SHELL181 |
| Layered option | ON |
| Mesh type | brick mesh |
| Mesh size | 2-5 $\mu$m |
| Stress gradient | 12 MPa/$\mu$m |
| Gold Young modulus | 75 GPa |
| Gold Poisson's ratio | 0.42 |

### 3.5.4 Contact modeling for ohmic switches

The electro-mechanical finite-element modeling of a cantilever ohmic switch is perfectly similar to the one presented in Section 3.5.2 for a capacitive switch. Nevertheless the stress gradient should be carefully considered for cantilever beams in order to have an acceptable matching with the measured switch actuation voltage. Table 3.3 reports the settings used to perform the simulation of the cantilever switch. Fig. 3.19-a illustrates the cantilever beam at the initial conditions, by assuming a stress gradient $\Gamma_s$ equal to 12 MPa/$\mu$m, whereas Fig. 3.19-b shows the deformed shape after the application of $V_{bias} = 50$ V. From Fig. 3.19-a it is also possible to note that for $\Gamma_s = 12$ MPa/$\mu$m, the corresponding tip up-deflection is around 1.2 $\mu$m. The resulting actuation voltage is 48 V for $\Gamma_s = 12$ MPa/$\mu$m, while it is 34 V for $\Gamma_s = 0$ MPa/$\mu$m.

Table 3.3: ANSYS finite element properties used to simulate the contact in the ohmic switches manufactured in FBK.

| **Parameter** | **Value** |
|---|---|
| Structural element | SOLID186 |
| Contact-pairs element | CONTA174-TARGE170 |
| EM coupled element | TRANS126 |
| Layered option | ON |
| Mesh type | brick/prism mapped mesh |
| Mesh size | 2-5 $\mu$m |
| Normal stiffness factor | 0.01 |
| Residual stress | 50 MPa |
| Stress gradient | 12 MPa/$\mu$m |
| Gold Young modulus | 75 GPa |
| Gold Poisson's ratio | 0.42 |
| Act. pads gap | 2.7 $\mu$m |
| Contact bumps gap | 1.7 $\mu$m |

Another remarkable aspect to consider for this kind of simulations is

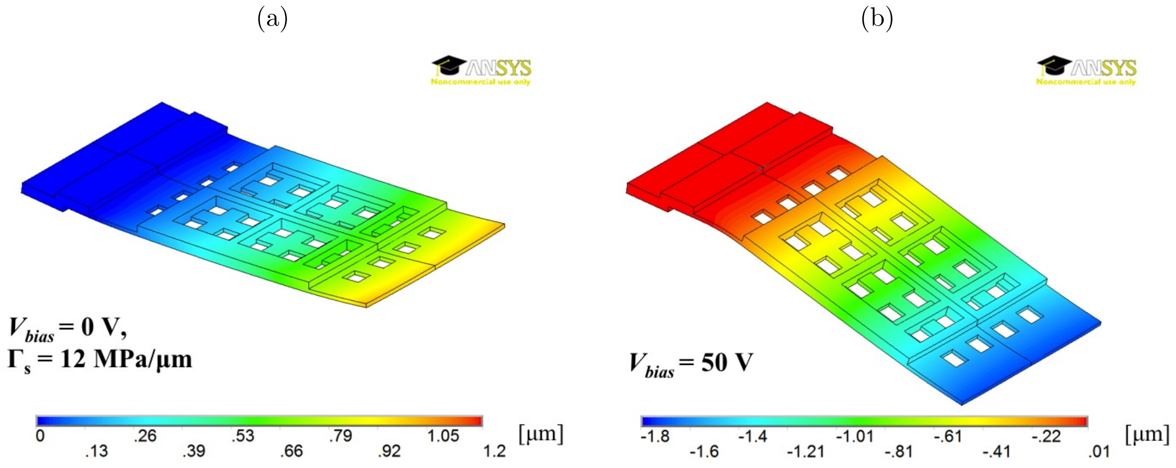

Figure 3.19: FEM simulation of the cantilever switch from Fig. 3.14-b: (a) nodal displacement only due to stress gradient, and (b) nodal displacement when a bias voltage of 50 V is applied.

the modeling of the ohmic contact. For simulations involving the pull-in/pull-out voltage calculations, TRANS126 elements behave also as contact elements, but they are not dedicated for the simulation of the contacts. Moreover TRANS126 elements do not provide any information about the pressure, friction and status of the contact. Therefore this kind of analysis requires the generation of contact-pairs elements (*target* elements and *contact* elements) along the surfaces which are supposed to get in contact. For an analysis employing a 3D model, a *surface-to-surface* contact between the membrane and the bumps is realized by generating TARGE170 and CONTA174 elements on the corresponding surfaces. An important setting constant affecting the final results is the *normal stiffness factor*, which could be set to 0.01 to help convergence in this kind of problems. Also, the element key-options should be set in order for the contact stiffness to be update at each sub-step, since some simulations can involve an abrupt change of the status of the contact elements, leading to convergence problems. These elements also allow for a multiphysics simulation of the contact, involving structural, thermal, and electric degrees of freedom, use-

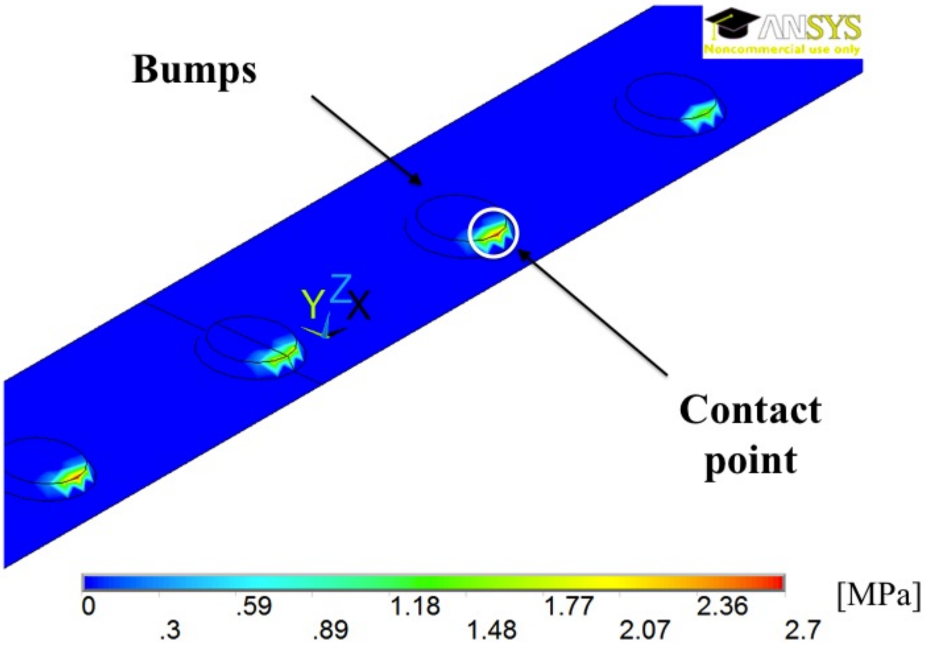

Figure 3.20: Contact pressure applied on contact bumps by the actuated membrane from Fig. 3.19(b).

ful for the study of the contact resistance evolution as a function of the contact pressure [88].

As a result, the simulation requires more computational effort, but it is able to provide information about the contact force. An example of the results obtained by ANSYS simulations is reported in Fig. 3.20, showing the contact pressure distribution on bumps of the case-study cantilever device. In this case, the simulated contact force on bumps is equal to 13 $\mu$N at $V_{bias}$ = 50 V. Switch design may be optimized accounting for the contact force value in order to achieve a low contact resistance.

### 3.5.5 2.5D electromagnetic model of a ohmic switch

A cantilever switch in a coplanar waveguide was simulated by means of the full-wave software ADS Momentum. The simulation procedure consists of the definition of the dielectric layers properties, the mapping as a *strip* (microstrip and coplanar) or *slot* (slotline) of the conductors and the settings of the *ports*. Table 3.4 reports the material properties and mesh settings employed for this kind of simulation. One of the most important parameter to set is the thickness of the *air* layer, which provides information about the membrane *gap*. The gap chosen for the simulation of the the

(a)

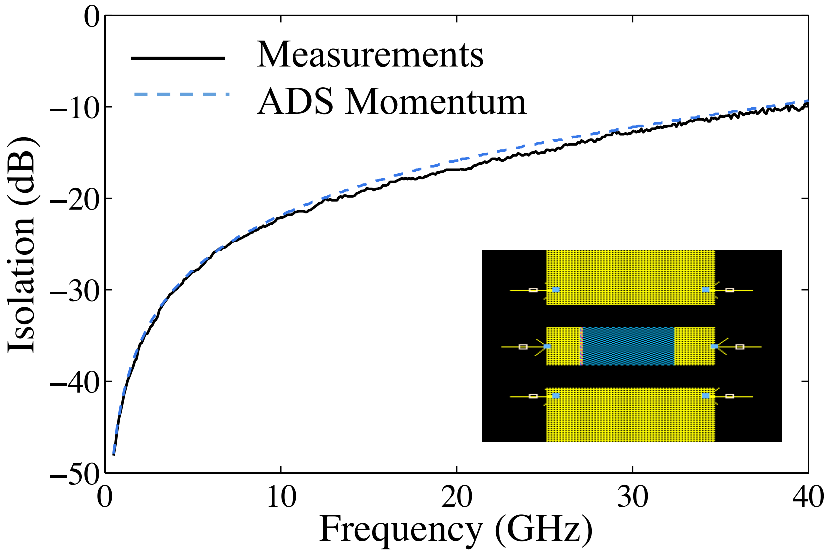

(b)

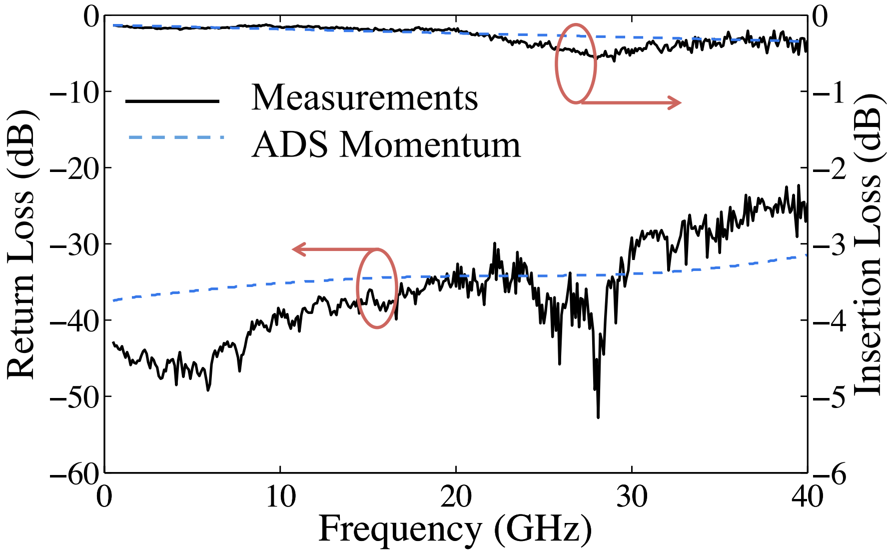

Figure 3.21: Comparison between S-parameters Momentum simulations (— — —) and measurements (—) of a series ohmic switch in OFF (a) and ON (b) state.

Table 3.4: Material properties and settings used in Momentum and HFSS for the simulations of FBK switches.

| **Parameter** | **Momentum** | **HFSS** |
|---|---|---|
| Substrate | Silicon | Silicon |
| $\varepsilon_r$ | 11 | 11 |
| $\tan\delta$ | 0 | 0.006 |
| Mesh (cell per wavelength) | 40 | - |
| *DeltaS* | - | 0.01 |
| Port type | *Coplanar* | *Wave Port* |
| Air gap | 2.7 $\mu$m | 2.4 $\mu$m |
| Gold conductivity | $4 \times 10^7$ S/m | $4 \times 10^7$ S/m |

cantilever is 2.7 $\mu$m, resulting in a OFF capacitance equal to about 10 fF. In case of air-bridge switches, when the membrane is actuated the gap is ideally 0 $\mu$m. However, an effective non-zero gap can be used to simulate the residual air between the membrane and the capacitance dielectric, due to the surface material roughness. The data generated by the simulation can be loaded in the ADS circuit environment for further comparison with circuit models and measurements, as in the way depicted in Fig. 3.21.

### 3.5.6 3D electromagnetic model of a capacitive switch

The electromagnetic model of the capacitive switch from Fig. 3.14-a was developed in HFSS$^{\mathrm{TM}}$, and the resulting S-parameters are compared with measurements. The accuracy of the model is controlled by setting the parameter *DeltaS*, which is utilized by the software as a criterion for the solution convergence. The solution proceeds for a number of steps. At each step the S-parameters are compared with the computed S-parameters results from previous step. When the difference between S-parameters calculated at two contiguous steps is less than the criterion defined by means of *DeltaS*, convergence is considered accomplished. Therefore higher accuracy is achieved for smaller values of *DeltaS*. Moreover, the model mesh

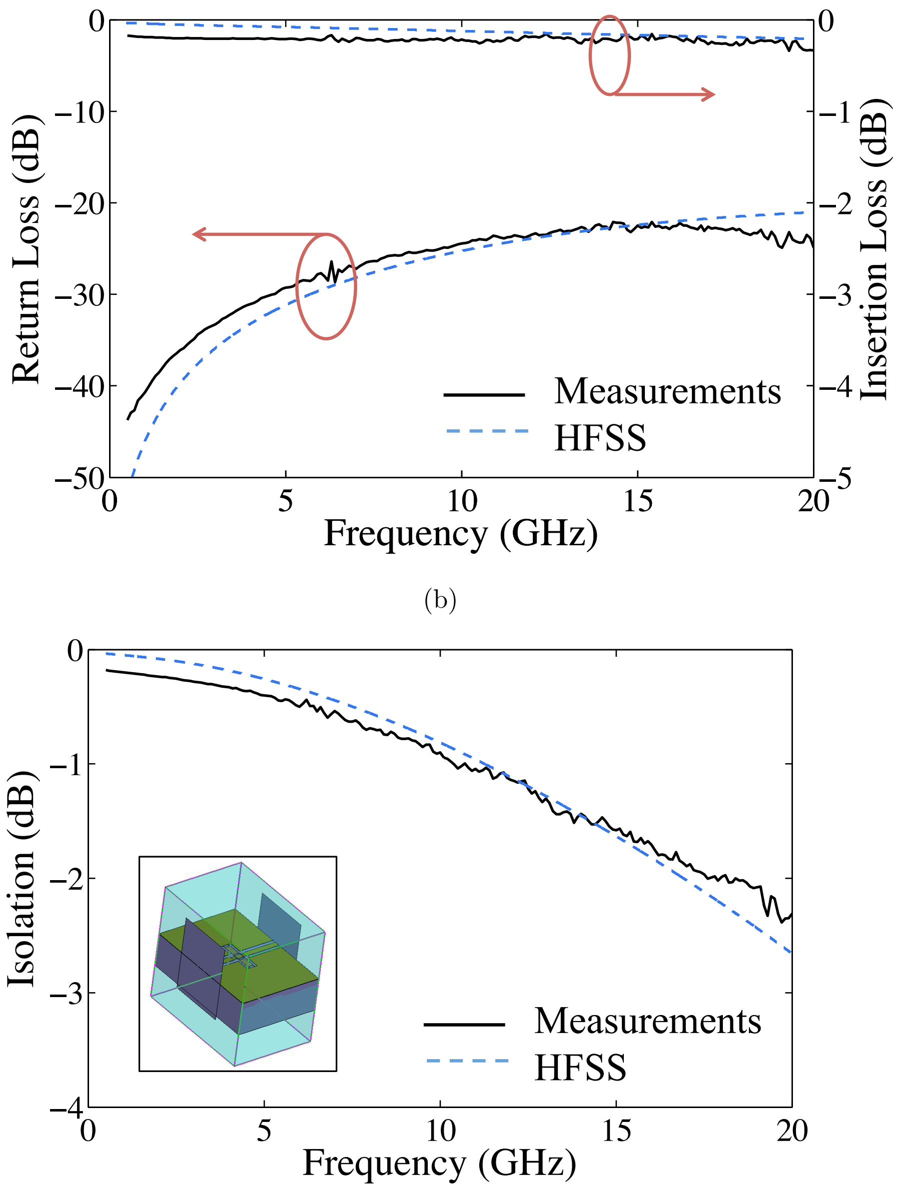
(a)

(b)

Figure 3.22: Comparison between S-parameters HFSS simulations (– – –) and measurements (—) of a shunt capacitive switch in OFF (a) and ON (b) state.

is refined at every step.

Fig. 3.22 shows the simulated S-parameters of the capacitive switch in OFF and ON states compared to the measurement data up to 20 GHz. The ON-state can be simulated with an acceptable approximation by drawing the model of the membrane so that it contacts the bottom RF line. The material parameters and analysis settings employed for this simulation are listed in Table 3.4. Material properties are basically the same as those utilized for Momentum simulations. For a good compromise between accuracy and simulation speed, *DeltaS* was chosen equal to 0.01. Unlike Momentum results, HFSS simulation provides quantitative information about electric and magnetic fields magnitude and distribution, and also about power losses in each conductor or dielectric solid object.

## 3.6 Conclusions

This Chapter introduced the basic concepts concerning the mechanical and electromagnetic modeling of RF MEMS capacitive and ohmic switches. Some simulation tools such as ANSYS, ADS Momentum and HFSS were briefly introduced and applied to some case studies for the modeling of ohmic and capacitive switches.

The presented modeling methodologies can be used for the simulation of various RF MEMS devices with different geometries, configurations, and stress conditions. Therefore the usage of these tools represent an excellent method for an accurate evaluation of important functional parameters such as actuation and release voltages, contact force, insertion and return loss, isolation, and their sensitivity to process and environmental conditions such as temperature, operating power and stress. As a consequence the described simulation procedures were extensively exploited to achieve the results that will be presented in this thesis.

# Chapter 4

# Long-Term Stress Reliability

## 4.1 Introduction

One of the most important requirement of redundancy switches for satellite applications is their ability to change their status (from OFF to ON, and vice-versa) after having been biased for a long-time period (at least 15 years). The accomplishment of this functionality is a very hard task for MEMS switches. As illustrated in Chapter 2, dielectric charging and contact micro-weldings may occur during switch lifetime, resulting in the *stiction* of the moveable membrane. The former may happen in any kind of switches when a bias voltage is applied. The latter is common in ohmic switches, where a metal-to metal contact is employed.

In the following Chapter, a brief review about the main mechanisms inducing stiction is presented, focusing on contact degradation and dielectric charging phenomena. Especially the last aspect is discussed in detail, illustrating the most used predictive models for the charging-induced failure. In addition the Chapter reports a long-term reliability characterization on RF switches manufactured in FBK, highlighting how a different membrane design may affect the switch lifetime.

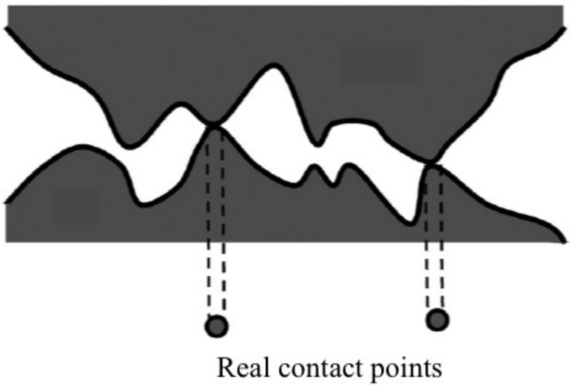

Figure 4.1: Cross-section schematic of the micro-asperities of two contacting surfaces [52].

## 4.2 Review of contact degradation mechanisms

The physics of the metal-to-metal contact is extremely complex and still not completely understood. As already illustrated in Chapter 2, two metal surfaces contacting repeatedly each other may experience degrading phenomena such as *wear*, *hardening*, and *pitting*, which may improve or worsen the roughness of the surfaces. The effective contact area, which impacts on the contact resistance and then on the switch insertion loss, is determined by the shape and the topology of the asperities, as depicted in Fig. 4.1. If a constant or variable current is forced to go through the contact, the situation is even more complicated because of the high-temperature spots which may arise from the Joule effect.

In many works the quality of the contact between two metals is monitored by measuring the contact resistance for incremental mechanical loads [89]. As a result, three different contact regimes, also depicted in Fig. 4.2, may be commonly identified:

- An *unstable* contact regime, that is the very beginning of contact phenomenon, where contact resistance is still high both because the roughness of the contact surface dominates among other effects and surface contaminants are quite relevant [52].

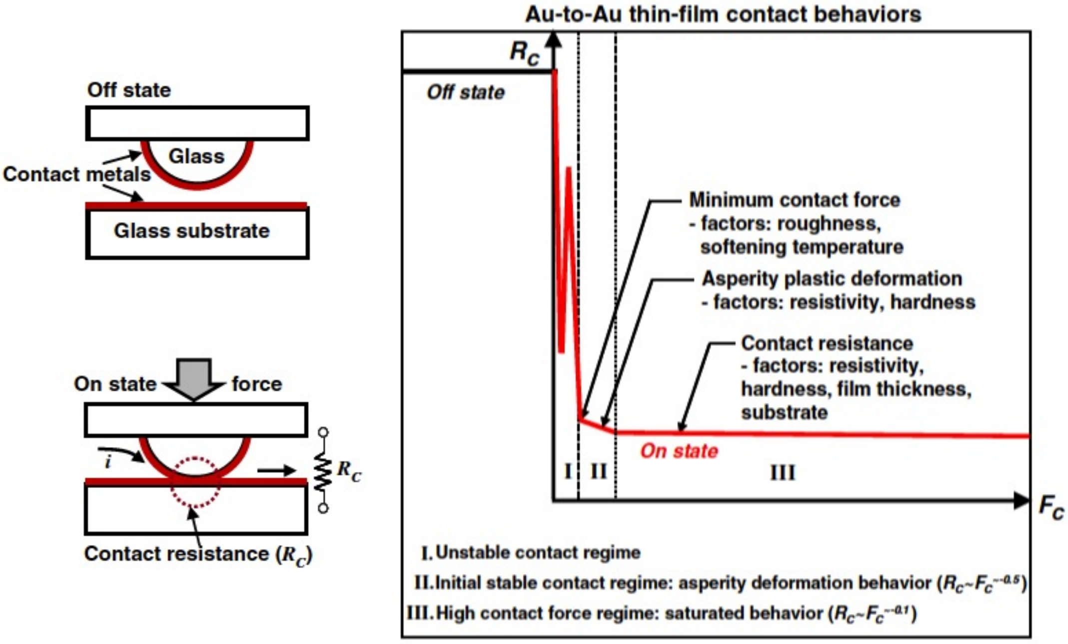

Figure 4.2: Measurement procedure and resulting contact resistance versus contact force plot. Three contact behavioral regions are distinguished [89].

- A *transition region* where the asperity plastic deformation starts to begin. In this case, a minimum contact resistance value may be observed and chosen as a reference of the beginning of the transition region. This value can also decrease when the current flowing through the contact increases [89].

- A *high contact force* regime, where contact resistance assumes a low constant value and some parameters like *resistivity*, *hardness* and *thickness* of the contact material start to influence the quality of the contact. It has been proved that a thicker film used for the contact provides a lower contact resistance at the stable regime [90].

The relationship between contact force and contact resistance depends also on the amount of DC current used for the resistance measurement. Two different behaviors may be detected in case of low current ($< 1$ mA) or high current ($> 1$ mA) flowing through the contact [89].

At *low current*, the *softening* of the contact can occur. This happens at a so-called local *super-temperature* of 100 °C and it can facilitate the plastic deformation of local bumps and then the asperities creep. However, at low current adhesion phenomena dominate in the contact status. Adhesion mainly depends on Van der Waals forces (about 0.01 - 2 mN from literature [51]), which increase when the contact surface gets wider after asperities smoothing. The separation between the two contact surfaces is *brittle*-type.

On the other hand, when a *high current* is applied, local temperature may reach the melting temperature of the material. Nano wires may grow during the separation causing short circuits due to the welding of the two surfaces. In this case the separation is *ductile*-type [51]. Plastic deformations and erosion of asperities may increase the total roughness, providing low adhesion forces. The dominating failure becomes the *micro-welding* among localized asperities.

In addition, material properties assume a very important role in the prevention of adhesion or welding mechanisms. An harder material like platinum or other gold alloys provide better resistance to wear and material transfer, but the most common gold-to-gold contact shows the best performance in terms of contact resistance. As can be seen from Fig. 4.3-a and Fig. 4.3-b, Au-Pt, Au-Ir and Pt-Pt contacts seem to be good candidates for high power MEMS switches, despite sliglthly worse performances in terms of insertion loss with respect to Au-Au contact [91].

For very thin metal layers, the hardness of a material depends also on the bulk substrate. If $r$ is the deformation radius, within a distance of $3r$ the hardness of substrate influences plastic deformation.

If the utilization of different metal materials or alloys is not allowed because of process compatibility, an improvement of the mechanical design could be the key solution to have an good contact force resulting in low switch ON-state loss. High restoring force is also required in order

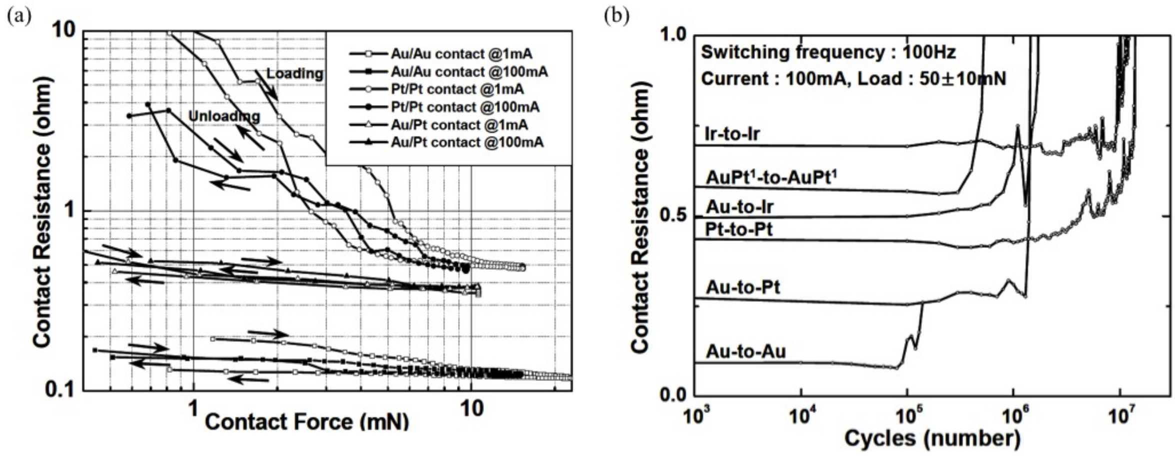

Figure 4.3: (a) Plot of contact resistance versus contact force, and (b) contact resistance evolution with respect to cycling load at 100 mA for different kind of contact materials and material alloys [91].

to overcome adhesion and local welding problems also at high currents. From literature [4] [92] the most used range of contact force in commercial switches is 100 - 1000 $\mu$N.

## 4.3 Review of dielectric charging models

The charging is intrinsically related to the structure of the switch. A common situation of dielectric charging can be described in a very simple manner as follows.

The electro-mechanical energy transduction occurs since a potential difference is applied between a *fixed* electrode and a *movable* or *mobile* electrode. When the bias voltage is higher than the pull-in voltage, the movable electrode collapses towards the fixed one, and an electrical insulating layer is needed to prevent the formation of an electric short. Then a large voltage is applied to thin gap, resulting in a very high localized electric field. Free electrons are then injected from the metal surfaces into the dielectric layer, where they remain *trapped* because of its intrinsic *defects* (such as vacancies or interstitials). The trapping and de-trapping mechanisms are ruled by different *time constants* and *activation energies*. Such a situation is illustrated in Fig. 4.4.

If the whole effect of the injected charges is modeled with a *sheet* $\sigma_s$ of charges at the surface, its influence on the electrostatic force is given by:

$$F_e = \frac{A}{2\varepsilon_0 g_0}\left(V_{bias} - \frac{d_\varepsilon \sigma_s}{\varepsilon_0 \varepsilon_r}\right)^2, \tag{4.1}$$

where $d_\varepsilon$ and $\varepsilon_r$ are the thickness and the permittivity of the dielectric layer respectively, $V_{bias}$ is the bias voltage, and $A$ is the electrode area. According to the sign of charges, the built-in electrostatic force may increase or lower the electrostatic force provided only by the bias voltage $V_{bias}$. Thus the main evidence of charging is a *variation* or *shift* of the pull-in/pull-out voltages of the RF MEMS switch, given by:

$$\Delta V = \frac{d_\varepsilon \sigma_s}{\varepsilon_0 \varepsilon_r}. \tag{4.2}$$

Thus the charging process eventually may induce the *stiction* of the suspended membrane in down-state if the built-in voltage expressed by Eq. 4.1 is higher than the switch pull-out voltage.

The dielectric charging effect on RF MEMS device has been extensively studied in the last decade. Most of the works dealt with the physics of the dielectrics, leveraging on previous studies developed for CMOS technology [93]. However, most of what was observed in MEMS switches could not be fully explained and different models were proposed based on empirical data.

In [94] and [44] authors distinguish between bulk and surface charges. The former are injected from the bottom electrode to the dielectric and they charge and discharge quickly, usually at the same rate. The latter charge very fast and discharge very slowly, and also they are also particularly

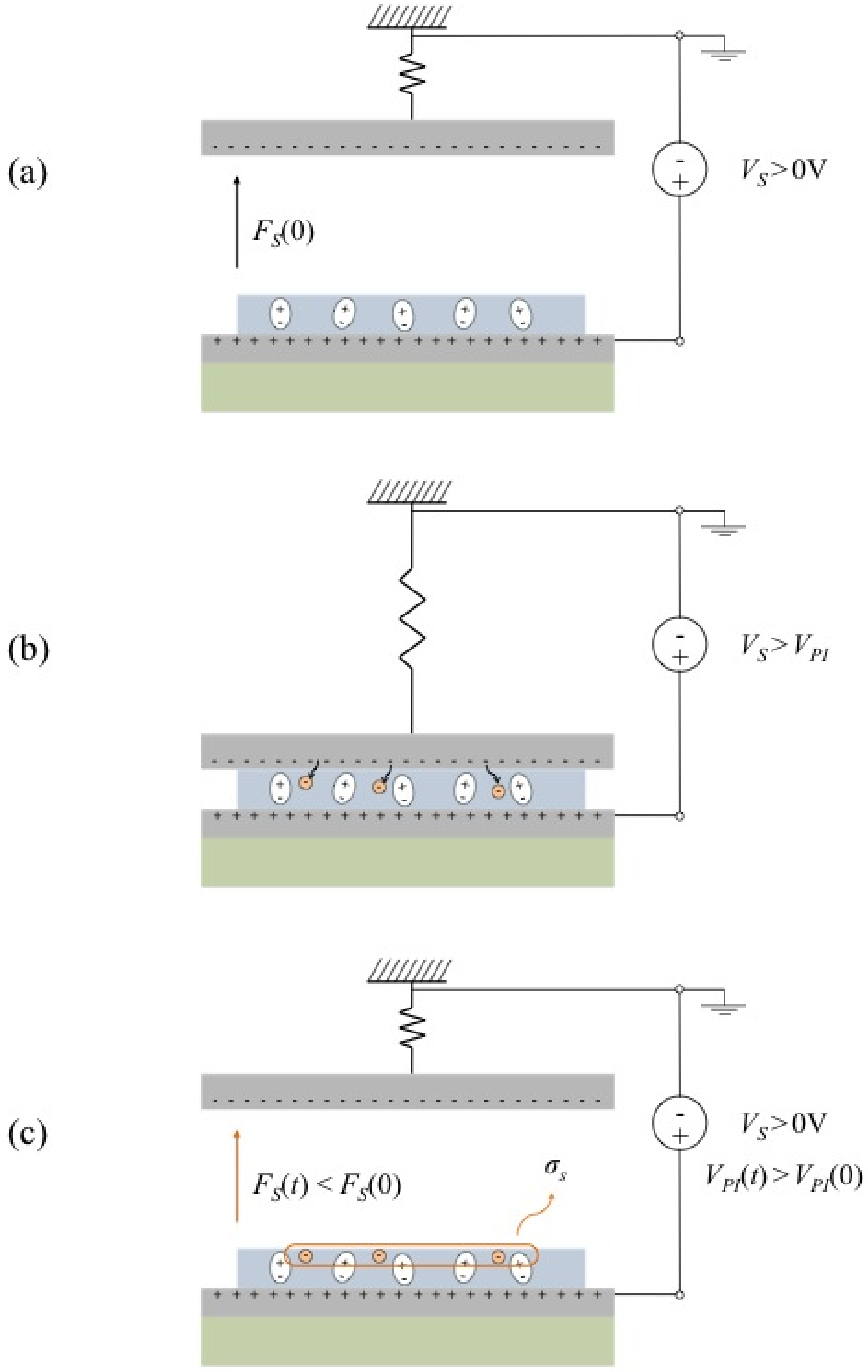

Figure 4.4: Charge injection in to the insulating layer on a parallel-plates capacitor MEMS model: (a) initial dipole polarization; (b) charge injection after the membrane pull-in; (c) surface charging influence on the electrostatic force.

dependent on external humidity [63]. In addition, the charging process is fitted by a multiple trapping time constant expression, which influences the variation in pull-in voltage such as:

$$\Delta V(t) = \sum_{j=1} V_j \left[1 - e^{-\left(\frac{t}{\tau_j}\right)}\right] \tag{4.3}$$

where $\tau_j$ is the time constant of the $j$-th trapping mechanism, usually dependent on temperature, and $V_j$ is equal to:

$$V_j = V_{bias} e^{\left(\frac{V_{bias}}{V_{j0}}\right)} \tag{4.4}$$

where $V_{j0}$ is another fitting parameter. The variation of *pull-out* voltage follows a similar behavior, except than the fitting parameters may differ a little bit. However, as explained before, the pull-out variation is the most significant parameter to monitor, since, when it equals the pull-out voltage value, the membrane is inevitably in stiction. Trapping mechanisms can be activated or accelerated by increasing the working temperature or the voltage stress. Again, all the parameters depend also on the kind of material used as insulating layer and the quality of the material itself.

In [48], the charging description is based on the super-imposition of different polarization mechanisms. Also *intrinsic* and *extrinsic* space charges are considered as polarization components, along with the *dipole* polarization. The combination of all these effects is modeled by considering a distribution of relaxation time constants:

$$\Delta V(t) = V_0 \left[1 - e^{-\left(\frac{t}{\tau_0}\right)^{\beta}}\right] \tag{4.5}$$

where $\tau_0$ is a fitting time constant which depends on temperature, $V_0$ is the saturation value and $\beta$ accounts for the distribution of time constants. The parameter $V_0$ may have a similar dependency to the bias voltage as the one explicated in Eq. 4.4. The activation of fast and slow polarization mechanisms is observed by monitoring also the variation of the *capacitance* value with time, even if no contact between suspended membrane and dielectric occurs [45].

All the above models assume that the charge distribution is *uniform* along the dielectric covering the pad. Consider now a *capacitance-voltage* (CV) characteristic, as the one shown in Fig. 3.16, but where also the capacitance variation for negative values of bias voltages is reported. According to Eq. (4.1) the primary effect of such a charge is to *shift* the whole CV characteristic towards positive or negative directions of voltage axis. The sign of the direction depends on the sign of charge (for example, it is typically positive if negative charges are injected in to the dielectric layer).

On the other hand, in [95] the effect of a *not-uniform* charge distribution on the pull-in/pull-out voltage variations is considered and modeled. The non-uniformity may depend on the different positions of the dielectric-membrane contact points, and on the non-uniformity of the dielectric-membrane gap. According to the proposed model, the total *mean* value of charge is the responsible of the *shift*, whereas the non-uniform charge causes the *narrowing* of the CV-window characteristic. Both the effects are accounted for in the following expression:

$$V_{PO}(t) = \frac{\overline{\psi}(t) d_\varepsilon}{\varepsilon_0 \varepsilon_r} \pm \sqrt{\frac{2kg_0 d_\varepsilon^2}{\varepsilon_0 \varepsilon_r^2 A} - \frac{d_\varepsilon^2 \sigma^2(\overline{\psi}(t))}{\varepsilon_0^2 \varepsilon_r^2}} \tag{4.6}$$

where $\overline{\psi}(t)$ and $\sigma^2(\psi(t))$ are respectively the mean and the variance of the charge distribution. The same equation can be modified to account for the direct effect of the non-uniform distribution of dielectric-membrane gap on the voltage variations. In this case, the gap distribution is described with mean and variance values as well, and also the *co-variance* of both gap and charge distributions is included in the model.

A power law of time is instead adopted in [19] to described the voltage variation evolution, in the form:

$$\Delta V(t) = Bt^n, \tag{4.7}$$

where $B$ and $n$ are again fitting parameters. Eq. (4.7) can be seen as a particular case of Eq. (4.5). This work was one of the first examples of long-term stress characterization, where a constant bias voltage or *stress voltage* was applied according to a specified duty-cycle. The authors showed that the parameter $n$ decreases with bias waveform duty cycle, proposing a practical approach aiming at the improvement of the long-term stress switch lifetime.

The RF MEMS switches utilized for the above-described analysis are *dielectric-less*, which means that all the insulator layer covering the actuation pad has been removed by design. Therefore the dielectric charging observed from measurements occurs mainly into the *substrate* (which is quartz in this case) underneath the pad. This implies also an evidence of the combined effects of both bottom-injected charges and not-uniform charging, according to [44] and [95].

## 4.4 Dielectricless switches

### 4.4.1 Device description

Long-term stress characterization has been performed on FBK switches in order to evaluate their reliability as redundancy switches. Measured data were gathered and analyzed in comparison with the dielectric charging models described in Section 4.3. Especially the power law was employed for the prediction of the *time-to-failure* of the switch, defined as the time after a continuous applied voltage stress at which membrane stiction occurs. Unlike other analysis that can be found in literature, the following

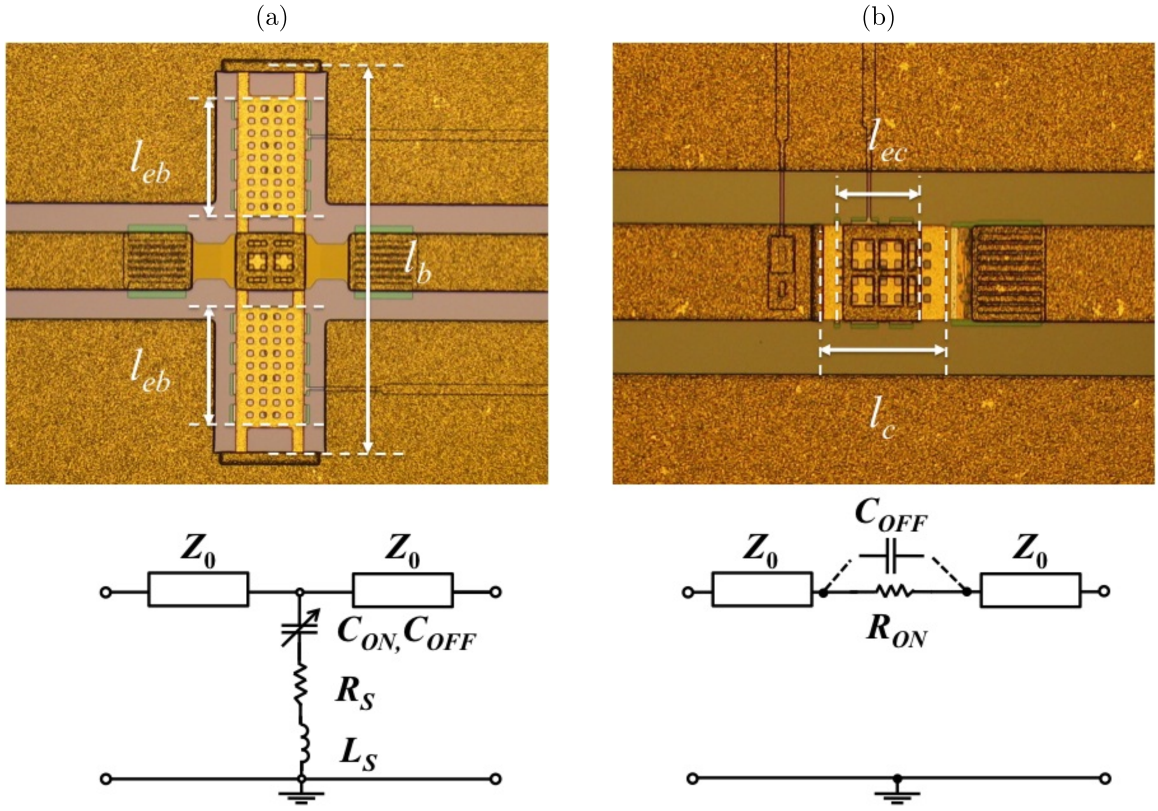

Figure 4.5: Pictures and corresponding equivalent circuits for (a) air-bridge and (b) cantilever switches. The lengths of the suspended beams and bias electrodes are also highlighted.

Table 4.1: Equivalent circuit parameters of the dielectric-less switches under test.

| **Parameter** | **Air-bridge [96]** | **Cantilever [21]** |
|---|---|---|
| OFF-state capacitance $C_{OFF}$ (fF) | 40 | 10 |
| ON-state capacitance $C_{ON}$ (fF) | 300 | - |
| Contact resistance $R_{ON}$ ($\Omega$) | - | 0.9 |
| Mem. inductance $L_S$ (pH) | 20 | - |
| Mem. resistance $R_S$ ($\Omega$) | 0.2 | - |

analysis aims at evaluating the effect of the switch geometry on the dielectric charging and then on the switch lifetime, providing some hints for a reliable switch design.

Two typologies of device are considered: a shunt capacitive air-bridge [96] and a series DC-contact cantilever beam [21], both integrated in a

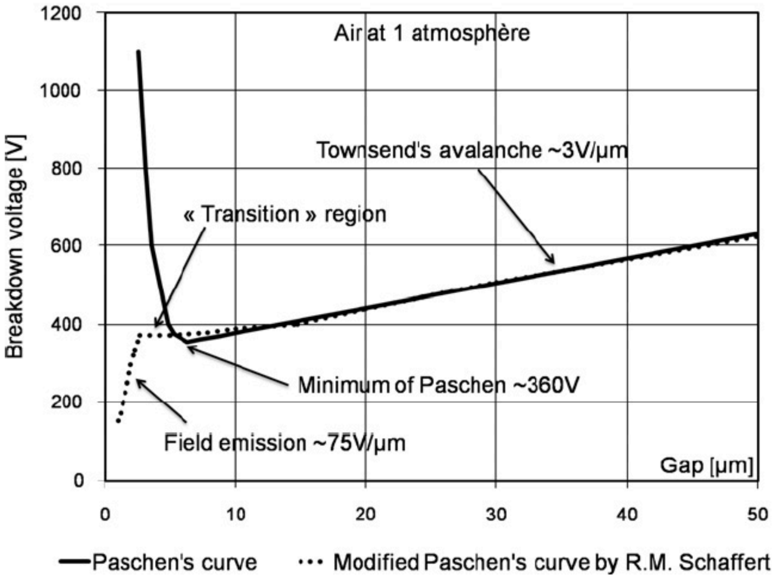

Figure 4.6: Modified Paschen's curve: breakdown voltage on the air at 1 atm [98]

$Z_0 = 50\ \Omega$ coplanar transmission line over high-resistivity ($> 5000\ \Omega\cdot$cm) silicon substrate. These switches have been already described and modeled in Section 3.5, and their pictures are reported again in Fig. 4.5, along with the equivalent circuit models. The lumped element values for the equivalent circuits are reported in Table 4.1. For the following analysis the same switches were designed *dielectric-less* in order to minimize the dielectric charging problem for short-time stress, as mentioned also in Section 4.3.

If the insulator layer is removed from the actuation pad, the design of mechanical *stoppers* is required in order to avoid the DC contact between top and bottom electrodes after the bridge snap-down. Mechanical stoppers may be included in the movable membrane, by means of a dedicated fabrication step [19] or placed besides or inside the bottom electrode [96]. Also the dielectric implemented in the RF capacitance (i.e. not used for the actuation pad) [18] and the contact bumps in ohmic switches [97] can serve as stoppers in dielectric-less switches.

In FBK switches, an array of mechanical stoppers or *pillars* is dis-

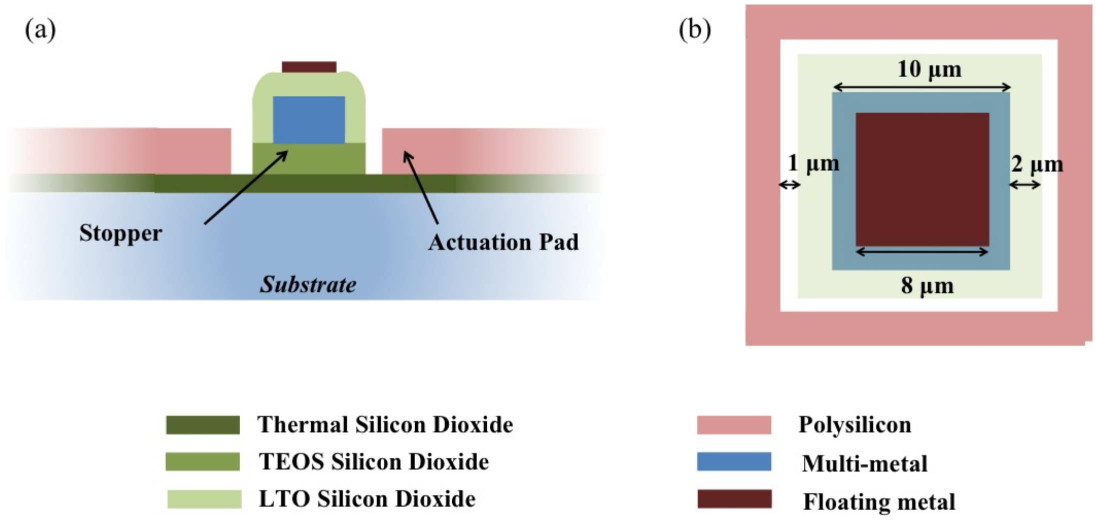

Figure 4.7: Cross section (a) and top view (b) geometry of the stopping pillars used for FBK dielectric-less switches.

tributed over the actuation pad, exploiting the metal and insulating layers available from technology, such as polysilicon (POLY), tetraethylorthosilane oxide (TEOS), TiN/Ti/Al/Ti/TiN multi-metal (METAL), low temperature oxide (LTO), and floating gold metal (FLOMET) (see Section 2.6). The introduction of stoppers may drastically change the ratio between pull-out and pull-in according to:

$$\frac{V_{PO}}{V_{PI}} = \sqrt{\frac{27}{4} K_s \frac{(g_0 - d_p)\left(d_p + d_\varepsilon/\varepsilon_r\right)^2}{\left(g_0 + d_\varepsilon/\varepsilon_r\right)^3}}, \tag{4.8}$$

where $g_0$ is the gap between membrane and actuation pad in up-state, and $d_p$ is the pillar height with respect to the pad, which corresponds also to the residual air-gap. The term $K_s$ accounts for the ratio between the pull-out and pull-in stiffnesses, which may be different according to what explained in Section 3.2.3.

The preferable choice is to design a stopping pillar by using TEOS (300 nm), METAL (630 nm), LTO (100 nm), and FLOMET (150 nm), providing a pillar height equal to 1180 nm. Considering the thickness of

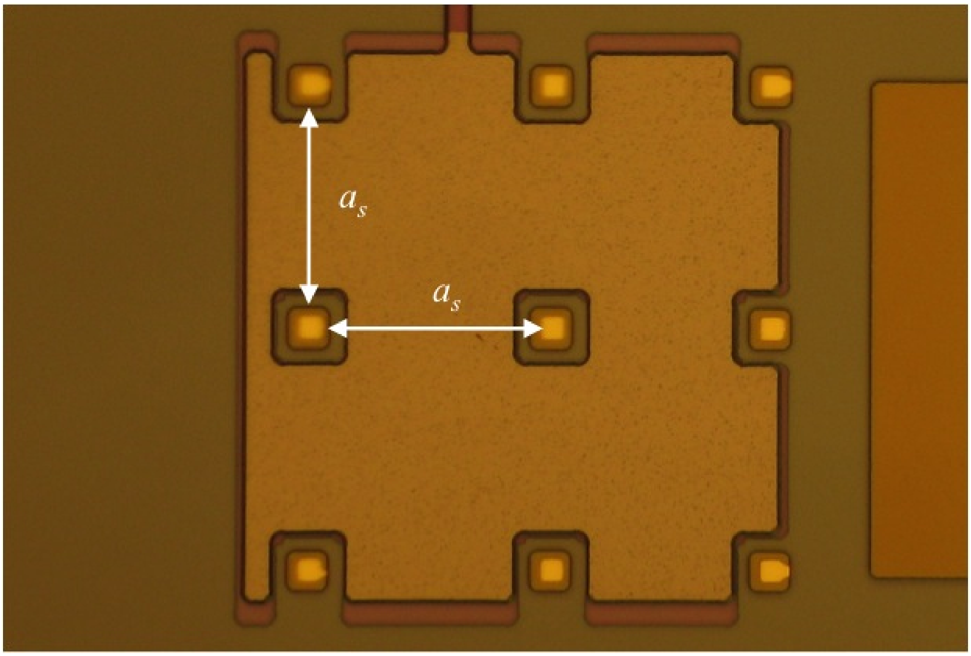

Figure 4.8: Microphotograph of the pillars matrix over the actuation electrode of a cantilever MEMS switch.

the actuation pad (made of polysilicon, 630 nm), the effective residual gap is ideally 550 nm. This solution is supposed to keep enough air-gap after the membrane snap-down, intending to avoid possible air breakdown [98], which can occur in microsystems for very small distances, according to the modified Paschen curve (Fig. 4.6). In addition, it allows for an increasing of pull-out/pull-in voltage ratio, which implies a higher restoring force available in case of stiction. Fig. 4.7 shows the cross-sections of a stopping pillar, whereas Fig. 4.8 illustrates how the pillars should appear from the top after the manufacturing process.

When the membrane snaps down, force distribution and stress change with respect to the up-state situation. The membrane cannot be longer modeled as a clamped-clamped or clamped-free bridge, but it is much more similar to an infinite flat plate resting on a set of dot-like pillars. Such a plate is subject to a very high electrostatic force $F_e$ due to the low residual gap $d_p$ between the polysilicon electrode and the gold membrane. If the pillars are patterned like a *square* with a side length $a_s$, the maximum displacement of the plate towards the electrode is equal to:

$$\Delta_{dp} = 0.063\frac{P_e}{E}\left(\frac{a_s^4}{t_b^3}\right), \tag{4.9}$$

where $E$ is the Young's modulus, $t_b$ is the plate thickness, and $P_e$ is the electrostatic pressure given by:

$$P_e = \frac{F_e}{a_s^2} = \frac{1}{2}\frac{\varepsilon_0 w_e l_e}{d_p^2}\frac{V_{bias}^2}{a_s^2}, \tag{4.10}$$

where $l_e$ and $w_e$ are the length and the width of the electrode, respectively, and $V_{bias}$ is the bias voltage provided to the suspended bridge. Note that Eq. 4.9 does not account for the real stiffness of the membrane, which is mostly affected by the residual stress, so it provides an overestimation of the displacement. For a residual gap of 550 nm and a bias voltage of 50 V, $a_s$ should be chosen lower than 50 $\mu$m in order for the pillars matrix to be effective.

Table 4.2: Finite elements properties used in the FEM simulation of the stoppers effect

| **Parameter** | **Value** |
|---|---|
| Structural element | SOLID186 |
| Contact-pairs element | CONTA174-TARGE170 |
| EM coupled element | TRANS126 |
| Layered option | OFF |
| Mesh type | brick/prism mapped mesh |
| Mesh size | 2-5 $\mu$m |
| Residual stress | 50 MPa |
| Gold Young modulus | 75 GPa |
| Gold Poisson's ratio | 0.42 |
| Act. pads gap | 2.7 $\mu$m |
| Contact stiffness factor | 0.1 |

As a further validation of the concept, FEM simulations were performed involving the snap-down of the capacitive switch of Fig. 3.14-a towards the mechanical stoppers. Half of the membrane was considered by exploiting the geometric symmetry with respect to the RF line. The stoppers were placed over the actuation electrode following either a square-shaped and or a "X"-shaped pattern, in order to evaluate how such a distribution can affect the switch performances. The parameters used for such a simulation are listed in Table 4.2.

As a result of the coupled-field simulation involving electro-mechanical and contact elements, information about the contact gap can be provided. For square-patterned pillars, Fig. 4.9-a shows the resulting residual gap between the snapped-down membrane and the electrode at 100 V. The minimum distance is around 0.32 $\mu$m at 100 V, which is less than the expected 0.55 $\mu$ given by the pillar height. The gray areas are out-of-scale, which means that the gap distance is lower than 0.32 $\mu$m, which happens over the pillars where the contact is established. Conversely, Fig. 4.9-b reports the $z$-axis displacement of the membrane from the initial position when bias voltages of 50 V and 100 V are applied. It is clear that for the highest voltage value the membrane tends to be pulled-down towards the electrode where the pillars are not present.

On the other hand, Fig. 4.10-a shows the membrane-electrode distance at 100 V when the pillars are X-patterned, and the corresponding $z$ axis displacement at 50 V and 100 V is reported in Fig. 4.10-b. The comparison between Fig. 4.9 and Fig. 4.10 shows that in the former a couple of grey spots are present over the electrode, corresponding to the largest distance points among the pillars.

The X-pattern seems to provide a slightly higher residual gap with respect to the square pattern at the same bias voltage conditions. However, this may not guarantee the functionality of the switch at such a high bias voltage. In fact, in the real case the nominal residual gap provided by the

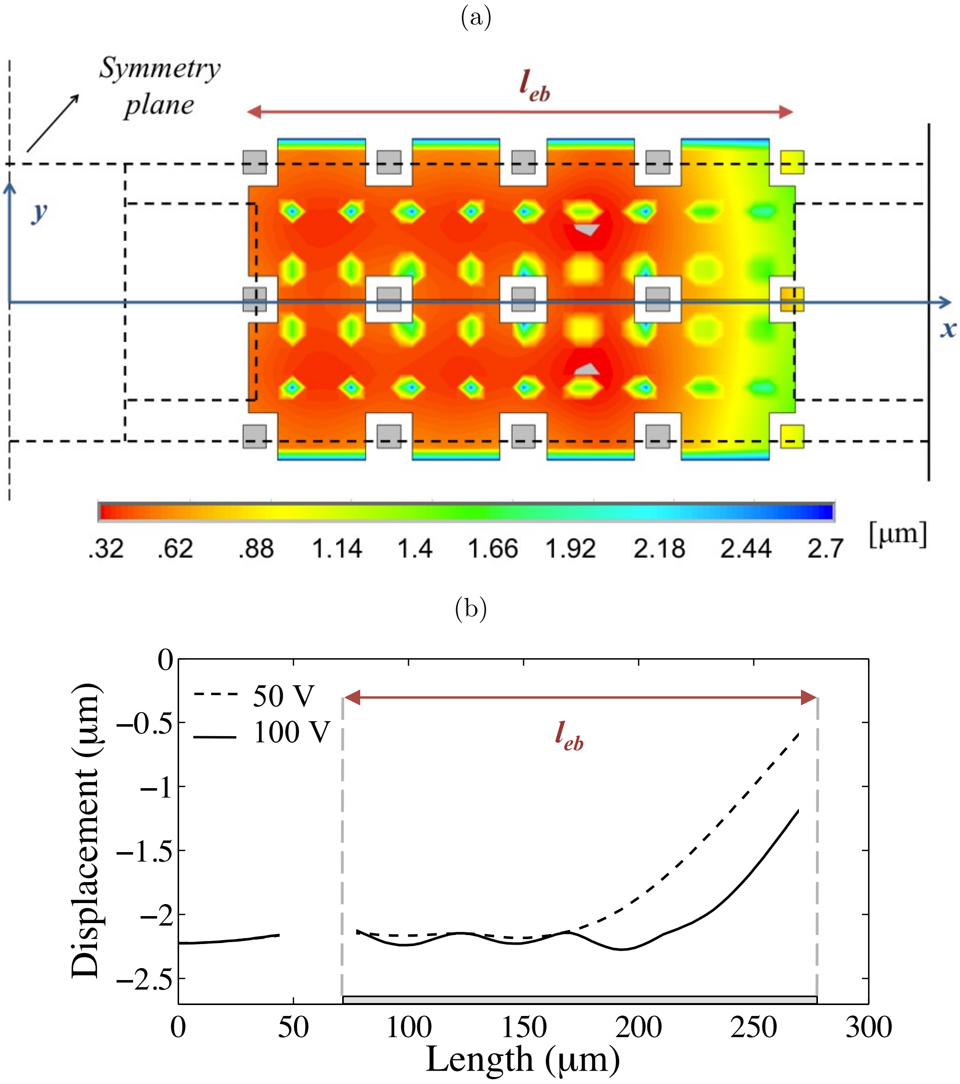

Figure 4.9: FEM simulation of the FBK capacitive switch with square-patterned pillars: (a) contact gap distance plot over the actuation electrode, and (b) membrane displacement at 50 V (dashed line) and 100 V (continuous line). The areas in gray are out-of-scale, meaning that the minimum distance is less than 0.32 $\mu$m.

pillars height (550 nm) can be smaller. Even if the simulation confirms the presence of a 300-nm large residual gap even at 100 V, the process uncertainties related to the thickness of the metal layers and the planarity property of the sacrificial layer need to be considered. Moreover, electrostatic discharge may occur for very small gaps, as stated before.

As a result the welding between membrane and electrodes on dielectric-

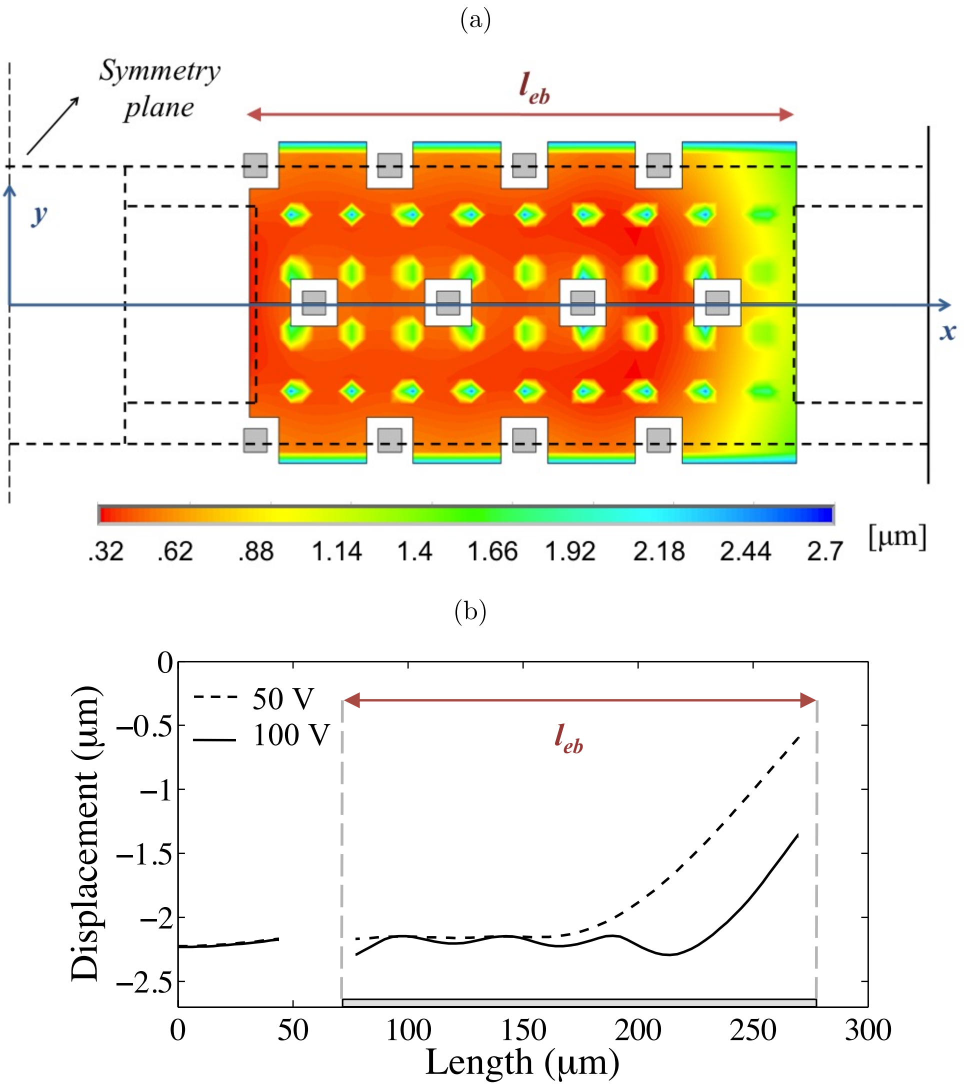

Figure 4.10: FEM simulation of the FBK capacitive switch with X-patterned pillars: (a) contact gap distance plot over the actuation electrode, and (b) membrane displacement at 50 V (dashed line) and 100 V (continuous line). The areas in gray are out-of-scale, meaning that the minimum distance is less than 0.32 $\mu$m.

less switch can happen even for values of bias voltages lower than 100 V if not only the pillars distance but also the pillar distribution is not designed properly. In addition, a stiffer membrane (for example, 5-$\mu$m thick instead of 2-$\mu$m thick) can be less subject to the bending due to high electrostatic force after the snap-down. Nevertheless, this could not be enough because the air breakdown may happen in any case. For this reason, a design providing a pull-in voltage lower than 60 V is preferable in order to avoid high localized electrostatic forces and air breakdown.

### 4.4.2 Experimental

The measurement setup utilized for long-term stress characterization is illustrated in Fig. 4.11. A constant bias voltage $V_{bias}$ (higher than actuation voltages) is continuously applied to the devices under test for increasing time intervals (from a minimum of 5 minutes to a maximum of 2 hours) by means of a source monitor unit. At the end of each interval, the instrument provides a positive and negative triangular voltage sweep up to 50 V and −50 V, and the capacitance (for air-bridge switches) or the resistance (for cantilever switches) variations are measured by a LCR meter. Sweep data are then recorded and processed to monitor the evolution of pull-in ($V_{PI}$) and pull-out ($V_{PO}$) voltages. The chosen voltage step was 0.25 V and the sweep totally lasts 50 s. Such a long sweep time affected the accuracy of the points taken for the first minutes of the stress, but it was observed to be not influent for more than 1-hour-long measurements.

Fig. 4.12 reports the air-bridge capacitance-voltage (CV) characteristic

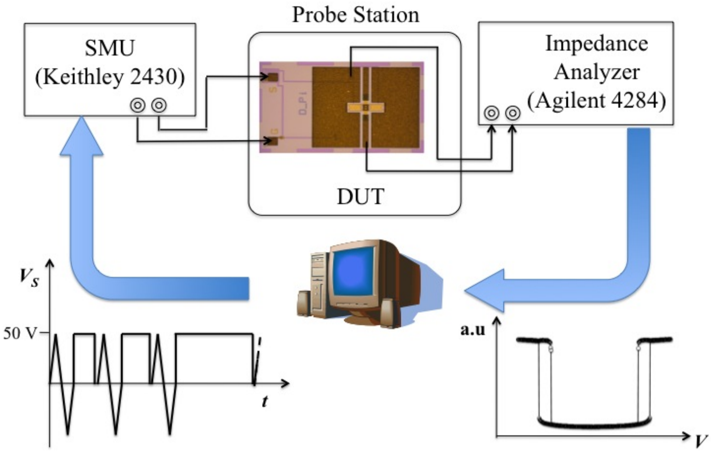

Figure 4.11: Measurement setup used for the long-term stress characterization.

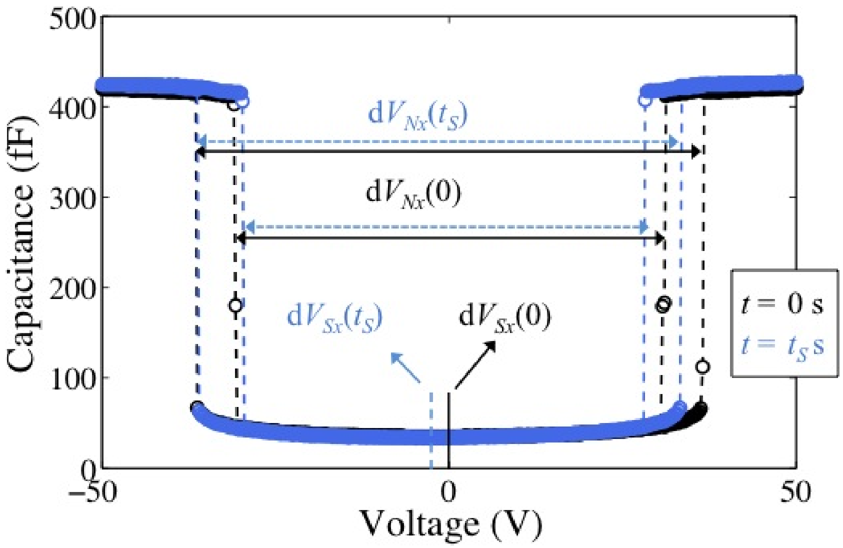

Figure 4.12: Capacitance-voltage characteristic of an air-bridge switch at a stress time of $t = 0$ s (black curve) and $t = t_s = 8$ hours (blue curve).

at $t = 0$ s and after $t = 8$ hrs. Although the dielectric has been removed from the top of the bias electrode, measurements clearly show that charging still occurs probably in the silicon oxide around and underneath the pad [99]. Two different CV characteristic variations may be identified: a *shift* of the minimum capacitance value and the *narrowing* of the CV window. The former is commonly considered due to charge injection [94], the latter is probably a symptom of not-uniform charge distribution [95]. Dual considerations can be made for resistance-voltage (RV) measurements in case of cantilever switches.

For a better understanding of the charging mechanisms, the phenomena of the C-V *shift* and C-V *narrowing* were processed separately. The positive and negative pull-in voltages are referred as $V_{PI}^{+}$ and $V_{PI}^{-}$, while $V_{PO}^{+}$ and $V_{PO}^{-}$ are the positive and negative pull-out voltages, respectively. According to Fig 4.12 one has:

$$dV_{Sx}(t) = \frac{V_x^+(t) + V_x^-(t)}{2}, \tag{4.11}$$

and

$$dV_{Nx}(t) = V_x^+(t) - V_x^-(t). \tag{4.12}$$

where the subscript $x$ stands alternatively for PI or PO. Eq. (4.11) provides information about the *asymmetry* of the CV characteristic, whereas Eq. (4.12) determines the *width* of the CV window at a time $t$. The values resulting at $t = 0$ s are extracted and adopted as reference values. Ideally, $dV_{Sx}(0) = 0$ V. However, a residual charge could exist. After a time $t$ of continuous stress, the variations with respect to the reference values are:

$$\Delta V_{Sx}(t) = dV_{Sx}(t) - dV_{Sx}(0), \tag{4.13}$$

and

$$\Delta V_{Nx}(t) = \frac{dV_{Nx}(0) - dV_{Nx}(t)}{2}. \tag{4.14}$$

Eq. (4.13) provides the voltage *shift*, while Eq. (4.14) is the voltage *narrowing*. Then the total voltage variation along time is:

$$\Delta V_x(t) = |\Delta V_{Sx}(t)| + \Delta V_{Nx}(t). \tag{4.15}$$

Note that the narrowing value is always positive according to Eq. (4.14). Instead the voltage shift can be negative or positive according to the sign of the charge injected in to the dielectric [44]. Thus the described data processing, already utilized in [99], is a generalization of other analysis techniques employing only positive or negative sweeps.

Fig. 4.13-a and Fig. 4.13-b report the measured parameters $\Delta V_{Sx}(t)$ and $\Delta V_{Nx}(t)$ for both the switch typologies under about totally 8 hours of 50 V stress. The voltage shift is clearly lower than the narrowing, which results to be the dominant effect of voltage variation, as expected for dielectric-less switches. Moreover one may observe that the voltage shift and narrowing are higher for cantilever switches.

Further measurements were performed with a voltage stress equal to

(a)

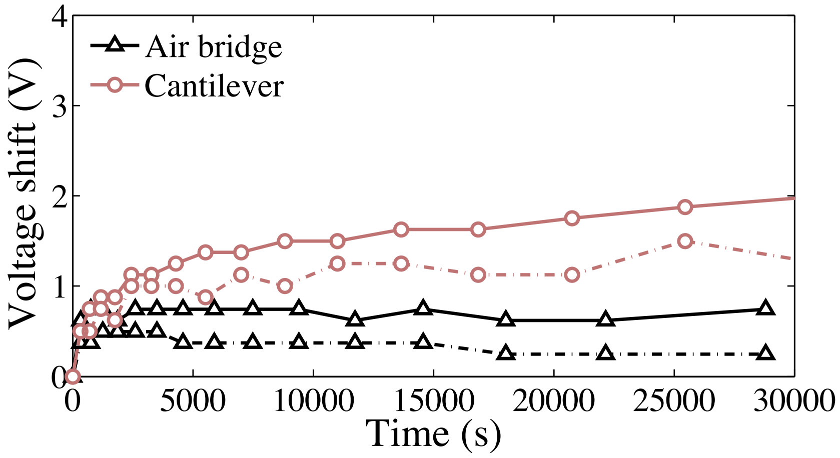

(b)

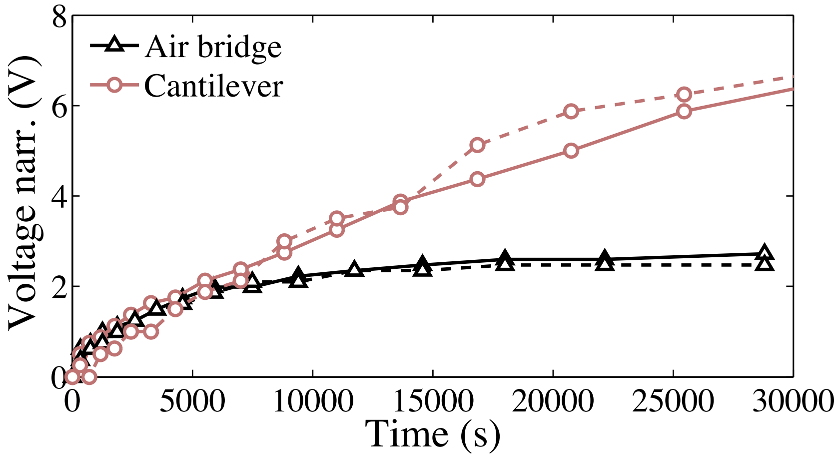

Figure 4.13: Measured evolution of voltage shift (a) and narrowing (b) for air bridge switch (in black) and cantilever switch (in red) for pull in (continuous line) and pull-out (dashed line). Applied voltage stress: 50 V.

$V_{bias} = 40, 50, 60$ V for air bridge and $V_{bias} = 50, 60, 70$ V stress for cantilever switches. Data can be fitted with a power law, such as $\Delta V = At^n$ [19]. According to [94] and [100], $A$ can be also written as $kV_0$, where $V_0 = V_{bias}\exp(V_{bias}/V_A)$. The total variation $\Delta V_x(t)$ can be then normalized to achieve overlapping curves for each value of voltage stress $V_{bias}$:

$$\frac{\Delta V_x(t)}{V_0} = kt^n \tag{4.16}$$

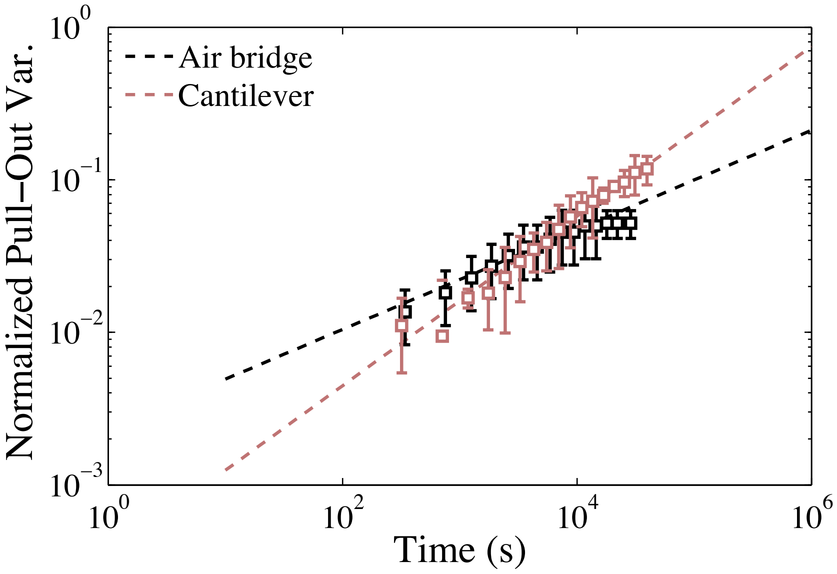

Figure 4.14: Average of the pull-out voltage variation data normalized to the corresponding stress voltages plotted versus the stress time.

In case of air bridge, $V_A = 1000$ V, which implies $V_0 \approx V_{bias}$. For cantilever, $V_A$ is found to be around 85 V. The average normalized pull-out variation and the corresponding $3\sigma$-deviations are plotted in Fig. 4.14 for both the devices. The log-log scale clearly highlights the power trend of the data with time. It also allows for a successful fitting of the measured data with Eq. (4.16), and the consequent extraction of the parameter $n$ and $k$. By inverting Eq. (4.16), and putting $\Delta V_{PO}(t_F) = V_{PO} = \min(V_{PO}^{+}(0), |V_{PO}^{-}(0)|)$, it results:

$$t_F \approx \left(\frac{V_{PO}}{kV_0}\right)^{\frac{1}{n}}, \tag{4.17}$$

which may be used for a rough prediction of the time $t_F$ at which stiction can occur.

### 4.4.3 Discussion

Table 4.3 reports the value of $n$, and $k$ extracted for the measured pull-out variation of both the switch typologies, and the corresponding time-to-stiction prediction $t_F$, computed for $V_{bias} = 50$ V. Three samples per typologies were characterized in order to have a better assessment of the results. Despite a wide dispersion of the pull-in/pull-out voltages of the devices under test due to thickness and residual stress process uncertainties, there is only a minor difference among the fitting parameters for the same typology.

Table 4.3: List of parameters extracted from the Eq. (4.16) fitting with average measured pull-out variations.

| | | $V_{PI}$ (V) | $V_{PO}$ (V) | $k$ | $n$ | $t_F$(days) |
|---|---|---|---|---|---|---|
| Air bridge | S1 | 32.75 | 27.5 | $2.3 \times 10^{-3}$ | 0.32 | 209 |
| | S2 | 36.5 | 29.5 | $3.6 \times 10^{-3}$ | 0.27 | 1900 |
| | S3 | 40.25 | 33 | $2 \times 10^{-3}$ | 0.34 | 240 |
| Cantilever | S1 | 44.25 | 35.5 | $0.6 \times 10^{-3}$ | 0.53 | 4 |
| | S2 | 49.25 | 45.25 | $0.3 \times 10^{-3}$ | 0.55 | 5 |
| | S3 | 43 | 40.5 | $0.7 \times 10^{-3}$ | 0.48 | 11 |

On the other hand, the values differ significantly between the two typologies. Especially the parameter $n$, most sensitive to the voltage variation rate, is found to be around 0.3 for air bridge devices and around 0.5 for cantilever devices. Similar values are achieved if the fitting is performed on pull-in variation. As a result air bridge switches are expected to survive up to 200 days in the worst case, whereas in cantilever switches stiction can occur after only 4 days. One possible explanation is that such a difference is mostly, but not only, related to the geometry of the specific design, in particular to the shape assumed by the membrane after the snap-down.

To better understand this aspect, finite element simulations were performed with ANSYS$^{\text{TM}}$Multiphysics. First, preliminary electrostatic simulations were used to confirm the location of the not-uniform charge. A cross-section of the cantilever switch was considered as a proof of the con-

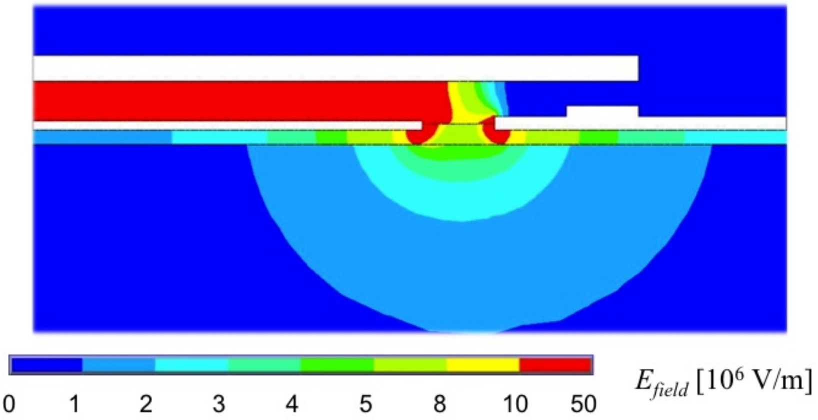

Figure 4.15: Cross-sectional view of the simulated electrostatic field distribution around the electrode of the cantilever switch when a voltage of 50 V is applied.

cept, but the results can be generalized to any kind of electrostatic MEMS switch. The results reported in Fig. 4.15 clearly show how the electric field is concentrated all along the edges of the polysilicon electrodes. Thus, if the dielectric is removed from the top of the electrode, it is likely that charges are injected into the dielectric layer surrounding the electrode borders, because of the high-intensity electric field localized at the electrode edges and corners. The possible cloud of charges may in turn contribute to the fringing electrostatic force acting on the suspended membrane, and this could also affect the potential at the electrode when $V_{bias}$ is applied. Moreover, their distribution is intrinsically not uniform along the plane parallel to the electrode.

In addition, electro-mechanical simulations were performed by following the procedures reported in Section 3.5. A residual stress of 50 MPa for air bridge and a stress gradient of 12 MPa/$\mu$m for the cantilever were considered to reproduce the initial conditions at $V_{bias} = 0$ V. The shape profile along the membrane length at 0 and 50 V were extracted and reported in Fig. 4.16-a (cantilever) and Fig. 4.16-b (air-bridge). Air bridge profile results quite flat over most of the electrode length, whereas the cantilever profile varies with a linear slope along the electrode length (around

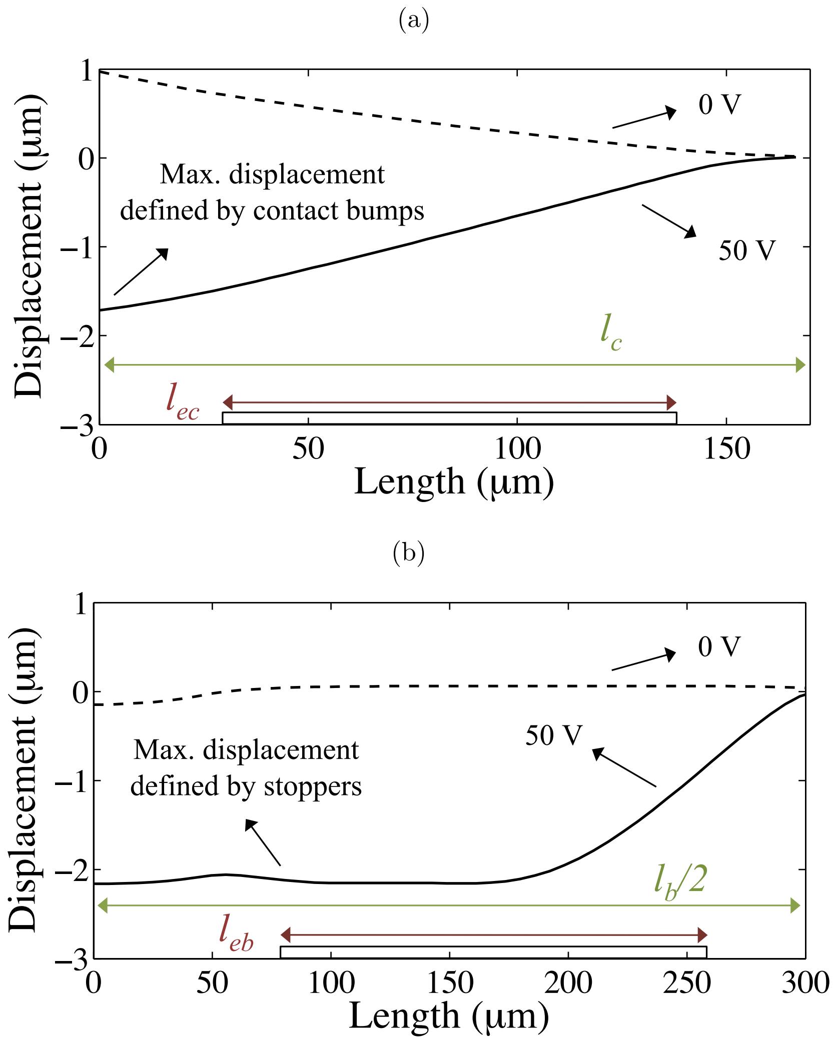

Figure 4.16: Displacement profile of cantilever switch (a) and air-bridge switch (b) at $V_{bias} = 0$V (dashed curve) and $V_{bias} = 50$ V (continuous curve).

0.0125 $\mu$m/$\mu$m from contact bumps to anchors). The not-uniform displacement causes a not-uniform intensity of the electric field, and this affects in turn the amount of injected charges. The difference in the deformed profile may be a possible and reasonable explanation for the voltage narrowing, which is mainly caused by a combination of non-uniform gap and charge distribution, as also stated in [95]

## 4.5 Conclusions

The influence of two different geometry configurations (air bridge and cantiliver) on the dielectric charging rate was analyzed in detail in this Chapter. Long-term characterization was performed on dielectric-less air-bridge capacitive and cantilever ohmic switches. Measured data were analyzed by evaluating the *narrowing* and the *shift* of the CV/RV characteristics. This approach was very helpful in order to separate the effects of the different charging contributions, offering a great insight of the dominant charging mechanism. Among the charging models available in literature, the power law of time was able to fit very well the measured data, providing a reliable prediction of the switch failure due to stiction. As a result of such analysis, the air bridge switch showed a predicted time to failure of about 200 days, whereas the cantilever was supposed to fail after 5 days. Finite element simulations showed that the different deformed profile of the two configurations may be a possible and reasonable explanation for the different charging rate.

# Chapter 5

# Power Handling

## 5.1 Introduction

As mentioned in Chapter 2, RF MEMS capacitive switches show extraordinary performances in terms of loss, power consumption and linearity. All these advantages make RF MEMS technology attractive also for applications in phased-array radar and communication systems [36]. However, before the switches can be deployed in these systems, robustness issues such as power-handling capacity must be addressed [101]. Presently, RF MEMS capacitive switches can typically handle RF power on the order of 1 W, but certain phased-array systems involve RF powers on the order of 10-100 W. Such high powers can significantly affect the electrical, mechanical and thermal properties of the switches and even cause temporary or permanent failures.

The following chapter reports measurements and characterization of the power handling capacity of RF MEMS capacitive switches manufactured at FBK. A compact model for power handling prediction is also proposed for the first time based on an advanced finite elements multi-physics analysis. Results show that FBK switch provides a power capacity comparable or even better than the best-in-practice air bridge switches, even without a geometry optimization.

## 5.2 Basic Theory

The main task of a RF MEMS switch is to permit or interdict the propagation of a microwave signal along a transmission line. A microwave signal is characterized by a given *power level* depending on the application. A MEMS switch may work in two operating modes related to the RF power traveling through it:

- *Cold switching*: the RF signal is turned off during the switching operation. This means that when the capacitive or ohmic contact is established at the actuation, no signal is going through the contact and the dynamics of the structure is not affected by the RF power.
- *Hot switching*: the RF signal is continuously propagating through the switch, even during the switching operation.

As a consequence of the RF signal propagation, the following phenomena can be observed:

- *DC contact degradation*

  As discussed in Chapter 4, several thermally-related issues affecting the quality of a DC contact may arise because of the RF power propagation. As a consequence of the Joule effect, the RF current flowing through an ohmic contact may lead to localized high temperature spots. The contact degradation involves a set of complex physical phenomena concerning the contact surface, such as softening, pitting, material transfer, and in some cases material melting. Most of them can be observed also at low and medium signal power, leading mainly to a drastic degradation of insertion loss and isolation properties of the MEMS switch. The use of particular metal alloys [55], and switch geometries providing high contact force [92] can reduce but not completely avoid these problems.

- *Self-biasing*:

  Self-biasing effect is related to the equivalent voltage, usually referred to as *root mean square* (RMS) voltage, provided by the power $P_{RF}$ of the propagating signal. For a RF MEMS *shunt* capacitive switch that is matched to a transmission line with $Z_0$ characteristic impedance ($|S_{11}| \approx 0$), the amplitude of the propagating wave is [54]:

  $$|V_0^+| = \sqrt{2P_{RF}Z_0}. \tag{5.1}$$

  Therefore the corresponding RMS voltage is:

  $$V_{RMS} = \frac{|V_0^+|}{\sqrt{2}} = \sqrt{P_{RF}Z_0}. \tag{5.2}$$

  The voltage expressed by Eq. 5.2 acts as a *bias voltage* for the suspended membrane, especially on capacitive switch where the OFF-state capacitance is usually large ($\approx 50-100$ fF). For $P_{RF} = 1$ W and $Z_0 = 50\ \Omega$, $V_{RMS} = 7.07$ V. This contribution is already significant for a centrally-actuated membrane with nominal pull-in voltage around 15-20 V. For higher values of power, the electrostatic force provided by $V_{RMS}$ may exceed the reacting force of the anchor springs, causing eventually the snap-down of the membrane even if $V_{bias} = 0$ V.

- *Latching*:

  This phenomenon happens when the RMS voltage related to the input power is equal or higher than the hold-down voltage $V_{PO}$ of the switch. This means that the membrane is no longer able to assume its up-position even if the bias voltage is removed. When a shunt capacitive switch is in down-position, the switch characteristic impedance is no longer matched with the port impedance $Z_0$, and, according to t-line theory, the RMS voltage is:

$$V_{RMS} = \frac{1}{\sqrt{2}} \frac{|V_0^+|}{\sqrt{1 + \left(\frac{\omega C_{down} Z_0}{2}\right)^2}} \simeq \frac{2\sqrt{P_{RF} Z_0}}{\omega C_{down} Z_0}, \tag{5.3}$$

for $\omega C_{down} Z_0 \gg 1$, where $C_{down}$ is the down-state capacitance and $\omega$ is the working angular frequency.

- *Self-heating*:

  Self-heating is the not-uniform temperature rise of the switch due to RF power dissipation. Firstly the not-uniform distribution of RF currents may lead to high current density concentrations at the edges of the conductors and of the suspended membrane. For critical values of current density (above 1 MA/cm$^2$ for gold) electro-migration and material thermal failure can occur, and this provides a sort of upper limitation for the switch power handling. However, a preliminary degradation mechanism is revealed by the temperature rise due to the power dissipated on the membrane. For a given material of thermal conductivity $k_b$, the temperature distribution due to a dissipated power $p_m$ per unit volume [W/m$^3$] is derived by the generalized steady-state conduction equation:

$$\nabla^2 T + \frac{\nabla p_m}{k_b} = 0. \tag{5.4}$$

  The bridge is usually modeled with a *thermal resistance* $R_{MEM}^{TH}$ defined as:

$$R_{MEM}^{TH} = \frac{1}{2} \frac{l_b/2}{w_b t_b k_b} \tag{5.5}$$

  where $l_b$, $w_b$ and $t_b$ are respectively the length, width and thickness of the membrane. From literature, this value is on the order of 1000

K/W, and it has been demonstrated that this is much smaller than the radiation and convention thermal resistances, making the conduction the main mode of heat transfer in MEMS switches [102]. The temperature rise acts on the thermal residual stress, which in turn reflects to the electro-mechanical properties of the membrane. This implies a reduction of the actuation and release voltages of a clamped-clamped membrane with initial tensile stress. Such an effect obviously amplifies the action of the RMS voltage on the membrane itself. The temperature rise is instead less effective in case of cantilever beam, although the limitations due to high current densities and self-biasing still remain.

The power handling of a capacitive switch can be evaluated in different ways. In ohmic switches, *lifetime-cycling* test are a good indicator of the contact degradation, which in turn reflects on the insertion loss or isolation electromagnetic parameters. In capacitive switches, electromagnetic parameters degradation still occurs if the membrane material is permanently damaged by critical values of high current densities spots [4]. However, the main failure indicator is the *pull-in/pull-out voltage shift* versus input power. As a general agreement, a capacitive switch is considered no longer functionally compliant for a 10 % of variation of pull-in voltage.

## 5.3 State-of-the-art for high power switches

Nowadays the design and reliability of RF MEMS switches for high power applications is one of the hottest topic in the RF MEMS field, along with the MEMS sensitivity to temperature variations. The approach reported in [62] is to optimize the anchor springs in order to reduce the temperature and residual stress variation sensitivity. As a result a MEMS switch capacitor characterized by a circular shape, and four anchor springs

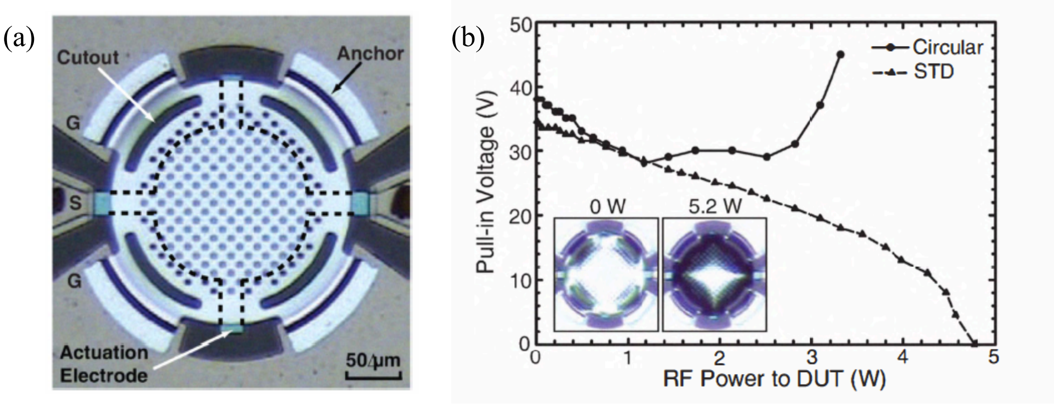

Figure 5.1: Circular-shape RF MEMS switched capacitor: (a) micrograph and (b) evolution of pull-in and pull-out voltages versus input RF power [62].

with central cutouts (Fig. 5.1), was manufactured and tested. The device showed a temperature sensitivity of -55mV/°C, which is one of the best result available in literature. Moreover, power handling tests was performed in hot-switching operations by monitoring the pull-in/pull-out voltages evolution. As a result, authors observed improved performances up to 5 W with respect to the rectangular-shaped clamped-clamped switches manufactured with the same technology.

A different approach was adopted in [61], where the low temperature sensitivity is achieved by using *molybdenum* (Mo) as *membrane* material. The use of a membrane material with a thermal expansion coefficient (4.8 ppm/°C) similar to the one of the substrate material (pyrex glass, 3.25 ppm/°C) results in a temperature sensitivity of 35 mV/°C. However, power handling is still below 1 W, despite the similar thermal properties of membrane and substrate. This is a further symptom of the not-uniform temperature load produced by the self-heating effect.

A different membrane material was also tested in [103]. A thick silicon membrane was employed as movable electrode, so that the metal loss is given only by the coplanar transmission line conductors. The semiconductor material guarantees the correct ground polarization to the DC bias

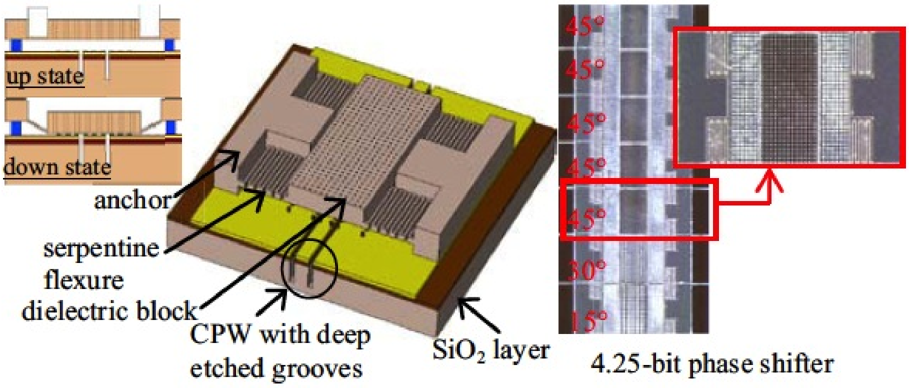

Figure 5.2: Sketch and pictures of the dielectric-block MEMS switch reported in [103].

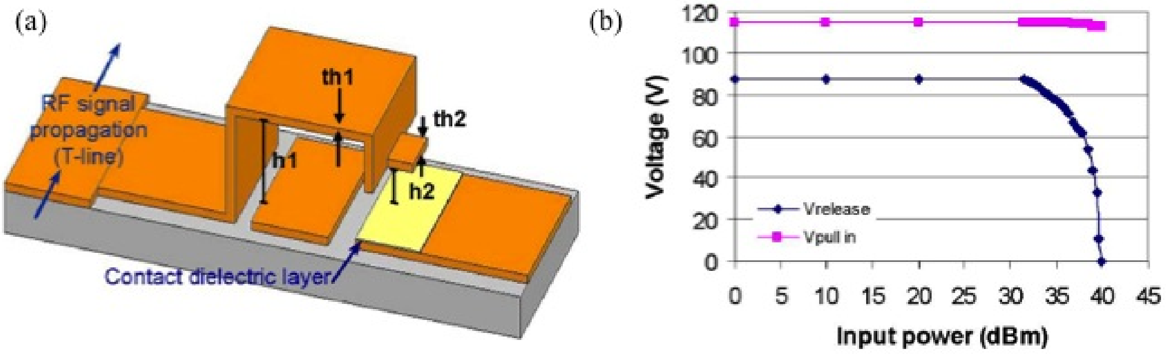

Figure 5.3: MEMS varactor from [104]: (a) device sketch, and (b) $V_{PI}/V_{PO}$ evolution under high power conditions.

network. Although a drastic reduction of the temperature rise over the membrane is demonstrated, no further reliability tests about cycling or pull-in voltage evolution have been reported so far for such a switch.

In [104] a MEMS varactor composed by a cantilever beam was presented. The cantilever configuration allows the device to be less sensitive to self-heating effect, showing a power handling capability up to 30 W.

Radant DC-contact switches [11] were demonstrated to handle at least 1000 cycles under 10 W RF power in hot-switching mode, up to 1-million cycles under 1 W power in cold-switching mode, and up to 1-trillion cycles under low-power signals. A picture of the device and related cycling characterization are shown in Fig. 5.4. Recent developments [55] demonstrated the employment of these devices for a 5-W phase shifter able to handle

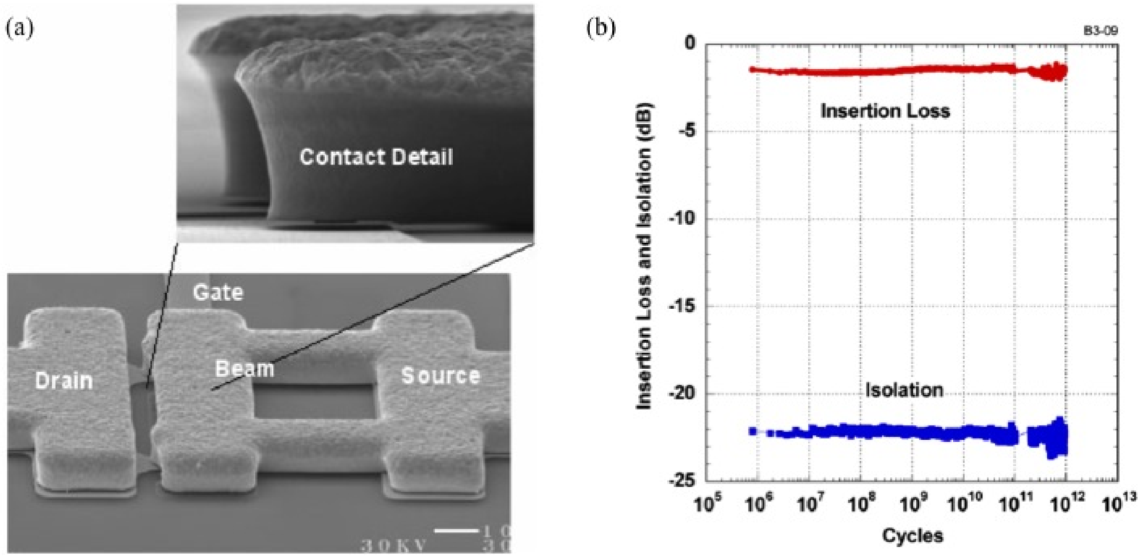

Figure 5.4: High power Radant switch [11]: (a) Micrograph and (b) RF parameters evolution under cycling actuations.

up to 1-billion cycles. These outstanding performances have been achieved by means of a careful choice, and manufacturing process of the contact materials. Similar high power performances still need to be demonstrated for MEMS switches based on clamped-clamped beams.

## 5.4 Multiphysics Analysis of a FBK capacitive switch

### 5.4.1 The Multiphysics approach

As mentioned so far, the power handling problem of RF MEMS switches involves complex electric and thermal phenomena which are strictly related between each other. Analytical closed-formulas often are not enough to understand or predict the shift in the pull-in voltage or the complete failure of RF switches under high power conditions. This is especially true when RF switches are adopted in complex high-power impedance matching networks or phase shifters, where the characteristic impedance of the network usually changes during the circuit operations.

A *multi-physics* numerical analysis is then required to accurately evaluate both the *self-biasing* and the *self-heating* effects, and see how different materials and different geometries may affect the power handling of the MEMS switch. Although such an analysis is usually computationally demanding, it offers a great insight in the identification of the significant parameters to be optimized for the improvement of the switch power handling capacity.

Such a multi-physics approach was applied to a MEMS capacitive switch manufactured at FBK and characterized at high powers in collaboration with Lehigh University. It involves the coupled-utilization of an electromagnetic numerical software (HFSS$^{TM}$[83], see Section 3.5.6) and a multi-physics numerical software for the thermal and electro-mechanical numerical models (ANSYS$^{TM}$[83], see Section 3.5.2). The switch was fabricated on high-resistivity silicon, and quartz substrates for a better understanding of the electro-magnetic and thermal aspects of the problem.

The following analysis was performed considering hot-switching conditions, and it is limited to the up-state position of the membrane.

### 5.4.2 Device under test

Fig. 5.5-a illustrates a photograph of the electrostatically actuated RF MEMS capacitive shunt switch used for the following analysis and already described in Section 3.5.2. The cross section view of the switch is also reported again for clarity in Fig. 5.5-b. To evaluate the substrate effect on switch power handling, the same device was fabricated on high-resistivity silicon, and quartz. Table 5.1 compares the thermal and electromagnetic properties of the silicon and quartz substrates. Table 5.2 shows that the switches on silicon and quartz have slightly different residual stresses and pull-in voltages due to some parameters uncertainties in fabrication. The switches typically have a pull-in voltage of 39 V on silicon and 43 V on

quartz. The difference is mostly related to observed deviations in nominal thickness and residual stress values given by the process flow.

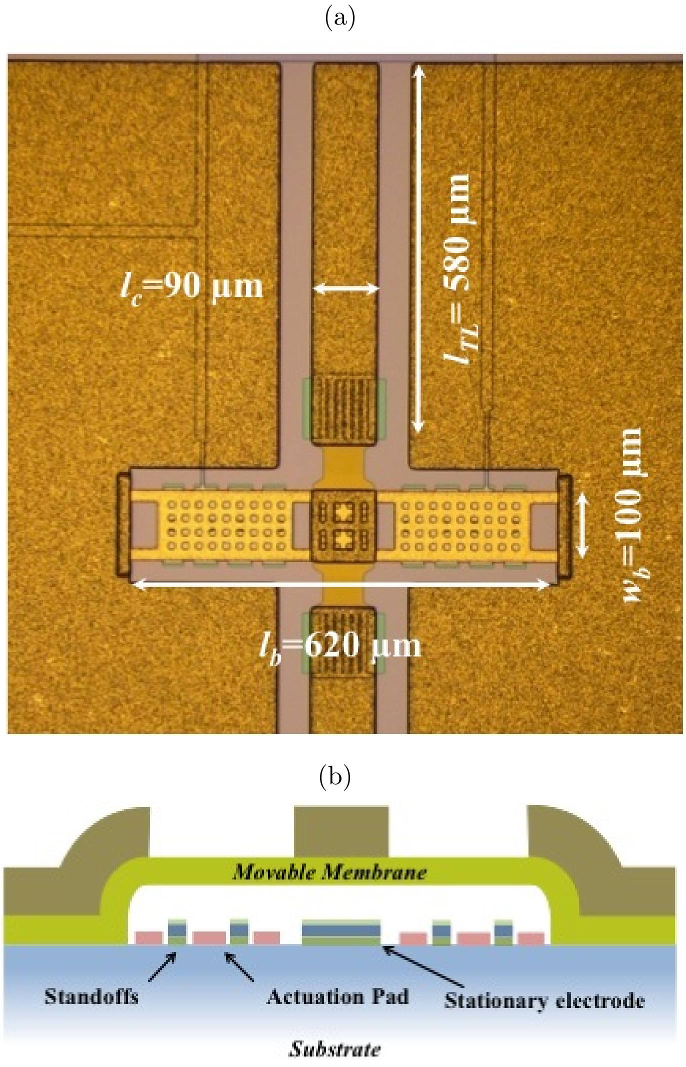

Figure 5.5: (a) Top view, and (b) cross-sectional schematic of an electrostatic RF MEMS capacitive shunt switch under test. See Fig. 2.15 for the meaning of the layer colors

Fig. 5.6 represents the equivalent circuit model of the capacitive switch. At 15 GHz, the insertion losses are 0.3 dB, and 0.2 dB on high-resistivity silicon, and quartz, respectively, which are inversely proportional to the substrate resistivity.

Table 5.1: Substrate properties and equivalent circuit parameters.

| **Parameter** | **Silicon** | **Quartz** |
|---|---|---|
| Substrate dielectric constant ($\varepsilon$) | 11 | 3.8 |
| Substrate resistivity $\rho$ ($\Omega$·cm) | 5000 | $10^{19}$ |
| Substrate loss tangent $\delta$ | 0.006 | 0.0001 |
| Subst. thermal expansion coeff. $\alpha$ (ppm/°C) | 2.6 | 0.4 |
| Subst. shunt resistance $R_{SUB}$ ($\Omega$) | 2000 | 6000 |
| Subst. shunt capacitance $C_{SUB}$ (pF) | 1.89 | 0.0015 |
| Transmission line impedance $Z_{TL}$ ($\Omega$) | 50 | 75 |
| Transmission line length $\theta_{TL}$ (°) | 25 | 16 |
| Transmission line resistance $R_{TL}$ ($\Omega$) | 0.4 | |
| OFF-state membrane capacitance $C_U$ (fF) | 40 | |
| ON-state membrane capacitance $C_D$ (fF) | 300 | |
| Membrane inductance $L_S$ (pH) | 2 | |
| Membrane resistance $R_S$ ($\Omega$) | 0.2 | 0.18 |

### 5.4.3 Simulation Procedure

Fig. 5.7 illustrates the multiphysics simulation procedure for analyzing the power-handling capacity of RF MEMS capacitive switches. First, the finite-element electromagnetic simulator HFSS was used to analyze the entire switch die under both small- and large-signal conditions. Small-signal simulations between 0.5 and 20 GHz of the insertion and return losses were validated through S-parameter measurements (Fig. 5.8). Large-signal sim-

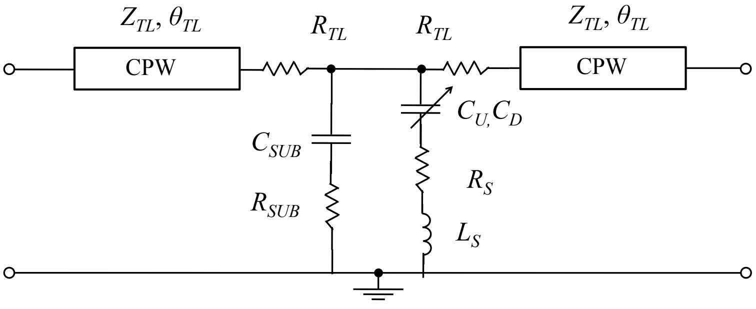

Figure 5.6: Equivalent circuit model of the capacitive RF MEMS switches under test.

Table 5.2: Air bridge dimensions and electromechanical properties.

| **Parameter** | **Silicon** | **Quartz** |
|---|---|---|
| Membrane length $l_b$ ($\mu$m) | 620 | |
| Membrane width $w_b$ ($\mu$m) | 100 | |
| Membrane thickness $t_b$ ($\mu$m) | 1.9 | 2.3 |
| Membrane stress $\sigma_0$ (MPa) | 60 | 45 |
| Membrane pull-in voltage $V_{PI}$ (V) | 39 | 43 |

ulations at different frequencies and input powers were then performed to obtain the field and current distributions across the entire die. Dielectrics and conductors are considered lossy to include all the dissipated power. Further accuracy is provided by the utilization of *mixed-order* elements for the model. From the field distribution, the RMS average voltage $V_{RMS}$ inducing the self-biasing was extracted and validated through the equivalent-circuit model. This value was determined by integrating the simulated electric field $E$ across the 2.7 $\mu$m air gap $g_0$ between the membrane and the stationary electrode:

$$V_{RMS} = \frac{1}{\sqrt{2}} \int_{-g_0}^{0} |E| dz. \tag{5.6}$$

Fig. 5.9 reports that the values of RMS voltages from HFSS agree with those extracted from the equivalent-circuit model under $P_{RF} = 1$ W between 3 GHz and 18 GHz. This confirms that the self-biasing effect can be accurately simulated by using HFSS.

From the HFSS-simulated current distribution, power losses on the surface of conductors and in the bulk of dielectrics were exported to ANSYS to analyze the thermal domain. Using ANSYS, surface losses are mapped into heat flux loads while volume losses are mapped into heat generation loads. A scaling factor is used to account for the different mesh sizes of HFSS and ANSYS. The heat transfer is assumed to be through conduction

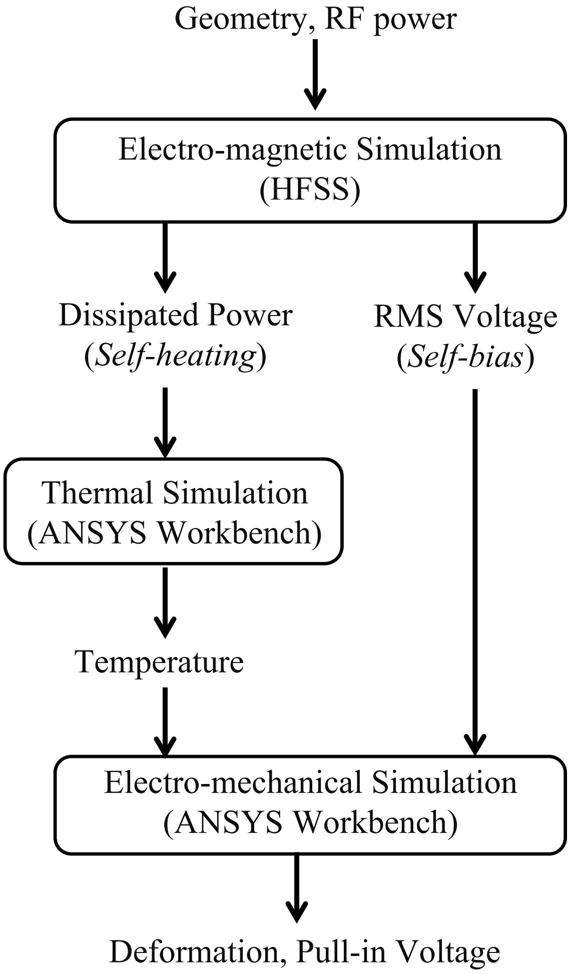

Figure 5.7: Simulation procedure for the evaluation of pull-in voltage RF power dependence.

with negligible convection and radiation [102].

Finally, an electro-mechanical analysis of the same model is performed in order to simulate the pull-in of the membrane. Self-heating is applied as a temperature load (resulting from the previous thermal analysis), whereas self-biasing is modeled by applying a voltage to the central part of the membrane depending on the electric field distribution (which is a result obtained from the previous electromagnetic analysis).

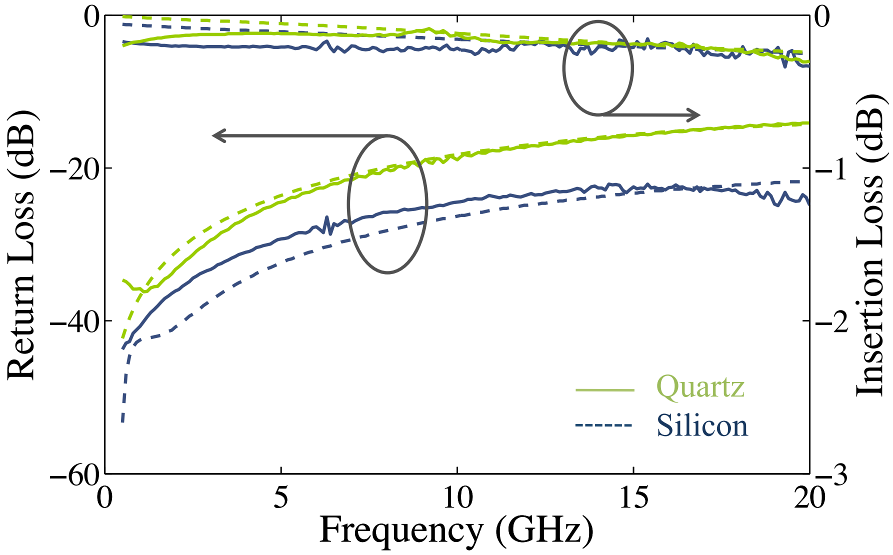

Figure 5.8: HFSS-simulated (dashed) vs. measured (continuous) small-signal insertion and return losses.

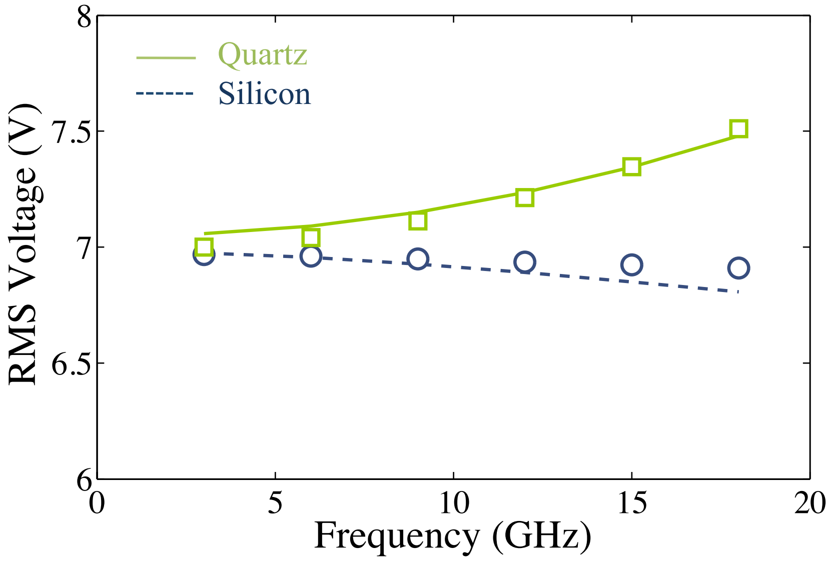

Figure 5.9: Circuit (curve) and HFSS (symbols) simulated equivalent RF voltage under the membrane in up position.

### 5.4.4 Results

The procedure described above is applied to the capacitive RF MEMS switch finite-element model in case of high-resistivity silicon and quartz substrates, accounting also for some thickness and residual stress uncer-

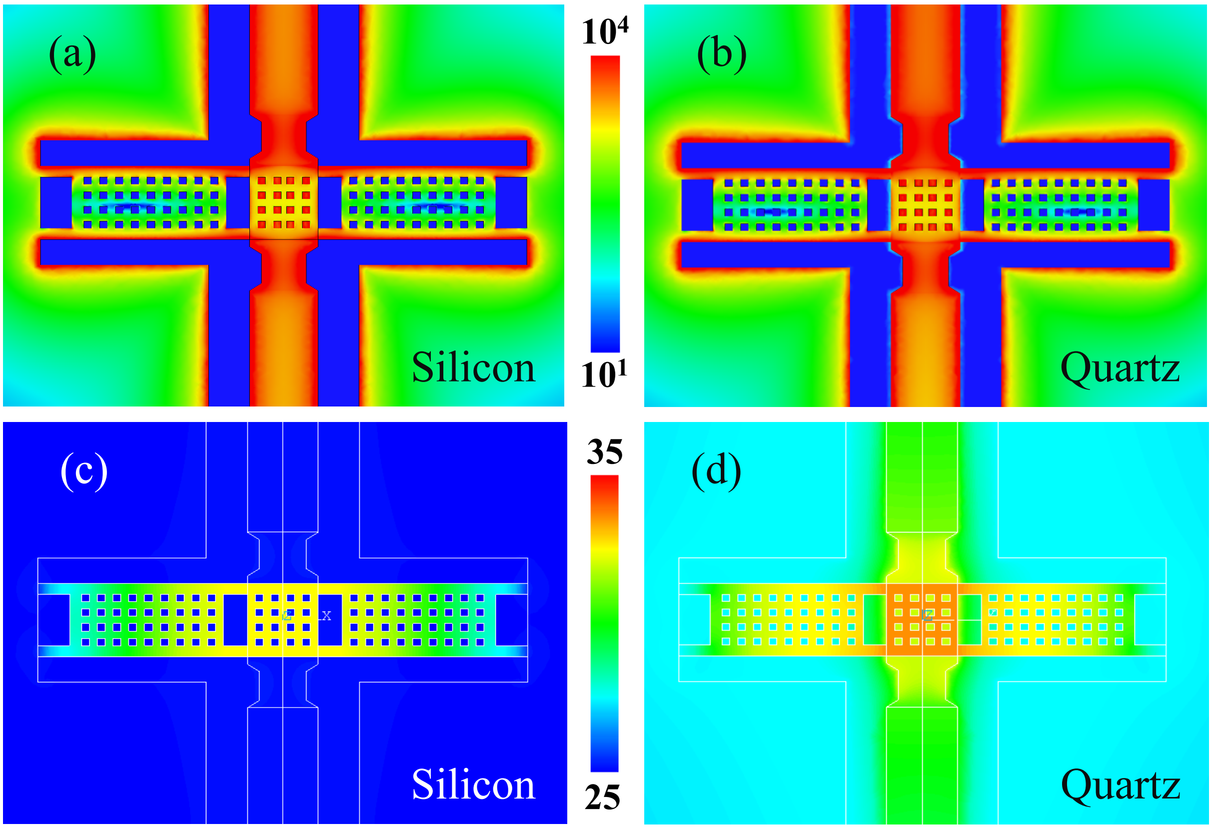

Figure 5.10: Simulated surface (a, b) current and (c, d) temperature distributions for the switches on (a, c) silicon and (b, d) quartz under 1 W input signal at 15 GHz.

tainties. A more complex analysis would involve a feedback iteration between the structural and electromagnetic domains to account for the up-state capacitance variation effect due to the self-bias on S-parameters and membrane losses.

The electromagnetic models of the RF MEMS switches are built in HFSS and validated from 0.5 to 20 GHz by comparing the S-parameters simulation results with the corresponding measurements. A single frequency simulation at 15 GHz is then performed with very fine mesh in order to improve the accuracy in the calculation of losses. The surface RF currents distribution at 15 GHz is reported in Fig. 5.10 along with the corresponding temperature distribution achieved from ANSYS. As reported in Fig. 5.10-a and Fig. 5.10-b the surface current distribution has just slightly differences between the two substrates in terms of absolute values. On the other hand, Fig. 5.10-c and Fig. 5.10-d show vividly the difference between the simulated temperatures on silicon and quartz. According to the color scale of the figure, in case of silicon there is only appreciable temperature rise, whose maximum is at the center of the membrane. In comparison, the peak temperature on quartz is higher and the entire switch including the center and ground conductors of the coplanar transmission line is heated up. Fig. 5.11 shows the anchor-to-anchor temperature profile along the membrane under 1 W, 3 W and 5 W RF power inputs at 15 GHz. It can be seen that in general the membrane on quartz is always hotter than that on silicon and the difference increases with increasing power. In addition, the anchor temperature also increases with increasing power, especially on quartz. This implies that for thermally insulating substrates such as quartz, the anchor should not be assumed to be at the ambient temperature and heat transfer needs to be considered across both the membrane and the substrate. The above observation is further illustrated in Fig. 5.12. Since no dependency of the conductor resistivity on heating is considered at these temperature values, the relationship between temperature rise and power appears linear.

## 5.5 Experimental validation

To evaluate the robustness of the switches in handling hot-switching RF power, power measurements were performed in a 50-$\Omega$ system at 15 GHz and 25 °C. Each measurement was performed under a constant input power with the bias voltage gradually increased until the output power abruptly dropped. The bias voltage at this point was deemed the pull-in voltage. The maximum input power was limited to 5.6 W by the power amplifier and wafer probes used in the measurements. Measurement results are

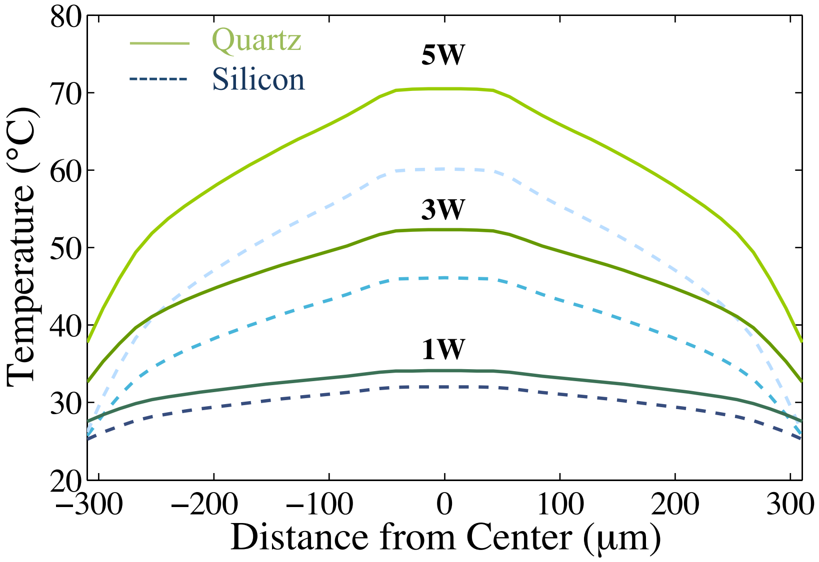

Figure 5.11: Simulated anchor-to-anchor temperature profiles along the membrane under different RF power at 15 GHz

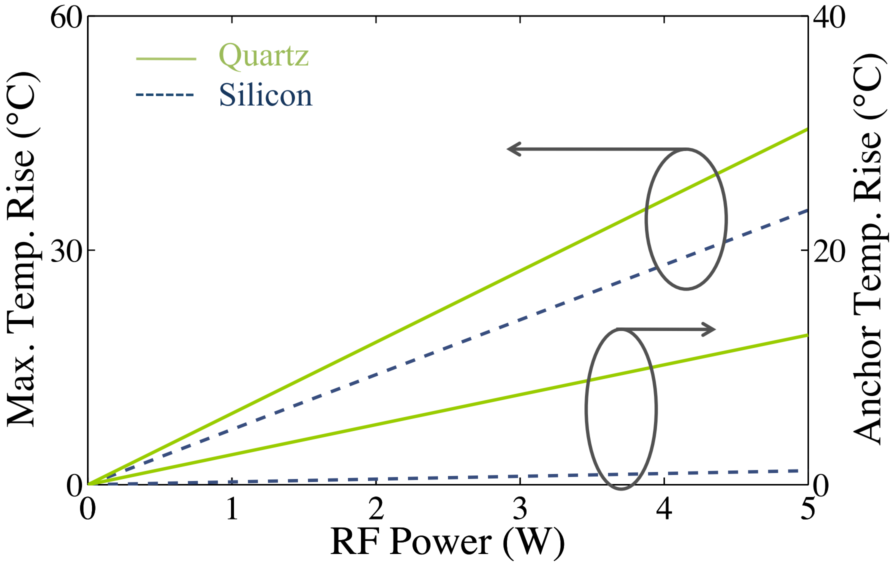

Figure 5.12: Simulated temperature rise at the (left axis) center and (right axis) anchor of the membrane on (– – –) silicon and (—) quartz under different RF powers at 15 GHz

compared to the electromechanical simulations which followed the thermal simulations described previously, showing perfect agreement as reported in Fig. 5.13.

Such a result confirms the importance of substrate thermal conductivity in the evaluation of the power handling. If the self-heating was neglected, the pull-in voltage characteristic for both the switches would assume a behavior much more similar to the iso-thermal characteristic plotted also in Fig. 5.13. Only the pull-in characteristic of the switch on silicon substrate is close to isothermal curve, underlining the self-biasing as the dominant effect in the shift of the pull-in voltage. The dominant effect in case of switch on quartz substrate is instead the self-heating, since the slope of the characteristic is much higher than the silicon case and in turn than the isothermal case. Moreover, a switch failure occurs slightly above 3 W in case of quartz substrate, while the switch on silicon keep working up to 5.6 W. The switch pull-in on quartz is no longer detected probably because the equivalent RF voltage is enough to produce the snap-down of the membrane, whose residual stress and, as a result, the whole stiffness is decreased by the temperature rise. Simulations performed at 5 W also showed that the application of both the thermal load and the equivalent RF voltage is enough to actuate the switch on quartz, without any application of bias voltage.

Since measured and simulated pull-in voltages appear to decrease quite linearly with RF power, they can be fitted by a linear trend line, whose slope, expressed in V/W, is a good indicator of the power-handling capability of the switches. Therefore, simulations were performed and compared with power measurements also at 6, 9 and 12 GHz, in addition to the above-described results at 15 GHz. Fig. 5.14 shows that the simulated and measured slopes in the pull-in voltage were in general agreement for both the silicon and quartz switches. Moreover, the slope values increase with frequency following a trend that can be considered approximatively linear within the frequency range explored.

It is worthwhile to not that the simulation procedure described pre-

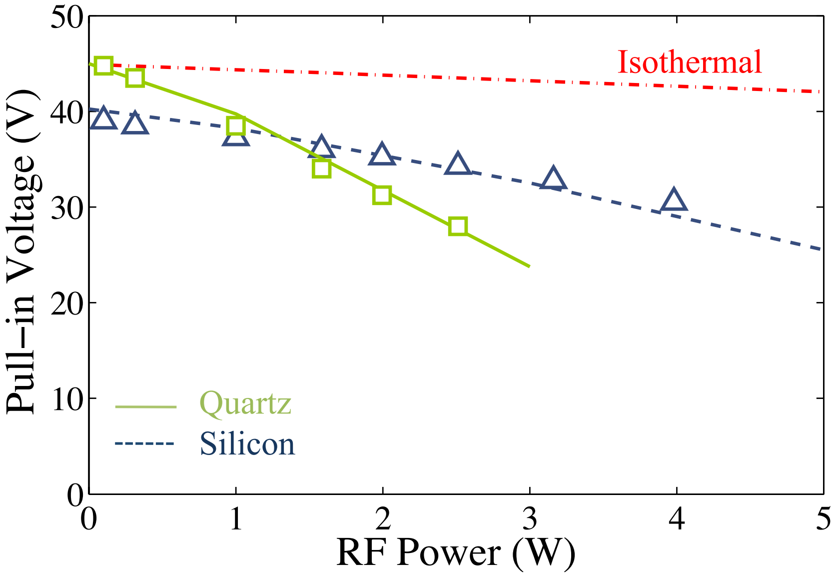

Figure 5.13: FEM (curve) and measured (symbols) pull-in voltages as a function of different RF powers at 15 GHz.

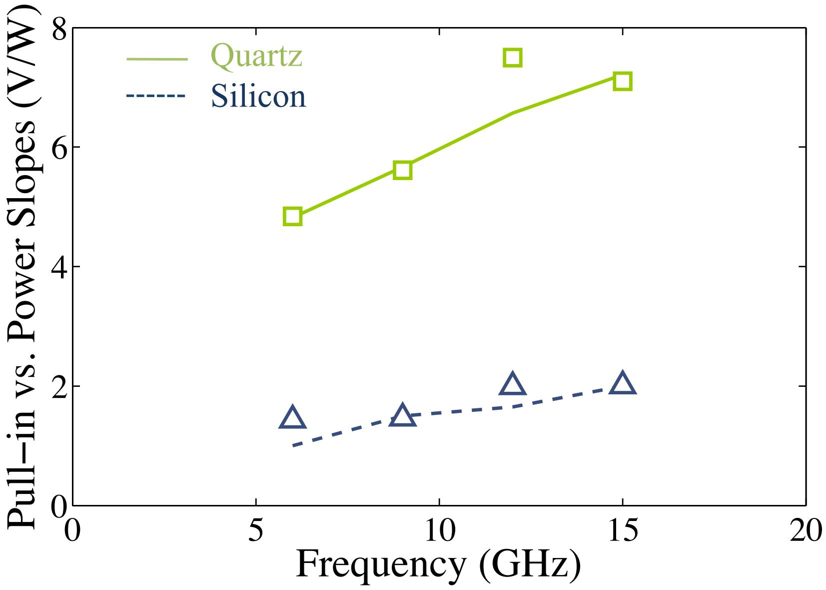

Figure 5.14: FEM (curve) and measured (symbols) pull-in voltages VS. RF powers slopes as a function of different frequencies.

viously could be iterated to account for the temperature dependence of electric resistivity and the effect of structural deformation on the field and current distributions. However, the typical maximum temperature rise is on the order of 10 °C over a 1 W power range and the electrical resistivity does not vary by more than 3 % [105]. In addition, the switch capacitance with the membrane suspended varies only by few fF as extracted from power measurements (Fig. 5.15) [96]. For these reasons the iterative analysis is not critically required to the present switches.

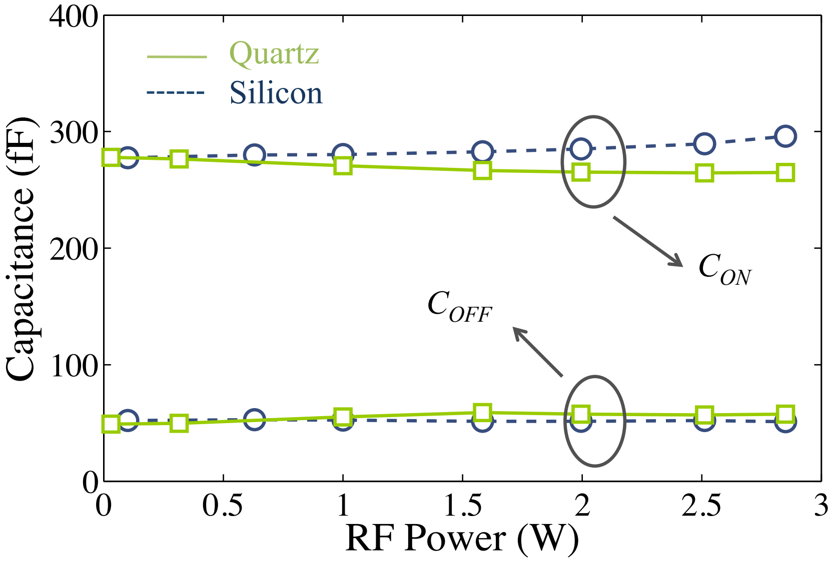

Figure 5.15: ON state and OFF state capacitances extracted from power measurements for (– – –) silicon and (—) quartz substrate.

Once the multiphysics simulation was validated through experimental data, it could be used to determine the parameter values in a compact model as discussed in the next section.

## 5.6 Self-biasing

The root-mean-square RF voltage acting on the suspended membrane is different in case of different substrates because of the different transmission line impedances. In case of quartz, standing waves in the switch can have a significant effect on the overall self-biasing of the membrane. Fig. 5.16 reports the general situation in terms of multiple reflections when

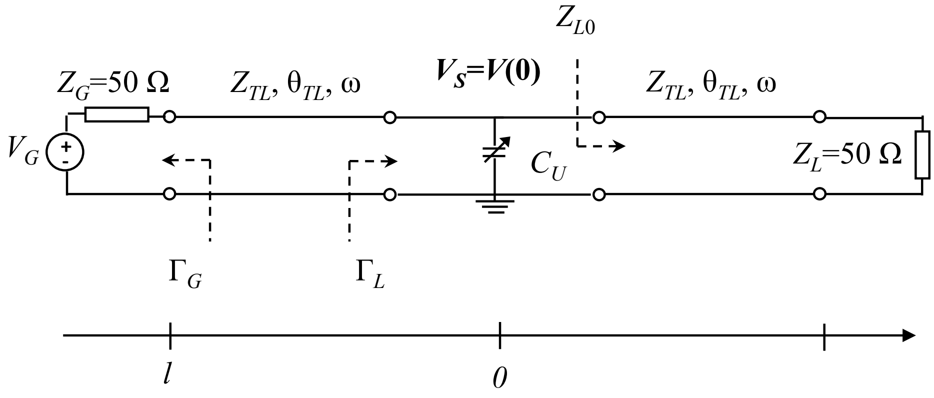

Figure 5.16: Circuit model for both unmatched load and generator.

the transmission line impedance $Z_{TL}$ is different from generator and load impedances as in the case of quartz substrate. The generator and load impedances model the measurement setup ports and are both equal to $Z_G = Z_L = 50\ \Omega$. According to the transmission line theory, a signal generator of voltage $V_G$ and impedance $Z_G$ is able to provide an input power $P_{IN}$ so that:

$$V_G = 2\sqrt{P_{IN} Z_G}. \tag{5.7}$$

The voltage and current at the membrane are:

$$V_S = \frac{V_G Z_{TL}}{Z_G + Z_{TL}} \frac{(1 + \Gamma_L)\, e^{-j2\theta_{TL}}}{1 - \Gamma_L \Gamma_G e^{-j2\theta_{TL}}}, \tag{5.8}$$

$$I_S = \frac{V_G}{Z_G + Z_{TL}} \frac{(1 - \Gamma_L)\, e^{-j2\theta_{TL}}}{1 - \Gamma_L \Gamma_G e^{-j2\theta_{TL}}}, \tag{5.9}$$

where $Z_{TL}$ and $\theta_{TL}$ are the impedance and electrical length of the transmission line between the generator and the switch, and:

$$Z_{L0} = Z_{TL} \frac{Z_G + jZ_{TL} \tan\theta_{TL}}{Z_{TL} + jZ_G \tan\theta_{TL}}. \tag{5.10}$$

Moreover, according to Fig.5.16, one can define:

$$\Gamma_G = \frac{Z_G - Z_{TL}}{Z_G + Z_{TL}}, \tag{5.11}$$

and

$$\Gamma_L = \frac{Y_{TL} - (Y_{L0} + j\omega C_U)}{Y_{TL} + (Y_{L0} + j\omega C_U)}, \tag{5.12}$$

where $Y_{TL} = 1/Z_{TL}$, $Y_{L0} = 1/Z_{L0}$, and $C_U$ is the up-state capacitance. The power delivered to the membrane is then equal to:

$$\begin{aligned} P_S &= \frac{1}{2}\,\mathrm{Re}\left\{V_S I_S^*\right\} \\ &= 4P_{IN}\frac{Z_G Z_{TL}}{(Z_g + Z_{TL})^2}\frac{1 - |\Gamma_L|^2}{|1 - \Gamma_L \Gamma_G e^{-j2\theta_{TL}}|^2} \\ &= \eta_{RF} P_{IN}\frac{Z_G}{Z_{TL}}\frac{1 - |\Gamma_L|^2}{|1 + \Gamma_L|^2}, \end{aligned} \tag{5.13}$$

where:

$$\eta_{RF} = \left(\frac{2Z_{TL}}{Z_G + Z_{TL}}\frac{|1 + \Gamma_L|}{|1 - \Gamma_L \Gamma_G e^{-j2\theta_{TL}}|}\right)^2 \tag{5.14}$$

is a *power scaling factor* which is convenient to account for the increased power at the switch due to impedance mismatching. As a general case, finally the RMS voltage acting on the suspended membrane is:

$$V_{RMS} = \frac{|V_S|}{\sqrt{2}} = \sqrt{\eta_{RF} P_{IN} Z_G}. \tag{5.15}$$

In case of quartz substrate, $Z_G = Z_L = 50\ \Omega$, while $Z_{TL}$, $\theta_{TL}$ and $C_U$ are listed in Table 5.1. Consequently, $\Gamma_G = 0.2\angle 180°$ and $\Gamma_L = 0.155\angle 176°$. Moroever, $\eta_{RF}$ is found to be around 1.07 at 15 GHz. This shows that in the mismatched case the power experienced by the membrane may be approximately 10 % higher than that in the matched case. On the other hand, for matched transmission line, as in the case of silicon substrate, $Z_{TL}$ $= Z_0 = 50\ \Omega$, $\Gamma_G = \Gamma_L = 0$ so $\eta_{RF} = 1$, $V_S = \sqrt{2P_{RF} Z_0}$, and $P_S = P_{IN}$, in accordance with the well-known theory already presented in Section 5.2.

## 5.7 Self-heating

The linear behavior reported in Fig. 5.12 suggests the possibility to use a linear thermal model accounting for the effect of the substrate thermal conductivity. Despite the high complexity of the problem, which involves not-uniform current and temperature distributions, the thermal model can be consistently enclosed in the lumped circuit pictured in Fig. 5.17.

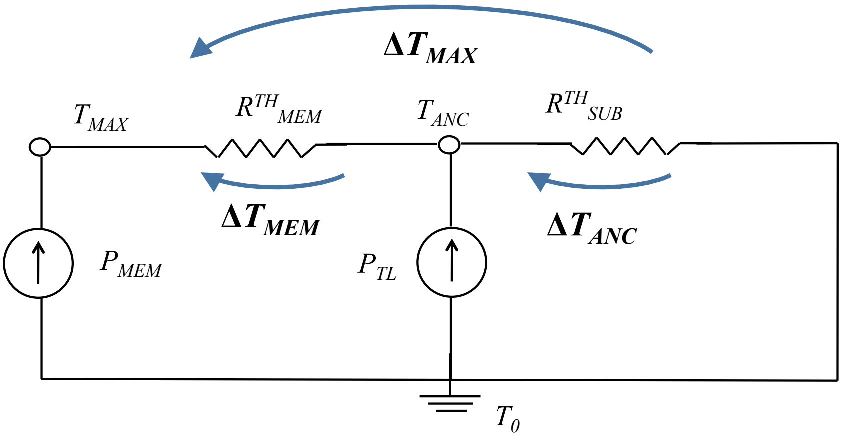

Figure 5.17: Equivalent thermal lumped model accounting for substrate thermal resistance.

According to this, the maximum temperature rise at the center of the membrane is:

$$\begin{aligned}\Delta T_{MAX} &= \Delta T_{MEM} + \Delta T_{ANC} \\ &= P_{MEM} R^{TH}_{MEM} + (P_{MEM} + P_{TL}) R^{TH}_{SUB}.\end{aligned} \tag{5.16}$$

The values of $R^{TH}_{SUB}$ and $R^{TH}_{MEM}$ can be extracted from simulation data. In fact, from ANSYS thermal simulation we have $\Delta T_{MEM} = 32$ °C and 35 °C, $\Delta T_{ANC} = 25.2$ °C and 27.8 °C for silicon and quartz respectively, whereas from HFSS results and $P_{MEM} = 2.15$ mW, $P_{TL} = 18.2$ mW for silicon, and $P_{MEM} = 1.76$ mW, $P_{TL} = 14.7$ mW for quartz substrate. As a result, $R^{TH}_{MEM} = 3159.5$ °C/W, $R^{TH}_{SUB} = 11.5$ °C/W for silicon and $R^{TH}_{MEM} = 3722$ °C/W, $R^{TH}_{SUB} = 155.5$ °C/W for quartz. To better illustrate the difference between quartz and silicon, Eq. 5.16 can be rearranged as:

$$\Delta T_{MAX} = \left[1 + \left(1 + \frac{P_{TL}}{P_{MEM}}\right)\frac{R^{TH}_{SUB}}{R^{TH}_{MEM}}\right] P_{MEM} R^{TH}_{MEM}$$

$$= \beta_{TH} P_{MEM} R^{TH}_{MEM}, \tag{5.17}$$

where:

$$\begin{aligned}\beta_{TH} &= 1 + \left(1 + \frac{P_{TL}}{P_{MEM}}\right)\frac{R^{TH}_{SUB}}{R^{TH}_{MEM}} \\ &\approx 1 + \frac{P_{TL}}{P_{MEM}}\frac{R^{TH}_{SUB}}{R^{TH}_{MEM}}\end{aligned} \tag{5.18}$$

is a figure of merit accounting for the effect of the substrate on the thermal characteristics of the switch. In fact such a notation is also useful to highlight the ratio between power losses and between substrate and thermal resistances. It is easy to prove that $P_{TL}/P_{MEM} \approx 10$ for any substrate, whereas $R^{TH}_{SUB}/R^{TH}_{MEM} \approx 0.1$ and $0.01$ for quartz and silicon respectively. Therefore in case of high thermal conductivity substrate $\beta_{TH} \approx 1$ and the membrane thermal resistance is enough to account for self-heating. For low thermal conductivity substrate, $\beta_{TH}$ is greater than 1, so it needs to be considered in self-heating prediction.

A useful approximation may be employed to estimate the thermal resistance values without performing the thermal simulation. Membrane thermal resistance can be achieved with [106]:

$$R^{TH}_{MEM} = \frac{\gamma_1 l_b}{2\kappa_b t_b w_b} \tag{5.19}$$

Table 5.3: Lumped Thermal Parameters extracted from simulation results.

| **Parameter** | **Silicon** | **Quartz** |
|---|---|---|
| Membrane thermal conductivity $\kappa_b$ (W/cm°C) | 3.18 | |
| Subst. thermal conductivity $\kappa_{SUB}$ (W/cm°C) | 1.56 | 0.02 |
| Membrane Loss (@1W) $P_{MEM}$ (mW) | 2.15 | 1.76 |
| Transmission Line Loss (@1W) $P_{TL}$ (mW) | 18.2 | 14.7 |
| Membrane thermal resistance $R^{TH}_{MEM}$ (°C/W) | 3159 | 3722 |
| Substrate thermal resistance $R^{TH}_{SUB}$ (°C/W) | 11.56 | 155.5 |
| Shape parameter $\gamma_1$ | 1.23 | 1.75 |
| Shape parameter $\gamma_2$ | 0.36 | 0.063 |
| Shape parameter $\gamma_3$ | 0.7 | 0.95 |
| Matching coefficient $\eta_{RF}$ | 1 | 1.07 |
| Thermal coefficient $\beta_{TH}$ | 1.04 | 1.6 |

where $l_b$, $w_b$, and $t_b$, and are length, width, and thickness of the suspended membrane respectively, whereas $\kappa_b$ is the thermal conductivity of the membrane material and $\gamma_1$ is a parameter accounting for the geometry complexity and the not-uniform distribution of the RF current. The substrate thermal resistance is:

$$R^{TH}_{SUB} = \frac{\gamma_2 t_{SUB}}{\kappa_{SUB} l_{SUB} w_{EFF}} \tag{5.20}$$

where $l_{SUB}$ is the length of the die, $t_{SUB}$ is the thickness of the substrate, and $w_{EFF}$ is an effective width accounting for the region of the coplanar conductors where the RF currents are mostly concentrated. For the analyzed geometry at 15 GHz, $w_{EFF}$ is chosen equal to 80 $\mu$m. The parameter $\kappa_{SUB}$ is the thermal conductivity of the substrate, whereas $\gamma_2$ is a shape-factor with the same function of $\gamma_1$. The same values of simulated thermal resistances are achieved by an appropriate choice of $\gamma_1$ and $\gamma_2$. In Table 5.3 the extracted parameters for the thermal lumped circuit that models the measured RF MEMS switches are listed. As a result, the parameter $\beta_{TH}$ is exactly equal to 1.035 for silicon and 1.6 for quartz. This demonstrates the effectiveness of the figure of merit $\beta_{TH}$ in considering the effect of the substrate. The power dissipated on the membrane may be also calculated analytically by applying Eq. 5.15:

$$\begin{aligned} P_{MEM} &= \frac{1}{2} R_S |I_{MEM}|^2 \\ &= \frac{1}{2} R_S C_U^2 \omega^2 \eta_{RF} Z_G P_{RF} \\ &= \phi_{TH} \eta_{RF} P_{RF} \end{aligned} \tag{5.21}$$

where $R_S$ is the series resistance of the membrane extracted from S-parameter measurements, and:

$$\phi_{TH} = \frac{1}{2} R_S C_U^2 \omega^2 Z_G \tag{5.22}$$

is a parameter accounting in a compact way for the factors contributing to the membrane loss. The above expression is useful to relate approximatively the value of $P_{MEM}$ extracted from HFSS simulation with the input RF power.

## 5.8 Pull-in shift estimation

Assuming a uniform stress distribution along the suspended membrane, the effect of RF power on the membrane residual stress variation is achieved combining Eq. 5.21 and Eq. 5.16 [61]:

$$\begin{aligned} \Delta\sigma_0 &= E \Delta\alpha (\Delta T_{MAX}) \\ &= E \Delta\alpha \beta_{TH} R_{MEM}^{TH} \phi_{TH} \eta_{RF} P_{RF} \\ &= \delta_{TH} \beta_{TH} \eta_{RF} P_{RF}, \end{aligned} \tag{5.23}$$

where $E$ is the Young's modulus of the membrane, $\Delta\alpha = \alpha_{MEM} - \alpha_{SUB}$ is the difference between the thermal expansion coefficients of the membrane and the substrate, and

$$\delta_{TH} = E\Delta\alpha R^{TH}_{MEM}\phi_{TH}. \tag{5.24}$$

Note that the parameter $\beta_{TH}$ does not depend on the input power since it depends on the ratio between membrane loss and transmission line loss. Again, $\beta_{TH}$ includes the ratio between shape parameters $\gamma_2/\gamma_1$.

Eq. 5.23 apparently fails when the suspended membrane and the substrate has pretty much similar expansion coefficient. This situation leads to a stress variation theoretically equal to zero, but this is actually true only if both the membrane and the substrate are subject to a uniform temperature load, which is not the case described here. Thus an alternative way to account for the stress change is to consider the different temperature rise which actually occurs in the membrane and in the substrate for a thermal load given by the RF power. Consequently Eq. 5.23 changes as follows:

$$\begin{aligned}\Delta\sigma_0 &= E\left[\alpha_{MEM}\Delta T_{MEM} + \left(\alpha_{MEM} - \alpha_{SUB}\right)\Delta T_{ANC}\right]\\ &= E\left[\alpha_{MEM}\Delta T_{MEM} + \left(\alpha_{MEM} - \alpha_{SUB}\right)\left(\Delta T_{MAX} - \Delta T_{MEM}\right)\right]\\ &= E\Delta\alpha\Delta T_{MAX}\left(1 + \frac{\alpha_{SUB}}{\Delta\alpha}\frac{\Delta T_{MEM}}{\Delta T_{MAX}}\right)\\ &= \delta'_{TH}\beta_{TH}\eta_{RF}P_{RF}, \end{aligned} \tag{5.25}$$

where:

$$\delta'_{TH} = E\Delta\alpha R^{TH}_{MEM}\phi_{TH}\left(1 + \frac{\alpha_{SUB}}{\Delta\alpha}\frac{\Delta T_{MEM}}{\Delta T_{MAX}}\right). \tag{5.26}$$

In case of metal membrane and ceramic substrate, which is in general the most common situation, $\alpha_{SUB}/\Delta\alpha$ is much lower than 1. However when the membrane material is chosen to have a thermal expansion coefficient similar to the substrate for low temperature sensitivity design [61], $\alpha_{SUB}/\Delta\alpha \gg 1$, and the term acquires significant importance on the membrane stress variation.

Considering the effect of both the self-heating from Eq.5.23 and the RMS voltage expressed in Eq. 5.15, the pull-in voltage for the analyzed capacitive switches may be approximated to:

$$\begin{aligned} V_{PI} &= \sqrt{\frac{16\gamma_3(\sigma_0 - \delta_{TH}\beta_{TH}\eta_{RF}P_{RF})(1-\nu)g_0^3}{27\varepsilon_0 L_e^2} - \eta_{RF}Z_G P_{RF}} \\ &= V_{PI0}\sqrt{1 - \left(\frac{\delta_{TH}\beta_{TH}}{\sigma_0} + \frac{Z_G}{V_{PI0}^2}\right)\eta_{RF}P_{RF}} \end{aligned} \tag{5.27}$$

where $V_{PI0}$ is the pull-in voltage when $P_{RF} = 0$ W, $\varepsilon_0$ is the vacuum permittivity, $g_0$ is the gap between membrane and electrodes, $\nu$ is the membrane material Poisson's ratio, $L_e$ is the electrode length, and $\gamma_3$ compensates the deviations of the above formula due to geometry complexity. For low values of $P_{RF}$, the above expression can be linearized around a working RF power, retrieving the pull-in variation with respect to the initial pull-in voltage:

$$\Delta V_{PI} \approx \frac{dV_{PI}}{dP_{RF}}P_{RF} = S_{PH}P_{RF} \tag{5.28}$$

so the power handling sensitivity is defined as

$$S_{PH} = \frac{1}{2}\left(\frac{\delta_{TH}\beta_{TH}}{\sigma_0} + \frac{Z_G}{V_{PI0}^2}\right)\eta_{RF}V_{PI0}. \tag{5.29}$$

Such a value can be easily employed as a figure of merit for the power handling prediction, as already used previously in Fig. 5.14 for the evaluation of the simulated voltage shift at different frequencies. For the analyzed cases, the power handling sensitivity at 15 GHz of the switch on silicon is lower than 2 V/W, while it is around 7 V/W for the switch on quartz. In case of $\delta_{TH}\beta_{TH} \approx 0$, the switch operates in isothermal behavior and the self-biasing is the dominant effect due to high power, as already shown in Fig. 5.13. Moreover, also the residual stress has a significant effect on the switch power capacity. In fact Eq. 5.29 emphasizes that low values of $\sigma_0$ make the overall stiffness more sensitive to the stress variations accounted with $\delta_{TH}\beta_{TH}$.

## 5.9 Conclusions

In conclusion, finite element simulations showed that for switches fabricated on thermally insulating substrates, the self heating of the substrate has a significant impact on the temperature rise of the membrane and it needs to be taken into account. The simulation also showed that for switches embedded in mismatched transmission lines, the RF power delivered and dissipated in the switches could be increased by standing waves. The parameter values extracted from the simulation data were incorporated into the above-described compact model to enable quick evaluation of the pull-in voltage decrease with increasing RF power. The whole approach has been validated by power measurements performed from 6 to 15 GHz, and provides good hints for the future design of power-robust MEMS switches.

# Chapter 6

# Design Solutions for Redundancy Switches

## 6.1 Introduction

In this Chapter, the problem of long-term reliability is addressed from a design point of view. As shown in Chapter 4, dielectric charging and/or contact degradation may induce the *stiction* of the suspended membrane especially after a long-term continuous bias voltage. Design solutions such as the use of dielectric-less electrodes or high-restoring force geometries could be not enough to avoid this problem. Therefore a dedicated mechanism able to actively *pull-up* the membrane in case of down-state stiction seems to be a more suitable solution to guarantee the stiction recovering after a very long stress voltage time, since it can counteract against possible sticking forces.

Here an active push/pull or *toggle* mechanism is proposed and implemented in different switch typologies. The mechanical model, based on the work reported in [72], is briefly described accounting also for the effect of a uniform charging in the insulating layer. The fabrication and the characterization of a capacitive MEMS switch based on this toggle mechanism are also reported, along with a deep analysis of the switch reliability under a continuous long-term stress voltage. The toggle concept is also implemented in the design of a *bistable* switch, where the bistability property can be accomplished by using a tensile-compressive stress converter geometry.

## 6.2 Toggle mechanism concept

### 6.2.1 Description

The active push/pull or *toggle* MEMS switch exploits torsional anchor springs and a third electrode to mechanically restore the OFF-state of the switch in case of ON-state stiction. Fig. 6.1 shows the top and cross-section view of the MEMS switch employing this concept. The switch consists of a suspended membrane anchored to a fixed support by means of four torsion springs. Such a membrane is composed of different parts: a central part realizing the mobile plate of the variable capacitor, two *mobile electrodes* implementing the toggle mechanism, and two couples of *levers* connecting the central part and the mobile electrodes. The bridge can be pushed *up* or *down* by applying a voltage on two couples of fixed electrodes, which are symmetric with respect to the central RF line underneath the membrane. The couple of fixed electrodes closer to the RF line are referred to as *pull-in* (PI) electrodes, whereas the couple of fixed electrodes placed at the extremities of the membrane are called *pull-out* (PO) electrodes. In order to distinguish the toggle *pull-in* and *pull-out* active mechanisms from the pull-in and pull-out voltages of a standard switch configuration, the latter will be referred to as *actuation* and *release* voltages. The mechanism works as follows. When no voltage is applied, the membrane is flat with respect to the RF line, and this situation can be referred to as the *zero-bias state* (Fig. 6.2-a). When $V_{bias}^{PI} > 0$ V and $V_{bias}^{PO} = 0$ V, the anchor springs start to torque, allowing the central part to move towards the underpass RF signal line, thus producing an increase of capacitance. The capacitance assumes

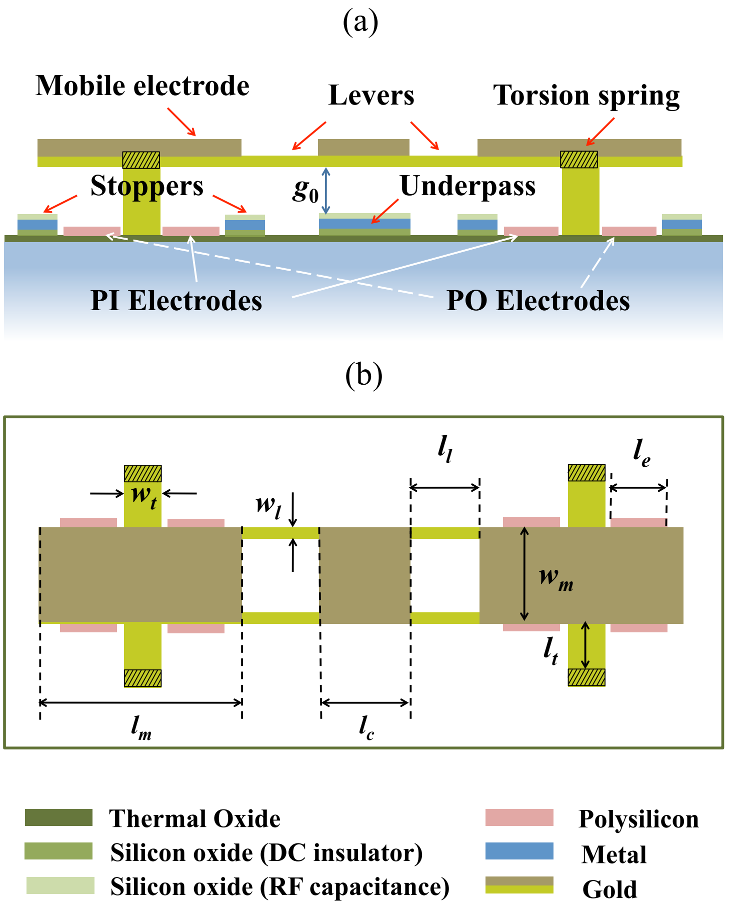

Figure 6.1: Sketch illustrating the cross section (a) and the top view (b) of the device along with the corresponding description of the layers.

its maximum value $C_{ON}$ (Fig. 6.2-b) when $V_{bias}^{PI} > V_{act}^{PI}$. On the other hand, when $V_{bias}^{PO} > 0$ V and $V_{bias}^{PI} = 0$ V, the bridge central part starts moving upwards, lowering the device capacitance down to its minimum value $C_{OFF}$, which is achieved when $V_{bias}^{PO} > V_{act}^{PO}$ (Fig. 6.2-c).

### 6.2.2 Model

The analytical model describing the toggle mechanism is extensively explained in [107] and [72]. Here a brief outline is reported, where half of the model from Fig. 6.2-a is considered. Fig. 6.3-a and Fig. 6.3-b depict the model of half the switch in case of bias on PI and PO fixed electrodes,

**(a) Zero-Bias State**

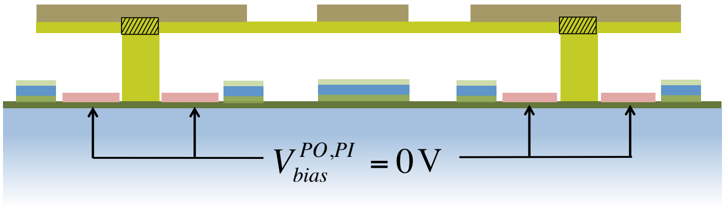

**(b) Pull-in Actuation**

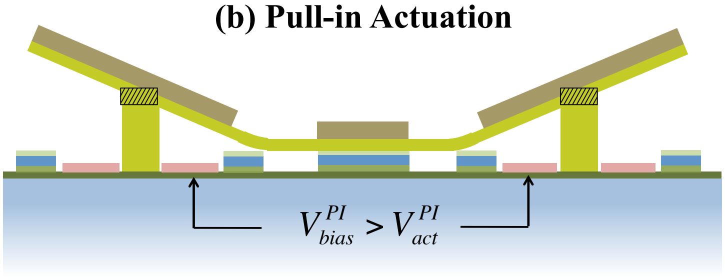

**(c) Pull-out Actuation**

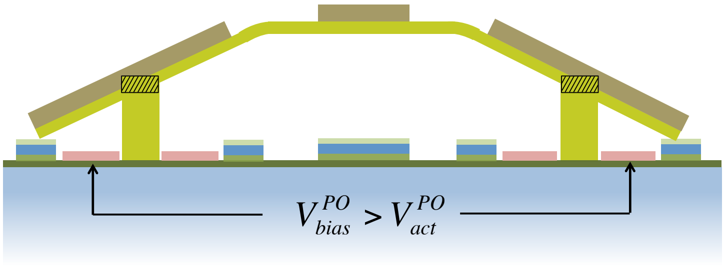

Figure 6.2: Sketch illustrating the cross section of the device when (a) zero bias voltage is applied, (b) pull in actuation or (c) pull-out actuation occurs.

respectively. The electrostatic force $f_e^\gamma$ (where $\gamma$ stands for $PI, PO$) acting on the mobile electrodes after the application of a bias voltage is also annotated, with the corresponding reaction moment $M_A$ at the point A and the reaction forces $F_A$ and $F_B$ at the points A (anchors) and B (connecting levers) respectively.

Under the assumption that the anchor springs experiment a pure rotation movement (i.e., the spring bending stiffness is infinite, so the $z$ displacement of point A is zero), it is considered only the balance of mo-

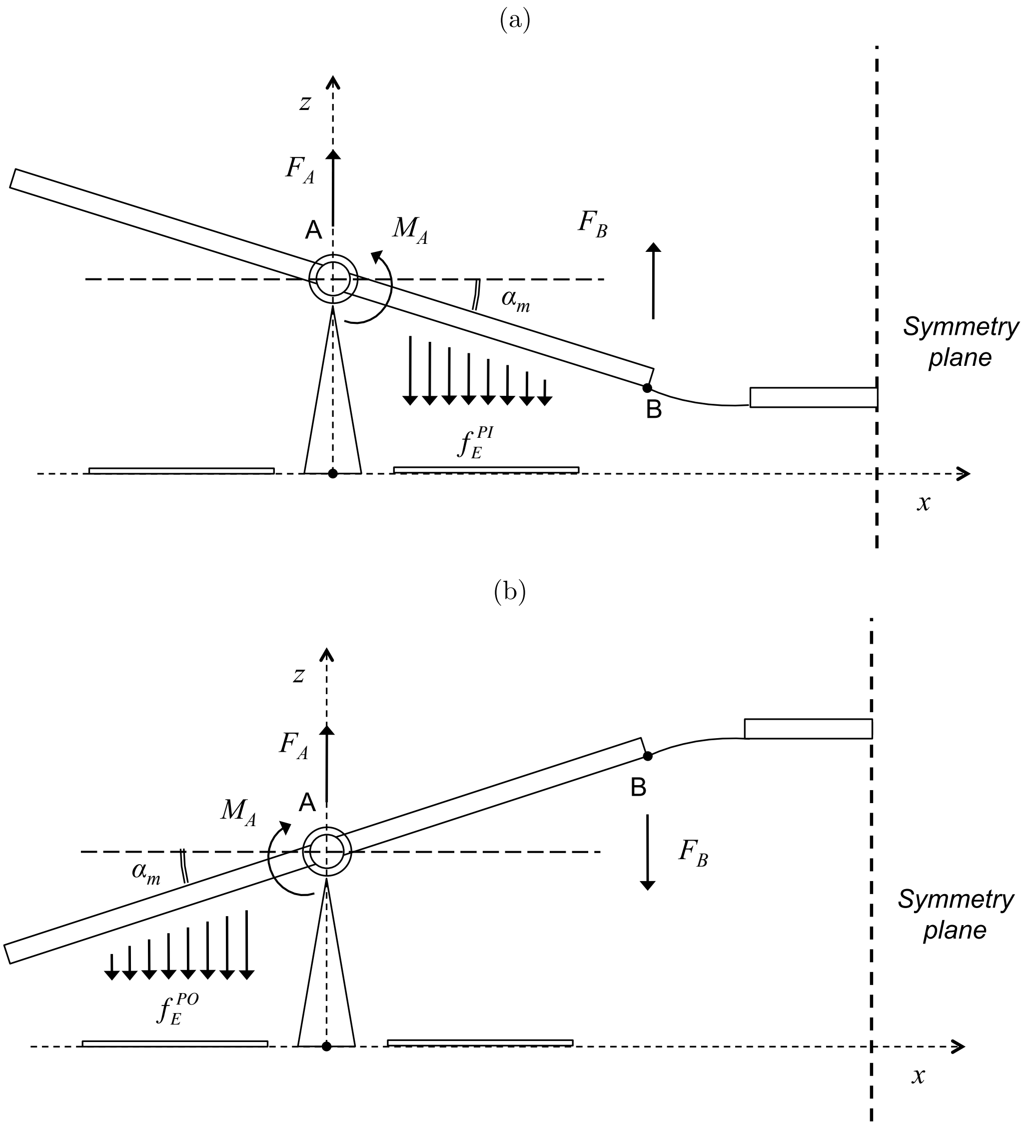

Figure 6.3: Schematic diagram representing the left half of the switch, including forces and moments acting on the mobile electrode in case of PI bias (a) and PO bias (b).

ments affecting the membrane rotation with respect to the anchor points. The membrane displacement is defined in terms of rotation by means of a *tilt* angle $\alpha_m$. Thus the whole mechanical system depicted in Fig. 6.3 is in *equilibrium* if the sum of moments is equal to zero, which means that:

$$M_e^{\gamma} = M_A + F_B l_{pm} \tag{6.1}$$

where $M_e^\gamma$ (with $\gamma = PI, PO$) is the electrostatic moment resulting from the application of the distributed electrostatic force $f_e^\gamma$ at the fixed electrode, $l_{pm}$, indicated in Fig. 6.1-b is the distance between point A and B, and $M_A$ and $M_B = F_B l_{pm}$ are the reaction moments provided by the springs and the connecting levers. For a given bias voltage $V_{bias}^\gamma$, the distributed electrostatic force is:

$$f_e^\gamma = \frac{dF_e^\gamma(x)}{dx} = -\varepsilon_r \varepsilon_0 w_m \frac{V_{bias}^\gamma}{g_0 - \alpha_m x} \tag{6.2}$$

where $w_m$ is the membrane width, $g_0$ is the gap between membrane and fixed electrode, and $x$ is the distance from the anchor point according to the reference system used in Fig. 6.3. Assuming that the distance between the fixed electrode and the anchor point A is negligible with respect to the electrode length, the electrostatic moment is calculated by integrating the partial electrostatic moment $dM_e^\gamma = x dF_e^\gamma$ from 0 to $l_e$ (fixed electrode length), so one has:

$$\begin{aligned} M_e^\gamma &= \varepsilon_0 w_m \frac{{V_{bias}^\gamma}^2}{\alpha_m^2} \left[ \frac{1}{1 - \alpha_m l_e / g_0} - 1 + \ln\left(1 - \alpha_m l_e / g_0\right) \right] && (6.3) \\ &= \beta(\alpha_m) {V_{bias}^\gamma}^2. && (6.4) \end{aligned}$$

Given $w_l$, $l_l$, and $t_l$ respectively the width, length and thickness of the lever, and $w_t$, $l_t$, and $t_t$ the width, length and thickness of the anchor spring, the reaction moment at the anchors is:

$$M_A = 2 k_t \alpha_m, \tag{6.5}$$

and the reaction force due to the lever can be demonstrated to be [72]:

$$F_B = \frac{2}{l_l^2} E I_l \alpha_m, \tag{6.6}$$

where $E$ is the Young's modulus of the membrane material, $I_l = w_b t_b^3/12$ is the moment of inertia of the lever, and $k_t$ is the torsional constant of the anchor spring. This last parameter is defined as [108]:

$$k_t = C_1 \frac{E}{2(1-\nu)} \frac{w_t t_t^3}{l_t}. \tag{6.7}$$

The constant $C_1$ of Eq. ( 6.7) depends on the $w_t/t_t$ ratio and it is called *torsion coefficient*. For a rectangular-shaped beam with $w_t/t_t \approx 5$, $C_1$ is approximatively equal to 0.25. For $w_t/t_t > 10$, $C_1$ is equal to 0.33 [108]. Such a stiffness is accounted for twice in Eq. (6.5) because of the presence of the two torsion springs in parallel. By considering the maximum tilt angle $l_{pm}/g_0 = \tan\alpha_{max} \approx \alpha_{max}$, and rearranging together Eq. 6.5 and Eq. 6.6 as follows:

$$K = 2\frac{1}{l_l^2} E I_l l_{pm} + 2k_t, \tag{6.8}$$

so that $M_B + F_B l_{pm} = K\alpha_m$, Eq. 6.1 can be solved according to $\alpha_m$. Thus it can be demonstrated that the actuation voltage due to torsion movement is equal to:

$$V_{act}^{\gamma} = \sqrt{\frac{K}{2.4\varepsilon_0 w_m} \frac{g_0^3}{l_e^3}}. \tag{6.9}$$

For the above expressions, the effect of the residual stress and other nonlinear effect such as the spring bending are neglected. Moreover, Eq. 6.1 is applicable to the force and moment balance for a bias voltage applied alternatively to both pull-in and pull-out electrode, as depicted also in Fig. 6.3.

The tilt angle $\alpha_m$ defines also a maximum range $\Delta_g$ along the $z$-axis where the membrane can move up and down without incurring in a sudden *snap-through* (i.e. a snap-down on the PI or PO electrodes), behaving like a wide-tuning *varactor* device [109]. In this range the moment balance expressed in Eq. 6.1 is still valid. The maximum displacement from the

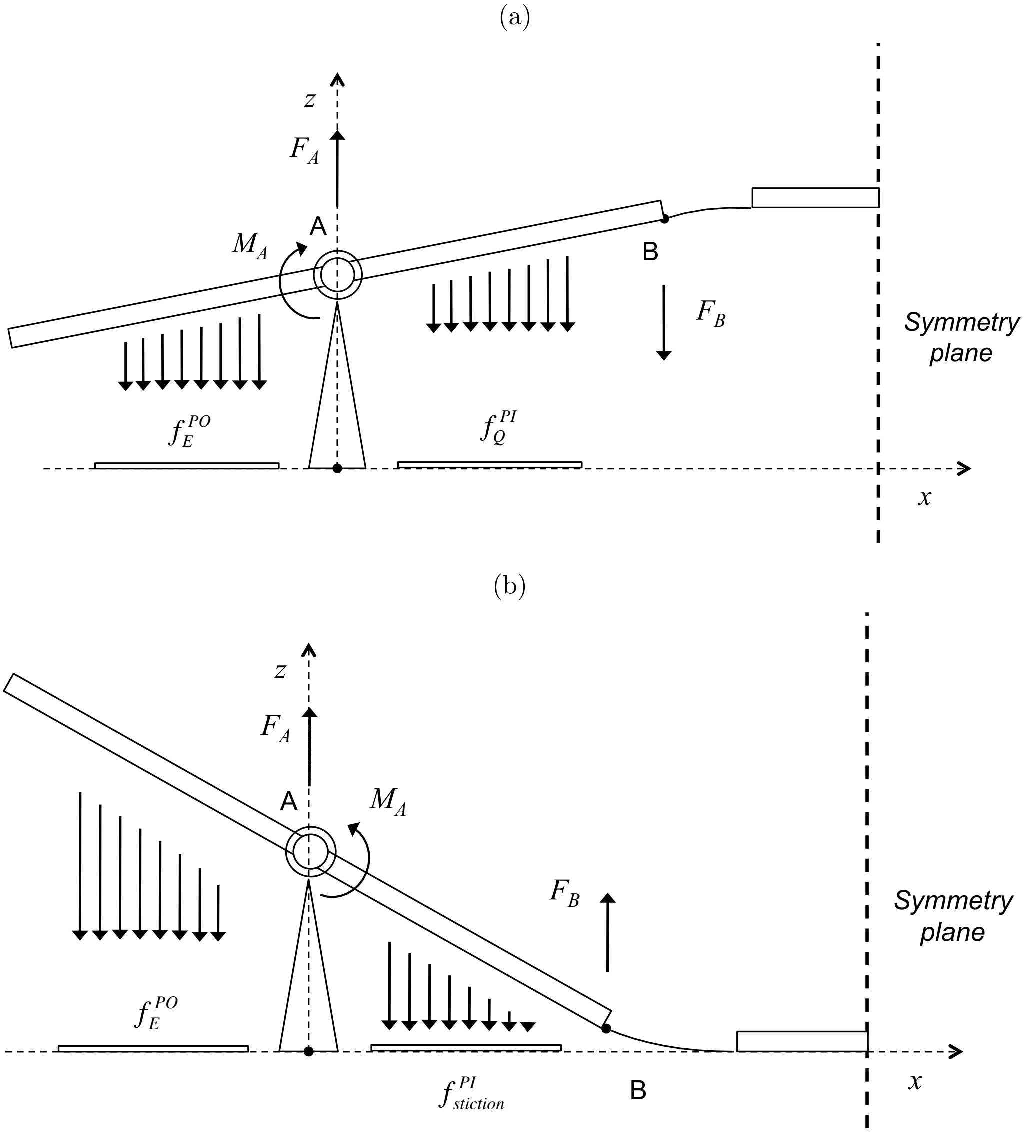

Figure 6.4: Schematic diagram representing the left half of the switch, where the effect of the equivalent force due to the charging at the PI is considered in absence of stiction (a) and in case of stiction (b).

zero-bias position allowed before the snap-through is [72]:

$$\Delta_g = \left(l_{pm} + \frac{1}{3}L_l\right)\alpha_{max} = \left(l_{pm} + \frac{1}{3}l_l\right)\frac{g_0}{l_e} \tag{6.10}$$

where $\alpha_{max}$ is the tilt angle at which the PI or PO actuation occurs. The half of the mobile electrode length $l_{pm}$ and the lever length $l_l$ along with the fixed electrode length $l_e$ can be dimensioned in order to avoid the membrane snap-down, i.e. the instability point in the moment balance, resulting in a *soft* actuation. Such a condition occurs when $\Delta_g = g_0$. So it can be demonstrated that:

$$l_e = 0.45 \left( 1 + \frac{1}{3} \frac{l_l}{l_m} \right). \tag{6.11}$$

When the switch is kept in the ON state ($V_{bias}^{PI} > V_{act}^{PI}$ and $V_{bias}^{PO} = 0$ V) for a time $t$, charging occurs on the dielectric covering or around the pull-in electrode. Now let's consider that a uniform surface charge $Q(t)$ is present over the insulating layer at the top of the PI electrodes after a time $t$. According to Fig. 6.4-a, If $V_{bias}^{PO} > 0$ V and $V_{bias}^{PI} = 0$ V at the time $t$, the moment balance leads to:

$$M_e^{PO}(t) = M_e^{Q}(t) + M_A + F_B l_{pm}, \tag{6.12}$$

where $M_A$ and $F_B$ are given by Eq. 6.5 and Eq. 6.6, and:

$$M_e^{Q}(t) = \beta(\alpha_m) \left[ V_{eq}^{PI}(t) \right]^2 \tag{6.13}$$

is the electrostatic moment due to an equivalent voltage $V_{eq}^{PI}(t)$ induced by injected charge $Q(t)$. The pull-out actuation (expressed by Eq. 6.9 for $t = 0$ s) is then modified as follows:

$$V_{act}^{PO}(t) = \sqrt{\frac{g_0^3}{l_e} \frac{K}{\varepsilon_0 w_m} + [V_{eq}^{PI}(t)]^2} \approx V_{act}^{PO}(0) \left( 1 + \frac{1}{2} \left[ \frac{V_{eq}^{PI}(t)}{V_{act}^{PO}(0)} \right]^2 \right). \tag{6.14}$$

From Eq. 6.16, the PO actuation voltage is expected to increase regardless the sign of the charge injected inside the dielectric around the PI electrode. In addition, the pull-out actuation shift $\Delta V_{act}^{PO}(t) = V_{act}^{PO}(t) - V_{act}^{PO}(0)$ qualitatively follows the same trend as the PI variation, but it is also scaled by a factor equal to the square of the pull-out actuation voltage at $t = 0$ s.

If the amount of charge is large enough to cause the *stiction* of the mobile electrode at the PI electrodes, the balance of moments changes as depicted in Fig. 6.4-b, and it results in:

$$M_e^{PO} = M_e^Q - M_A - F_B l_{pm}, \tag{6.15}$$

which eventually leads to:

$$V_{act}^{PO}(t) = \sqrt{[V_{st}^{PI}(t)]^2 - \frac{g_0^3}{l_e} \frac{K}{\varepsilon_0 w_m}} \approx V_{st}^{PI}(t) \left(1 - \frac{1}{2} \left[\frac{V_{act}^{PO}(0)}{V_{st}^{PI}(t)}\right]^2\right), \tag{6.16}$$

where $V_{st}^{PI}(t)$ is the equivalent voltage which keeps the membrane stuck in the down position, and it is higher than $V_{act}^{PO}(0)$ by definition.

### 6.2.3 Optimization

The initial approach in the design of the toggle switch aimed at the optimization of the membrane dimensions in order to have an actuation voltage lower than 60 V. Moreover, anchor springs could exhibit a tendency to *bend* because of the electrostatic force applied to the mobile electrode, making the toggle mechanism ineffective. The spring constant due to bending related to an anchor spring of the same geometry as the previously described is:

$$k_b = 2 \frac{w_t t_t^3}{l_t^3}. \tag{6.17}$$

Consequently, if the mobile electrode is much more stiff than anchor springs and it moves rigidly and flat toward the fixed electrodes, the pull-in voltage is:

$$V_{act,b} = \sqrt{\frac{8}{27} \frac{2k_b}{\varepsilon_0 w_m l_e} g_0^3}. \tag{6.18}$$

In the real case, the bending and the torsion of the spring occur simultaneously, and the respective stiffness may influence each other, resulting in a non-linear relationship between forces and spring stiffness. To simplify the modeling, these two effects were considered *decoupled*, so the bending and torsion flexures are both considered linear.

The resulting actuation voltages due to spring bending and torsion were modeled and analyzed accordingly as a function of the device geometric parameters. Fig. 6.5 shows the variation of the actuation voltage due to the torsion and the bending of the anchor springs as a function of spring $w_t/l_t$ ratio. In this case, top electrode length $l_{pm}$ and lever length $l_l$ are fixed to 120 $\mu$m and 60 $\mu$m respectively. The dashed line in red indicates the upper limit for the acceptable torsion actuation voltage. From the graphs it is possible to note that for $t_t = 5$ $\mu$m (BRIDGE + CPW layers in FBK process, see Chapter 2) the actuation voltage due to the spring bending is safely much higher than the torsion actuation voltage, which is however much higher than the required voltage value. For $t_t = 2$ $\mu$m (only BRIDGE layer) the actuation voltage due to torsion stiffness remains widely under 60 V, and the choice of a $w_t/l_t$ ratio equal to 0.3 represent a good compromise for having a high bending actuation voltage as well.

Fig. 6.6 shows the actuation voltage dependent only on torsion stiffness as a function of half of the mobile electrode length $l_{pm}$ for different values of connecting lever length. A $w_t/l_t$ ratio equal to 0.3 was considered as a result of the previous analysis. Even in this case the red dashed line marks an upper limit for the acceptable value of the actuation voltage. Moreover, the length of the half-mobile electrode should be chosen lower than 200 $\mu$m in order to make the membrane less sensitive to stress gradient. A good compromise between actuation voltage and low stress gradient sensitivity is to choose $l_{pm} = 120$ $\mu$m (and consequently $l_m = 250$ $\mu$m, accounting also for the spring width $w_t = 10$ $\mu$m), $l_l = 60$ $\mu$m and $l_e = 65$ $\mu$m. Since

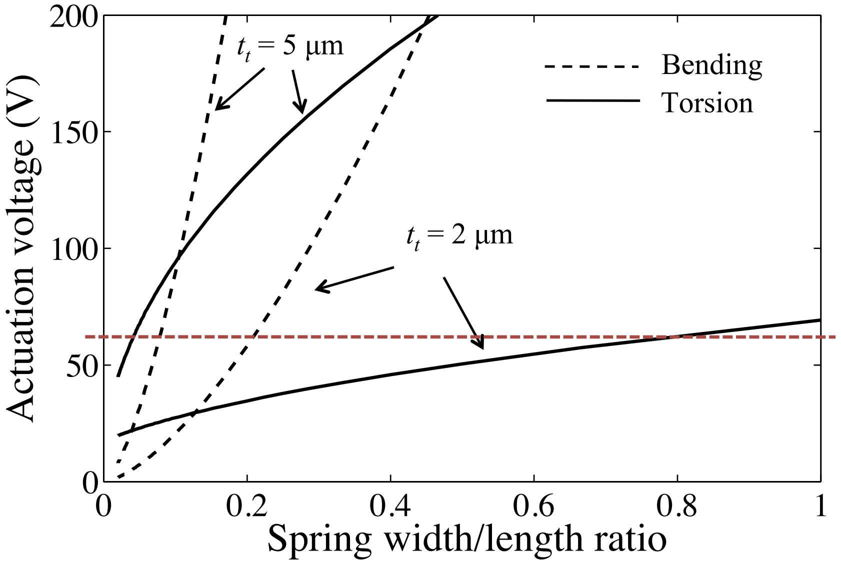

Figure 6.5: Toggle switch actuation voltage due to the torsion (continuous line) and the bending (dashed line) of the anchor springs as a function of spring width/length ratio for different values of spring thickness.The dashed red line marks the upper limit for the acceptable actuation voltage.

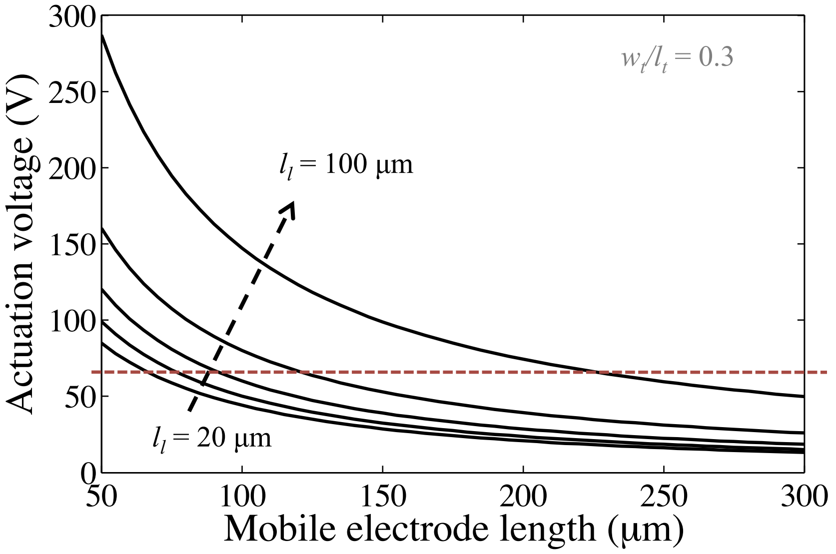

Figure 6.6: Toggle switch actuation voltage as a function of the mobile electrode length for different values of connecting lever length. The dashed red line marks the upper limit for the acceptable actuation voltage.

$l_{pm} < l_e$, this choice allows the membrane to avoid the contact with the fixed electrodes when it actuates. Nevertheless, the condition expressed by

Eq. 6.11 is not accomplished, but this is not a relevant issue since the toggle mechanism is implemented in a switch and not in a varactor. As a result, the theoretical actuation voltage due to spring torsion is found to be about 57 V, while the snap-down of the membrane caused by the spring bending occurs at around 200 V. Table 6.1 summarizes all the chosen dimensions for the toggle capacitive switch.

Table 6.1: Geometrical dimensions and material properties of the toggle switch.

| | |
|---|---|
| Membrane Young's Modulus ($E$) | 75 GPa |
| Membrane Poisson's ration ($\nu$) | 0.44 |
| Membrane residual stress ($\sigma_0$) | 50 MPa |
| Spring length ($l_t$) | 30 $\mu$m |
| Spring width ($w_t$) | 10 $\mu$m |
| Mobile electrode length ($l_m$) | 250 $\mu$m |
| Membrane width ($w_m$) | 90 $\mu$m |
| Central part length ($l_c$) | 90 $\mu$m |
| Lever length ($l_l$) | 60 $\mu$m |
| Lever width ($w_l$) | 10 $\mu$m |
| Fixed electrodes length ($l_e$) | 65 $\mu$m |
| Air gap ($g_0$) | 2.75 $\mu$m |

Since the analytical model neglects some non-linearities such as the effect of residual stress in thin layers, a finite element method (FEM) simulation was performed by using ANSYS$^{TM}$Multiphysics [83]. A residual stress of $\sigma_0 = 50$ MPa (typical value for the available fabrication process) was considered. FEM results confirmed that actuation occurs mostly because of the rotation of anchor springs, whereas exhibit insignificant bending for $V_{bias}^{PI,PO} = 80$ V, as reported in Fig. 6.7.

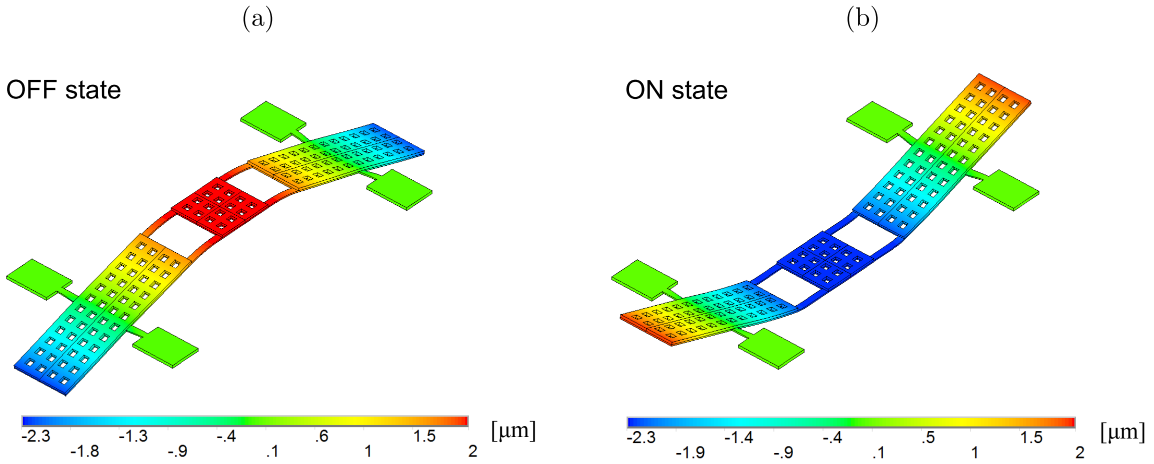

Figure 6.7: FEM displacement solution of the toggle switch for (a) PI and (b) PO actuation when $V_{bias} = 80$ V is applied alternatively to PI and PO electrodes.

## 6.3 Experimental results on toggle switch

### 6.3.1 Fabrication

A picture of the fabricated device is shown in Fig. 6.8. The toggle switch was manufactured on a high resistivity 525-$\mu$m thick silicon substrate by using the well-established 8-mask process of the FBK foundry [110]. The switch is integrated in a 50 $\Omega$ coplanar waveguide (CPW), and consists of a 720-$\mu$m long and 2-$\mu$m thick electroplated gold membrane anchored to CPW ground by means of four 30-$\mu$m long springs. The central part of the membrane and the movable electrodes are also reinforced by an additional 3.5-$\mu$m thick layer of electroplated gold for increased stiffness. The two couples of pull-in and pull-out electrodes are made of 0.63-$\mu$m thick polysilicon layer. The central part of the membrane is a 90-$\mu$m x 90-$\mu$m square suspended above 0.63-$\mu$m thick Ti/TiN/Al/Ti/TiN layer and 0.1-$\mu$m thick low temperature oxide (LTO) underpass. An experimental low temperature release step was performed at the end of the manufacturing process in order to guarantee minimal stress gradient and good planarity

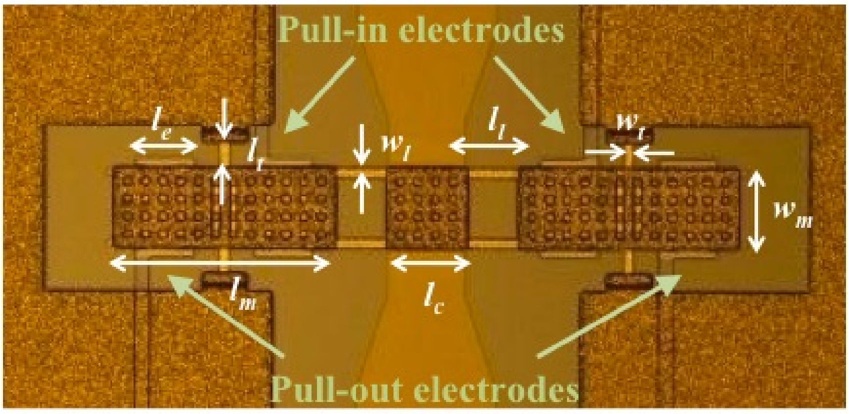

Figure 6.8: Micrograph of the manufactured toggle switch with an indication of the most relevant geometrical parameters.

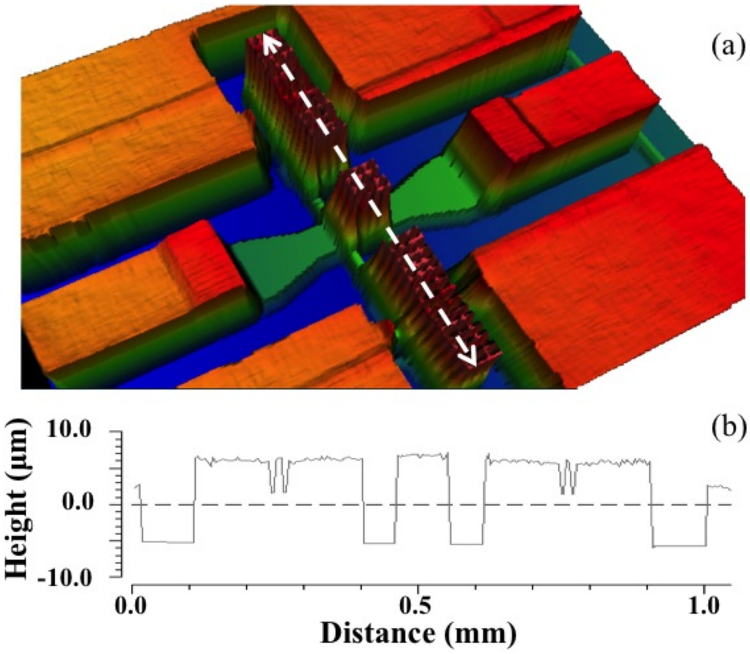

Figure 6.9: Profile measurement of a realized device obtained with a Zygo Optical Profiler. (a) 3-D view. (b) Longitudinal profile along the switch.

of the gold membrane, as shown in Fig. 6.9 [79].

Mechanical stoppers are introduced under the movable electrodes, next to the fixed actuation electrodes. This allows for the removal of the insulating layer from the top of the fixed electrodes. Since some dielectric layer still surrounds the dielectric-less electrode, a certain amount of charge injected from the electrodes to such a dielectric layer (which in this case is thermal oxide) is expected. The effect of this charging is relevant especially for continuous long actuation [19]. In addition, the mechanical stoppers are designed thicker than the underpass layer, so that a 0.1-$\mu$m air-gap is still present when the switch is ON. This allows for a repeatable $C_{ON}/C_{OFF}$ ratio of about 12.

### 6.3.2 Characterization

The manufactured device was experimentally characterized to evaluate its electromechanical and electromagnetic properties. First of all PI-PO actuation voltages and mechanical resonance were measured as a further validation of the FEM model. The mechanical resonant frequency was measured by means of the Laser Doppler Vibrometer integrated into a Polytec MSA-500 optical profilometer. The comparison between simulations and measurements showed excellent agreement, as reported in Table 6.2.

Table 6.2: Mechanical Properties of the capacitive toggle switch.

| | Simulation | Measurements |
|---|---|---|
| Resonant frequency ($f_0$) | 12.1 kHz | 12.6 kHz |
| PI actuation voltage ($V_{act}^{PI}$) | 54.5 V | 54 V |
| PI release voltage ($V_{rel}^{PI}$) | 48 V | 50 V |
| PO actuation voltage ($V_{act}^{PO}$) | 54.5 V | 52 V |
| PO release voltage ($V_{rel}^{PO}$) | 48 V | 50 V |

Then the electromagnetic properties of the switch were extracted from S-parameter measurements, by using a simple equivalent circuit model where the membrane works as a variable capacitance. In case of the toggle switch, $C_{ON}$ is the capacitance assumed at the pull-in actuation, whereas $C_{OFF}$ is the value of the capacitance at the pull-out actuation. Moreover, if $C_0$ is the capacitance value when no bias is applied to either the pull-in or pull-out electrodes, $C_{OFF}$ is lower than $C_0$ by design, allowing for an enhanced

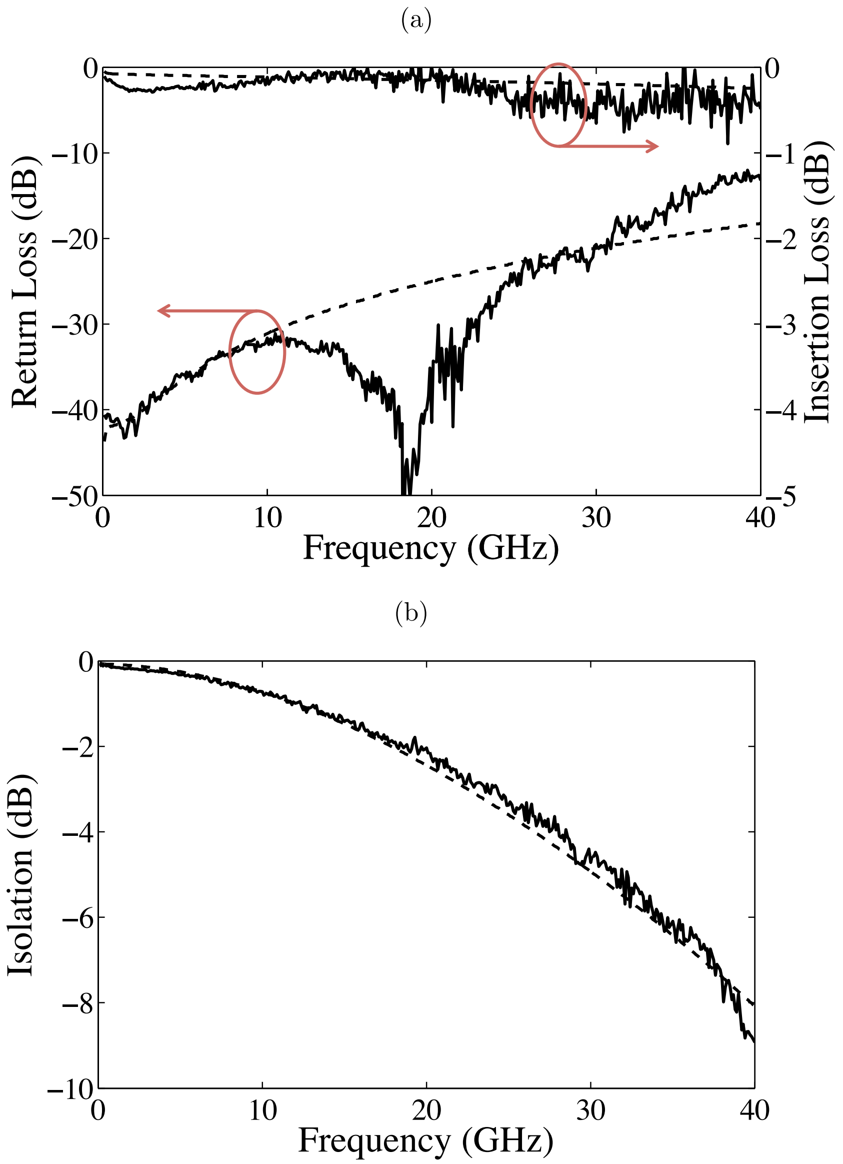

Figure 6.10: S-parameters measurements (continuous line) and circuit simulations (dashed line) for the OFF (a) and ON (b) state of the toggle switch.

capacitance ratio $C_r = C_{ON}/C_{OFF}$.

Fig. 6.10 reports OFF and ON state S-parameter measurements performed from 0.1 to 40 GHz, and the corresponding fitting with the equivalent circuit, which is reported in Fig. 6.11. Such a curve fitting allowed for the extraction of the circuit element values reported in Table 6.3. Measurements show insertion loss better than 0.5 dB and return loss better than

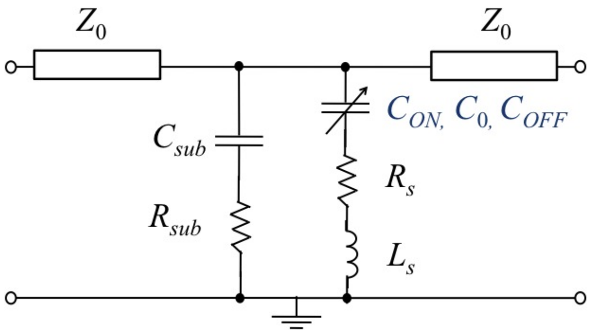

Figure 6.11: Equivalent lumped circuit of the toggle switch.

Table 6.3: Electromagnetic properties and equivalent circuit parameters of the capacitive toggle switch.

| | |
|---|---|
| Substrate dielectric constant ($\varepsilon_{Si}$) | 11 |
| Oxide dielectric constant ($\varepsilon_{ox}$) | 4 |
| Substrate capacitance ($C_{sub}$) | 500 fF |
| Substrate resistance ($R_{sub}$) | 3000 kΩ |
| Substrate loss ($\tan\delta$) | 0.002 |
| TL characteristic impedance ($Z_0$) | 50 Ω |
| Membrane inductance ($L_s$) | 19 pH |
| Membrane resistance ($R_s$) | 0.2 Ω |
| Zero-bias capacitance ($C_0$) | 27.6 fF |
| OFF-state capacitance ($C_{OFF}$) | 20.6 fF |
| ON-state capacitance ($C_{ON}$) | 249.4 fF |
| Capacitance ratio ($C_r$) | 12 |

15 dB over the whole frequency range. In the ON state the switch presents an isolation of about 10 dB at 40 GHz corresponding to a $C_{ON}/C_{OFF}$ ratio of 12, which is in a good agreement with the theoretical one. The stoppers placed besides the actuation electrodes indeed prevent the toggle central part to contact the RF line underneath, and consequently high values of $C_{ON}$ cannot be reached. On the other hand this allows for a very predictable and repeatable $C_{ON}$ since the latter is not sensitive to dielectric roughness, bridge shape factors or applied voltage.

The adopted circuital model does not account for the transmission line impedance variation in correspondence of the MEMS membrane due to the larger CPW slot width, which is needed to pattern the pull-in and pull-out electrodes. This cause a slight mismatch between the equivalent and measured return loss around 20 GHz, even though the envelopes of the two curves are pretty similar in the entire 0.1-40 GHz frequency band. This allows also for the usage of the simple equivalent circuit of Fig. 6.11 to model with pretty high accuracy the capacitance variation for different values of PI/PO bias voltages [109].

In addition, the switch was tested by monitoring the S-parameters evolution for more than 50 million cycles. The test was performed by means of a Hp 8114A pulse generator, generating a 1 KHz, 50% duty cycle, square waveform with a peak value equal to 80 V, which was applied at the PI electrodes while the PO electrodes were set to 0 V. Electric and mechanical parameters did not exhibit significant changes up to 52 million cycles, as illustrated in Fig. 6.12.

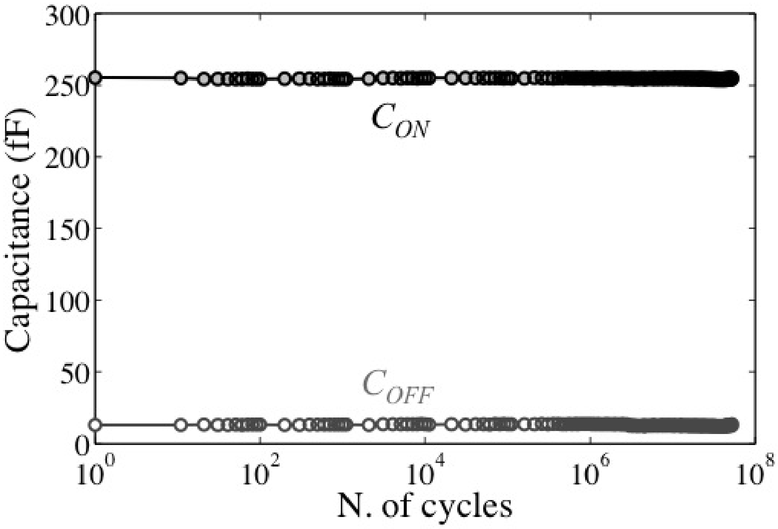

Figure 6.12: Zero-bias (△) and ON-capacitance (O) evolution extracted from the measured S-parameters as a function of the number of cycles.

### 6.3.3 Long-term reliability

The long term reliability of the switch was analyzed by keeping the toggle switch ON for a considerable amount of time. Then the effect of the dielectric charging on the whole switch operation is evaluated by monitoring the evolution of the electromechanical and electromagnetic properties during the test. For this purpose the measurement setup depicted in Fig. 6.13-a was employed. The setup is based on a Hp 8753E Vector Network Analyzer and a dual channel Keithley 2612 source meter, which allows for a simultaneous control of PI and PO electrodes. The control waveforms utilized for the test are represented in Fig. 6.13-b for clarity.

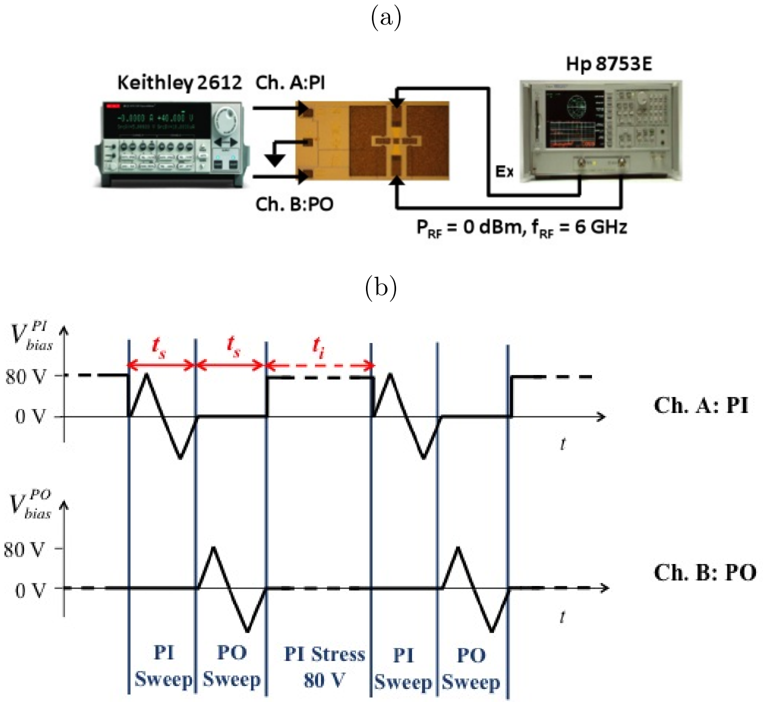

Figure 6.13: (a) Schematic of the measurement setup employed for long term performance evaluation of the switches under test, and (b) resulting waveforms applied to the PI and PO electrodes to monitor the S-parameters evolution at 6 GHz.

A continuous stress voltage of 80 V is provided to PI electrodes for increasingly longer time intervals $t_i$ (from few seconds up to $\sim$ 1 hour). Meanwhile, PO electrodes are biased at 0 V. After the stress interval, a $t_s$-

long triangular voltage waveform is applied to the PI electrodes, sweeping from 0 V up to 80 V, and then back to $-80$ V and 0 V. Immediately after, the same waveform is applied to the PO electrodes, keeping the PI electrodes at 0 V. This procedure is then repeated for a longer time $t_{i+1}$. During the sweep time $t_s$ the Vector Network Analyzer acquires the S-parameters at selected sample intervals, constantly applying a 6 GHz, 0 dBm RF signal at the switch input port.

As a result, for $t_s << t_i$ this procedure guarantees the simultaneous evaluation of the pull-in ($V_{act}^{PI}$,$V_{rel}^{PI}$) and pull-out ($V_{act}^{PO}$,$V_{rel}^{PO}$) voltages, by monitoring the S-parameters evolution at 6 GHz with respect to the test time. As expected, the PI actuation voltage decreases in time since the electrodes under stress inject charges into the substrate.

After about 6 hrs 36 min, the switch is stuck in down position. Nevertheless, after the application of a voltage sweep on the PO electrodes, the membrane is able to release and assumes again its up-state position (Fig. 6.14-a), even if charges still remain on the substrate underneath the PI electrodes. Moreover, the OFF state capacitance $C_{OFF}$ remains mostly constant over the same time range (Fig. 6.14-b), ensuring also constant long-term switch performances even in presence of dielectric charging. Fig. 6.14-b shows also a decrease of the ON state capacitance, which was unexpected. This is probably due to some mechanical deformations of the membrane induced by the pressing of the mobile electrodes on the stoppers. However, the capacitance ratio $C_r$ experiments just a slight change of about 10% of its value at $t = 0$ s.

The effectiveness of the toggle mechanism can be proved empirically for periods of time longer than 10 hours (i.e. the test duration) by extrapolating the trend of actuation and release voltages over time. Thus the voltage shifts $\Delta V_x^{PI}(t) = \left|V_x^{PI}(t) - V_x^{PI}(0)\right|$ and $\Delta V_x^{PO}(t) = \left|V_x^{PO}(t) - V_x^{PO}(0)\right|$

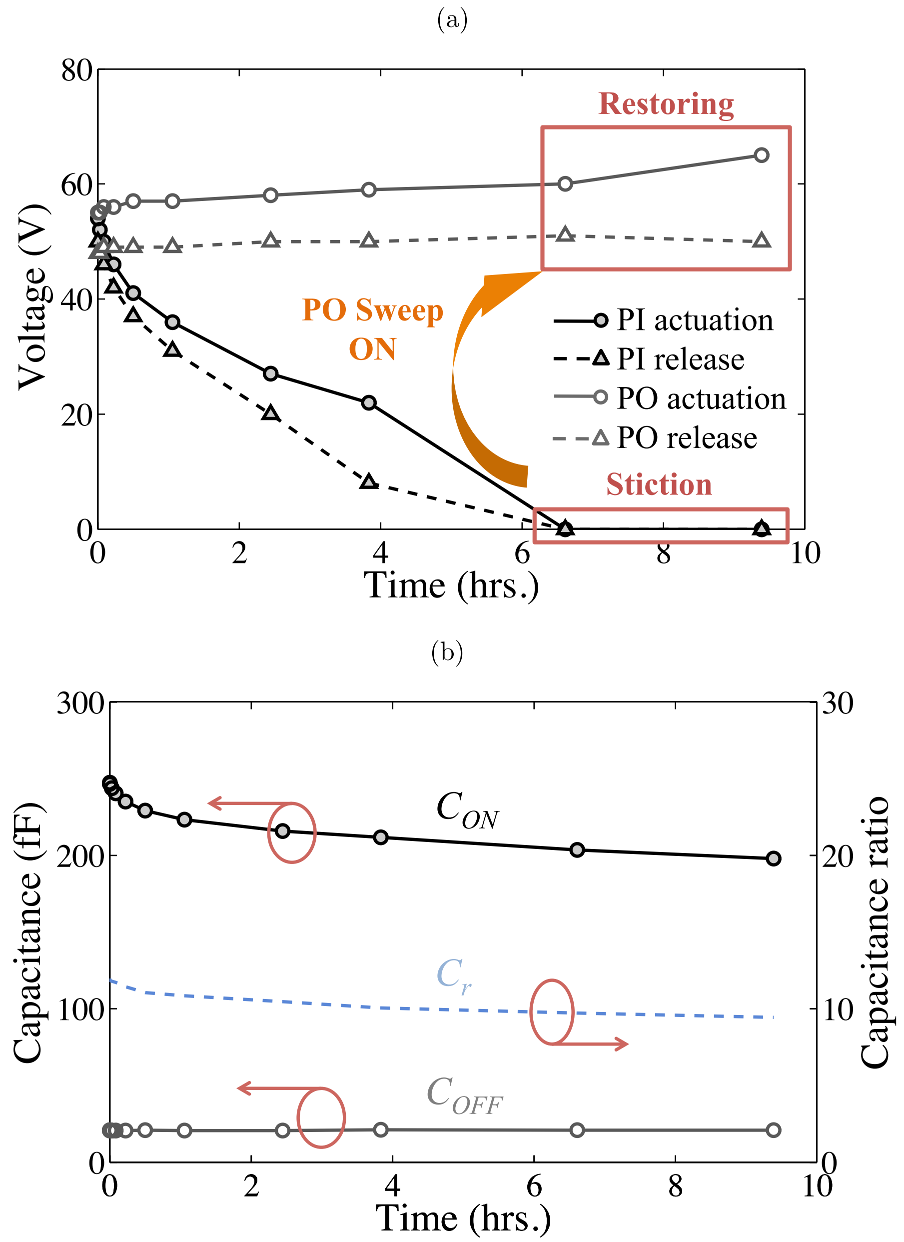

Figure 6.14: Long term reliability results: (a) evolution of actuation (o) and release (△) voltages for PI (black) and PO (grey) electrodes, and (b) evolution of ON (black) and OFF (grey) capacitances and capacitance ratio (blue) over stress time. Note that in case of ON-state stiction, the sweep on PO electrodes allows the switch to restore the OFF position.

are calculated and fitted by the following power law [19]:

$$\Delta V_x^\gamma(t) = At^n, \tag{6.19}$$

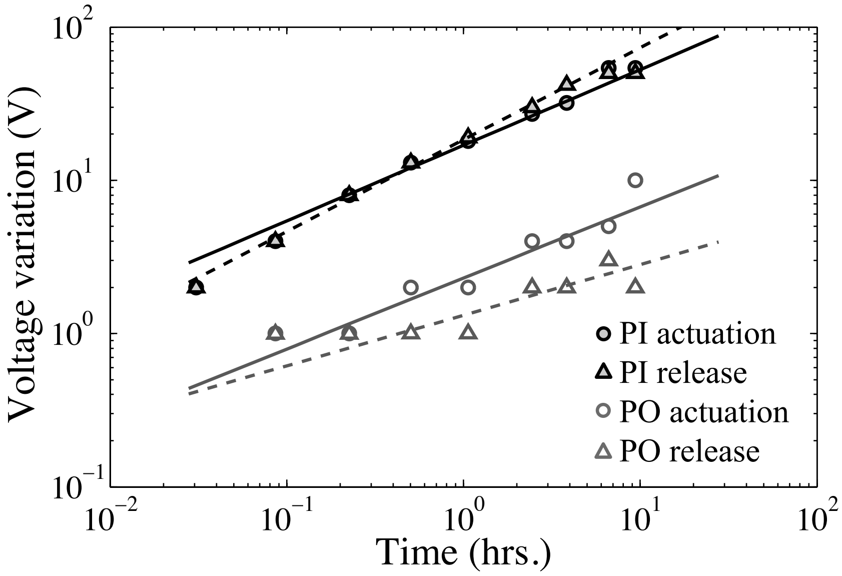

Figure 6.15: Evolution of actuation (o) and release (△) voltage *shifts* for PI (black) and PO (grey) electrodes.

where the subscript $x$ stands for $act$ (actuation) and $rel$ (release), and the superscript $\gamma$ stands for $PI$ and $PO$.

Fig. 6.15 shows the log-log scale plot of PI-PO voltage shifts evolution versus time and the corresponding fitting curves. The data points measured in the first 10 s have not been considered since the corresponding stress intervals were comparable with the sweep time $t_s$. The extracted fitting parameters $A$ and $n$ are reported in Table 6.4 for all cases. The PI release trend provides information about the temporary ON-state stiction. In this case, the best fit values for $A$ and $n$ are 0.14 and 0.6, respectively. Thus ON-state stiction is estimated to occur at a time $t_{f,ON}$, which can be calculated from Eq. (6.19) when $\Delta V_{rel}^{PI}(t_{f,ON}) = V_{rel}^{PI}(0)$ as follows:

$$t_{f,ON} = \left( \frac{V_{rel}^{PI}(0)}{A} \right)^{\frac{1}{n}}. \tag{6.20}$$

By using the values of $A$ and $n$ found for the PI release, $t_{f,ON}$ is found to be approximatively 6 hours, as also observed previously.

Table 6.4: Voltage shift fitting parameters.

|  | $A$ | $n$ |
|---|---|---|
| PI act. shift ($\Delta V_{act}^{PI}$) | 0.3 | 0.5 |
| PI rel shift ($\Delta V_{rel}^{PI}$) | 0.14 | 0.6 |
| PO act. shift ($\Delta V_{act}^{PO}$) | 0.05 | 0.5 |
| PO rel shift ($\Delta V_{rel}^{PO}$) | 0.09 | 0.3 |

For a switch in standard configuration (i.e. without pull-out mechanism), the value of $t_{f,ON}$ represents the time-to-failure at which the membrane is no longer able to change its status through the mechanical restoring force of the anchor springs. Conversely, in the toggle switch the total restoring force can be increased by the bias voltage provided at the PO electrodes, thus the upper lifetime limit of the switch depends no longer on the PI release shift but on the PO actuation shift. According to Fig. 6.15, PO actuation voltage shift follows qualitatively the same trend as the PI actuation/release shift, with $n = 0.5$. However, $A$ is equal to 0.3 and 0.05 for PI and PO actuation, respectively. This implies that PO actuation shift is scaled by a factor $0.3/0.05 = 6$ with respect to the PI actuation shift. On the other hand, the PO release evolution is not easy to evaluate since the related voltage shift is comparable with the voltage sweep step ($\approx$ 1 V).

The switch effectively fails working when the bias voltage provided to PO electrodes is not enough to recover the stuck membrane, and this happens for $\Delta V_{act}^{PO}(t_{f,eff}) = V_{bias}^{PO} - V_{act}^{PO}(0)$, where $t_{f,eff}$ is the effective switch time-to-failure. As a result, supposing that the PO actuation shift preserves the same trend after the ON-state stiction of the membrane, for $V_{bias}^{PO} = 80$ V $t_{f,eff}$ can be calculated as:

$$t_{f,eff} = \left( \frac{V_{bias}^{PO} - V_{act}^{PO}(0)}{A} \right)^{\frac{1}{n}}. \tag{6.21}$$

By utilizing $A$ and $n$ extracted from the PO actuation, the effective time-to-failure is around 180 hours. Therefore the switch lifetime is improved by a factor of $\sim$30 because of the toggle mechanism. Note that the contribution of the PO shift is only due to the charging occurring at the PI electrodes. Note also that this calculation supposes that the charging mechanism at the PI electrodes is following the exponential law forever, i.e. no saturation effects are present. In real case we can expect that at a certain time the charging effect reaches a saturation level and the corresponding down-state electric force becomes almost constant. Once this force will be known, the toggle switch can be designed so to have a pull-out force larger than the charging force at the pull-in and consequently being able to recover the switch at any time.

## 6.4 Ohmic toggle switch

The toggle mechanism can be easily implemented in series DC-contact switches. In this case, its main advantage with respect to the standard MEMS switch is that it allows for the recovering of the switch OFF-state position not only in case of dielectric charging but also in case of *contact microwelding.* The latter can occur even for short-term actuation, because of high current density flowing through the contact or because of the presence of contaminants on the contact surfaces. As a proof of the concept, a device similar to the capacitive switch presented so far was designed and fabricated by adopting an approach similar to that described in the previous Section. The micrograph of the ohmic toggle switch is shown in Fig. 6.16, where the position of the contact bumps is also highlighted. The RF line is interrupted underneath the membrane, so a couple of 50 $\mu$m wide contact wings were added in order to provide the connection between the two branches of the RF line when the switch is ON. The membrane

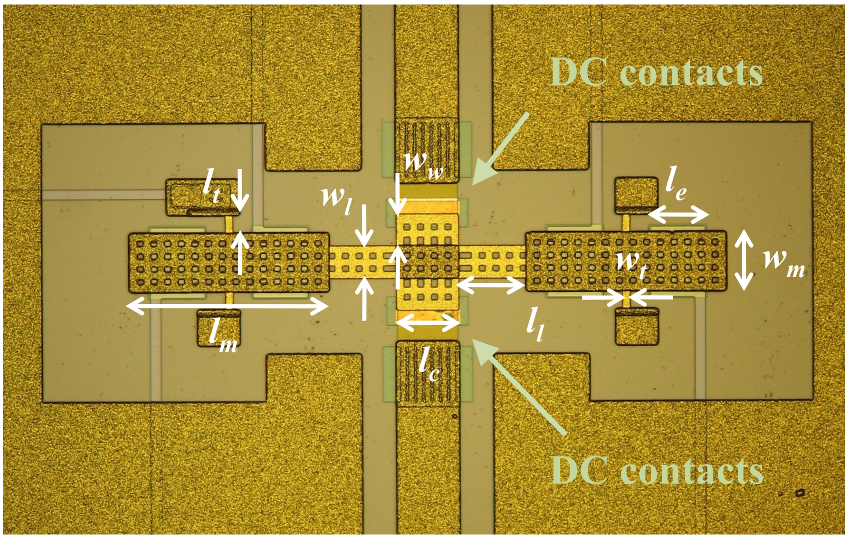

Figure 6.16: Micrograph of the manufactured DC-contact series toggle switch on 50 Ω coplanar transmission line.

dimensions are reported in Table 6.5.

Table 6.5: Geometrical dimensions of the ohmic toggle switch.

| | |
|---|---|
| Spring length ($l_t$) | 30 $\mu$m |
| Spring width ($w_t$) | 10 $\mu$m |
| Mobile electrode length ($l_m$) | 290 $\mu$m |
| Membrane width ($w_m$) | 90 $\mu$m |
| Central part length ($l_c$) | 90 $\mu$m |
| Lever length ($l_l$) | 100 $\mu$m |
| Lever width ($w_l$) | 50 $\mu$m |
| Wing width ($w_w$) | 50 $\mu$m |
| Fixed electrodes length ($l_e$) | 80 $\mu$m |

DC characterization was performed on the ohmic toggle switch by varying the compliance of the drained current through the RF line. A voltage sweep from 0 to 100 V was initially applied to the PI electrodes of all the samples under test. In one sample, microwelding was detected after the flowing of a 1 mA current between the input and output port. Further measurements on the PI electrodes confirmed that the switch was stuck to

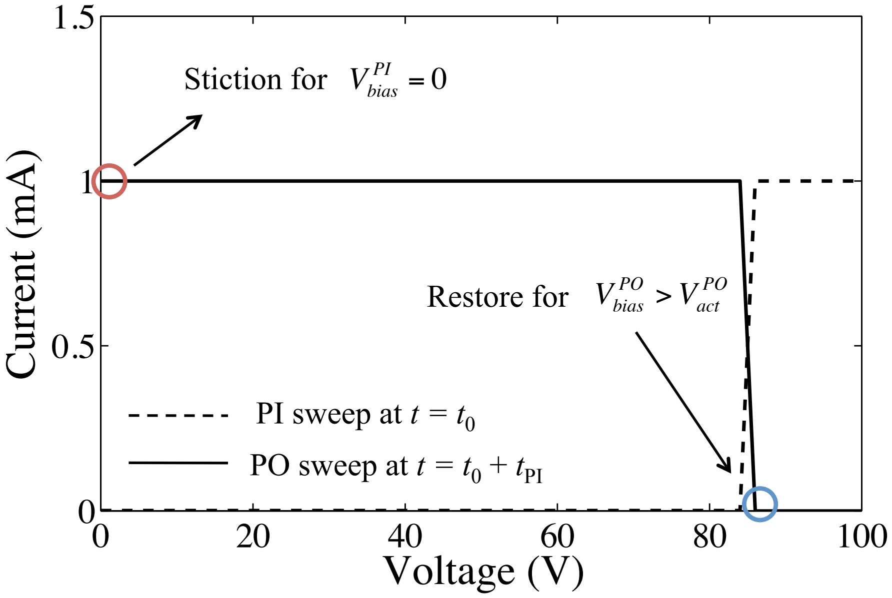

Figure 6.17: I-V characteristic of the ohmic toggle switch. A voltage sweep is applied to PI electrode at the time $t_0$, causing the stiction of the membrane (dashed line). At a time $t_0 + t_{PI}$ the voltage sweep is provided to PO electrodes (continuous line), recovering effectively the switch OFF-state.

the ON-state even if $V_{bias}^{PI} = 0$ V. Therefore a voltage sweep was performed on PO electrodes, showing immediate recovering of the switch OFF state in correspondence of the PO actuation voltage. Measurement results are shown in Fig. 6.17, proving the effectiveness of the toggle mechanisms in recovering of the switch OFF-state in case of stiction due also to microweldings.

## 6.5 Toggle mechanism for bi-stable switches

The active control of the switch states provided by the toggle mechanism showed its effectiveness to recover the switch functionality in case of stiction due to dielectric charging and microweldings. However, a further improvement of this concept can consist in the usage of the PO/PI electrodes *only* for the switch commutation, without providing any voltage to *preserve* the switch status. In order to accomplish this task, the movable membrane needs to reach a *stable* status when the switch is turned ON or OFF, which means that the device has to be mechanically *bistable*.

A bistable MEMS switch potentially realizable by using FBK technology should exhibit an *out-of-plane* instability (see Section 2.5), since the thickness of the suspended structures are much lower than the other dimensions. It is also preferable that such a device could show an actuation voltage lower than 80 V. Moreover, the final device needs to be integrated in a 50 Ω coplanar waveguide/microstrip transmission line.

The out-of-plane bistablity is the most difficult point to implement. The gold layer membrane needs to experience a controlled *buckling* after the sacrificial layer removal. The resulting shape will correspond to one of the stable status. However, the process residual stress is *tensile* ($\sigma_0 > 0$), while a *compressive* stress ($\sigma_0 < 0$) is needed in order to induce the buckling of the suspended structure. A tensile-compressive stress *converter* structure is then needed for this purpose.

### 6.5.1 Buckling of a compressive beam

In general, for a clamped-clamped beam subject to a *compressive* stress, the formulas expressed in Section 3.2.1 are not valid, since they can be used only in case of tensile stress. On the other hand, the main concern about this situation is the tendency of the beam to buckle downwards or upwards. This may eventually lead to the permanent buckling of the beam.

When buckling occurs, the beam assumes a *stable* position, and the corresponding beam deformation $v(x)$ can be calculated by solving the Euler-Bernoulli equation [111] for an axial load $P_t$ and no lateral loads:

$$\frac{d^4 v(x)}{dx^4} + \frac{P_t}{EI_b}\frac{d^2 v(x)}{dx^2} = 0 \tag{6.22}$$

where $E$ is the material beam Young's modulus, $I_b = w_b t_b^3/12$ is the moment of inertia of the beam, and $w_b$ and $t_b$ are the width and the thickness of the beam, respectively. In this case, the axial load $P_t$ is related to the compressive stress $\sigma_b$ as $P_t = \sigma_b w_b t_b$. From Eq. 6.22 it can be demonstrated that the buckling condition occurs when the stress is higher than a threshold value called *critical stress*:

$$\sigma_{cr} = \frac{\pi^2 E t_b^2}{3 l_b^2 (1 - \nu)} \tag{6.23}$$

where $l_b$ is the length of the beam, and $\nu$ is the material beam Poisson's ratio. Eq. 6.23 is also called *Euler buckling criterion.*

### 6.5.2 The Guckel Ring

If the residual stress of the thin film layer is tensile, Eq. 6.23 is not applicable, and a tensile-compressive stress converter is needed. Such a device can be implemented by exploiting the test structure geometry proposed by Guckel *et. al* [112] for process residual stress evaluation. These structures are designed to buckle once the internal stress exceeds a threshold value. A picture of a typical configuration of a Guckel ring is reported in Fig. 6.18-a. The ring converts the tensile stress of the thin film layer by inducing a compression on the beam placed along the diameter of the ring. The boundary conditions of this central beam are slightly different from the case of a clamped-clamped beam, since here the beam is anchored to the internal side of the ring. This means that at the beam sides a torsion torque $M_A = k_t \alpha_m$ in addition to the axial force $P_t$ needs to be considered as boundary conditions as depicted in Fig. 6.18-b. The moment balance at the equilibrium is:

$$M_G = M_\Gamma - k_t \alpha_m + P_t v(x) + E I_b \frac{d^2 v(x)}{dx^2} = 0 \tag{6.24}$$

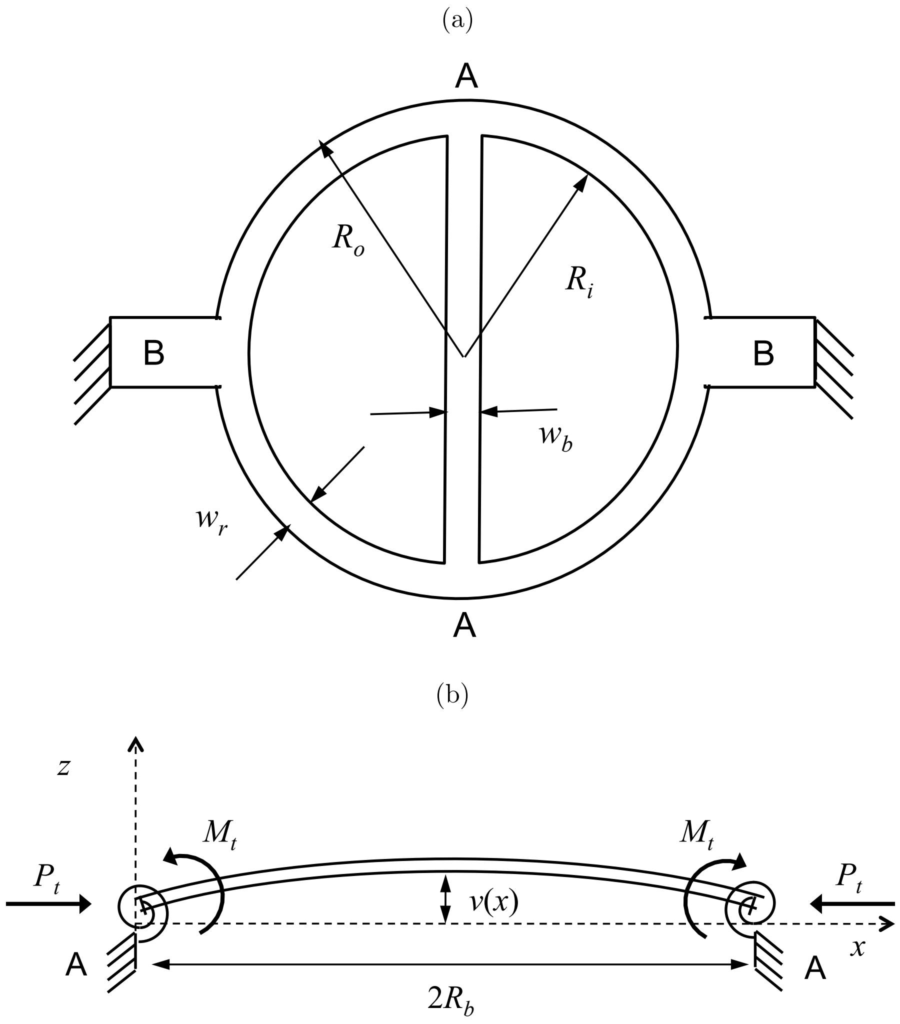

Figure 6.18: Tensile-compressive stress converter: (a) top view and (b) side view

where $\alpha_m$ is the tilt angle of the beam with respect the ring plane, $P_t = \sigma_b w_b t_b$, and $I_b = w_b t_b^3/12$, where $w_b$ and $t_b$ are in this case the width and the thickness of the central beam, $\sigma_b$ is the compressive stress that is developing along the beam, and $k_t$ is the torsion stiffness. $M_\Gamma$ is the *residual moment* due to the presence of a stress gradient $\Gamma_s$, which can be neglected if $\Gamma_s$ approaches 0 MPa/$\mu$m. The torsion stiffness at the beam supports for Guckel rings is found to be [112]:

$$k_t = 4\frac{C_1 E w_r t_r^3}{\pi R_b(6C_1 + 1 + \nu)}\left[1 - \frac{4(1+\nu-6C_1)^2}{\pi^2(1+\nu+6C_1)^2}\right]^{-1} \tag{6.25}$$

where $C_1$ is the torsion coefficient ($\approx 0.33$), $R_b = (R_o + R_i)/2$, where $R_o$ and $R_i$ are the outer and inner radius of the ring, respectively, $w_r$ is the ring section width (i.e. $w_r = R_o - R_i$), and $t_r$ is the ring thickness. By differentiating both the members of Eq. 6.24, one has:

$$\frac{d^4v(x)}{dx^4} + \xi_R^2 \frac{d^2v(x)}{dx^2} = 0, \tag{6.26}$$

where

$$\xi_R^2 = \frac{P_t}{EI_b}. \tag{6.27}$$

After applying the appropriate boundary conditions, the non-trivial solutions of this Equation need to satisfy the following condition:

$$\tan(\xi_R R_b) = -\xi_R \frac{EI_b}{k_t} \tag{6.28}$$

$$= -\gamma_R \xi_R R_b \tag{6.29}$$

where $\gamma_R = EI_b/(k_t R_b)$ is a geometric constant. The first non-trivial solution of Eq. 6.28 defines the first mode of buckling. Thus the critical *tensile* residual stress of the thin film at which the beam buckling occurs is given by:

$$\sigma_{cr} = \frac{\sigma_b}{\Phi_R} = \frac{(\xi_R R_b)^2 E t_b^2}{12 R_b^2} \frac{1}{\Phi_R} \tag{6.30}$$

where $\Phi_R$ is referred to as *conversion efficiency.* The conversion efficiency is defined as the ratio between the displacement of the beam-ring connection (identified with A in Fig. 6.18-a) and the displacement of the ring anchor points (point B in Fig. 6.18-a), and it is equal to:

$$\Phi_R = -\frac{2w_b\phi_2^2}{2w_r\phi_1 + w_b\phi_1^2 + w_b\phi_2^2} \tag{6.31}$$

where $\phi_1$ and $\phi_2$ are form factors. Under the hypothesis of thin ring (i.e. $R_i \approx R_o$), they are defined as:

$$\phi_1 = R_b \left( \frac{\pi}{8} - \frac{1}{\pi} \right), \tag{6.32}$$

and

$$\phi_2 = R_b \left( \frac{1}{4} - \frac{1}{\pi} \right). \tag{6.33}$$

If thick rings are considered, i.e. inner radius significantly shorter than outer radius, then the theory of curved beams needs to be used, and the form factors result to be:

$$\phi_1 = \left( \frac{\pi}{4} - \frac{2}{\pi} \right) \frac{R_b}{e} - \frac{2e}{\pi R} + \frac{4}{\pi} - \frac{\pi}{4} + \frac{\pi k_f (1+\nu)}{2}, \tag{6.34}$$

and

$$\phi_2 = \left( \frac{1}{2} - \frac{2}{\pi} \right) \frac{R_b}{e} - \frac{2e}{\pi R} - \frac{4}{\pi} - \frac{1}{2} + k_f (1+\nu), \tag{6.35}$$

where $k_f$ is a form factor equal to 1.2 [108], and $e$ is the ring *eccentricity* defined as $e = R_b - w_r / \ln(R_0/R_i)$. The conversion efficiency is plotted in Fig. 6.19 as a function of the ring inner radius $R_i$ for different values of ring width $w_r$. Fig. 6.20 shows instead the resulting value of tensile stress as a function of the critical value of ring radius (i.e. the ring size at which the buckling occurs) for $t_r = 2\ \mu$m and $t_r = 5\ \mu$m, corresponding to the two thickness available in FBK technology.

As said before, Guckel rings are used as test structures for the evaluation of thin film stress. The main approach consists in the design of an array of rings with increasing radius size. If $R_b^+$ is the largest unbuckled radius and $R_b^-$ is the smallest buckled radius, the effective tensile stress developed in the process is comprised between the corresponding critical stress values $\sigma_{cr}^+$ and $\sigma_{cr}^-$ calculated by using Eq. 6.30.

### 6.5.3 Bistability criteria

The solution of Eq. 6.26 allows for the calculation of *one* beam stable

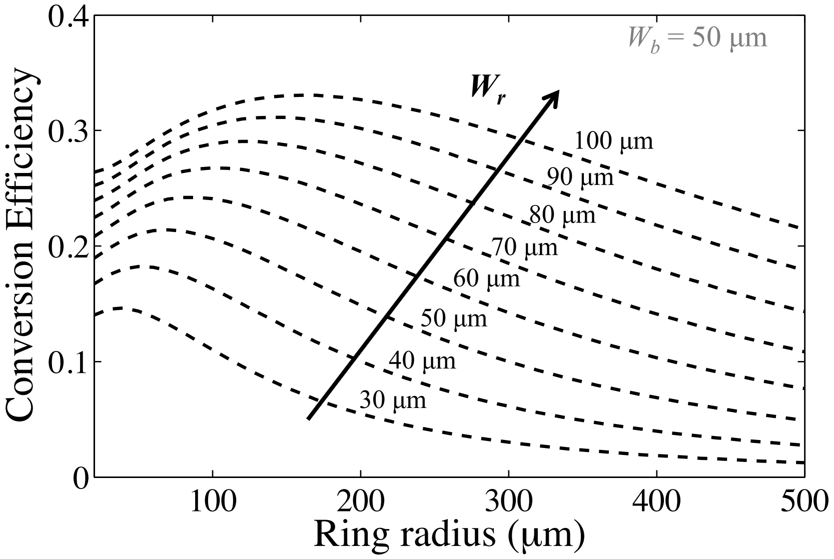

Figure 6.19: Tensile-compressive stress conversion efficiency as a function of the inner ring radius for different values of ring width.

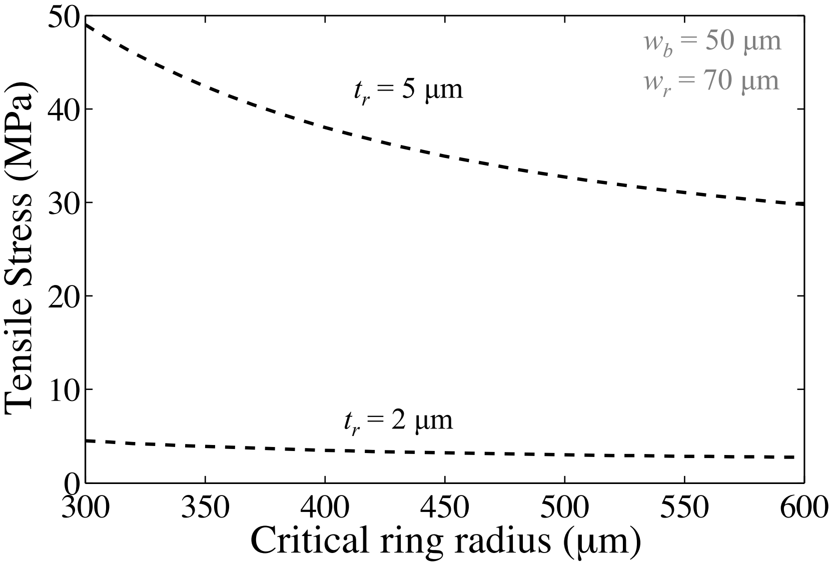

Figure 6.20: Thin film tensile stress as a function of the critical radius for a ring thickness of 2 and 5 $\mu$m.

state and the corresponding buckling shape. However, this is not enough to guarantee the bi-stability of the device. Indeed the bistable behavior can be achieved if the membrane shape is able to switch from a stable position to another stable position after the application of a certain amount of *external* force. Then the membrane shape at the stable position is found by solving the equilibrium equation:

$$M_\Gamma - M_E - k_t\alpha_m + P_t v(x) + EI_b \frac{d^2v(x)}{dx^2} = 0 \tag{6.36}$$

which is equal to Eq. 6.24, except for the addition of the term $M_E$, which represent the *external moment* applied to change the stable position. The solution of such Equation is quite complex and requires a numerical approach, since $P_t$ changes as a function of the value of the external moment. A rigorous calculation can be found in the bi-stable switch reported in [113], where the external moment is provided by a coupled electro-thermal control. In this case the control is *electrostatic*, then $M_E$ is supposed to be an electrostatic moment provided by the control voltage $V_{bias}$. From a qualitative point of view, the bi-stability can be accomplished if the following conditions are satisfied:

- The provided electrostatic moment needs to be high enough to cause the snap-through of the membrane from one position to another. This condition is satisfied when $M_E$ results higher than a *threshold moment* $M_T$. Such a value can be calculated by considering the solution of the Equation $\partial M_E/\partial P_t = 0$.

- The residual moment $M_\Gamma$, which depends on the stress gradient of the structure, has to be lower than the threshold moment $M_T$, otherwise $M_E$ will never reach the snap-through condition. If $M_\Gamma$ were higher than $M_T$, the intrinsic bi-stable nature of a buckled beam would be lost because of the stress gradient.

The main limitation of the analytical model represented by Eq. 6.36 is that the beam behavior is considered intrinsically *linear*, that is, under the assumption of *small displacements*. Other models like the one proposed in [114] include also large deformation effects, aiming at a more accurate prediction of the resulting buckled beam shape and instability conditions.

### 6.5.4 Switch design and characterization

The classic Guckel ring geometry can be re-designed in order to be used as a RF switch with *two stable states.* To achieve this, a possible approach is to integrate the toggle mechanism in the ring by adding two stiffer mobile electrodes at the central beam sides, as depicted in Fig. 6.21-a. The ring may also be split in two parts to allow for an easy integration in a coplanar waveguide (Fig. 6.21-b).

The external moment $M_E$ is then provided to the supporting edges as an electrostatic moment by exploiting PI electrodes (which are placed internally to the ring) or PO electrodes (placed outside the ring). The expression of the electrostatic moment can be obtained in the same manner of Eq. 6.3. If the beam is buckled-up, a voltage is applied to the PI electrodes allowing the beam to change its stable state. If the beam is buckled down, the voltage applied to the PO electrodes pulls the beam up again. The lateral view of the concept is depicted in Fig. 6.21-c. In both the cases, the voltage needs to be provided only to switch the beam from a stable state to the other, completely avoiding the long term voltage stress of the insulating layer covering the PI/PO electrodes.

The analytical study presented for a simple Guckel ring structure may be helpful for the fast design of a real device. Unlike the classic Guckel ring approach presented before, in this case the initial residual stress is basically known from previous measurements on the available manufacturing process, with a slight uncertainty. Then the parametric results reported in Fig. 6.19 and Fig. 6.20 can be used to extract possible dimensions for radius, width and thickness of the ring.

A good approach could be choosing a ring radius around 300-500 $\mu$m

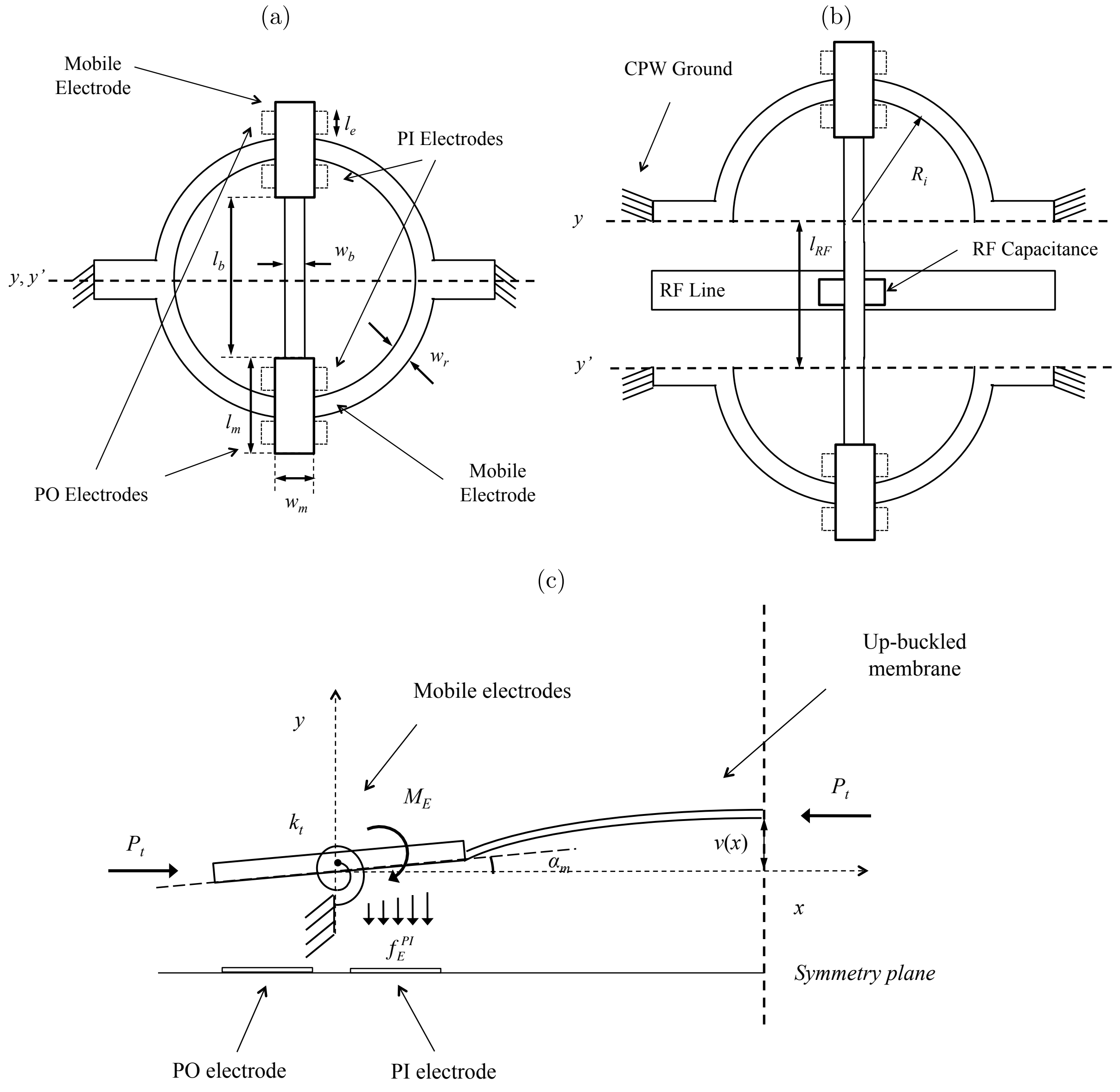

Figure 6.21: Bistable toggle switch: (a) test structure and (b) capacitive switch top view, and (c) torsion electrode side view

in order to make the buckling occur at stress values lower than 80 MPa, in agreement with the available process stress characterization. As shown in Fig. 6.20, a ring thickness of 2-$\mu$m may lead to membrane buckling for very low values of stress, leading to a possible excessive deformation of the central beam after the buckling. Such a thin structure is also more sensitive to deformation if even a slight stress gradient is present after the structure release. So a ring thickness of 5-$\mu$m is preferable. In addition, a ring width of the order of 70-90 $\mu$m may be suitable to increase the conversion efficiency, according to Fig. 6.19.

Table 6.6: Geometrical dimensions of the bistable toggle device.

| | Test structure (V1) | RF switch (V2) |
|---|---|---|
| Ring inner radius ($R_i$) | 500 $\mu$m | 400 $\mu$m |
| Ring width ($w_r$) | 70 $\mu$m | 90 $\mu$m |
| Ring thickness ($t_r$) | 5 $\mu$m | 5 $\mu$m |
| Mobile electrode length ($l_m$) | 290 $\mu$m | 310 $\mu$m |
| Fixed electrode length ($l_e$) | 100 $\mu$m | 100 $\mu$m |
| Central beam length ($l_b$) | 780 $\mu$m | 860 $\mu$m |
| Central beam width ($w_b$) | 50 $\mu$m | 50 $\mu$m |
| $y$-$y'$ distance ($l_{RF}$) | 0 $\mu$m | 250 $\mu$m |

As a proof of the concept, from this analysis two devices were designed and manufactured by means of the 8-mask manufacturing process available in FBK foundry. As explained before, the bi-stability can be guaranteed only if the residual moment due to the stress gradient is lower than the threshold moment causing the beam snap-through. Therefore the same experimental low temperature release procedure used for the toggle switch was utilized [79]. Table 6.6 sums up all the chosen dimensions for the manufactured devices.

The first device, identified as V1, is a Guckel ring implementing a toggle mechanism, as the one depicted in Fig. 6.21-a, and it serves for test purposes. The device consists of a 5-$\mu$m thick and 70-$\mu$m wide gold ring with a 500-$\mu$m inner long radius. The central beam is made of a 2-$\mu$m thick gold layer. As a consequence of the chosen geometry, the device can not be integrated in a planar microwave transmission line. Then the propagation or the interdiction of the signal through such a switch is detected by

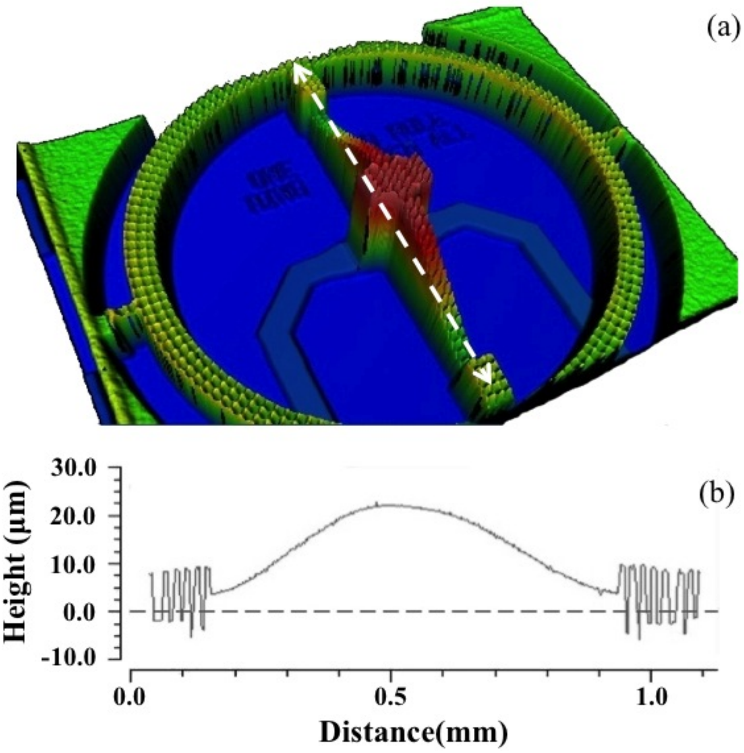

Figure 6.22: Optical profiler measurement of the bistable switch test structure: (a) 3-D view and (b) cross-section profile.

external DC pads $V^+$ and $V^-$, connecting to two separated sensing lines. So, when the beam is buckled-down, it closes a contact between the two sensing lines. Fig. 6.22 shows an optical profiler image of the bistable test-structure switch. Results show an excellent planarity of the ring, whereas the central beam is buckled up to 17 $\mu$m with respect to the planar ring bottom surface.

The second device (V2), shown in Fig. 6.23, consists of a ring split in two parts in order to allow for its integration in a 50 $\Omega$ coplanar waveguide as a capacitive shunt switch. The ring is 5-$\mu$m thick, and the radius of each semi-circle is 400-$\mu$m long. The 2-$\mu$m thick central beam is 780-$\mu$m long, considering the distance between one mobile electrodes to the other. Thus the additional beam length with respect to the ring radius (indicated as the $y$-$y'$ distance in Fig. 6.21-b) is 250 $\mu$m. The suspended part is made of

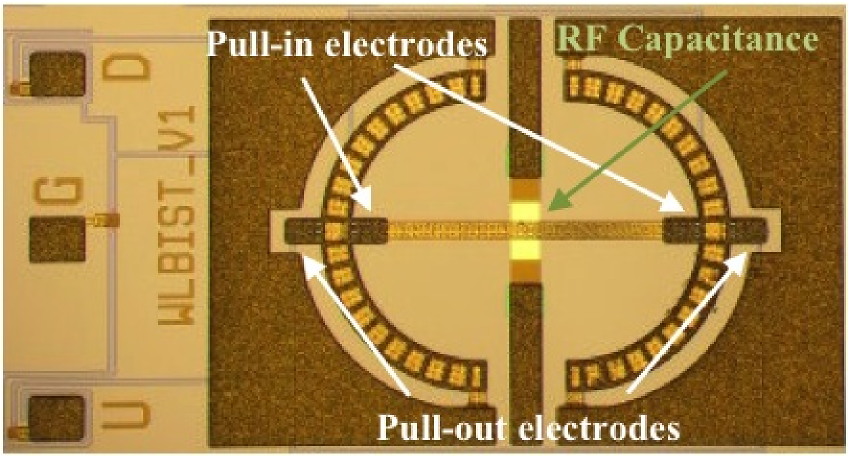

Figure 6.23: Micrograph of the capacitive bistable toggle switch on coplanar waveguide.

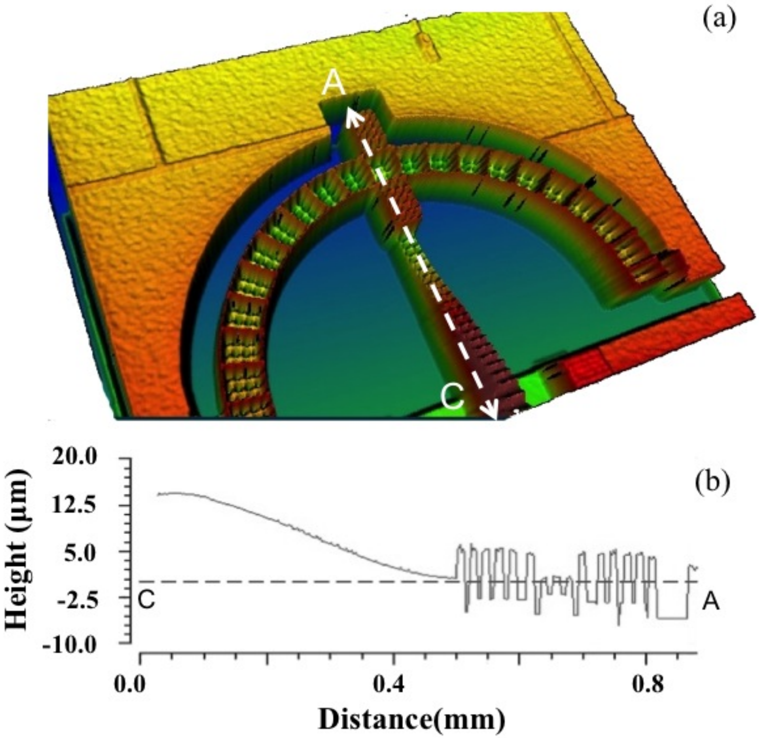

Figure 6.24: Optical profiler measurement of the bistable capacitive switch: (a) 3-D view and (b) cross-section profile.

electroplated gold, and a low temperature release process was adopted for this device as well. Even in this case optical profiler measurements show a good planarity of the ring surface, whereas the central beam is buckled up, as reported in Fig. 6.24.

### 6.5.5 Result discussion

The manufactured devices were tested in FBK by means of I-V and C-V measurement setup. Although from optical inspection the initial conditions of both the devices appeared to be quite promising, functional measurements performed on different samples showed that the devices do not work as expected. A reasonable explanation is that the up-buckling of the central beams is too large (from 16 $\mu$m to 20 $\mu$m of displacement from the bottom ring surface) to be switched to a down-buckling. From an analytical point of view, this means that the compressive stress along the central beam is related to a load force $P_t$ that the provided electrostatic moment $M_E$ cannot outperform.

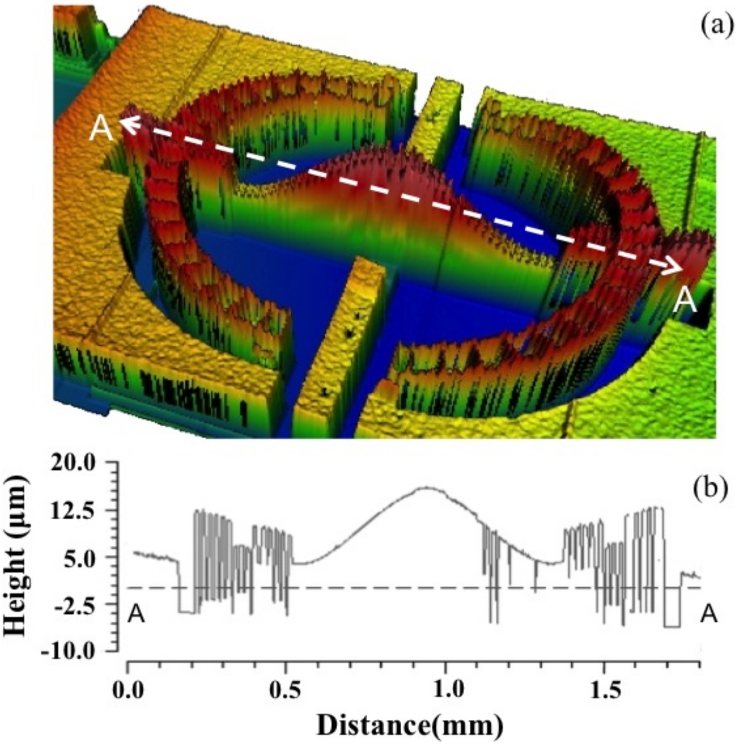

Figure 6.25: 3-D view (a) and height profile (b) of the bistable toggle switch after the CV characterization.

This explanation is supported by what observed in one of the CV measurements. Both the devices were measured by using a low-frequency setup employing a LCR meter for the measurement of the impedance (device V1) and capacitance (device V2) as a function of bias voltage. Since both the device beams were initially buckled up, the control voltage was provided to the PI electrodes. In one of the V2 samples, a slight increase of capacitance was detected, and then the resulting capacitance value, higher than the initial value, remained stable. This is symptomatic of the membrane change from one stable position to another because of the application of a voltage sweep. This was also confirmed by the subsequent optical inspection, which showed a drastic change in the ring and beam anchor points shape after the test, as depicted in Fig. 6.25, with respect to the initial shape, already shown in Fig. 6.24. Since the two optical measurements were taken very far from each other in time, a stress relaxation may be considered also a possible explanation for what observed. However, the fact that many samples next to the one under test are still planar, along with the detected capacitance variation, strongly supports the hypothesis of bias voltage-induced buckling.

Table 6.7: Finite elements properties used in the ANSYS simulations of the bistable test structure V1.

| **Parameter** | **Value** |
|---|---|
| Structural element type | SOLID186 |
| Mesh type | brick mapped mesh |
| Mesh size | 5 $\mu$m |
| Residual stress | 50 MPa |
| Stress gradient | 0 MPa/$\mu$m |
| Membrane Young modulus | 70% of 75 GPa |
| Membrane Poisson's ratio | 0.42 |
| Act. pads gap | 2.7 $\mu$m |
| RF line gap | 2.4 $\mu$m |

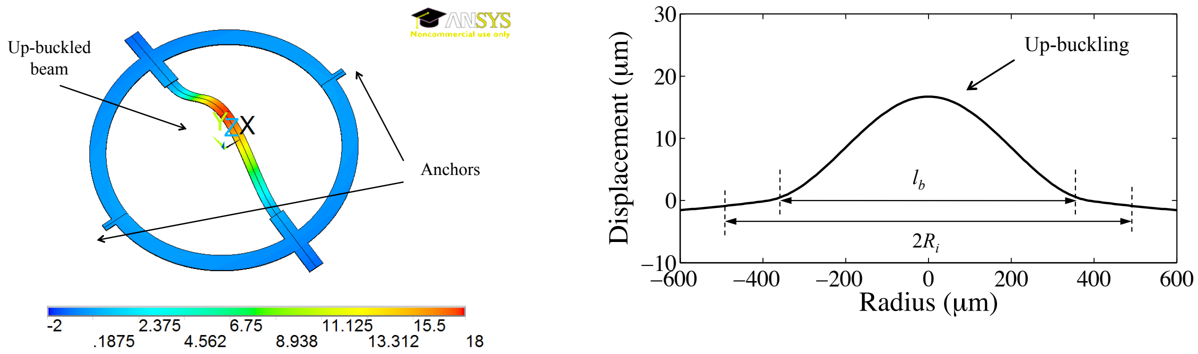
(a) (b)

Figure 6.26: FEM simulation results: (a) 3-D displacement and (b) profile along $x$-axis.

Preliminary finite element simulations were performed to reproduce the initial buckling. The parameters used for the simulations are listed in Table 6.7. A 70% of the total gold Young modulus was considered to account for the holes over the ring and the beam. As illustrated in Fig. 6.26 the simulated beam profile shows good agreement with the one measured optically. The maximum displacement achieved from the FEM model is slightly lower than 18 $\mu$m. Such a result is encouraging for the future re-design of the bistable switch, which is currently on going. In fact such a FEM model can be easily employed to design ring radius and width in order to achieve a maximum upward buckling around 3 $\mu$m, which is comparable with the maximum downward displacement set by the air gap. The critical aspects of the FEM optimization of such a structure are the pull-in/pull-out simulations, which require high computational effort to achieve a convergence in case of large displacements (from up to down buckling and vice-versa, corresponding to an abrupt change of the elements status). A further development of the analytical model will facilitate this task. A novel version of the design is estimated to be ready for the next fabrication run.

## 6.6 Conclusions

This Chapter focused on the design, modeling and characterization of active restoring mechanisms implemented in capacitive and ohmic MEMS switches. First a push/pull or toggle capacitive switch was presented and modeled in detail. A long-term characterization under continuous voltage stress was reported, demonstrating the effectiveness of the proposed mechanism for the recovering of the switch OFF-state in case of stiction caused by dielectric charging at the ON-state. Results showed indeed that even if stiction occurred after 6 hours of continuously applied bias voltage at the PI electrodes, the application of a bias voltage at the PO electrodes was effective to restore the OFF-state capacitance of the switch. The proposed predictive model accounting for the effect of the charging at the PI electrodes on the PO actuation voltage showed that the switch lifetime may be improved by a factor 30 by means of such a mechanism. In addition, the toggle mechanism was implemented also in a series ohmic switch, demonstrating to work successfully in recovering the switch OFF-state in case of microweldings on contact bumps.

Such a concept was also utilized for the design of an out-of-plane bistable switch. Measurement results showed the possibility to create compressive buckling on suspended beam in agreement with theory. They also showed that it is basically possible to change the shape of a buckled beam from one stable state to another. In addition the FEM model of the bi-stable test structure was fully validated by optical measurements. Further simulations are on-going at the moment in order to demonstrate also the possibility to achieve a bistable push/pull mechanism implemented in a RF switch.

# Chapter 7

# Conclusion

The research activity described in this thesis investigated novel design concepts and models for high reliability electrostatic RF MEMS switches. This work was developed within the ESA-ESTEC project on high reliability redundancy switches for space application. RF MEMS switches have been promising to replace the bulky electro-mechanical switches currently used in redundancy networks, assuring similar or even better performances, and leading to a drastic reduction of the size and the weight of the overall system. As a strict requirement redundancy switches in MEMS technology have to survive up to 10-15 years without any degradation in their electromechanical and electromagnetic properties. For this reason, in this thesis most of the attention has been turned to the RF MEMS long-term reliability analysis, involving both the study and the modeling of the membrane ON-state *stiction* (due to dielectric charging, contact degradation or high RF power effects) and the design of novel self-recovering mechanisms.

Long-term measurements have been performed up to 8 hours for different geometries, dielectrics, substrates and bias voltages. Moreover, an innovative analysis approach separating the effects (the *narrowing* and/or the *shift* of capacitance - voltage characteristic) of the different charging contributions was proposed and extensively used. As a result, it has been observed that the beam geometry influences the dielectric charging rate. In particular, if the charging is modeled by means of a power law of time, the charging rate $n$ for cantilever-type switches is higher than the charging rate of air bridge-type switches (0.5 versus 0.3), so the predicted time-to-failure is estimated to occur in the worst case after 4 days and 200 days for cantilever and air bridge switches respectively. This is probably due to the lower beam air-gap uniformity of the cantilever beam after the actuation. Moreover, this result suggests that a large planarity of the actuated membrane is preferred to increase the switch reliability. The above results were summarized in a paper to appear at the European Microwave Conference 2011. Finite elements models were also extensively utilized to evaluate the membrane deformation before and after the actuation, and the electric field distribution around the actuation electrode. FEM results showed high concentration of the electric field around the edges of the actuation electrode, so charge injection is demonstrated to occur also in the dielectric layers around and underneath the pad. Novel switch designs based on these analyses are currently under fabrication in FBK foundry.

Another important failure mechanism is related to power handling capacity of the RF MEMS switches. High power measurements were performed over capacitive switches on quartz and silicon substrates in the advanced RF testing laboratory at Lehigh University, USA, demonstrating the importance of the circuit environment and the substrate properties in the evaluation of the power handling. In fact, switches on silicon could handle up to 5.6 W, while the same switches on quartz showed failure at 3 W. As a proof of concept, a finite element multi-physics model involving electromagnetic, thermal, and structural domains has been implemented. Such a procedure was validated by the measurements, and it was able to reproduce the voltage sensitivity to RF power, which was 2 V/W for switches on silicon and 7 V/W for switches on quartz. An electromagnetic-thermal-mechanical compact model was also proposed for the first time, allowing for a fast evaluation of the switch power capacity. These results were included in several conference papers and they were finally summarized in a paper accepted for publication in the Elsevier Solid State Electronics journal.

An effective way to make the switch more reliable is to include in the design a self-restoring mechanism. This idea has been developed in the design of an active push/pull toggle switch, where a suspended membrane is anchored to the substrate by means of four torsion springs. Such a switch exploits also a pair of pull-in electrodes for the membrane down position (or switch ON state, as used in standard switches) and a pair of pull-out electrodes for the up position (or switch OFF state). The switch showed excellent RF performances in terms of return loss and insertion loss. It was also proved to handle more than 50 million of cycles. Long-term characterization up to 9 hours demonstrated that the membrane can recover its OFF state after the occurrence of the stiction by simply biasing the pull-out electrodes for voltage values higher then the PO actuation. An empirical model describing the toggle switch electromechanical parameters evolution was also proposed, estimating that the pull-out voltage is no longer able to restore the OFF position after 180 hours of continuous bias voltage at the pull-in electrodes. Thus the restoring mechanism is estimated to improve the lifetime of the switch up to 30 times, and it was the main innovation reported in a special issue on RF MEMS to be published at the International Journal of Microwave and Wireless Technologies, edited by Cambridge University Press.

In addition, the same self-recovering mechanism was exploited in the design of a bi-stable RF MEMS switch. A tensile-compressive stress converter structure has been designed in order to achieve an out-of-plane buckling (upwards or downwards) of the membrane. Such a structure was then readjusted in order to work as a RF switch, where the membrane can assume *two stable states* corresponding to its upwards and downwards buckling. The toggle mechanism was integrated in the switch for the control of the two stable states. The bias voltage is applied only for the time required to switch between the two stable status, so the effect of the dielectric charging for long time operations can be avoided. The novel structure has been recently manufactured with an experimental low temperature release process. The membrane was buckled up and no stress gradient was detected as predicted by finite element analysis. Nevertheless, an inaccurate prediction of the residual stress affected the full functionality of the switch, so further analysis and geometry optimization of the device were performed to overcome this problem for the next device fabrication run.

It is also worth noting that a significant improvement of the manufacturing process has been achieved in the last four years by adopting different materials, new process steps and innovative membrane release procedures. Better control of the residual stress and stress gradient, along with a better uniformity of the electroplated gold thickness will provide a significant contribution to the RF MEMS reliability assessment.

# Bibliography

[1] R. Osiander, M. A. G. Darrin, and J. L. Champion, *MEMS and Microstructures in Aerospace Applications.* Taylor & Francis, 2006.

[2] F. T. Assal, J. V. Evans, C. E. Mahle, A. I. Zaghloul, and R. K. Gupta, “Switch matrix including both B switching elements and crossbar switch matrices,” Patent, Jun., 1993, u.S. Patent 522 032 0.

[3] S. M. Senturia, *Microsystem Design.* Kluwer Academic Publishers, 2003.

[4] G. M. Rebeiz, *RF MEMS: Theory, Design, and Technology.* John Wiley & Sons, Inc., 2003.

[5] N. Barker and G. Rebeiz, “Optimization of distributed MEMS transmission-line phase shifters-U-band and W-band designs,” *IEEE Transactions on Microwave Theory and Techniques*, vol. 48, no. 11, pp. 1957 – 1966, Nov. 2000.

[6] V. K. Varadan, K. J. Vinoy, and K. J. Jose, *RF MEMS and Their Applications.* John Wiley & Sons, Inc., 2003.

[7] D. M. Pozar, *Microwave Engineering.* John Wiley & Sons, Inc., 1998.

[8] G. Rebeiz, K. Entesari, I. Reines, S. J. Park, M. El-tanani, A. Grichener, and A. Brown, "Tuning in to RF MEMS," *IEEE Microwave Magazine*, vol. 10, no. 6, pp. 55 –72, 2009.

[9] A. Verger, A. Pothier, C. Guines, A. Crunteanu, P. Blondy, J. Orlianges, J. Dhennin, F. Courtade, and O. Vendier, "Sub-hundred nanosecond reconfiguration capabilities of nanogap RF MEMS switched capacitor," in *IEEE MTT-S International Microwave Symposium Digest*, May 2010, pp. 1238 –1241.

[10] H. De Los Santos, G. Fischer, H. Tilmans, and J. van Beek, "RF MEMS for ubiquitous wireless connectivity. Part II. Application," *IEEE Microwave Magazine*, vol. 5, no. 4, pp. 50 – 65, Dec. 2004.

[11] H. Newman, J. Ebel, D. Judy, and J. Maciel, "Lifetime Measurements on a High-Reliability RF-MEMS Contact Switch," *IEEE Microwave and Wireless Components Letters*, vol. 18, no. 2, pp. 100 –102, Feb 2008.

[12] B. Pillans, J. Kleber, C. Goldsmith, and M. Eberly, "RF power handling of capacitive RF MEMS devices," in *IEEE MTT-S International Microwave Symposium Digest*, 2002.

[13] J. Costa, T. Ivanov, M. Carroll, J. Hammond, E. Glass, J. Jorgenson, D. Denning, D. Kerr, J. Reed, Q. Ren, S. Crist, T. Mercier, S. Kim, T. Mckay, P. Gorisse, and J. Gering, "Silicon RFCMOS SOI technology with above-IC MEMS integration for front end wireless applications," in *IEEE Bipolar/BiCMOS Circuits and Technology Meeting (BCTM)*, 2008, pp. 204 –207.

[14] J. Muldavin, C. Bozler, S. Rabe, P. Wyatt, and C. Keast, "Wafer-Scale Packaged RF Microelectromechanical Switches," *Microwave*

*Theory and Techniques, IEEE Transactions on*, vol. 56, no. 2, pp. 522 –529, 2008.

[15] M. Fujii, I. Kimura, T. Satoh, and K. Imanaka, "RF MEMS Switch with Wafer Level Package Utilizing Frit Glass Bonding," in *IEEE European Microwave Conference (EuMC)*, 2002, pp. 1 –3.

[16] C. Goldsmith, D. Forehand, Z. Peng, J. Hwang, and I. Ebel, "High-Cycle Life Testing of RF MEMS Switches," in *IEEE MTT-S International Microwave Symposium*, 2007, pp. 1805 –1808.

[17] A. Grichener and G. Rebeiz, "High-Reliability RF-MEMS Switched Capacitors With Digital and Analog Tuning Characteristics," *IEEE Transactions on Microwave Theory and Techniques*, vol. 58, no. 10, pp. 2692 –2701, 2010.

[18] B. Lakshminarayanan, D. Mercier, and G. Rebeiz, "High-Reliability Miniature RF-MEMS Switched Capacitors," *IEEE Transactions on Microwave Theory and Techniques*, vol. 56, no. 4, pp. 971 –981, 2008.

[19] D. Mardivirin, A. Pothier, A. Crunteanu, B. Vialle, and P. Blondy, "Charging in Dielectricless Capacitive RF-MEMS Switches," *IEEE Transactions on Microwave Theory and Techniques*, vol. 57, no. 1, pp. 231 –236, 2009.

[20] T. Rijks, J. van Beek, P. Steeneken, M. Ulenaers, J. De Coster, and R. Puers, "RF MEMS tunable capacitors with large tuning ratio," in *17th IEEE International Conference on. MEMS*, 2004.

[21] F. Casini, P. Farinelli, G. Mannocchi, S. DiNardo, B. Margesin, G. De Angelis, R. Marcelli, O. Vendier, and L. Vietzorreck, "High performance RF-MEMS SP4T switches in CPW technology for space

applications," in *IEEE European Microwave Conference (EuMC)*, 2010, pp. 89 –92.

[22] www.wispry.com.

[23] J. De Luis, A. Morris, Q. Gu, and F. De Flaviis, "A tunable asymmetric notch filter using RFMEMS," in *IEEE MTT-S International Microwave Symposium Digest*, May 2010, pp. 1146 –1149.

[24] www.isuppli.com.

[25] www.peregrine-semi.com.

[26] J. Costa, T. Ivanov, M. Carroll, J. Hammond, E. Glass, J. Jorgenson, D. Denning, D. Kerr, J. Reed, Q. Ren, S. Crist, T. Mercier, S. Kim, T. Mckay, P. Gorisse, and J. Gering, "Silicon RFCMOS SOI technology with above-IC MEMS integration for front end wireless applications," in *IEEE Bipolar/BiCMOS Circuits and Technology Meeting (BCTM)*, 2008, pp. 204 –207.

[27] I. Reines, S. J. Park, and G. M. Rebeiz, "Compact Low-Loss Tunable-Band Bandstop Filter With Miniature RF-MEMS Switches," *IEEE Transactions on Microwave Theory and Techniques*, vol. 58, no. 7, pp. 1887 –1895, 2010.

[28] A. Ocera, P. Farinelli, F. Cherubini, P. Mezzanotte, R. Sorrentino, B. Margesin, and F. Giacomozzi, "A MEMS-Reconfigurable Power Divider on High Resistivity Silicon Substrate," in *IEEE/MTT-S International Microwave Symposium*, 2007, pp. 501 –504.

[29] M. Kim, J. Hacker, R. Mihailovich, and J. DeNatale, "A DC-to-40 GHz four-bit RF MEMS true-time delay network," *IEEE Microwave and Wireless Components Letters*, vol. 11, no. 2, pp. 56 –58, Feb. 2001.

[30] T. Vaha-Heikkila, J. Varis, J. Tuovinen, and G. Rebeiz, “A 20-50 GHz RF MEMS single-stub impedance tuner,” *IEEE Microwave and Wireless Components Letters*, vol. 15, no. 4, pp. 205 – 207, 2005.

[31] J. Iannacci, F. Giacomozzi, S. Colpo, B. Margesin, and M. Bartek, “A general purpose reconfigurable MEMS-based attenuator for Radio Frequency and microwave applications,” in *IEEE EUROCON ’09*, May 2009, pp. 1197 –1205.

[32] J. Schaffner, R. Loo, D. Sievenpiper, F. Dolezal, G. Tangonan, J. Colburn, J. Lynch, J. Lee, S. Livingston, R. Broas, and M. Wu, “Reconfigurable aperture antennas using RF MEMS switches for multi-octave tunability and beam steering,” in *Antennas and Propagation Society International Symposium, 2000. IEEE*, 2000, pp. 321 –324 vol.1.

[33] K. Entesari and G. Rebeiz, “A differential 4-bit 6.5-10-GHz RF MEMS tunable filter,” *IEEE Transactions on Microwave Theory and Techniques*, vol. 53, no. 3, pp. 1103 – 1110, 2005.

[34] G. Rebeiz, G.-L. Tan, and J. Hayden, “RF MEMS phase shifters: design and applications,” *IEEE Microwave Magazine*, vol. 3, no. 2, pp. 72 –81, Jun. 2002.

[35] G. Rebeiz and K. jin Koh, “Silicon RFICs for phased arrays,” *IEEE Microwave Magazine*, vol. 10, no. 3, pp. 96 –103, May 2009.

[36] J. Herd, S. Duffy, M. Weber, G. Brigham, C. Weigand, and D. Cursio, “Advanced Architecture for a Low Cost Multifunction Phased Array Radar,” in *IEEE MTT-S International Microwave Symposium Digest*, May 2010, pp. 676 –679.

[37] M. Daneshmand and R. Mansour, “Redundancy RF MEMS Multiport Switches and Switch Matrices,” *Journal of Microelectromechanical Systems*, vol. 16, no. 2, pp. 296 –303, 2007.

[38] S. Dinardo, P. Farinelli, F. Giacomozzi, G. Mannocchi, R. Marcelli, B. Margesin, P. Mezzanotte, V. Mulloni, P. Russer, R. Sorrentino, F. Vitulli, and L. Vietzorreck, “Broadband RF-MEMS Based SPDT,” in *IEEE European Microwave Conference (EuMC)*, 2006, pp. 1727 – 1730.

[39] W. Auer, E. Hettlage, and G. Ruff, “RF-switches: Application and design,” in *ESA, Proceedings of the 3rd European Space Mechanisms and Tribology Symposium p 191-195 (SEE N88-21191 14-18)*, Dec. 1987, pp. 191–195.

[40] P. Farinelli, E. Chiuppesi, F. Di Maggio, B. Margesin, S. Colpo, A. Ocera, M. Russo, and I. Pomona, “Development of different k-band MEMS phase shifter designs for satellite COTM terminals,” in *IEEE European Microwave Conference (EuMC)*, Oct. 2009, pp. 1868 –1871.

[41] J. P. Laboratory, “MEMS Reliability Assurance Guidelines for Space Applications,” 1999.

[42] C. Goldsmith, J. Maciel, and J. McKillop, “Demonstrating Reliability,” *IEEE Microwave Magazine*, vol. 8, no. 6, pp. 56 –60, 2007.

[43] D. K. Schroder, *Semiconductor material and device characterization.* John Wiley & Sons, Inc., 2006.

[44] Z. Peng, X. Yuan, J. Hwang, D. Forehand, and C. Goldsmith, “Top vs. bottom charging of the dielectric in RF MEMS capacitive

switches," in *IEEE Asia-Pacific Microwave Conference (APMC)*, 2006, pp. 1535 –1538.

[45] G. Papaioannou, G. Wang, D. Bessas, and J. Papapolymerou, "Contactless Dielectric Charging Mechanisms in RF-MEMS Capacitive Switches," in *IEEE European Microwave Conference (EuMC)*, Sept. 2006, pp. 1739 –1742.

[46] E. Papandreou, M. Lamhamdi, C. Skoulikidou, P. Pons, G. Papaioannou, and R. Plana, "Structure dependent charging process in RF MEMS capacitive switches," *Microelectronics Reliability*, vol. 4, pp. 1812 –1817, 2007.

[47] C. Goldsmith, A. Sumant, O. Auciello, J. Carlisle, H. Zeng, J. Hwang, C. Palego, W. Wang, R. Carpick, V. P. Adiga, A. Datta, C. Gudeman, S. O'Brien, and S. Sampath, "Charging characteristics of ultra-nano-crystalline diamond in RF MEMS capacitive switches," in *IEEE MTT-S International Microwave Symposium Digest*, May 2010, p. 1.

[48] G. Papaioannou, M.-N. Exarchos, V. Theonas, G. Wang, and J. Papapolymerou, "Temperature study of the dielectric polarization effects of capacitive RF MEMS switches," *IEEE Transactions on Microwave Theory and Techniques*, vol. 53, no. 11, pp. 3467 – 3473, 2005.

[49] P. Czarnecki, X. Rottenberg, P. Soussan, P. Ekkels, P. Muller, P. Nolmans, W. D. Raedt, H. Tilmans, R. Puers, L. Marchand, and I. D. Wolf, "Effect of substrate charging on the reliability of capacitive RF MEMS switches," *Sensors and Actuators A: Physical*, vol. 154, no. 2, pp. 261 – 268, 2009.

[50] W. de Groot, J. Webster, D. Felnhofer, and E. Gusev, "Review of Device and Reliability Physics of Dielectrics in Electrostatically Driven

MEMS Devices," *IEEE Transactions on Device and Materials Reliability*, vol. 9, no. 2, pp. 190 –202, June 2009.

[51] S. Patton and J. Zabinski, "Fundamental studies of Au contacts in MEMS RF switches," *Tribology Letters*, vol. 18, pp. 215–230, 2005, 10.1007/s11249-004-1778-3.

[52] O. Rezvanian, M. A. Zikry, C. Brown, and J. Krim, "Surface roughness, asperity contact and gold RF MEMS switch behavior," *Journal of Micromechanics and Microengineering*, vol. 17, no. 10, p. 2006, 2007.

[53] B. Jensen, L. Chow, R. Webbink, K. Saitou, J. Volakis, and K. Kurabayashi, "Force dependence of RF MEMS switch contact heating," in *17th IEEE International Conference on. MEMS*, 2004, pp. 137 – 140.

[54] D. Peroulis, S. Pacheco, and L. Katehi, "RF MEMS switches with enhanced power-handling capabilities," *IEEE Transactions on Microwave Theory and Techniques*, vol. 52, no. 1, pp. 59 – 68, Jan. 2004.

[55] J. Lampen, S. Majumder, C. Ji, and J. Maciel, "Low-loss, MEMS based, broadband phase shifters," in *IEEE International Symposium on Phased Array Systems and Technology (ARRAY)*, oct 2010, pp. 219 –224.

[56] A. Tazzoli, V. Peretti, and G. Meneghesso, "Electrostatic Discharge and Cycling Effects on Ohmic and Capacitive RF-MEMS Switches," *IEEE Transactions on Device and Materials Reliability*, vol. 7, no. 3, pp. 429 –437, Sept. 2007.

[57] A. Soma and G. De Pasquale, "MEMS Mechanical Fatigue: Experimental Results on Gold Microbeams," *Journal of Microelectromechanical Systems*, vol. 18, no. 4, pp. 828 –835, 2009.

[58] M. McLean, W. Brown, and R. Vinci, "Temperature-Dependent Viscoelasticity in Thin Au Films and Consequences for MEMS Devices," *Journal of Microelectromechanical Systems*, vol. 19, no. 6, pp. 1299 –1308, Dec. 2010.

[59] W. van Spengen, P. Czarnecki, R. Poets, J. van Beek, and I. De Wolf, "The influence of the package environment on the functioning and reliability of RF-MEMS switches," in *IEEE International Reliability Physics Symposium*, 2005, pp. 337 – 341.

[60] C. Goldsmith and D. Forehand, "Temperature variation of actuation voltage in capacitive MEMS switches," *IEEE Microwave and Wireless Components Letters*, vol. 15, no. 10, pp. 718 – 720, Oct. 2005.

[61] C. Palego, J. Deng, Z. Peng, S. Halder, J. Hwang, D. Forehand, D. Scarbrough, C. Goldsmith, I. Johnston, S. Sampath, and A. Datta, "Robustness of RF MEMS Capacitive Switches With Molybdenum Membranes," *IEEE Transactions on Microwave Theory and Techniques*, vol. 57, no. 12, pp. 3262 –3269, Dec. 2009.

[62] I. Reines, B. Pillans, and G. Rebeiz, "Performance of Temperature-Stable RF MEMS Switched Capacitors Under High RF Power Conditions," in *IEEE MTT-S International Microwave Symposium Digest*, may 2010, pp. 292 –295.

[63] Z. Peng, C. Palego, J. Hwang, D. Forehand, C. Goldsmith, C. Moody, A. Malczewski, B. Pillans, R. Daigler, and J. Papapolymerou, "Impact of Humidity on Dielectric Charging in RF MEMS Capaci-

tive Switches," *IEEE Microwave and Wireless Components Letters*, vol. 19, no. 5, pp. 299 –301, May 2009.

[64] A. Tazzoli, G. Cellere, E. Autizi, V. Peretti, A. Paccagnella, and G. Meneghesso, "Radiation Sensitivity of Ohmic RF-MEMS Switches for Spatial Applications," in *IEEE 22nd International Conference on Micro Electro Mechanical Systems*, Jan. 2009, pp. 634 –637.

[65] A. Morris and S. Cunningham, "Challenges and Solutions for Cost-effective RF-MEMS Packaging," in *IEEE/CPMT International Electronic Manufacturing Technology Symposium (IEMT)*, Oct. 2007, pp. 278 –285.

[66] H. Tilmans, H. Ziad, H. Jansen, O. Di Monaco, A. Jourdain, W. De Raedt, X. Rottenberg, E. De Backer, A. Decaussernaeker, and K. Baert, "Wafer-level packaged RF-MEMS switches fabricated in a CMOS fab," in *IEEE International Electron Devices Meeting (IEDM)*, 2001.

[67] N. Nishijima, J.-J. Hung, and G. Rebeiz, "A low-voltage high contact force RF-MEMS switch," in *IEEE MTT-S International Microwave Symposium Digest*, vol. 2, 2004, pp. 577 – 580 Vol.2.

[68] D. Peroulis, S. Pacheco, and L. Katehi, "RF MEMS switches with enhanced power-handling capabilities," *IEEE Transactions on Microwave Theory and Techniques*, vol. 52, no. 1, pp. 59 – 68, Jan. 2004.

[69] J. Iannacci, A. Repchankova, A. Faes, A. Tazzoli, G. Meneghesso, and G. F. D. Betta, "Enhancement of RF-MEMS switch reliability through an active anti-stiction heat-based mechanism," *Microelectronics Reliability*, vol. 50, no. 9-11, pp. 1599 – 1603, 2010.

[70] R. Robin, O. Millet, K. Segueni, and L. Buchaillot, "Low Actuation Voltage SPDT RF MEMS K Band Switch using a Single Gold Membrane," in *IEEE 22nd International Conference on Micro Electro Mechanical Systems*, Jan. 2009, pp. 872 –875.

[71] W. Simon, T. Mack, B. Schauwecker, K. Strohm, and J.-F. Luy, "Toggle switch: investigations of an RF MEMS switch for power applications," *IEEE Proceedings on Microwaves, Antennas and Propagation*, vol. 152, no. 5, pp. 378 – 384, Oct. 2005.

[72] K. Rangra, B. Margesin, L. Lorenzelli, F. Giacomozzi, C. Collini, M. Zen, G. Soncini, L. del Tin, and R. Gaddi, "Symmetric toggle switch–a new type of rf MEMS switch for telecommunication applications: Design and fabrication," *Sensors and Actuators A: Physical*, vol. 123-124, pp. 505 – 514, 2005.

[73] M. Daneshmand, S. Fouladi, R. Mansour, M. Lisi, and T. Stajcer, "Thermally Actuated Latching RF MEMS Switch and Its Characteristics," *IEEE Transactions on Microwave Theory and Techniques*, vol. 57, no. 12, pp. 3229 –3238, Dec. 2009.

[74] A. Michael, C. Y. Kwok, K. Yu, and M. Mackenzie, "A Novel Bistable Two-Way Actuated Out-of-Plane Electrothermal Microbridge," *Journal of Microelectromechanical Systems*, vol. 17, no. 1, pp. 58 –69, 2008 2008.

[75] M. Sterner, N. Roxhed, G. Stemme, and J. Oberhammer, "Static zero-power-consumption coplanar waveguide embedded dc-to-rf metal-contact mems switches in two-port and three-port configuration," *IEEE Transactions on Electron Devices*, vol. 57, no. 7, pp. 1659 –1669, July 2010.

[76] Y. hua Zhang, G. Ding, X. Shun, D. Gu, B. Cai, and Z. Lai, "Preparing of a high speed bistable electromagnetic RF MEMS switch," *Sensors and Actuators A: Physical*, vol. 134, no. 2, pp. 532 – 537, 2007.

[77] S. M. Sze, *Semiconductor devices: Physics and Technology.* John Wiley & Sons, Inc., 2002.

[78] X. Rottenberg, H. Jansen, P. Fiorini, W. De Raedt, and H. A. C. Tilmans, "Novel RF-MEMS capacitive switching structures," in *IEEE European Microwave Conference (EuMC)*, Sept. 2002, pp. 1 –4.

[79] V. Mulloni, F. Giacomozzi, and B. Margesin, "Controlling stress and stress gradient during the release process in gold suspended microstructures," *Sensors and Actuators A: Physical*, vol. 162, no. 1, pp. 93 – 99, 2010.

[80] N. Lobontiu and E. Garcia, *Mechanics of MEMS.* Kluwer Academic Publisher, 2005.

[81] www.agilent.com.

[82] K. J. Bathe, *Finite element procedures in engineering analysis.* Prentice-Hall, 1982.

[83] www.ansys.com.

[84] Z. Cendes and J.-F. Lee, "The transfinite element method for modeling MMIC devices," *IEEE Transactions on Microwave Theory and Techniques*, vol. 36, no. 12, pp. 1639 –1649, Dec 1988.

[85] *Momentum User's Manual.* USA: Agilent Technologies, 2006.

[86] R. F. Harrington, *Field Computation by Moment Methods.* USA: Oxford University Press, 1993.

[87] R. R. E. Wang, T. Nelson, "Back to Elements - Tetrahedra vs. Hexahedra," in *Proceedings on International ANSYS Conference*, 2004.

[88] F. Solazzi, A. Repchankova, P. Farinelli, J. Iannacci, A. Faes, and B. Margesin, "Contact Modeling of RF MEMS Switches based on FEM Simulations," in *Proceedings on 10th International Symposium on RF MEMS and RF Microsystems*, July 2009.

[89] H. Kwon, S.-S. Jang, Y.-H. Park, T.-S. Kim, Y.-D. Kim, H.-J. Nam, and Y.-C. Joo, "Investigation of the electrical contact behaviors in Au-to-Au thin-film contacts for RF MEMS switches," *Journal of Micromechanics and Microengineering*, vol. 18, no. 10, p. 105010, 2008.

[90] R. Saha and W. D. Nix, "Effects of the substrate on the determination of thin film mechanical properties by nanoindentation," *Acta Materialia*, vol. 50, no. 1, pp. 23 – 38, 2002.

[91] H. Kwon, D.-J. Choi, J.-H. Park, H.-C. Lee, Y.-H. Park, Y.-D. Kim, H.-J. Nam, Y.-C. Joo, and J.-U. Bu, "Contact materials and reliability for high power RF-MEMS switches," in *IEEE 20th International Conference on Micro Electro Mechanical Systems*, Jan. 2007, pp. 231 –234.

[92] C. D. Patel and G. M. Rebeiz, "RF MEMS Metal-Contact Switches With mN-Contact and Restoring Forces and Low Process Sensitivity," *IEEE Transactions on Microwave Theory and Techniques*, 2011.

[93] K. C. Kao, *Dielectric Relaxation in Solids.* Elsevier Academic Press, 2004.

[94] X. Yuan, Z. Peng, J. Hwang, D. Forehand, and C. Goldsmith, "Acceleration of Dielectric Charging in RF MEMS Capacitive Switches,"

*IEEE Transactions on Device and Materials Reliability*, vol. 6, no. 4, pp. 556 –563, 2006.

[95] X. Rottenberg, I. De Wolf, B. Nauwelaers, W. De Raedt, and H. Tilmans, “Analytical Model of the DC Actuation of Electrostatic MEMS Devices With Distributed Dielectric Charging and Nonplanar Electrodes,” *Journal of Microelectromechanical Systems*, vol. 16, no. 5, pp. 1243 –1253, 2007.

[96] C. Palego, F. Solazzi, S. Halder, J. C. M. Hwang, P. Farinelli, R. Sorrentino, A. Faes, V. Mulloni, and B. Margesin, “Effect of Substrate on Temperature Range and Power Capacity of RF MEMS Capacitive Switches,” in *IEEE European Microwave Conference (EuMC)*, Sept. 2010, pp. 505 –508.

[97] L. Larcher, R. Brama, M. Ganzerli, J. Iannacci, B. Margesin, M. Bedani, and A. Gnudi, “A MEMS Reconfigurable Quad-Band Class-E Power Amplifier for GSM Standard,” in *IEEE 22nd International Conference on Micro Electro Mechanical Systems 2009*, 2009, pp. 864 –867.

[98] J. Ruan, G. Papaioannou, N. Nolhier, N. Mauran, M. Bafleur, F. Coccetti, and R. Plana, “ESD failure signature in capacitive RF MEMS switches,” *Microelectronics Reliability*, vol. 48, no. 8-9, pp. 1237 – 1240, 2008.

[99] A. Tazzoli, E. Autizi, M. Barbato, G. Meneghesso, F. Solazzi, P. Farinelli, F. Giacomozzi, J. Iannacci, B. Margesin, and R. Sorrentino, “Evolution of Electrical Parameters of Dielectric-less Ohmic RF-MEMS Switches during Continuous Actuation Stress,” in *Proceedings of the European Solid State Device Research Conference (ESSDERC ’09)*, Sept. 2009, pp. 343 –346.

[100] R. Herfst and al., "Time and voltage dependence of dielectric charging in RF MEMS capacitive switches," in *IEEE IRPS 2007*, April 2007.

[101] J. Hwang and C. Goldsmith, "Robust RF MEMS Switches and phase Shifters for Aerospace Applications," in *IEEE International Symposium on Radio-Frequency Integration Technology (RFIT '09)*, 2009, pp. 245 –248.

[102] J. Rizk, E. Chaiban, and G. Rebeiz, "Steady State Thermal Analysis and High-Power Reliability Considerations of RF MEMS Capacitive Switches," in *IEEE MTT-S International Microwave Symposium Digest*, vol. 1, 2002, pp. 239 –242.

[103] N. Somjit, G. Stemme, and J. Oberhammer, "Comparison of thermal characteristics of novel RF MEMS dielectric-block phase shifter to conventional MEMS phase-shifter concepts," in *IEEE European Microwave Conference (EuMC)*, Sept. 2010, pp. 509 –512.

[104] C. Palego, A. Pothier, T. Gasseling, A. Crunteanu, C. Cibert, C. Champeaux, P. Tristant, A. Catherinot, and P. Blondy, "RF-MEMS Switched Varactor for High Power Applications," in *IEEE MTT-S International Microwave Symposium Digest*, June 2006, pp. 35 –38.

[105] Y. Nishi, A. Igarashi, and K. Mikagi, "Temperature dependence of electrical resistivity for gold and lead," *Journal on Materials Science Letters*, vol. 1, no. 6, pp. 87 – 88, 1988.

[106] C. Palego, S. Hadler, B. Baloglu, Z. Peng, J. Hwang, H. Nied, D. Forehand, and C. Goldsmith, "Microwave intermodulation technique for monitoring the mechanical stress in RF MEMS capacitive switches,"

in *IEEE MTT-S International Microwave Symposium Digest*, June 2008, pp. 29 –32.

[107] C. Venkatesh, S. Pati, N. Bhat, and R. Pratap, “A torsional MEMS varactor with wide dynamic range and low actuation voltage,” *Sensors and Actuators A: Physical*, vol. 121, no. 2, pp. 480 – 487, 2005.

[108] F. Kreith, *Mechanical Engineering Handbook.* USA: CRC Press, 1999.

[109] P. Farinelli, F. Solazzi, C. Calaza, B. Margesin, and R. Sorrentino, “A Wide Tuning Range MEMS Varactor Based on a Toggle Push-Pull Mechanism,” in *IEEE European Microwave Integrated Circuit Conference (EuMIC)*, Oct. 2008, pp. 474 –477.

[110] P. Farinelli, B. Margesin, F. Giacomozzi, G. Mannocchi, S. Catoni, R. Marcelli, L. Vietzorreck, F. Vitulli, R. Sorrentino, and F. Deborgies, “”A low contact-resistance winged-bridge RF-MEMS series switch for wide-band applications”,” in European Microwave Association, vol. 10, Dec 2009.

[111] S. P. Timoshenko and J. M. Gere, *Theory of elastic stability.* USA: McGraw-Hill, 1985.

[112] H. Guckel, D. Burns, C. Rutigliano, E. Lovell, and B. Choi, “Diagnostic microstructures for the measurement of intrinsic strain in thin films,” *Journal of Micromechanics and Microengineering*, vol. 2, no. 2, p. 86, 1992.

[113] A. Michael and C. Y. Kwok, “Design criteria for bi-stable behavior in a buckled multi-layered MEMS bridge,” *Journal of Micromechanics and Microengineering*, vol. 16, no. 10, p. 2034, 2006.

[114] M. Brake, M. Baker, N. Moore, D. Crowson, J. Mitchell, and J. Houston, “Modeling and Measurement of a Bistable Beam in a Microelectromechanical System,” *Journal of Microelectromechanical Systems*, vol. 19, no. 6, pp. 1503 –1514, Dec. 2010.